

THESIS

BREAKUP OF TEMPERATURE INVERSIONS
IN COLORADO MOUNTAIN VALLEYS

Submitted by

C. David Whiteman

Department of Atmospheric Science

In partial fulfillment of the requirements

for the Degree of Doctor of Philosophy

Colorado State University

Fort Collins, Colorado

Summer, 1980

02
812
WAS
1980

COLORADO STATE UNIVERSITY

June 16, 1980

WE HEREBY RECOMMEND THAT THE THESIS PREPARED UNDER OUR SUPERVISION
BY C. David Whiteman
ENTITLED Breakup of Temperature Inversions in Colorado Mountain
Valleys
BE ACCEPTED AS FULFILLING IN PART REQUIREMENTS FOR THE DEGREE OF
Doctor of Philosophy

Committee on Graduate Work

[Redacted Signature]

Advisor

COLORADO STATE UNIVERSITY LIBRARIES

ABSTRACT OF THESIS

BREAKUP OF TEMPERATURE INVERSIONS IN COLORADO MOUNTAIN VALLEYS

Tethered balloon observations of temperature inversion breakup have been collected in seven deep Colorado mountain valleys on clear undisturbed weather days in all seasons. By sunrise, the nocturnal inversions (for 21 case studies) build to about the level of the surrounding ridgetops. On average, inversions are 604 m deep with a vertical potential temperature gradient of $.0295^{\circ}\text{K m}^{-1}$. The inversions are typically destroyed within $3\frac{1}{2}$ to 5 hours following sunrise, except when the valley is snow covered or the ground is moist. Inversions are destroyed by the growth of convective boundary layers (CBLs) over the valley floor and sidewalls, and by the descent of the top of the nocturnal inversion. The descent of the top of the inversion plays a major role in most cases. During inversion destruction, specific local wind systems are associated with layers in the vertical temperature structure profiles, but the wind structure evolution is not as consistent from day to day as the temperature structure evolution.

Three patterns of temperature structure evolution have been identified from the data. These patterns have led to a hypothesis to account for inversion destruction, in which heat and mass are entrained from the elevated inversion layer into the CBLs and are carried up the sidewalls in the slope flows. Sensible heat flux from the valley surfaces provides the energy to cause the CBLs to grow and provides the energy required to remove mass from the base of the inversion layer in the upslope flows, allowing the inversion layer to sink and warm.

Based on this hypothesis a thermodynamic model of inversion breakup has been developed. The model is composed of two coupled

equations which relate the inversion descent rate and CBL ascent rate to the sensible heat flux. The primary inputs to the model are the valley width, sidewall inclination angles, the characteristics of the valley inversion at sunrise, and an estimate of sensible heat flux obtained from solar radiation calculations. The outputs, obtained by a numerical integration of the model equations, are the time-dependent heights of the valley floor CBL and the inversion top, and vertical potential temperature profiles of the valley atmosphere. The model predicts that valley inversions will be more easily destroyed if the initial inversion is shallow or weak, if the sensible heat flux is strong, or if the valley is narrow.

Model results are compared with observations of inversion breakup taken in the Eagle and Yampa Valleys in different seasons. Simulations were obtained by fitting two constants in the model (relating to the surface energy budget and energy partitioning) to the data. The model accurately simulates the evolution of vertical potential temperature profiles and predicts the time of inversion destruction. The model indicates that a substantial fraction of the heat flux is used to drive the upslope flows that cause mass to diverge from the valley and result in a sinking of the inversion. This provides a means by which the valley atmosphere is rapidly warmed through its entire depth.

C. David Whiteman
Atmospheric Science Department
Colorado State University
Fort Collins, Colorado 80523
Summer, 1980

ACKNOWLEDGEMENTS

The author wishes to thank Dr. Thomas B. McKee for his many contributions to the research reported here. Dr. McKee provided valuable advice, encouragement, and support in all aspects of the work from the design of the experimental program, to conduct of the field experiments, and development of concepts and mathematical models. He has provided important comments and advice on early drafts of the dissertation, as well. His help is greatly appreciated.

Special support came from my wife, Johanna, who translated many of the German language papers referenced in the dissertation, provided expert editorial assistance, and expressed interest and encouragement through the whole course of the research.

The efforts of my graduate committee in directing the course of the research and making valuable constructive comments on the dissertation are appreciated.

The Field Observing Facility of the National Center for Atmospheric Research provided tethersonde, rawinsonde and other equipment as well as the valuable services of a field technician. The success of the field experiments is in large part due to the diligent professional efforts of Bob McBeth and Gerry Albright and the support of other NCAR personnel, including Steve Semmer and Gerry English. Special arrangements were made by Bob McBeth to allow the author to test and calibrate tethersonde and airsonde equipment in the NCAR Environmental Chamber and Wind Tunnel Facilities as well as at the BAO Tower experiments of October, 1978.

Thanks are due Mr. David Call, the manufacturer of the commercial tethered balloon/upper air sounding equipment that was used by the

author to collect some of the field data, for his valuable suggestions concerning the usage of the equipment, for his special efforts in making timely repairs and modifications to improve the equipment, and for his encouragement of independent calibration and testing.

Dr. Douglas Fox of the U.S. Forest Service, Rocky Mountain Forest and Range Experiment Station, helped to organize the field program at Vail, Colorado, in December, 1975, that began the author's field program. He also funded some of the author's early work until NSF funding was obtained.

A number of people provided or assisted in finding operating locations in the valleys where data were collected. These include: Ray Miller, Steve Miller, and Jim Krentler of Edwards; Dennis Murphy and Vail Associates of Vail; Matt Smith of Eagle-Vail; Tom Dunlop and Jim Smith of Aspen; Vic Mobley of Buford; Rol Holt of Paonia; Buck Rose of Poudre Canyon; Fred Johnson of Rifle; and LTV Corporation of Steamboat Springs.

Dr. John Benci, Mr. Nolan Doesken, and Dr. Owen Rhea provided weather forecasts for the field operations.

The following people participated in the collection of field data: students Eric Anderson, Greg Byrd, Mark DeMaria, James Kuenning, George Heuer, Bill Lees, Don Monteverde, and Keith Timbre; Dr. John Benci, former Assistant State Climatologist; Nolan Doesken, Assistant State Climatologist; and Ed Hamill. Ray Miller and Vic Mobley helped collect wind data. Vail Associates provided wind data from Avon, Colorado.

Data handling was accomplished with the help of Carol Chesney, Ann Briggs, and Craig Snively. Boone Seagraves provided computer

programming support. Odie Panella typed early versions of some of the chapters.

The research was supported by the Atmospheric Sciences Section, National Science Foundation under Grant ATM76-84405.

TABLE OF CONTENTS

<u>Chapter</u>		<u>Page</u>
I	INTRODUCTION	1
II	REVIEW OF PREVIOUS WORK	4
	A. General Reviews	4
	B. Inversion Breakup Over Homogeneous Terrain	5
	C. Valley Temperature Inversion Breakup	7
	D. Valley Wind Systems	13
	1. Along-Valley Wind Systems	13
	2. Along-Slope Wind Systems	18
	3. Interrelationships Between Along-Valley and Along-Slope Wind Systems	20
III	EXPERIMENTAL DESIGN	28
	A. Location of Experiments	28
	B. Synoptic Weather Conditions	33
	C. Equipment	34
	1. Tethered Balloon Data Collection Systems	34
	a. Data Collection Procedures	40
	b. Processing of Data	41
	2. Upper Air Sounding Systems	44
	a. Data Collection Procedures	46
	b. Processing of Data	47
	3. Other Equipment	49
	D. Summary of Experiments	50
IV	ANALYSIS OF DATA	52
	A. Three Patterns of Vertical Temperature Structure Evolution	52
	1. Example of Pattern 1 Temperature Structure Evolution	56
	2. Example of Pattern 2 Temperature Structure Evolution	57
	3. Example of Pattern 3 Temperature Structure Evolution	61
	B. Vertical Temperature Structure Evolution Data-21 Case Studies	63
	1. Time Relationships	67
	2. Characteristics of Fully Developed Inversions	68
	a. Depth of Valley Inversions	70
	b. Strength of Valley Inversions	71
	c. Vertical Temperature Gradients in Valley Inversions	72
	d. Seasonal Differences in Valley Inversions	72
	e. General Shape of Temperature Profiles	72

TABLE OF CONTENTS (continued)

<u>Chapter</u>		<u>Page</u>
	f. Deformations in the Profiles	77
	g. Comparison of Valley Inversions to Inversions at Grand Junction	79
	3. Inversion Descent and CBL Ascent	82
	4. Temperature Changes in the Valley Atmosphere	85
	a. Neutral Layer	87
	b. Inversion Layer	88
	c. Convective Boundary Layer	88
C.	Wind Structure Evolution	89
	1. Gradient Level Wind System	96
	2. Along-Incline Wind System	97
	3. Along-Valley Wind System	101
	4. Along-Floor Wind System	105
	5. Along-Slope Wind System	107
D.	Two-Dimensional Structure of Valley Atmosphere .	109
	1. Case Studies	115
	2. Cross-sectional Wind and Temperature Structure Evolution	118
V	MATHEMATICAL DESCRIPTION OF TEMPERATURE INVERSION DESTRUCTION	122
A.	Scale Analysis of General Equations	122
B.	Hypothesis-An Explanation of Valley Inversion Destruction	132
C.	Mathematical Model of Inversion Destruction . . .	135
	1. General Equations	135
	2. Pattern 2 Inversion Destruction	140
	3. Pattern 1 Inversion Destruction	143
	4. Pattern 3 Inversion Destruction	149
	5. Model Modification to Account for Warming of the Neutral Layer	151
D.	Comparison of Model Results with Data	154
	1. Pattern 2 Simulation-Yampa Valley, 23 February 1978	161
	2. Pattern 3 Simulation-Eagle Valley, 16 October 1977	165
VI	SUMMARY AND CONCLUSIONS	170
VII	SUGGESTIONS FOR FUTURE RESEARCH	178
VIII	REFERENCES	180
	APPENDIX A Topographic Maps of Valley Experimental Areas	187

TABLE OF CONTENTS (continued)

<u>Chapter</u>	<u>Page</u>
APPENDIX B Tests of Tethersonde Data	
Collection System	191
A. Wind Speed	192
B. Wind Direction	198
C. Dry and Wet Bulb Temperature	201
D. Pressure	206
E. Summary	208
APPENDIX C Tests of Airsonde Data	
Collection System	211
A. Rawinsonde-Airsonde Intercomparisons	212
1. First Intercomparison	213
2. Second Intercomparison	215
3. Third Intercomparison	215
4. Fourth Intercomparison	215
5. Fifth Intercomparison	218
B. Environmental Chamber-Airsonde Tests	218
1. Pressure Steps at Constant Temperature	220
2. Temperature Steps at Constant Pressure	220
C. Conclusions	223
APPENDIX D Tethersonde Data	226
APPENDIX E Extraterrestrial Solar Radiation	245

LIST OF TABLES

<u>Table</u>		<u>Page</u>
1	Topographic Characteristics of Experimental Sites	32
2	Summary of Experimental Data	51
3	Synoptic Data for Selected Case Studies	64
4	Summary of Inversion Destruction Data	65
5	1115 GMT Grand Junction Rawinsonde Data Corresponding to Valley Data of Table 4	80
6	Classification of Wind Systems	91
7	18 October 1977 Slope Sounding Data	108
8	Scale Analysis of General Equations	128
9	Model Input Parameters	156
10	Recovery Versus Elapsed Time for a First Order Sensor . .	203
11	Tethersonde Temperature Time Constant Determinations . .	204
12	Operating Characteristics of Tethersonde System TS-1A-1 .	209
13	Comparison of Concurrent Airsonde and Rawinsonde Data . .	219
14	Equation of Time Correction	250

LIST OF FIGURES

<u>Figure</u>		<u>Page</u>
1	Vertical temperature structure evolution at Tamsweg, Austria on 22-23 September 1941. Adapted from Ekhart (1949). The circled numbers indicate the hour of the soundings using a 24 hour clock	9
2	Vertical temperature structure evolution in the Mürz Valley at Neuberg, Austria on 24-25 March 1973. Adapted from Machalek (1974)	10
3	Wind system terminology	12
4	Schematic representation of energy to volume relationships between valley and plain	14
5	Scorer's (1958) scheme for the heating of a valley stable layer	22
6	Wagner's (1938) diagram of the slope wind systems during the time of up-valley wind	22
7	Schematic illustration of the normal diurnal variations of the air currents in a valley (After F. Defant, 1949). From Reid (1976)	24
8	Location of experimental area in western Colorado (DEN = Denver, GJT = Grand Junction). Base map copyright by Denoyer-Geppert Co. Used by permission . . .	29
9	Closeup of experimental area showing valley watersheds. The lowest experimental site in each watershed is shown by a dot	30
10	Tethersonde battery-powered airborne sensor and telemetry package	36
11	Normal operating configuration of tethersonde balloon and airborne package	37
12	Tethersonde equipment. Left rear-electric winch. Left to right, foreground-cassette recorder, Hewlett-Packard HP-97 Programmable Printer/Calculator, ground station with airborne package	38
13	Airsonde	45
14	Three patterns of temperature structure evolution. Potential temperature profiles are on the left and time-height analyses of CBL height and inversion top height are on the right	53

LIST OF FIGURES (continued)

<u>Figure</u>		<u>Page</u>
15	Example of Pattern 1 temperature structure evolution. Tethersonde data. Yampa Valley, 9 August 1978	58
16	Example of Pattern 2 temperature structure evolution. Tethersonde data. Yampa Valley, 23 February 1978	59
17	Example of Pattern 3 temperature structure evolution. Tethersonde data. Eagle Valley, 16 October 1977	62
18	Time-integrated solar flux on an extraterrestrial horizontal surface as a function of time of day for selected days of the year. For latitude of Steamboat Springs, Colorado	69
19	Time-integrated solar flux on an extraterrestrial horizontal surface as a function of month of year for the first n hours following sunrise. For latitude and longitude of Steamboat Springs, Colorado	69
20	Near-sunrise potential temperature profiles	73
21	Schematic diagram showing the general shape of the vertical potential temperature profiles at sunrise	75
22	Schematic diagram showing the general shape of the vertical potential temperature profiles soon after sunrise on the valley floor	75
23	Petkovšek's (1978) three types of potential temperature deformations. (a) Mixing, (b) Mixing with cooling, and (c) Mixing with warming	78
24	CBL ascent/inversion top descent for inversion destruction in the Yampa Valley. The date, site, and time of sunrise are indicated on the curves	83
25	Same as Figure 24 for the South Fork of the White Valley	83
26	Same as Figure 24 for the Eagle Valley	84
27	Same as Figure 24 for the Gore Valley	84
28	Representation of energy required to break an inversion	86
29	Typical correspondence between temperature and wind structure during valley inversion destruction	92

LIST OF FIGURES (continued)

<u>Figure</u>		<u>Page</u>
30	An upslope wind typically blows in the CBL that develops over the sidewalls during inversion destruction. Shown in the figure are two concurrent vertical potential temperature soundings, one from the valley floor and one from a sidewall	92
31	Typical wind system development at mid-morning during inversion breakup	93
32	Cross section of the slope of a mountain range at mid-morning showing the inclined thermal boundary layers and appropriate length scales. Potential temperature profiles are superimposed. The inclination angle of the western slope is given by η	95
33	Valley cross section showing the along-slope length scale, L_4 . Potential temperature profiles are superimposed. The inclination angle of the sidewall is given by α	95
34	Ekhart's (1948) diagram of the structure of the atmosphere above a mountain range	97
35	Example of up-incline wind system. Eagle Valley, 13 October 1978. Winds below the dashed line on the right side of the figure blow from west to east up the inclined western slope of the Rocky Mountains. The up-incline flow occurs within a CBL that extends to a height of 4500 m MSL (sounding number 1). The dashed potential temperature line (not data) emphasizes the potential temperature "jump" at the top of the CBL or mixed layer. Denver and Grand Junction afternoon (1715 MDT) rawinsonde soundings are shown for comparison	99
36	Channeling of up-incline winds into a valley	101
37	Time-height analysis of along-valley wind components (m sec^{-1}) as determined from tethersonde profiles taken from the floor of the Eagle Valley on 13 October 1977	104
38	Time-height analysis of cross-valley wind components (m sec^{-1}) as determined from tethersonde profiles taken from the floor of the Eagle Valley on 13 October 1977	104
39	Normalized profiles of upslope wind components in the slope flow layer over Slope Site 1 in the Eagle Valley, 18 October 1977	110

LIST OF FIGURES (continued)

<u>Figure</u>		<u>Page</u>
40	Time series of upslope wind components observed with a tethersonde 10 meters above Slope Site 1 in the Eagle Valley, 18 October 1977	110
41	Dual tethersonde data taken from a valley floor site and a valley sidewall site in the Eagle Valley on 18 October 1977. Dotted lines in the sidewall wind soundings show the vertical extent of the upslope wind layer. Dotted lines in the wind soundings taken from a site on the valley floor show the vertical extent of the up-floor wind	111
42	Dual tethersonde data taken from a valley floor site and a valley sidewall site in the Eagle Valley on 11 October 1978	112
43	Same as Figure 42 for 12 October 1978	113
44	Same as Figure 42 for 19 October 1978	114
45	Heights of CBL and inversion top as measured from dual tethersonde soundings taken from sites on the floor and on one sidewall of the Eagle Valley, 18 October 1977. Arrow indicates time of theoretical sunrise	116
46	Same as Figure 45 for 11 October 1978. First arrow indicates time of theoretical sunrise, second arrow is time of actual sunrise on the slope, and third arrow is time of actual sunrise at the valley floor site	117
47	Same as Figure 46 for 12 October 1978	119
48	Same as Figure 45 for 19 October 1978	119
49	Effect of various physical processes on temperature structure. Top to bottom, advection, subsidence, and heat flux convergence	130
50	Illustration of the hypothesis of inversion destruction. On the right side of the diagram, cross sections of a valley are shown at times t_1 , t_2 , t_3 , t_4 , and t_D . On the left are corresponding potential temperature profiles as taken from the valley center. At sunrise, t_1 , an inversion is present in the valley. At t_2 , a time after sunlight has illuminated the valley floor and slopes, a growing CBL is present over the valley surfaces. Mass and heat are entrained into the CBLs from the stable core above and carried up the sidewalls in the upslope flows. This results in a sinking of the stable core and growth of the CBLs (t_3 and t_4) until the inversion is broken (t_D) and a turbulent, well-mixed, neutral atmosphere prevails through the valley depth	133

LIST OF FIGURES (continued)

<u>Figure</u>		<u>Page</u>
51	Valley geometry and potential temperature profiles used to formulate a mathematical model of inversion destruction	136
52	Descent of inversion top as a function of time for the reference inversion simulation and for two simulations for which the single parameters indicated were changed. Pattern 2 destruction	142
53	Sensitivity of inversion destruction time to various model parameters for Pattern 2 destruction . .	144
54	Growth of CBL over flat terrain as a function of time for the modified reference inversion ($\alpha = 0, \ell \rightarrow \infty$) and for two simulations in which single parameters were changed to the values indicated. Pattern 1 destruction	146
55	Sensitivity of inversion destruction time to various model parameters for Pattern 1 inversion destruction over flat terrain	147
56	Ascent of CBL and descent of inversion top as a function of time for Pattern 1 inversion destruction in a valley for the reference simulation and for two simulations in which single parameters were changed to the values indicated	148
57	Ascent of CBL and descent of inversion top as a function of time for Pattern 3 destruction of the reference inversion for different values of k	151
58	Ascent of CBL and descent of inversion top for Pattern 3 destruction ($k = 0.2$) of the reference inversion, and for two simulations in which single parameters were changed to the values indicated	152
59	Representation of the surface energy budget	158
60	Seasonal dependence of extraterrestrial solar irradiance at solar noon for latitude of Steamboat Springs, Colorado. The value of the solar constant (1353 W m^{-2}) is given for reference	161
61	Extraterrestrial solar flux calculated for valley floor and sidewall surfaces of Yampa Valley, 23 February 1978	163
62	Comparison of model simulation of $h(t)$ with actual data for the Yampa Valley, 23 February 1978	163

LIST OF FIGURES (continued)

<u>Figure</u>		<u>Page</u>
63	Comparison of model simulation of potential temperature structure with data for the Yampa Valley on 23 February 1978	164
64	Extraterrestrial solar flux calculated for valley floor and sidewall surfaces of Eagle Valley, 16 October 1977	167
65	Comparison of model simulation of H(t) and h(t) with actual data for the Eagle Valley, 16 October 1977	167
66	Comparison of model simulation of potential temperature structure with data from the Eagle Valley on 16 October 1977	169
67	Topographic map of Eagle and Gore Valleys. North is at the top of the figure. Contour interval is 500 feet. The first dot on the left indicates the location of the Steve Miller Residence and the Ray Miller Ranch (sites 8 and 9, Table 1). The remaining dots indicate (left to right) sites 13, 14, 15, 16 and 17	188
68	Topographic map of South Fork of White Valley. North is at the top of the figure. Contour interval is 500 feet. The three dots (left to right) indicate sites 4, 5 and 6, Table 1	189
69	Topographic map of Yampa Valley. North is at the top of the figure. Contour interval is 500 feet. The two dots (left to right) indicate sites 2 and 3, Table 1	190
70	NCAR Wind Tunnel. Photo courtesy of NCAR	193
71	Closeup of test section of NCAR Wind Tunnel. Control panels are on the operator's console at right. Photo courtesy of NCAR	193
72	NCAR Computer-Controlled Environmental Chamber. The one-cubic-meter chamber is on the left and the computer controller is on the right. Photo courtesy of NCAR	194
73	Comparison of tethersonde wind speed data to wind tunnel data	195
74	Tethersonde balloon trajectory in strong winds	197
75	The tethersonde balloon does not respond to eddies less than about $\frac{1}{2}$ the size of the balloon	200

LIST OF FIGURES (continued)

<u>Figure</u>		<u>Page</u>
76	The balloon may respond slowly to a 180 degree wind direction change when profiling. The balloon may drift overhead, and change direction only when a tight tether line is encountered	200
77	Test of tethersonde wind direction data	201
78	Tests of tethersonde temperature data in the NCAR Environmental Chamber	202
79	Test of response time of tethersonde temperature system	204
80	Tests of tethersonde pressure data in the NCAR Environmental Chamber	207
81	Drive train for Rawinsonde/Airsonde intercomparison flights	213
82	Airsonde/Rawinsonde intercomparison, 22 September 1978	216
83	Airsonde/Rawinsonde intercomparison, 26 September 1978	217
84	Airsonde/Rawinsonde intercomparison, 27 September 1978	220
85	Pressure comparison data for five airsondes in NCAR Environmental Chamber tests	222
86	Temperature comparison data for six airsondes in NCAR Environmental Chamber tests	224
87	Tethersonde data. Yampa Valley, 10 August 1978	227
88	Tethersonde data. South Fork White Valley, 26 August 1978	228
89	Tethersonde data. South Fork White Valley, Stillwater Site, 27 August 1978	229
90	Tethersonde data. South Fork White Valley, Mobley Site, 27 August 1978	230
91	Tethersonde data. South Fork White Valley, Mobley Site, 29 August 1978	231
92	Tethersonde data. South Fork White Valley, River Cabin Site, 29 August 1978	232

LIST OF FIGURES (continued)

<u>Figure</u>		<u>Page</u>
93	Tethersonde data. Eagle Valley, 13 October 1977 . . .	233
94	Tethersonde data. Eagle Valley, 14 October 1977 . . .	234
95	Tethersonde data. Eagle Valley, 20 April 1978	235
96	Tethersonde data. Eagle Valley, 8 July 1978	236
97	Tethersonde data. Eagle Valley, 9 July 1978	237
98	Tethersonde data. Eagle Valley, 11 October 1978 . . .	238
99	Tethersonde data. Eagle Valley, 12 October 1978 . . .	239
100	Tethersonde data. Eagle Valley, 19 October 1978 . . .	240
101	Tethersonde data. Gore Valley, 10 December 1975 . . .	241
102	Tethersonde data. Gore Valley, 19 October 1977	242
103	Tethersonde data. Gore Valley, 6 July 1978	243
104	Tethersonde data. Gore Valley, 7 July 1978	244

Chapter I

INTRODUCTION

Temperature in the atmosphere normally decreases with height. An atmospheric layer in which temperature increases with height is known as a temperature inversion. The various types of temperature inversions are generally classified by their position in the atmosphere (elevated or surface-based inversions) and by the processes that are primarily responsible for their formation (radiation, subsidence, turbulence, or frontal inversions). Surface-based radiation inversions are a common and important feature of the meteorology and climate of mountain valleys. They are recognized by many mountain travelers who observe a strong decrease in temperature when descending into a mountain valley after dark, especially in the winter. The basic characteristics of the typical inversion evolution on clear weather days are fairly well known. Temperature inversions begin to build up in valleys around sunset, when the air over the slopes and valley floor cools in response to loss of long wave radiation from the ground. Inversion buildup is facilitated by the flow of cooled air down the slopes to form a pool of cold air over the valley floor. Temperature inversions are usually destroyed after sunrise as a positive radiation balance at the ground results in heat transfer to the valley atmosphere. The details of the physics of the evolution are poorly understood, however, due mainly to a shortage of relevant observational data. This shortage of observational data on the structure and evolution of valley temperature inversions has been recognized by many investigators who have studied closely related problems. Scorer (1973), while considering air pollution dispersion in complex terrain, stated that "very little in

the way of detailed recordings of the wind and structure of the atmosphere has been done in valleys, which is where most of our air pollution problems occur." Geiger (1965), in reviewing valley wind circulation literature, also comments on the lack of vertical structure data, stating that "Only rarely have valley winds been investigated both in vertical extent and in their relation to temperature." Similarly, Reid (1976), in a study of dispersion in a valley atmosphere, stated that "New and basic research is needed on the structure and development of mountain valley inversions." The importance of studying the evolution of valley inversions and wind structures has become increasingly apparent in the U.S. over the past 15 years as solutions have been sought for problems in agriculture, forest management, biometeorology, climate, and especially air pollution. It is generally acknowledged that the air pollution dispersion capabilities of the valley atmosphere will be a crucial determinant in the search for environmentally acceptable recreational and energy development sites. The dispersion capabilities depend on the interrelated evolutions of wind systems and temperature structure. A great deal of effort has been expended on the study of the evolution of turbulent and mean wind structure in valleys of the world, but, almost without exception, the studies have neglected the related evolution of thermal structure, despite known interrelationships between thermal and turbulent structure over homogeneous terrain.

Theoretical studies of valley meteorology in general and thermal structure in particular are at a very early stage. This is due to the lack of observational data required to verify theoretical work and in part to the restricted use of traditional theoretical tools, such as similarity theory, previously developed for flat terrain.

This dissertation is an effort to gain a better understanding of the general characteristics of inversion evolution over complex terrain by studying one stage in the evolution of valley temperature inversions, namely the breakup or destruction of the nocturnal inversion. First, previous literature is reviewed to find out what is already known about temperature inversion structure evolution during the inversion breakup period. Related information concerning inversions over flat terrain and valley wind systems is also briefly reviewed in order to gain a broader perspective on the problem. After a discussion of experimental design, inversion destruction data collected during an observational program in different seasons in Colorado mountain valleys is reviewed and analyzed. Twenty-one case studies from four valleys were selected for analysis from 375 tethered balloon ascents and 53 airsonde soundings collected in twelve field experiments. A general picture of the inversion destruction phenomenon is developed by induction. Through a combined use of observations and theory, the most important physical processes leading to inversion destruction are identified, and an hypothesis is developed to explain the observations. From the hypothesis, a thermodynamic model of temperature structure evolution is developed that can simulate inversion breakup. The model is tested against specific data sets to determine how well it performs in simulating the evolution of temperature inversion structure in specific instances where valley topography, initial inversion structure and other external parameters differ.

Chapter II

REVIEW OF PREVIOUS WORK

A. General Reviews

A number of general reviews of research on temperature inversions are available. A selected annotated bibliography on temperature inversions in the troposphere was published by R. S. Quiroz (1956). This work includes many references to radiative inversions and to early studies conducted in mountain valleys. Austin's (1957) report includes an important review of ground-based inversions, as does Belmont's (1958) paper. Other sources, dealing mostly with the effects of temperature inversions in the near-ground environment on climate and frost danger, are the important works of Geiger (1965), Yoshino (1975), and Schnelle (1963). Geiger's book reviews temperature inversion research up to 1960. Yoshino's book extends Geiger's review and includes several more recent studies of temperature inversions. Schnelle's book is a comprehensive review of the biological and meteorological aspects of frost damage. It includes a bibliography on frost literature and a chapter on frost forecasting, both by M. Schneider, as well as chapters by A. Baumgartner entitled "The Influence of Terrain on the Location and Movement of Nocturnal Cold Air" and "Heat Exchanges of Surfaces and Plants." Unfortunately, this important book has not yet been translated into English, and has thus not been widely read by English-speaking meteorologists. The paper by Holzworth and Fisher (1979), summarizing temperature inversion data as taken from the U.S. rawinsonde network is also to be recommended as an important general reference on temperature inversion characteristics.

B. Inversion Breakup Over Homogeneous Terrain

New instrumentation systems and new theoretical tools developed during the last 20 years have greatly increased our understanding of the physical processes responsible for the breakup of temperature inversions over homogeneous terrain. Mathematical models of inversion breakup have been developed that describe the general features of the changing thermal structure. Formulation, testing, and verification of these models have been facilitated by carefully designed field programs in which the changes in temperature structure have been observed on appropriate time and space scales.

A surface-based radiation inversion over flat terrain is generally broken by the upward growth from the ground of a convective boundary layer (CBL). The inversion is destroyed when the convective boundary layer reaches the top of the inversion. Originally, the encroachment of a warming CBL into the base of an inversion layer was thought to be accomplished solely by the upward flux of sensible heat from the ground after sunrise (Carson and Smith, 1974). The CBL grows as mass is transported across the top boundary of the CBL from the elevated inversion layer above. More recently, the role of downward sensible heat flux at the top of the CBL has been recognized as being a significant factor in explaining the evolution of temperature structure that accompanies inversion breakup. The downward heat flux at this level is associated with the transport of mass from the warmer stable core into the CBL below. Ball (1960a) was the first to develop a thermodynamic model of inversion breakup due to CBL growth that had, as its basis, conservation of potential heat and mass. Ball's model, formulated to predict the upward growth of a mixed layer into an inversion, stressed

the importance of surface heating and penetrative convection in producing two effects. First, the air in the CBL increases in potential temperature due to heating at its base and the entrainment of warm air into it at its top and, second, the growth of the CBL is due to a net transfer of mass downward at its top. The growth rate of the CBL, and thus the rate at which the inversion is destroyed, is affected primarily by the upward sensible heat flux at the ground and the characteristics of the fully-developed inversion at sunrise. A synoptic scale subsidence field, if present at the top of the growing CBL, is a factor that will slow its growth rate since its existence implies that mass diverges horizontally from the CBL. Ball's thermodynamic model was formulated in terms of potential temperature, rather than actual temperature. The advantages of this formulation are such that its use in thermodynamic models of CBL growth has become general practice. The presence of water vapor in the atmosphere could be accounted for in CBL models by using virtual potential temperature as the temperature variable. However, in dry convective models potential temperature is usually used. In terms of potential temperature, an inversion is generally considered to be a layer in which potential temperature increases with height or in which the temperature lapse rate is less than the dry adiabatic lapse rate. For thermodynamic calculations, a CBL is usually considered to be a layer in which potential temperature is independent of height. It has been pointed out by Tennekes (1973) and others that, in reality, a small variation of potential temperature with height is usual within the CBL.

A number of other investigators have since made contributions to the further development of Ball's ideas. Lilly (1968) improved Ball's

model by providing more realistic bounds on the downward flux of sensible heat at the top of the CBL. The laboratory similarity modeling work of Deardorff et al., (1969) has improved the understanding of the processes that occur when convective plumes penetrate into an elevated stable layer. Stull (1973) has applied this work to develop a model of CBL growth with a more detailed parameterization of the processes occurring at the interface. An alternative mathematical formulation of CBL ascent has been developed by Tennekes (1973). By and large, the models have been successful in simulating CBL growth in a variety of conditions where the effects of advection are not pronounced (e.g., Tennekes and van Ulden, 1974; Yamada and Berman, 1979). The formulation and the testing of the various models has benefitted greatly from carefully designed field experiments where frequent soundings and surface energy budget data were taken during the period of CBL growth. Acoustic sounders (Hall, 1972) and tethered balloons (Readings et al., 1973), among other sensors, have proven to be useful observational tools for studying temperature inversion breakup.

C. Valley Temperature Inversion Breakup

Two investigators, E. Ekhart and A. Machalek, have previously reported on inversion breakup in deep mountain valleys. Their contributions are particularly significant since they represent frequent observations of the evolving temperature structure through the entire depth of the valley inversions. Neither investigator had corresponding wind structure data, however.

Ekhart (1949) presented a set of radiosonde soundings taken at approximately 2-hour intervals from Tamsweg, Austria, in the upper Mur Valley during a clear 24 hour period from noon on 22 September 1941

(Figure 1). This set of data shows both the buildup and the breakdown of a valley inversion. The evolution of the inversion during the 24 hour period was accompanied by a 23-24°C temperature range at the valley floor, and the inversion persisted, sometimes in an elevated form, for more than 3/4 of the period. The remnants of the previous night's inversion were still present during the first part of the warming cycle on September 22nd, extending from 240 to 630 m at 1100 LT. By 1500 LT the valley inversion had been broken and the well-mixed atmosphere was dry-adiabatic. Cooling began in late afternoon and continued through the night resulting in a 10°C inversion over a depth of 1000 m, approximately the depth of the basin. The period of inversion breakup on the morning of September 23rd is of particular interest here. The inversion layer underwent an abrupt change in structure between the pre-sunrise sounding at 0500 LT and the post-sunrise sounding at 0700 LT. In addition, a 200 m deep convective boundary layer developed adjacent to the ground. The depth of this layer did not increase significantly in later soundings, although the top of the inversion descended from 950 m to approximately 650 m by 1200 LT. Other observations taken during the same experimental program were published by Ekhardt in 1948. These observations were used to test Wagner's (1932, 1938) hypothesis of mountain and valley wind circulations. Sequential radiosonde observations taken from the Alpine valley station of Sulzau, Austria, on 5 September 1941, showed that the atmosphere above the level of the mountain crests has its own diurnal temperature oscillation that differs in amplitude and phase from that in the valley atmosphere below. Ekhardt concluded from this that the mountain chain acts as an elevated heat source during the day,

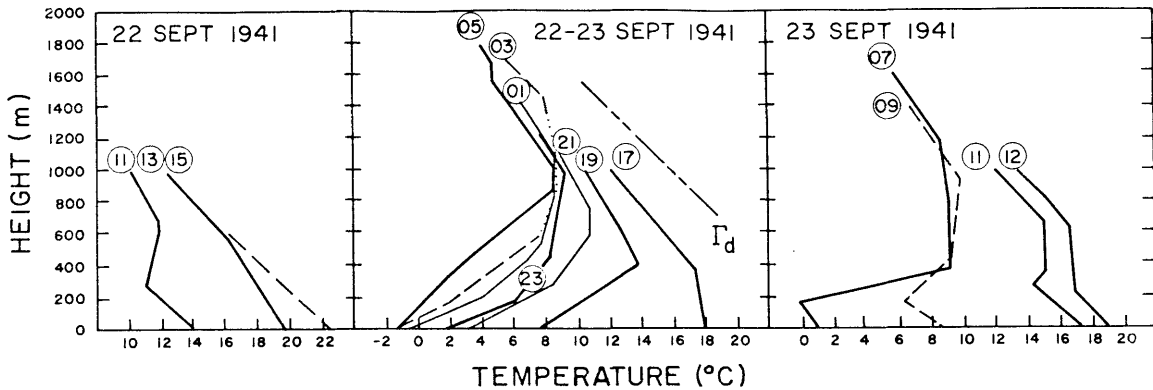


Figure 1. Vertical temperature structure evolution at Tamsweg, Austria on 22-23 September 1941. Adapted from Ekhart (1949). The circled numbers indicate the hour of the soundings using a 24 hour clock.

establishing a daily temperature variation above it that is independent of the valley (and slope) atmosphere.

Machalek (1974) has recently presented a valuable descriptive account of temperature structure evolution in the narrow Mürz Valley of Austria. A series of temperature profile measurements on good weather days was taken using a tethered balloon sounder and a network of thermographs on the mountain slopes. The Mürz Valley runs NW to SE with a base elevation of 700 m MSL and ridge elevations as high as 1600 m MSL. Several significant features of temperature structure evolution observed during this experiment were presented in the form of a case study for 24-25 March 1973 (Figure 2) and include:

(1) the initial development of a surface-based inversion in the valley as early as 1400 LT, apparently caused by cold air descending from the shaded slopes;

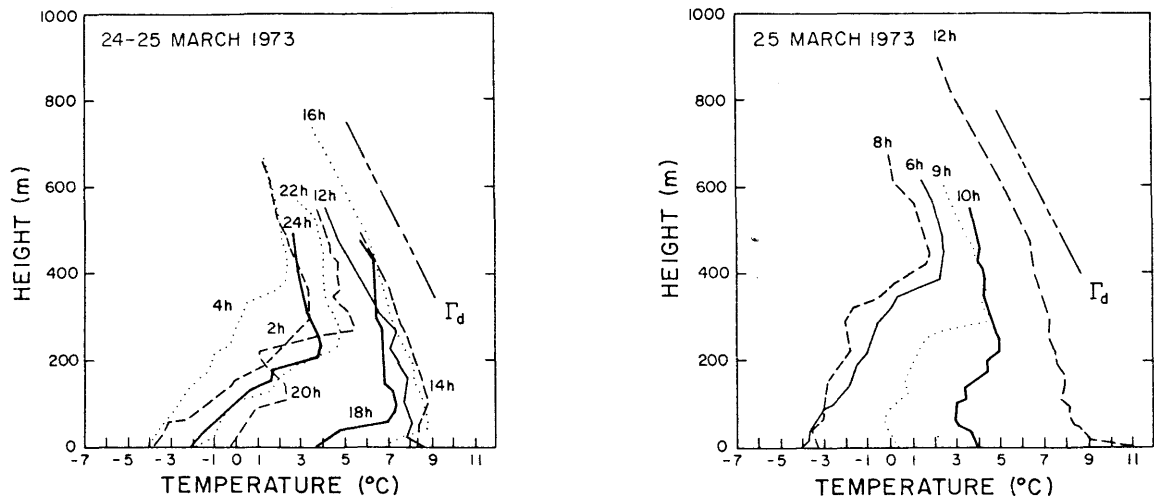


Figure 2. Vertical temperature structure evolution in the Mürz Valley at Neuberg, Austria on 24-25 March 1973. Adapted from Machalek (1974).

(2) the gradual buildup of inversion depth through the night, until reaching 500 m at 0600 LT with a temperature difference of almost 7°C; and

(3) the dissipation of the inversion in the hours between sunrise and noon accomplished by two processes, the heating of a boundary layer near the ground by solar insolation, and the lowering of the upper boundary of the inversion.

Several more recent observations of temperature inversion breakup in mountain valleys have been provided by Banta and Cotton (1979), George (1979), and Whiteman and McKee (1977, 1978, 1979, 1980). Banta and Cotton's observations were taken in Colorado at the edge of a broad, high plateau surrounded by mountains. The main features of the destruction of the 275 m deep nocturnal inversion were the reversal of

the nocturnal drainage flows after sunrise and the growth of a CBL containing upslope winds. Once the inversion was broken by the growing CBL in the afternoon, the strong westerly gradient winds in a neutral layer aloft were mixed downward to the surface. George's (1979) observations a few days earlier at the same location show a somewhat different outcome. Reversal of the initial shallow downslope winds occurred within one to two hours after sunrise and a CBL containing upslope winds grew upwards from the ground. But the initially strong westerly winds in a neutral layer above the inversion failed to mix downwards to the surface and were replaced by local upslope and up-valley winds.

Whiteman and McKee (1977) reported on early results of their first field program, conducted in December 1975 in Colorado's Gore Valley. Implications of the hypotheses developed from their research programs for the dispersal of valley air pollutants are presented by Whiteman and McKee (1978, 1979, 1980). In particular, their 1978 paper describes a grid-type air pollution model that can be applied to a valley cross section, in which upslope flows play a major role in transporting pollutants.

Finally an important study related to inversion breakup was conducted by Hewson and Gill (1944), who presented temperature data on a cross section of the broad Columbia Valley near Trail, British Columbia, obtained from aircraft composites. Unfortunately, the two case studies presented were of weak temperature inversions of only $2^{\circ}\text{C}/400\text{ m}$ and the data were composited so that the temporal resolution of changes in inversion structure was poor. Their observations showed, however, that cross-valley temperature differentials of up to $3\text{-}4^{\circ}\text{C}$ can

occur at certain times of the year on a constant height surface due to unequal heating of slopes. The asymmetry of the isotherm patterns stresses the importance of taking solar geometry into account in considering inversion breakup.

D. Valley Wind Systems

Local wind systems are an important aspect of the meteorology of mountain valleys. They have been scientifically studied since the 1840's and have been observed in mountain ranges throughout the world. Two classifications of diurnal valley wind systems are generally recognized. Along-valley winds blow parallel to the valley axis and are termed up- and down-valley winds. Along-slope winds blow parallel to the inclination of the sidewalls and are called upslope and down-slope winds (Figure 3). Up-valley and upslope winds are characteristic features of daytime wind circulations. Down-valley and downslope winds occur predominantly during the night.

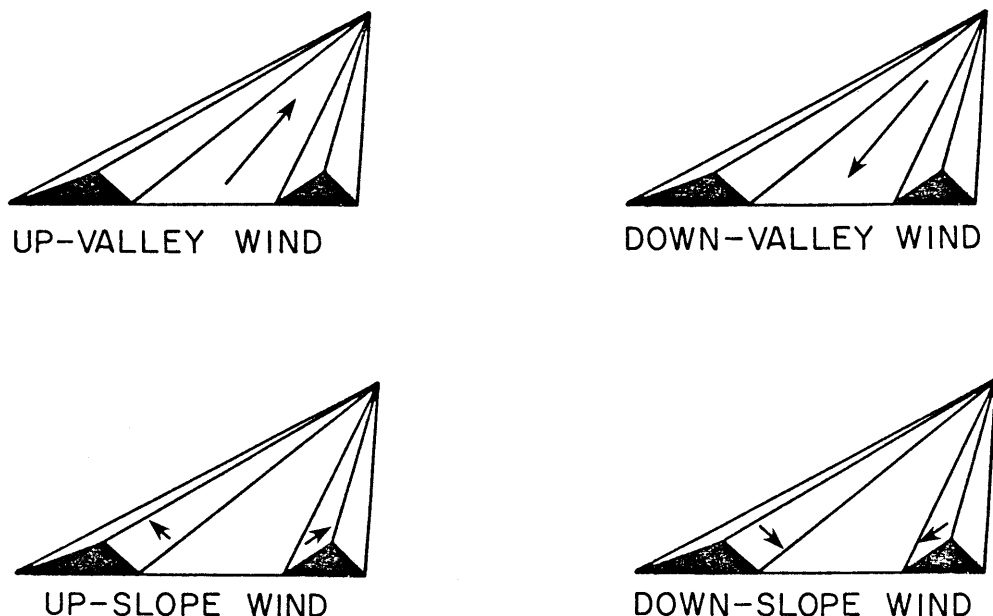


Figure 3. Wind system terminology.

The history of the development of scientific theories concerning the along-valley and slope wind systems is a rich one. An excellent summary of the development of these theories through the mid 1940's is available in English in an unpublished Ph.D. dissertation written at Ohio State University by H. B. Hawkes in 1947. Other summaries include those of Defant (1951) and Thyer (1966).

The presently accepted theory of valley wind systems originated with work carried out at Innsbruck, Austria in the 1930's by Ekhardt (1934) and Wagner (1932, 1938). The important papers of these two authors are well worth reading today, especially since English summaries of their work, such as the one by Defant (1951), are not complete.

1. Along-Valley Wind Systems

Along-valley winds, according to Wagner's (1938) theory, result from a diurnal forcing of the horizontal pressure gradient between valley and plains caused by the greater diurnal temperature range in a column of air within the valley than in a corresponding column at the same elevation over the adjacent plains. According to Wagner's theory, the along-valley wind systems constitute but one part of a closed system in which a corresponding return current above the ridgetops returns the required mass from mountain crest to plain or from plain to mountain crest. The greater temperature range within the valley, confirmed by Ekhardt (1948), is attributed to two factors (Hawkes, 1947). First, the column of air in the valley atmosphere is near surfaces (not only the valley floor, but also the sidewalls) where the diabatic processes of conduction, convection, and radiation take place. The impact of these processes is enhanced by the efficient means

available (e.g., the slope flows) to distribute the heating and cooling through the valley air mass and by the topography which confines the heating or cooling to the limited volume of the valley atmosphere. Over the plains at the same elevation, the column is a considerable distance above the surface. The effects of the diabatic heating processes decrease significantly with height, thus decreasing the diurnal temperature range in the column over the plains. Second, more energy per unit mass of air is available in a valley than over the plains. Solar flux across a horizontal surface is the same over the plains as it is over the valley. However, once this energy has been received at the ground, the portion of it available to heat the air is used to heat a smaller volume of air in the valley than over the plains (Figure 4), thereby resulting in a larger increase of temperature per unit mass. Similarly, loss of radiation from a valley at night goes to cool a smaller volume of air, resulting in a larger temperature decrease per unit mass.

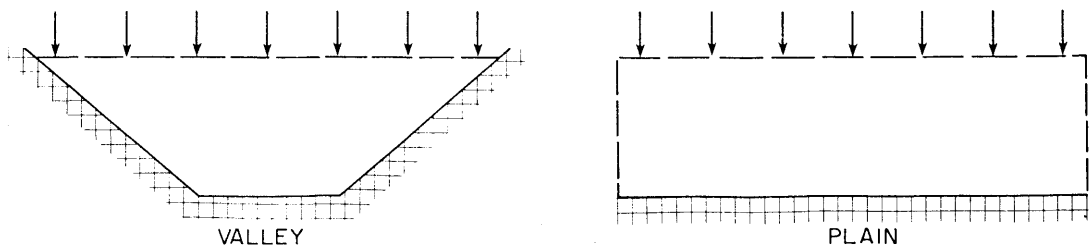


Figure 4. Schematic representation of energy to volume relationships between valley and plain.

The above summary of the theory of along-valley wind systems emphasizes the role of temperature changes in the valley atmosphere in producing the wind systems. However, most of the research on the along-valley wind systems has focused on the characteristics of the wind field itself rather than on the development of the thermal field within the valley or on a comparison between temperature profiles over the valley and plains. A notable exception is the important paper published by Ekhardt in 1948 in which a limited amount of temperature structure data was successfully applied to the verification of Wagner's theory. At least two other aspects of the theory need additional observational confirmation. First, the existence of an upper compensation current has received little modern observational attention, and second, a rigorous definition of the length scale over which horizontal pressure gradients are to be calculated has not been provided.

Defant's (1951) summary of the observed characteristics of along-valley wind systems states that these winds are best developed in the wide, deep valleys of the Alps and seem to be little influenced by the shape of the valley floor or its cross-sectional shape. The peak winds within the up-valley and down-valley wind systems often occur in mid or lower levels of the valley atmosphere, being reduced by friction nearer to the valley floor. The local winds are naturally best developed during undisturbed clear weather conditions. An abrupt windshift or a change to calm often marks the boundary between the valley wind and the overlying prevailing wind. The up-valley winds have been observed to reach slightly above the flanking mountain ridges, whereas the down-valley winds are often confined to lower levels of the valley

atmosphere. Average velocities are generally higher for the up-valley wind system than for the down-valley wind system. Hawkes (1947), in summarizing a ten year study of valley winds in Austria, states that average up-valley wind velocities were 3.7 m sec^{-1} , and average down-valley wind velocities were 2.2 m sec^{-1} . However, this relationship can be reversed by a channeling or funneling effect, as noted by Hawkes at Villach, Austria.

Much of the European work also indicates that, after sunrise, down-valley winds reverse rather abruptly to up-valley through the entire depth of the valley. Defant considers the time of the transition to be related to the size of the air mass within the valley, and thus to the valley cross section. The time of the transition is also a function of season, since the timing and amplitude of the thermal forcing is seasonally dependent. Hawkes' summary of the early Alpine research states that the transition from down-valley to up-valley occurs in less than one hour. The up-valley flow commences within the valley in a layer several hundred meters above the valley floor and extends rapidly upwards.

Much of the research since the summaries of Defant and Hawkes has been done in non-Alpine areas, and some significant differences in along-valley wind system evolution have been noted. Davidson and Rao (1958, 1963) discovered that up-valley winds apparently do not occur in some shallow and rather open-ended Vermont valleys. Similarly, Cross (1950) states that up-valley winds are absent at one site that he studied in the wide Columbia River Valley of the Northwestern United States. Gleeson (1953), in an important theoretical study, has suggested that the strength of the along-valley winds depends on the

slope of the valley floor. The steeper the slope, the stronger the wind systems. This contradicts data taken in the Alps and the theoretical work of Fleagle (1950) on downslope wind systems in which the wind speeds are inversely related to the slope angle. Buettner and Thyer's (1966) observations in the state of Washington reveal the presence of anti-wind systems. These wind systems prevail immediately above the valley and carry air in a direction opposite to that in the up- or down-valley wind system below. Their observations show that the wind system boundaries generally slope the same way as the valley bottom although not generally as steeply and that wind systems are better developed in the higher regions of the valley. Under wet or cloudy conditions the up-valley wind is often poorly developed. Their concurrent studies of wind systems in several valleys show that wind systems in all of the valleys in the region, regardless of orientation, develop to the same extent, suggesting that the direction of the overlying prevailing wind is not the dominant factor affecting wind system development. Rao's (1960) wind observations in Vermont valleys show an acceleration of down-valley winds with distance down the valley. He concluded that mass must be entrained from above in order to preserve the continuity of mass. Davidson and Rao (1958, 1963) found that the wind reversal from down-valley to up-valley in a number of Vermont valleys does not follow the pattern observed in Alpine experiments. Winds above the down-valley flow are the first to become up-valley. A slow descent of the top of the down-valley flow (or wind reversal point) then occurs at speeds ranging from $80-120 \text{ m hr}^{-1}$. Similar observations have been described by Pollak (1924), Ayer (1961), and Hewson and Longley (1944). Ayer's explanation for the phenomenon,

similar to that proposed by Davidson and Rao (1963) and by Lenschow et al., (1979), is that turbulent erosion of the top of a temperature inversion by the overlying up-valley flow was responsible for a decrease in the depth of the down-valley flow within the inversion. An alternate explanation was also offered, suggesting that the apparent descent could be due to drainage of a cold air mass out the end of the valley, thus allowing the up-valley winds aloft to penetrate deeper into the valley. Thyer and Buettner's (1962) data, in contrast, show that the transition occurs through the valley depth "within a few minutes, often slightly earlier at the surface than at higher levels." They did observe several cases, however, in which the wind reversal was accomplished by the descent of up-valley winds from aloft. The transitions took place at about the same time at all observation sites within a valley. Sterten and Knudsen (1961) and Sterten (1963) have presented an interesting explanation of valley wind reversals observed in Norway. Down-valley winds there are thought to be reversed as a convective boundary layer containing up-valley winds grows upwards from the valley floor, replacing the down-valley winds with up-valley winds. A criticism of this concept is that slope flows and their relationship to along-valley wind systems are not mentioned.

2. Along-Slope Wind Systems

Like the along-valley wind systems, the along-slope wind systems have a thermal origin, being driven by the temperature difference between the air that is heated or cooled adjacent to the inclined mountain slopes and the air at the same elevation over the valley center. This temperature difference results in a diurnal thermal forcing of horizontal pressure gradients that produces the winds that

carry air up the slopes during the day and down the slopes during the night. Despite the postulated thermal origin of the slope wind systems, the author is not aware of any published observations showing concurrent temperature profiles from mid valley and slope sites.

The observed characteristics of slope wind systems have been summarized by Hawkes (1947) and Defant (1951). Since the slope circulations are smaller than the valley circulations, they can easily be modified by topography, insolation, vegetative cover, and weather conditions. The upslope winds are known to be especially well developed where insolation is intense, as on south-facing slopes. The wind, clearly affected by terrain irregularities on the heated slope, is especially strong in terrain depressions but is suppressed on projecting ridges. The upslope wind system may develop at different times on different slopes depending on the time of illumination by the sun, determined in part by the surrounding topography. In fact, the upslope currents are known to respond rapidly to the sudden shading caused by a cloud drifting in front of the sun. The upslope winds may become detached from the slope at the ridge crest or at terrain features that project from the slope. When sufficient moisture is present the existence of these detached currents can be recognized in the development of isolated cumulus clouds. The thickness of the upslope flow increases with distance up the sidewall since the upslope flow entrains air from above as it moves up the slope. Moll's (1935) observations in the Vikar Valley of Austria show an upslope flow layer that ranges in depth from 10 m at the base of the slope to 100 m further up the hillside. Maximum slope flow depths of up to 260 m have been observed on south-facing slopes (Hawkes, 1947). Defant (1951) gives average

speeds within upslope flow layers of 2-4 m sec⁻¹. The vertical structure of winds within the layer exhibits a pronounced "nose" of peak winds some distance above the slope, with winds decreasing both toward the ground and toward the top of the layer.

More attention has been given to observational and theoretical studies of downslope flows, which are generally weaker and shallower than upslope flows. Research includes that of Prandtl (1942), Defant (1949, 1951), Ball (1960b), Fleagle (1950), Petkovšek and Hočevar (1971), Bergen (1969), Streten et al., (1974), and more recently Manins and Sawford (1979a, 1979b). Most of these studies have produced theoretical models of downslope flow. Unfortunately, suitable data is not available to check the performance of the models. Manin and Sawford's (1979b) comment on downslope wind studies is especially appropriate:

"The data are almost all confined to wind fields, and only rarely is information about their spatial and temporal variation included. Practically no temperature data are available."

Fortunately, data have been collected in several recent experiments investigating slope flows and their temperature relationships, including the Innsbruck Slope Wind Experiment (Freytag and Hennemuth, 1979), the South Park Experiments of Banta and Cotton (1979), and the U.S. Department of Energy's Atmospheric Studies in Complex Terrain (ASCOT) experiments (Dickerson and Gudiksen, 1980).

3. Interrelationships Between Along-Valley and Along-Slope Wind Systems

Two main mechanisms relating the along-valley and along-slope wind systems have been proposed (Hawkes, 1947). First, the along-slope wind

systems facilitate the transfer of heat to the valley atmosphere, resulting in a large diurnal temperature range in the valley atmosphere. This large temperature range provides the thermal diurnal forcing which drives the along-valley wind systems. However, the precise way in which the heat transfer occurs has not been clearly ascertained. For daytime, Scorer (1958) proposes that air heated over the sidewalls rises up the sidewalls and flows toward the valley center at various levels (Figure 5). Using this model, warming of the valley atmosphere occurs through subsidence and horizontal turbulent sensible heat flux convergence. Wagner (1938), in contrast, proposes that the valley atmosphere is warmed by a current of air that rises up the sidewalls, returns to the valley center above the valley, and descends in the center of the valley (Figure 6). Continuity of mass requires currents from the valley center toward the sidewalls, i.e., in the direction opposite that proposed by Scorer. Wagner's model can be criticized from an energetics point of view since, when a morning temperature inversion is present within the valley, it requires warm air at valley center to descend into a colder environment. This objection would be obviated, however, if the valley inversion layer sank at the same rate as the downward-directed current. Also, to the author's knowledge, supporting observations of the cross-valley convergence field above the ridgetops at valley center are not available. Scorer's model, on the other hand, contradicts the observed increase in depth of the upslope flow with distance up the sidewall (Moll, 1935). This increase in depth has been attributed to entrainment of mass into the slope flow layer from the overlying valley air mass. Scorer's conceptual model cannot account for this feature of the slope flow structure because it calls for transport in the wrong direction.

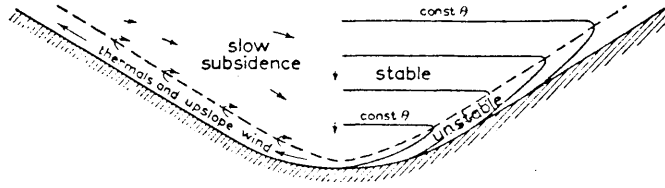


Figure 5. Scorer's (1958) scheme for the heating of a valley stable layer.

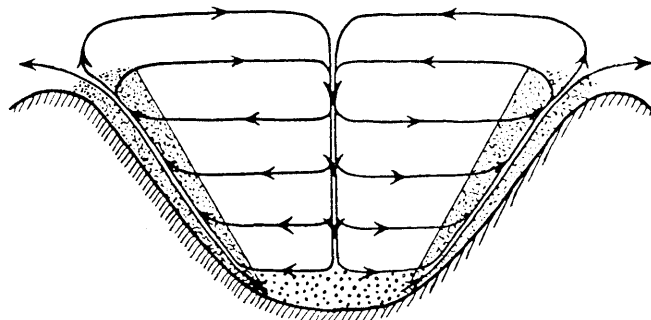


Figure 6. Wagner's (1938) diagram of the slope wind systems during the time of up-valley wind.

The second mechanism that relates the along-valley and along-slope wind systems was proposed by Wagner, but has been only briefly summarized by Defant (1951). According to this theory, the along-slope flows provide the required vertical motion to allow the horizontally moving along-valley winds to blow in a valley with an inclined floor. The valley winds are enhanced, retarded, or reversed depending on the amount of mass carried by the slope flows. A concise summary of this concept has been presented by Hawkes (1947):

"The movement of a particle of air in the valley wind is primarily in the horizontal, even when the valley is inclined considerably. To move the entire mass of air in the valley up the valley floor would be to cool the air mass adiabatically to such an extent that an opposing gradient from valley to plain would be established. To overcome this opposing gradient one would have to assume a temperature contrast between valley and plain five to ten times the magnitude of the observed or probable gradient. Thus an unweakened valley wind can take place only if the air mass as a whole can flow horizontally. The necessary work done in lifting and sinking is compensated by heat transfer along the slopes. It is only at the time of transition between the up- and down-valley wind that the air mass of the valley moves parallel to the valley floor. Under these conditions the system is soon destroyed and the opposing system develops."

On the basis of these two mechanisms, Defant (1949) has produced a schematic diagram illustrating the relationships between along-slope and along-valley wind systems. This diagram is reproduced below in Figure 7. Since Defant's diagram was published, a number of investigators have suggested modifications or have reported observations that differ from Defant's scheme. A few of the important suggestions, including those concerning wind structure during inversion breakup, are mentioned briefly below.

(1) Hewson and Gill (1944) proposed that, when unequal solar heating occurs on opposite sidewalls, a closed circulation develops

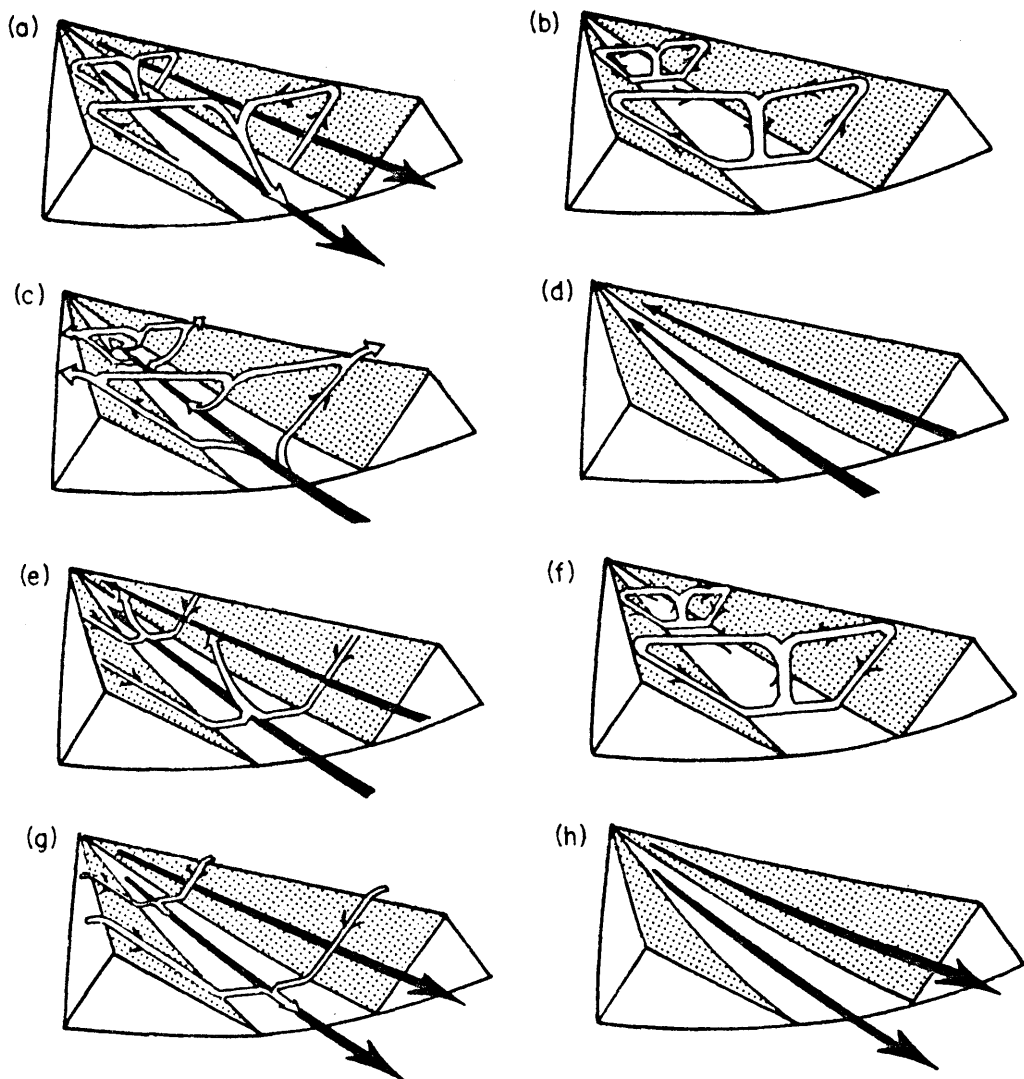


Figure 7. Schematic illustration of the normal diurnal variations of the air currents in a valley. (After F. Defant, 1949).

- (a) Sunrise; onset of upslope winds (white arrows), continuation of mountain wind (black arrows). Valley cold, plains warm.
 - (b) Forenoon (about 0900); strong slope winds, transition from mountain wind to valley wind. Valley temperature same as plains.
 - (c) Noon and early afternoon; diminishing slope winds, fully developed valley wind. Valley warmer than plains.
 - (d) Late afternoon; slope winds have ceased, valley wind continues. Valley continues warmer than plains.
 - (e) Evening; onset of downslope winds, diminishing valley wind. Valley only slightly warmer than plains.
 - (f) Early night; well-developed downslope winds, transition from valley wind to mountain wind. Valley and plains at same temperature.
 - (g) Middle of night; downslope winds continue, mountain wind fully developed. Valley colder than plains.
 - (h) Late night to morning; downslope winds have ceased, mountain wind fills valley. Valley colder than plains.
- From Reid (1976).

with upslope flow on one sidewall and downslope flows on the opposite sidewall. When this closed slope circulation is imposed on the along-valley winds, a helical circulation develops.

(2) Buettner and Thyer (1966) noted that Defant's scheme does not include the anti-wind systems that they observed on Mount Rainier, Washington. Their observations in Washington also indicate that the along-slope wind systems and the along-valley wind systems coexist at all times of the day. Thus, for their experimental area Defant's Figures (b), (d), (f), and (h) are incorrect. Finally, although they had no direct observations, they suggested that Defant's descending currents could not exist over the valley during the day since the anti-wind systems above the valley are probably fed from within the valley by upslope and up-valley currents. However, Hindman (1973), by observing the dissipation of clouds in a mountain valley in California, was able to obtain indirect evidence of sinking motions in the valley center during a morning period.

(3) Davidson and Rao (1958), in a study of a number of Vermont valleys, found that a definite return circulation or anti-wind circulation rarely existed. Furthermore, in some of the valleys investigated there was no discernible evidence for the regular development of the upslope or up-valley wind systems shown in Defant's Figures (a), (b), (c), and (d). Also, downslope motions persisted several hours after sunrise.

(4) Urfer-Henneberger (1964, 1970) has developed a conceptual model showing stages similar to Defant's for the linear Dischma Valley near Davos, Switzerland, based on a comprehensive series of surface measurements taken from points along the valley floor and positions on

the sidewalls. She doubts the existence of Defant's vertical motions over the mid-valley both during day and night and stresses the important influence of the progression of sunlight up and down the sidewalls, as well as the existence of cross-valley winds which do not necessarily need to form closed circulations.

(5) Sterten and Knudsen (1961) and Sterten (1963), investigating wind systems in a valley in southwestern Norway, arrived at a conceptual model that differs significantly from Defant's. Their model includes neither slope winds nor compensation flows. Instead, a nocturnal down-valley flow causes the valleys to fill up with cold air. After sunrise, air near the ground is heated and rises until it meets the "barrage zone" at the base of the cold air. Since it can rise no further, it flows up-valley under the overlying stable layer. The depth of the convective layer increases with time until the stable layer above is dissipated and up-valley winds occur through the whole depth of the valley.

(6) Other significant deviations from Defant's model include the previously mentioned wind system reversal. Defant's model (Figure 7a, b, c) shows a sudden reversal from down-valley to up-valley with an intermediate condition when only upslope winds occur. A very different view of this reversal comes from the work of Davidson and Rao (1963), Ayer (1961), Sterten (1963), and others.

One must not conclude, given the substantial deviations from Defant's model mentioned above, that his model is useless or inappropriate. Historically, his conceptual model has been extremely useful as a representation of wind structure within an idealized valley under a narrow range of synoptic conditions. It is becoming increasingly

apparent, however, that valley wind systems differ from valley to valley depending on external and internal atmospheric conditions and topography.

To this point, the review of literature has revealed that an improved understanding of temperature inversion breakup over homogeneous terrain followed careful observational work which, in turn, stimulated new theoretical approaches. In contrast, basic observations are not yet available for inversion breakup in mountain valleys. A great deal of information has been collected on valley wind systems, but its usefulness, and perhaps even the basic understanding of the observations, has been greatly diminished by the failure to collect concurrent temperature structure data. With this background in mind, a research program, described in the following chapter, is designed to investigate inversion breakup in the deep valleys of western Colorado.

Chapter III

EXPERIMENTAL DESIGN

The objective of the experimental program was to investigate the evolution of temperature inversion structure during undisturbed weather in a number of mountain valleys during different seasons, with the goal of elucidating the physical factors governing inversion destruction. To meet this objective, tethered balloon soundings of temperature and wind structure were to be made at approximately one hour intervals during the time of inversion breakup, from sunrise to late morning. Experiments were designed to be conducted by a small number of people able to respond quickly to suitable synoptic weather patterns with a minimum amount of portable equipment. Experimental campaigns were scheduled in different seasons of the year. Field support from the Field Observing Facility of the National Center for Atmospheric Research (NCAR) was arranged for the major experimental campaigns. During these campaigns NCAR equipment, usually including a small camper from which to operate, and the valuable services of an NCAR field technician were available.

A. Location of Experiments

Experiments, except in the Poudre Valley, were conducted in valleys on the western slope of the Rocky Mountains in western Colorado (Figures 8 and 9), where terrain elevations range from 1500 to nearly 4400 meters. Here the sunny, dry, continental climate of the region results in frequent temperature inversions (Holzworth and Fisher, 1979). Deep valleys having a simple linear shape and lack of topographic complexity were preferred to meet the experimental objective. Topographic characteristics of the valleys investigated are

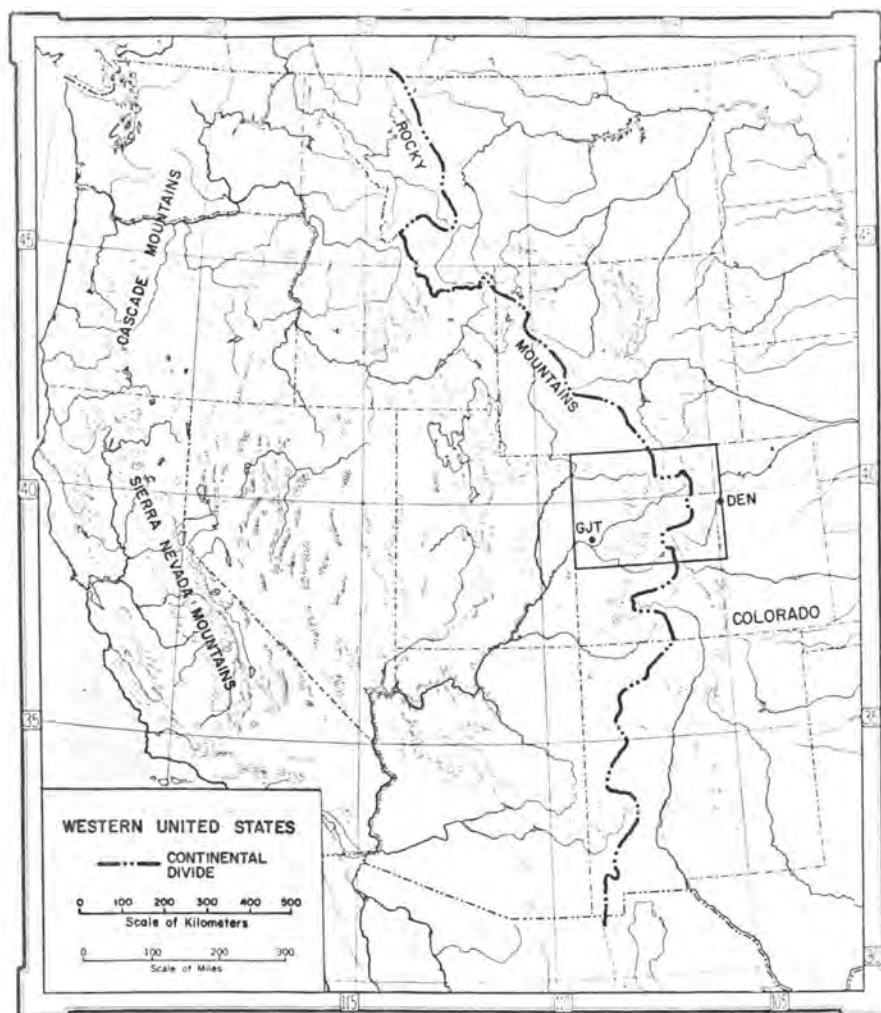


Figure 8. Location of experimental area in western Colorado (DEN = Denver, GJT = Grand Junction). Base map copyright by Denoyer-Geppert Co. Used by permission.

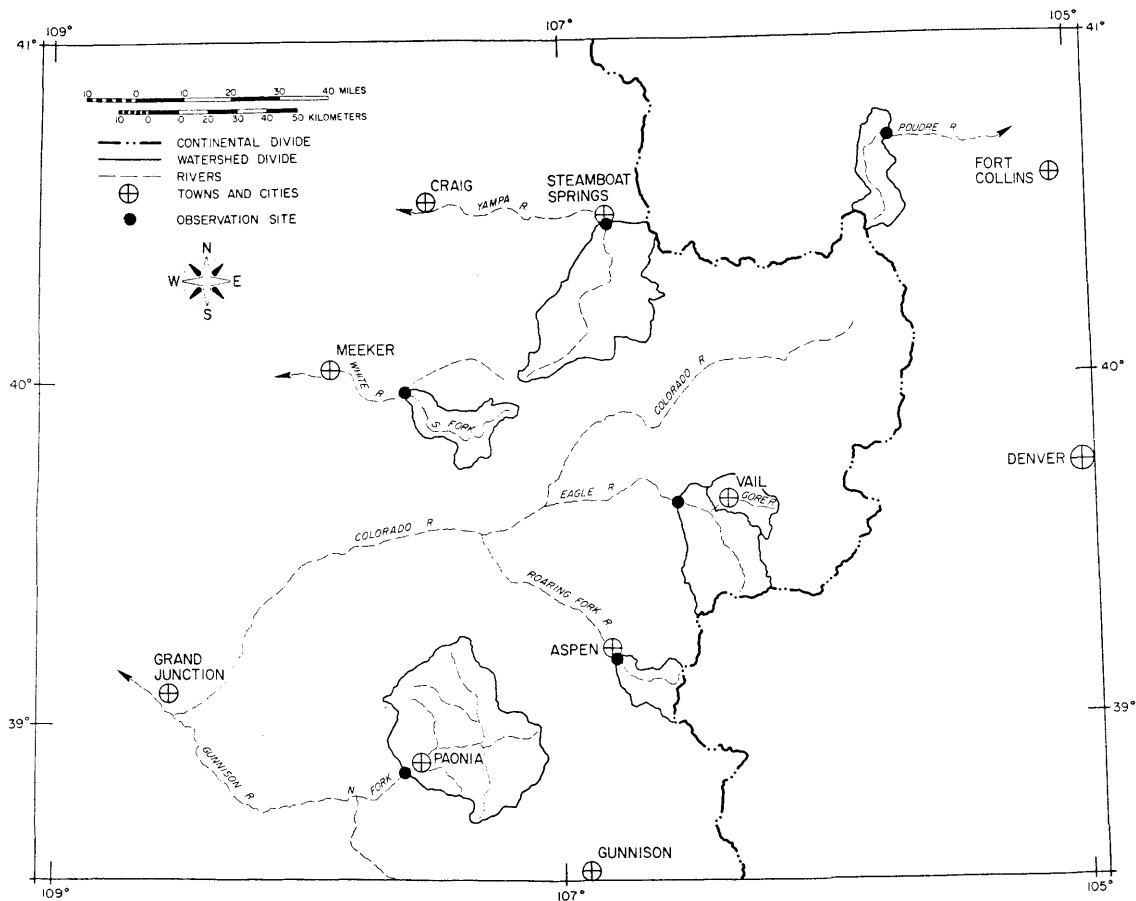


Figure 9. Closeup of experimental area showing valley watersheds. The lowest experimental site in each watershed is shown in the figure by a dot.

presented in Table 1, and topographic maps are provided in Appendix A. Some subjectivity is involved in obtaining the numbers in Table 1 from topographic maps of different scales. Nevertheless, accuracy and consistency were goals of the topographic analysis and the numbers in the table represent careful estimates. Several comments on the estimates are in order.

(1) All directions are relative to true north.

(2) The Up-Valley Direction is estimated for the immediate vicinity of the site by considering the direction of orientation of the valley floor rather than the course of the river at the site.

(3) The Height of Ridges Above Site is usually an average of the heights of the ridges on either side of the valley. If one ridge is appreciably higher than the other, the height of the lowest ridge is used.

(4) The Valley Floor Slope is determined for the immediate vicinity of the site from the largest scale topographic map available (usually a 7½ minute quadrangle). To determine the slope, the first contour passing across the river above the site and the first contour passing across the river below the site are located. The difference in the heights of the contours is determined and is divided by the distance between them as measured along the smoothed course of the river.

(5) The Distance Ridge to Ridge is the distance along a line perpendicular to the along-valley direction as it passes through the observation site. Adjustments are made to get a representative value when the ridge lines are not parallel to the valley axis. A special circumstance arose in the Poudre and Roaring Fork Valleys. Here the

Table 1. Topographic Characteristics of Experimental Sites

Valley Site	Latitude	Longitude	Altitude (m)	Height Above Valley Floor (m)	Up-Valley Direction (° TN)	Valley Floor Width (m)	Height of Ridges Above Site (m)	Distance Ridge to Ridge (km)	Valley Floor Slope (x10 ⁻³)	Slope Aspect	Slope Inclination (°)	Drainage Area (km ²)	Nearest Town	Maps
<u>Cache LaPoudre</u>														
1. Poudre Trout Rearing Ponds	40°42'03"	105°42'35"	2341	3	297	500	725 *600	5.7 *3.9	7.1	N S	27 27	398	Kinikini	Greeley 1/250,000; Larimer County 1; 30' Home; 7 1/2' Kinikini
<u>Yampa</u>														
2. Sombrero Ranch	40 27 27	106 48 50	2076	12	168	2580	450	5.5	2.6	E W	16 09	1370	Steamboat Springs	Craig 1/250,000; Routt County 4
3. Horseshoeing School	40 27 00	106 48 49	2070	6	168	2580	450	5.5	2.6	E W	16 09	1370		
<u>S. Fk. White R.</u>														
4. River Cabin	39 58 26	107 37 29	2129	2	078	--	300	5.0	11.4	--	--	448	Buford	Leadville 1/250,000; Rio Blanco County 3; 7 1/2' Big Beaver Reservoir; 7 1/2' Buford
5. Mobley's Y-Z Ranch	39 57 19	107 35 04	2175	2	128	400	350	3.0	10.0	N S	18 15	421		
6. Stillwater	29 55 03	107 32 43	2295	12	157	850	750	7.8	0.5	E W	12 12	405		
<u>Colorado</u>														
7. Fred Johnson Residence	39 32 12	107 45 44	1698	79	77	--	--	--	2.6	--	--	13000	Rifle	Leadville 1/250,000; 7 1/2' Rifle
<u>Eagle</u>														
8. Steve Miller Residence	39 38 23	106 34 33	2222	12	104	1450	700	9.2	7.0	N S	21 10	1061	Edwards	Leadville 1/250,000; Eagle County 2; Eagle County 4; 15' Minturn; 7 1/2' Edwards; 7 1/2' Grouse Mountain
9. Ray Miller Ranch	39 38 28	106 34 20	2228	18	104	1450	700	9.2	7.0	N S	21 10	1061		
10. Slope Site 1	39 39 53	106 34 14	2530	320	104	1450	400	9.2	7.0	N S	21 10	1061		
11. Slope Site 2	39 39 54	106 34 15	2533	323	104	1450	400	9.2	7.0	N S	21 10	1061		
12. Beaver Creek	39 36 10	106 31 06	2469	1	202		250	3.0	74.1	--	--	33		
13. Eagle-Vail Highway Garage	39 37 15	106 27 59	2324	6	115	300	550	5.3	15.2	N S	13 15	941		
<u>Gore</u>														
14. Susie's	39 37 12	106 25 39	2377	2	060	180	650	3.7	19.2	NW SE	19 13	250	Vail	Leadville 1/250,000; Eagle County 2; Eagle County 4; 15' Minturn; 7 1/2' Vail West; 7 1/2' Vail East.
15. Vail Safeway	39 37 50	106 25 06	2426	15	046	390	600	3.8	17.4	NW SE	14 24	233		
16. Vail Municipal Bldg	39 38 37	106 22 48	2493	15	093	530	700	5.1	13.4	N S	15 16	180		
17. Vail Golf Course	39 38 34	106 20 37	2518	10	077	320	650	3.0	9.4	N S	26 25	152		
<u>Roaring Fork</u>														
18. North Star Ranch	39 10 33	106 47 43	2443	2	141	600	750 *550	5.8 *2.7	11.3	NE SW	30 23	286	Aspen	Leadville 1/250,000; Pitkin County 2; 7 1/2' Aspen
<u>N. Fk. Gunnison</u>														
19. Kol Holt Residence	38 50 49	107 38 12	1686	6	054	3100	800	17.9	3.7	NW SE	04 08	1962	Paonia	Montrose 1/250,000; 7 1/2' Hotchkiss

valley sidewalls rose at a steep angle for some distance but then changed sharply to a low angle that continued until the ridge was attained. Two sets of values of Distance Ridge to Ridge and Height of Ridges Above Site are provided for these cases.

(6) The Drainage Area of the valley above each of the sites was obtained from a 1/500,000 U.S. Geological Survey Colorado map using a planimeter.

(7) Slope Aspect and Slope Inclination angles were determined along cross sections of the valley drawn through the observation sites. Aspect angles are relative to true north. A south-facing slope has an aspect angle of 180° . An east-facing slope has an aspect angle of 90° . Inclination angles were calculated from the edge of the valley floor to points on the sidewalls 300 and 500 meters above the observation site. When the two angles for a sidewall did not differ greatly, the angle calculated for the 300 meter point was used. If there was a significant difference, the most representative of the two angles was recorded.

B. Synoptic Weather Conditions

The experimental design called for observations of temperature inversions during clear, undisturbed weather. Clear skies and undisturbed weather are a fairly common feature of western Colorado climate, so that a large number of soundings were gathered under conditions that met the experimental criteria.

Weather forecasts were made both before and during each field campaign. Some experiments were shortened, postponed, or cancelled due to forecasts of unsuitable weather. Some forecasting difficulties occurred during the course of the experiments. Diurnal changes in

cloud cover were an especially difficult forecasting problem. Thin cirrus clouds often developed after sunrise despite apparently clear skies just before sunrise. On-site observations of cloud cover were important to the forecaster, since forecasts were made from Fort Collins.

The most suitable weather conditions for the experiments occurred with a 500 mb ridge over the western United States, often associated with a surface high pressure cell in the central or northern Great Basin. Under these conditions, upper level winds were generally light and skies were usually clear. This was not necessarily true in summer, however, when patchy middle and high level moisture was occasionally present.

C. Equipment

1. Tethered Balloon Data Collection Systems

Small portable tethered balloon data collection systems suitable for operation by one or two field personnel provided the basic experimental data. The systems utilized were thoroughly described by Morris et al., (1975). They consist of multiplexed meteorological sensors carried aloft on an airborne telemetry package by a blimp-shaped, helium-filled balloon, and a ground-receiving station. For the major campaigns NCAR supplied one of two such systems, but due to the needs of other experimenters, it was not possible to use the same instrument in all campaigns, resulting in some changes in data format.

CSU purchased a commercial version¹ of the tethered balloon data collection system in April, 1978. This instrument was used to supplement data obtained with the NCAR tethered balloon and allowed dual

¹Tethersonde®, Atmospheric Instrument Research Co., Boulder, CO 80303.

soundings from more than one location within a valley. The CSU version had basically the same sensors and telemetry as the NCAR version but provided for digital data acquisition at the ground station. A complete and useful Operation Manual for this digital data acquisition system is available from the tethersonde manufacturer. In addition to providing supplemental data during major campaigns, the CSU system was the sole tethered balloon system used in the shorter experiments. The operating specifications of the CSU system were carefully tested using the NCAR Environmental Chamber and Wind Tunnel Facilities. Test results are provided in Appendix B.

Photographs of the CSU tethered balloon data collection system are presented below in Figures 10 through 12. The battery-powered airborne sensor and telemetry package, weighing about 1 kg, is shown in Figure 21. The wind speed sensor, a 3-cup anemometer, and a fan-aspirated tubular radiation shield are located on the top of the package. The radiation shield consists of two concentric tubes. A bead thermistor is exposed in the middle of the airstream in the central cylinder and is followed by an identical bead thermistor covered by a wick. A distilled water reservoir on the top of the package feeds water to the wick of the wet bulb thermistor. Two sensors are located inside the package. A pressure transducer senses pressure changes as the package changes elevation or as local changes in pressure occur. A potentiometric compass, fixed to the base of the package, enables the package to sense wind direction. The package, in its normal operating position (Figure 10) hangs from the balloon on a rope ladder that resists torsional movements away from the orientation of the balloon. When wind direction is to be sensed by the multiplexing circuitry, an



Figure 10. Tethersonde battery-powered airborne sensor and telemetry package.



Figure 11. Normal operating configuration of tethered sonde balloon and airborne package.

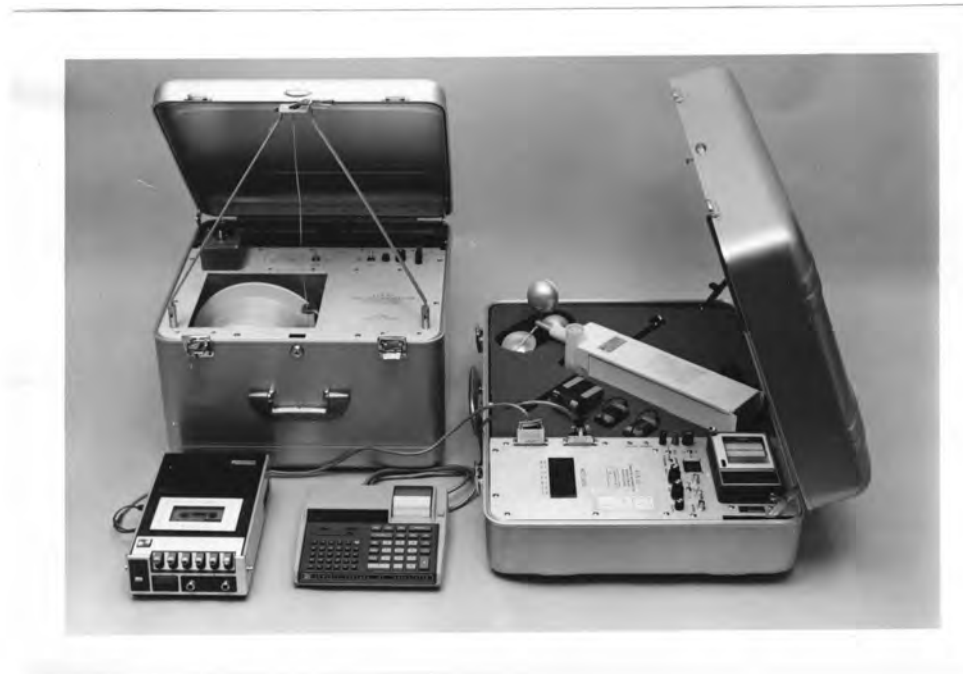


Figure 12. Tethersonde equipment. Left rear-electric winch. Left to right, foreground-cassette recorder, Hewlett-Packard HP-97 Programmable Printer/Calculator, ground station with airborne package.

electromagnetic field locks the compass needle, which is pointing north, to a potentiometer winding, which is fixed to the base of the compass and turns with the balloon. The resistance of the potentiometer winding is then an indicator of wind direction. The basic data transmitted by the airborne package included dry bulb temperature, wet bulb temperature, pressure, airborne battery voltage, wind direction, and wind speed. The data are transmitted by the airborne package at 403 Mhz in a time-multiplexed format such that a complete frame of basic data took approximately 20 to 30 seconds.

The balloon used with the data collection system is made of a light plastic material and can be obtained in two sizes, 3.25 and 4.25 m³. Holes in the plastic material can be easily patched using a special tape. A "stinger" at the rear of the balloon allows the volume of the helium in the balloon to expand slightly as the balloon ascends, thereby protecting the seams of the balloon from ripping under the strain of differential pressure.

An electric winch is used to control the ascent and descent rates of the balloon. The level-wind winch can be operated on 110 VAC or 12 VDC power and is controlled by a small switch box attached to the winch by 10 m of electric cable. The operator can control the speed of ascent/descent by varying the setting of a potentiometer. The winch is reversed by a toggle switch on the switch box. An emergency electronics override switch is available on the winch to apply full power to bring the balloon in at a rapid rate.

The ground station/carrying case portion of the data collection system contains a receiver/discriminator that receives the time-multiplexed signals from the airborne package and converts them to

meteorological units. Signal conditioning and further digital processing occur within the microprocessor-controlled ground station. A digital display flashes meteorological values as they are processed. Digital ports allow data to be sent to a Hewlett-Packard HP-97 Programmable Printer/Calculator where the data may be further processed and/or printed as they are collected. The data may also be recorded on a standard audio cassette recorder and played back at a later time into the ground station at a speeded up rate to be reconverted to a digital format for transmission to a computer in a standard computer compatible form. The ground station, powered by 110 VAC or 12 VDC, has the capability of recharging the nickel-cadmium batteries used to power the airborne package. Figure 12 shows all the components of the data collection system except for the balloon.

a. Data Collection Procedures

A set procedure was established for conducting atmospheric soundings with the tethered balloon data collection systems. Immediately before each sounding the tether sonde was attached to the balloon and tethered approximately one meter above the ground. The instrument package was carefully allowed to come to an equilibrium with the ambient conditions. A comparison was made between dry and wet bulb temperatures as indicated by the data collection system and concurrent values as determined by an Assmann psychrometer. The distilled water supply and airborne battery were checked every few flights and replenished or replaced when necessary. Dry and wet bulb comparisons were recorded on a special data sheet along with observations of wind speed and direction (when independent observations were available), cloud and weather observations, and the local time from which data were reckoned

by the digital data acquisition system. Additional comments on weather changes, times of sunrise or sunset, system performance, etc. were recorded as the balloon sounding progressed. Complete (up and down) profiles of the valley atmosphere usually took 30 to 50 minutes. The sounding frequency was approximately once per hour during the time of inversion destruction, usually beginning with a sounding at sunrise. Rough plots of the temperature soundings were usually made by hand during each balloon ascent so that the progress of inversion evolution could be monitored and informed operational decisions could be made as the experiments progressed. As the balloon left the ground on ascent or approached the ground on descent, the rate of ascent/descent was slowed in order to gain good spatial resolution of the temperature profiles in the near-ground layers. After reaching the ground on descent the instrument package was allowed to continue running until it came to equilibrium with ambient conditions. Up-soundings were generally preferred in the data analysis because of the equilibrium procedure used at the ground and because no "contamination" of data was every detected from the balloon on up-soundings.

b. Processing of Data

Tethered balloon data were processed in one of three ways:

(1) When the multiplexed data were available on recorder strip charts (NCAR system), a data reductionist coded the data onto Fortran coding forms for punching. The punched deck was then run with a computer program designed to convert the original data deck (values in ordinates from 00 to 99) to meteorological values (e.g., wind speeds in m sec^{-1}) and to punch the data in a standard format on new punch cards.

(2) When the data were available on HP-97 printer paper (early CSU system), a data reductionist coded the data onto a Fortran coding form for punching.

(3) When the data were available on cassette tape, the tape was played back to the tether-sonde ground station and a digital port transferred data to a Texas Instruments Silent 700 data terminal where it was recorded on digital magnetic tape. This tape was played into a Cyber 70 computer to create permanent files of data accessible by the computer. For ease in editing, the data were punched onto cards in the standard format.

Various quality control steps were incorporated in the processing of the basic data. For example, for NCAR system data, a listing of cards punched from Fortran coding forms was checked against the Fortran forms, and coding forms were spot-checked against the original data recordings by a second data reductionist. CSU system data, as processed from cassette tapes, was spot-checked against redundant HP-97 printer output. For the early CSU system data, listings of cards punched from HP-97 printer output were checked against the original printer output. A partial check of all data was accomplished by a computer program which scanned each sounding to determine the maximum and minimum values of each meteorological parameter.

The basic data were further processed on a digital computer. A clock-time, pressure, and height were assigned to each item of basic meteorological data by time interpolation. Wind directions were corrected to true north using the magnetic declination of the site. Using the hydrostatic equation, heights were calculated from tether-sonde pressure and temperature values. Other secondary meteorological

parameters such as potential temperature, mixing ratio, relative humidity, along- and cross-valley wind component, etc. were calculated using standard formulas. Special consideration was given to humidity calculations when the wick on the wet bulb thermistor was frozen.

Further explanation of the means used to determine heights from tethersonde data is necessary. The surface pressure at balloon launch time was used as the starting point of the height integration, corresponding to a height of zero meters. By the end of the down-sounding 30 to 50 minutes later, a non-zero height may be registered. The discrepancy could be attributed to several factors, including changes in surface pressure and drift of the airborne pressure sensor. Additionally while the valley atmosphere is approximately hydrostatic at any instant during the profile, changes in the valley atmosphere will occur during the profile, resulting in a sounding that is not strictly hydrostatic. A consistent means of processing the height soundings was thus required. This was accomplished in the following way:

- (1) Heights for the up-soundings were obtained by integrating upwards from the initial measured surface pressure, assumed to be at a height of zero meters.

- (2) Surface pressure was estimated for the end of each down-sounding by interpolating digital microbarograph readings taken routinely at the beginning of each ascent.

- (3) Pressure data in the down-sounding were all adjusted so that the final frame of data in the down-sounding had the pressure as determined in (2), above. Heights were then calculated by an upwards integration from this pressure. As a result the final soundings are

hydrostatic and any height discrepancies between the up- and down-soundings are found at the top of the soundings.

A final check of the data was obtained by visually scanning electrostatic plots of sounding data. Quality checked data were recorded on permanent files in a CDC Cyber 70 computer.

2. Upper Air Sounding Systems

Two upper air sounding systems were used at the sites during the course of the experiments to supplement the tethered balloon observations with data from higher levels of the atmosphere. Rawinsonde soundings were made during several of the experimental campaigns using either the GMD or RD65A Rawinsonde units provided by NCAR. The performance of the rawinsonde sets was not very satisfactory, however, due to undetermined electronic problems that produced noisy signals in the automatic tracking system of the RD65A.

A new commercial upper air sounding system² was also used during many of the experiments, both to supplement low level tethersonde data and to replace it when strong or turbulent winds might result in loss or damage to the tethersonde balloon or airborne package. This sounding system was very easy to use in the field, as it had been designed for use with the same ground station and peripheral equipment as the tethersonde.

The airsonde data collection system consists of an expendable sonde and 9 VDC transistor battery encased in a foam shell (Figure 13) with two helicoid vanes protruding from it. The sonde is attached to a 30 gram helium-filled pilot balloon by a length of lightweight nylon

²Airsonde®, Atmospheric Instrumentation Research, Inc., Boulder, CO 80303.

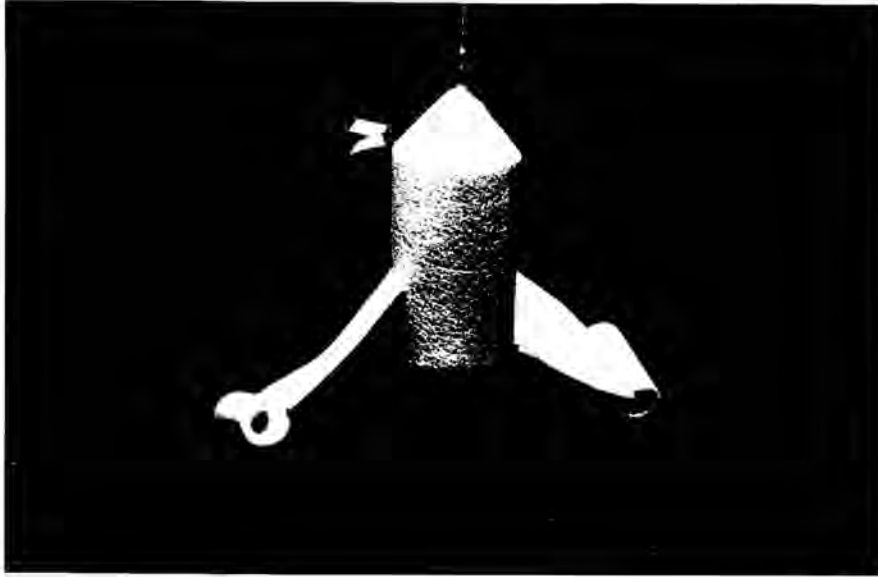


Figure 13. Airsonde.

cord tied to a swivel at the nose of the sonde. As the balloon ascends, the sonde rotates as air passes by the helicoid vanes. The rotation of the vanes aspirates thermistor temperature sensors that are exposed in cylindrical radiation shields on the ends of the blades. One of the thermistor beads is covered by a wetted cotton wick supplied by a distilled water reservoir. An aneroid strain gage pressure sensor is housed inside the sonde along with the electronics. As the balloon ascends, a time multiplexed signal containing wet and dry bulb temperature and pressure information is transmitted to the ground station. A scan of data is transmitted approximately every eight seconds. Since the aneroid strain gage is temperature sensitive, a temperature sensor is located within the sonde in close thermal contact with the strain gage. A microprocessor in the ground station compensates for the temperature sensitivity of the strain gage pressure sensor after the transmissions are received at the ground.

a. Data Collection Procedures

The sonde is activated by twisting two wires together to complete the circuit inside the sonde. The wet bulb reservoir is filled with distilled water, and the balloon is inflated with helium to attain a free lift sufficient to cause the airsonde to ascend at the rate of approximately 150 m min^{-1} . The ground station is then activated using the procedure specified by the manufacturer. As one step in this procedure, four calibration constants, as previously determined by the manufacturer for each airsonde, are keyed into the microprocessor at the ground station. These constants are necessary to allow the ground station to calculate the actual values of pressure as the sonde ascends and to compensate properly the pressure readings for the temperature sensitivity of the aneroid. A pre-flight check of airsonde-indicated temperature is made with an Assmann psychrometer, and a pressure reading is taken with a digital microbarograph. The airsonde pressure reading is adjusted using a thumb-wheel switch on the ground station until airsonde data is in agreement with the surface pressure value. A pre-flight data sheet is filled out, recording the pressure and temperatures, winds, weather, time of launch and other pertinent information. The airsonde is then released and data is collected automatically by the ground station as the balloon ascends. If a directional receiving antenna is used, an adjustment of the antenna may occasionally be necessary to maintain signal strength. The data, displayed by the ground station as the sonde ascends, may be recorded on audio cassette tape or printed out on the HP-97 Printer/Calculator.

When sufficient personnel were available, an optical theodolite was used at 30 second intervals during the flight to track the balloon

to determine upper air wind speeds and directions. Double theodolite observations were not required to obtain accurate height data, since this was provided by the pressure sensor in the airsonde. Theodolite observations were terminated when the balloon was lost in clouds or disappeared from view, or when the sounding was terminated due to reception of a noisy signal or apparently inaccurate data. Small pilot balloon lights made night observations possible.

b. Processing of Data

All airsonde data were recorded on audio cassette tapes in the field. Using the same procedure as specified for tethersonde data recorded on audio cassette tape, the data were put on permanent files on the CDC Cyber 70 computer, and a computer card was punched for each scan of data. The raw data were listed and checked for noisy or obviously bad data. If the pressure, temperature, or wet bulb data were obviously bad the bad data card was removed from the deck. The result was a data deck containing mostly good data, although some data contained low amplitude noise signals, especially at the upper levels of the sounding where signals were weak. The data were then processed by a computer program to calculate heights from an integration of the hydrostatic equation and to calculate secondary meteorological variables. The data were then plotted and underwent a final screening.

The airsonde system was still undergoing testing by the manufacturer when we began to use the prototype sondes in our experiments. Therefore, a series of tests of the airsonde data collection system was conducted to determine the accuracy and reliability of the data. Thanks to an opportunity offered by NCAR, multiple Rawinsonde/Airsonde intercomparison flights were made during September, 1978.

These intercomparisons pointed out a problem with the airsonde pressure data that was further investigated using the NCAR Environmental Chamber, with the support and encouragement of the airsonde manufacturer. A summary of the tests of airsonde performance is given in Appendix C. Test results disclosed that pressure data from some airsondes were being improperly temperature compensated. The problem was caused by the use of the same temperature compensation factors for all aneroid elements when, in fact, there were differences in the temperature responses of the individual aneroids. While airsonde temperature data were accurate, airsonde pressure data could be in error by ± 15 mb by the time individual sondes reached 300 mb. Due to the insulating effect of the foam body of the sonde, the pressure errors usually became significant only after the airsondes had reached pressure levels 150 mb below surface pressure. Since much of the airsonde data were collected before this information was known, pressure data from previous airsonde ascents had to be corrected, taking into account the fact that some soundings had good pressure data while others had pressure values that were too high or too low. The following correction method was used:

- (1) The 500 mb temperature was estimated at the site of each airsonde ascent by using 500 mb synoptic weather charts at 0000 and 1200 GMT and interpolating to the time of airsonde launch.

- (2) The airsonde sounding was searched until the 500 mb temperature as determined above was encountered. The pressure of this temperature observation was assumed to be 500 mb. Pressures in the sounding were then linearly adjusted from 150 mb above the surface to 500 mb.

(3) Airsonde soundings above the 500 mb level were discarded.

The above procedure provided estimates of 500 mb temperatures accurate to within about a degree Celsius. Assuming an average temperature lapse rate of $6^{\circ}\text{C km}^{-1}$, the resulting height data should be accurate to within about 170 m at 500 mb. The height (or pressure) data are more accurate at lower levels.

The final corrected form of the airsonde data was merged with theodolite data to obtain computer-generated plots of the soundings along with averaged wind speed and direction data for the 30 second intervals of theodolite observations.

3. Other Equipment

A commercial acoustic radar was utilized in some of the field experiments to provide a continuous, though qualitative, record of the evolution of atmospheric temperature layers in the lowest 1000 m of the valley atmosphere. The qualitative, but continuous, acoustic radar data supplemented the quantitative but intermittent tethered balloon observations. The acoustic radar was, therefore, useful in the field to monitor atmospheric changes between balloon soundings, as well as being useful in later analysis.

On the larger experiments a weather station was set up at the main observation site on the valley floor. Instruments included a wind set to obtain continuous records of wind direction and speed at a height of approximately three meters, a hygrothermograph exposed in a standard cotton-region shelter approximately five feet above ground, and a microbarograph that was kept in a heated building or camper at the site.

On-site checks and calibrations of the hygrothermograph and microbarograph data were made with a mercury-in-glass thermometer and with an accurate digital microbarograph. No calibration equipment was available to check the accuracy of the wind data in the field, although the equipment was of a research quality and appeared to work well. The wind sensors were carefully leveled in the field, the wind vane was set to true north, and zero and full-scale adjustments were made on the recorders.

On certain selected experiments microbarographs and/or hygrothermographs were exposed at multiple sites within the valleys. The altitudes of these sites were determined using a small portable altimeter-barometer and were checked against topographic maps and aerial photos.

The theodolite used for tracking airsondes was a standard type used by the weather services. It was calibrated using the procedures specified by the manufacturer, and was used with a standard tripod and pilot balloon timer. The theodolite was carefully leveled before each series of airsonde ascents and was set to true north using a magnetic compass.

D. Summary of Experiments

Table 2 provides a summary of the data collected in the field campaigns. Specified in the table are the general locations of the campaigns, the inclusive dates of data collection, and the types and quantities of data collected.

Table 2. Summary of Experimental Data.

Experiment/Dates	Data	Number of Soundings	Supporting Data, Comments, References
1. Gore Valley 4-18 Dec 1975	Tethersonde	58	Hygrothermographs (Whiteman and McKee, 1977) Mech. Weather Stations (Fox et al., 1976) Constant volume balloons Pilot balloons
2. Gore Valley 21-26 Jan 1977	Tethersonde	0	Instrument failure
3. Eagle Valley 11-20 Oct 1977	Tethersondes(2)	59	Acoustic radar
4. Yampa Valley 4-5 Feb 1978	Tethersonde	10	Acoustic radar
5. Yampa Valley 23-24 Feb 1978	Tethersonde	32	Acoustic radar
6. Eagle Valley 18-27 Apr 1978	Tethersondes(2) Airsonde	24 8	Acoustic radar, rawinsonde, hygrothermograph, microbarographs, wind set, pyranometer, net radiometer, theodolite
7. Eagle and Gore Valleys 6-9 Jul 1978	Tethersonde Airsonde	18 7	Theodolite
8. Poudre Valley 13-14 Jul 1978	Tethersonde	9	
9. Roaring Fork Valley 18-19 Jul 1978	Tethersonde Airsonde	8 3	
10. N. Fork Gunnison Valley 20-21 Jul 1978	Tethersonde Airsonde	1 10	Theodolite
11. S. Fork White Valley 22-30 Jul 1978	Tethersondes(2) Airsonde	85 20	Acoustic radar, hygrothermographs, microbarographs, theodolite, integrating pyranometer
12. Eagle Valley 9-20 Oct 1978	Tethersondes(2) Airsonde	71 5	Acoustic radar, hygrothermograph, microbarograph, wind set, theodolite

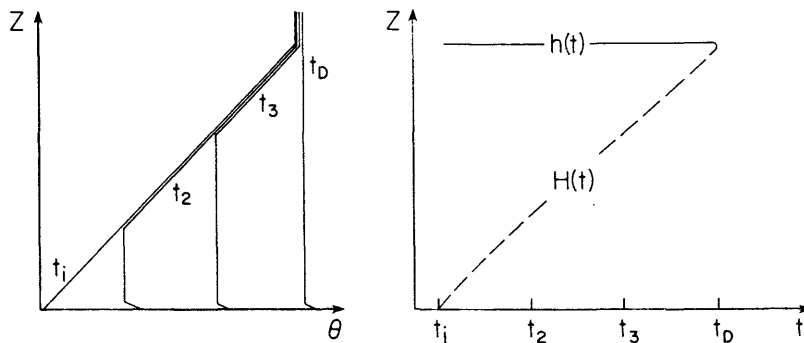
Chapter IV

ANALYSIS OF DATA

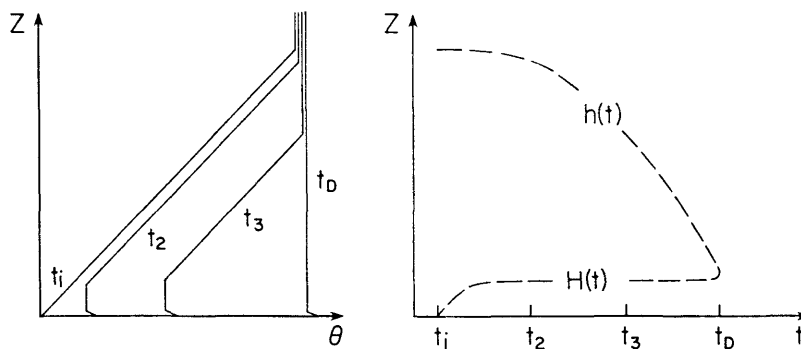
From the 375 tethersonde soundings and 53 airsonde soundings taken in seven Colorado valleys, a subset of 21 case studies of inversion destruction in four valleys was selected for further analysis. Three patterns of temperature structure evolution were observed in the valleys studied. Two of the patterns are special cases of the third pattern which was the most frequently observed. Each of the patterns is illustrated by means of examples taken from the data. The characteristics of the temperature structure evolution for these 21 cases are presented in a data table and summarized. The corresponding evolution of the wind structure is described and specific features of wind structure are illustrated by special analyses. Finally, four case studies are presented in which the two-dimensional cross-valley wind and temperature structure were observed using dual tethersonde systems.

A. Three Patterns of Vertical Temperature Structure Evolution

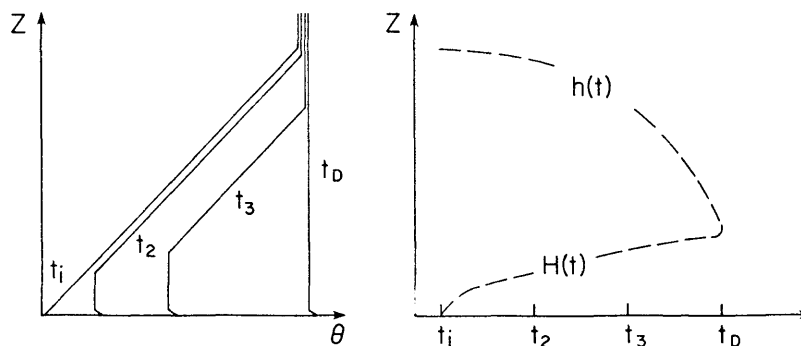
For the valleys studied, temperature structure during inversion breakup evolved following one of three patterns. The first pattern of inversion destruction (Figure 14a and b) is characterized by the upward growth from the ground of a convective boundary layer and describes inversion behavior over flat terrain. At sunrise, t_1 , the potential temperature profile is as shown in Figure 14a, and the height of the convective boundary layer, H , is zero (Figure 14b). Successive soundings taken at times t_2 and t_3 show the upward growth from the ground of a well-mixed convective boundary layer. At any given time the boundary layer has a potential temperature that is independent of



Pattern 1. Growth of CBL.



Pattern 2. Descent of inversion top and arrested growth of CBL.



Pattern 3. Descent of inversion top and continuous growth of CBL.

Figure 14. Three patterns of temperature structure evolution. Potential temperature profiles are on the left and time-height analyses of CBL height and inversion top height are on the right.

height, but the temperature of the boundary layer increases as a function of time. A shallow superadiabatic sublayer is typically present at the base of the convective boundary layer immediately above the ground. The inversion is finally destroyed at time t_D when the height of the convective boundary layer, $H(t)$, grows to the height of the top of the inversion, $h(t)$, producing a constant potential temperature atmosphere in the valley. Pattern 1 inversion destruction is thus characterized by the growth with time of a convective boundary layer, while the height of the top of the inversion remains fixed in time. Only one example of Pattern 1 inversion destruction was observed in the field experiments. This occurred on a summer day in the widest valley studied.

The second pattern of temperature structure evolution is very different from the first. The convective boundary layer over the valley floor, which begins to grow after sunlight illuminates the valley floor, plays only a minor role, its growth arrested after a certain shallow height is attained (Figure 14d). The inversion destruction is caused by the descent of the top of the inversion into the valley, which is accompanied by a warming of the valley atmosphere (Figure 14c). Despite this warming, the vertical potential temperature gradient in the inversion layer remains constant. The inversion is destroyed at time t_D when the warming finally results in a constant potential temperature within the valley, and the descending top of the inversion meets the fixed top of the CBL. This pattern of inversion destruction was observed twice during field experiments. Both cases occurred in winter when the valleys had extensive snow cover.

Pattern 3 temperature structure evolution is a combination of the first and second patterns. In Pattern 1, a convective boundary layer grows upwards into the inversion and the descent of the top of the inversion plays no role. In Pattern 2, inversion destruction is accomplished by a descending inversion top, and the role of the CBL is minimized. Pattern 3 represents a continuum of intermediate situations in which both the growth of the CBL and the descent of the inversion top are present. Figure 14e and f show the continued growth of a convective boundary layer, $H(t)$, and the accompanying descent of the inversion top, $h(t)$. The elevated remnant of the temperature inversion warms significantly but maintains its original potential temperature gradient. The inversion is finally destroyed at time t_D when the descending inversion top meets the ascending CBL, and a constant potential temperature is attained through the whole depth of the valley. Pattern 3 inversion destruction is the most common pattern in Colorado valleys. It was observed in all seasons, provided snow cover was absent, and seemed to be largely independent of topography, synoptic conditions, and upper level winds. Of 21 case studies of temperature structure evolution, 18 followed Pattern 3.

The three patterns of inversion destruction differ in the extent to which the CBL growth or inversion top descent is dominant. Three main features of the potential temperature profiles seen in the idealized patterns are the CBL, the elevated inversion, and the neutral layer above the inversion. Following are examples taken from the data illustrating the three patterns of potential temperature structure evolution.

1. Example of Pattern 1 Temperature Structure Evolution

An example of Pattern 1 inversion destruction was observed on the morning of 9 August 1978 in the Yampa Valley, 3 km upstream from Steamboat Springs. The data is given in Figure 15. The table at the base of the figure gives the tether sonde sounding number (U for an up-sounding, D for a down-sounding), the time interval¹ in which the sounding was conducted, and cloud and weather conditions during the sounding. Plots of potential temperature versus height form the main part of the figure and concurrent soundings of vertical wind structure, labeled with the sounding number, are located adjacent to the potential temperature plots. The orientation of the wind arrows at a particular height in the soundings can be compared to the up-valley direction provided on the figure. A wind speed legend is given so that the length of the wind arrows can be converted to actual wind speeds. The 1115 GMT² 700 mb Grand Junction vector wind is given for reference above the valley wind data (not necessarily at a height corresponding to the 700 mb pressure level). Some subjectivity is involved in estimating the heights of the inversion and CBL tops in the individual soundings. The primary means of making these estimates was to find the inflection points between potential temperature gradients in the three main temperature structure layers. In difficult cases, continuity of trends

¹Times presented in the text are local times (LT) in hours and minutes using a 24 hour clock in the Mountain Time Zone (time of 105th meridian). During the period of data collection, Mountain Standard Time (MST) was kept from 2 am on the last Sunday in October to 2 am on the last Sunday in April, with Mountain Daylight Time (MDT) kept during the remainder of the year. The time relationships with Greenwich (England) Mean Time were MST = GMT - 7 hours and MDT = GMT - 6 hours.

²In the United States, the general practice of the National Weather Service is to begin morning rawinsonde ascents at 1115 GMT rather than at 1200 GMT. For this reason, the morning rawinsonde ascent times in the text are given as 1115 GMT.

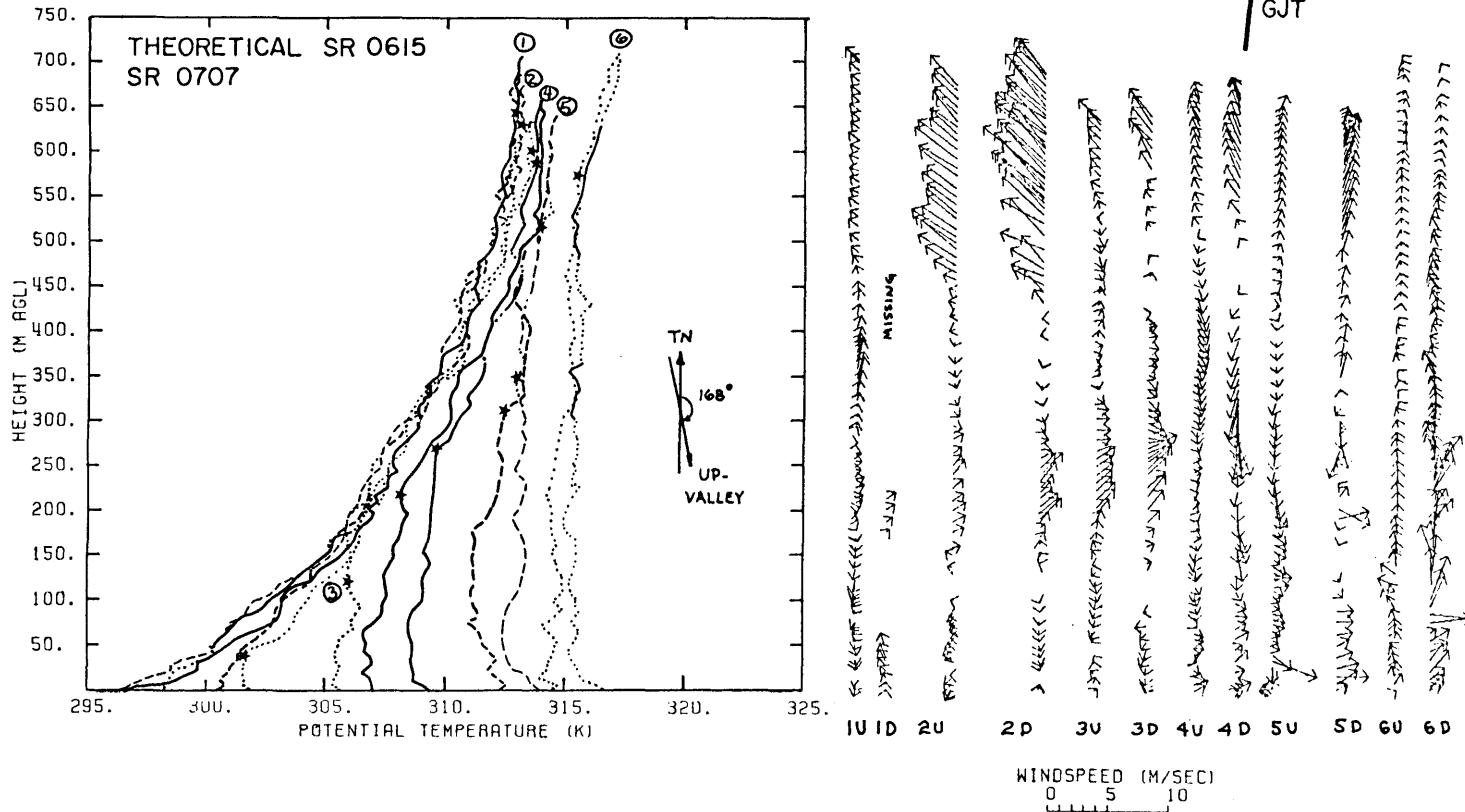
in the heights of the various layers was invoked. In some cases wind discontinuities at the boundaries of the layers helped in the analysis.

The basic features of the Pattern 1 inversion destruction are seen in the Yampa Valley data presented in Figure 15. The first sounding of the morning was taken before sunrise and reveals a hyperbola-shaped 650 m deep inversion with a strength of 16°K . Successive profiles show the development of a convective boundary layer that grows upward from the surface. Estimates of the heights of the CBL and inversion top are indicated on the figure by stars. Major warming occurs only in the convective boundary layer. The inversion destruction did not follow Pattern 1 perfectly, but showed some of the characteristics of Pattern 3 destruction as observed in most other valleys, including some warming of the inversion layer and an apparent, but minor, descent of the top of the inversion. Winds within the inversion were very weak and erratic during the inversion destruction except at the upper levels where SE winds of 4 or 5 m sec^{-1} prevailed for a time. Up-valley winds tended to form in the CBL as it grew upwards from the ground. After inversion destruction (sounding 5D) down-valley winds prevailed through the depth of the valley.

2. Example of Pattern 2 Temperature Structure Evolution

Pattern 2 inversion destruction was observed in the Yampa Valley on 23 February 1978 and in the Gore Valley on 10 December 1975. The 23 February 1978 data (Figure 16) are a particularly good example of Pattern 2 destruction. The first soundings of the morning show an intense potential temperature inversion of 30°K in 500 m. The inversion had a hyperbolic shape in the lowest level that resulted in a particularly intense potential temperature gradient of 183°K/km in the

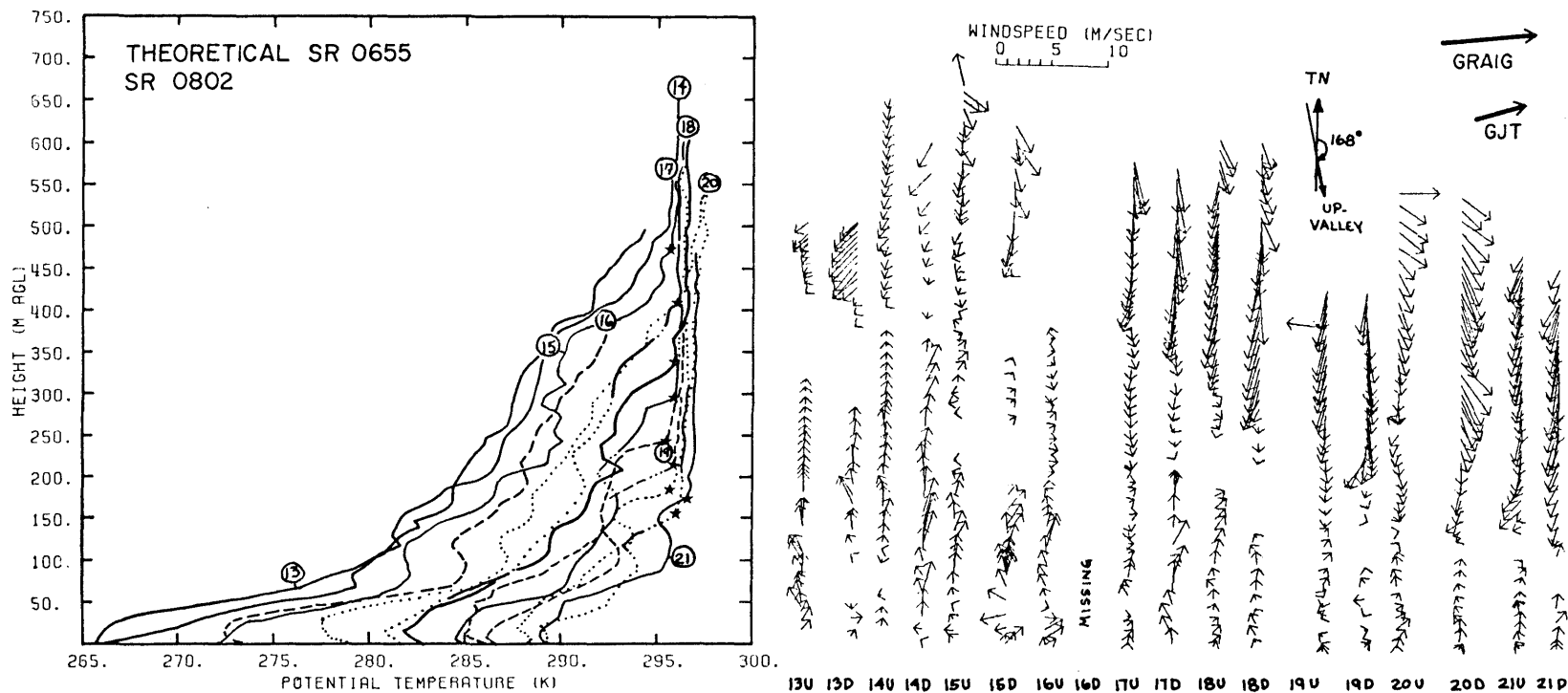
HORSESHOEING SCHOOL STEAMBOAT
 DATE 08/09/78



#	TIME (MDT)	WEATHER	#	TIME (MDT)	WEATHER	#	TIME (MDT)	WEATHER
1U	0541-0606	CLR	3U	0800-0820	CLR	5U	1005-1025	CLR
1D	0606-0626		3D	0820-0839		5D	1025-1044	Cu RDGTPS DSNT N & S
2U	0658-0717	CLR	4U	0857-0918	CLR	6U	1054-1115	CLR (FEW Cu OVR MT)
2D	0717-0742		4D	0918-0938		6D	1115-1143	WNERG & DSNT N & S

Figure 15. Example of Pattern 1 temperature structure evolution. Tethersonde data. Yampa Valley, 9 August 1978.

SOMBREDO STABLE STEAMBOAT SPGS
DATE 02/23/78



#	TIME (MST)	WEATHER	#	TIME (MST)	WEATHER	#	TIME (MST)	WEATHER
13U	0714-0736	CLR (FOG BNK UP-	16U	0959-1013	CLR	19U	1259-1316	CLR
13D	0736-0753	VALLEY)	16D	MISSING		19D	1316-1331	
14U	0802-0826	CLR (50m DEEP FG	17U	1100-1123	CLR	20U	1359-1423	CLR
14D	0826-0844	BNK UP-VALLEY)	17D	1123-1140		20D	1423-1444	
15U	0905-0929	CLR (THIN L YR FG	18U	1202-1225	CLR	21U	1508-1529	CLR
15D	0929-0956	S+ACRS VL W-GONE	18D	1225-1245		21D	1529-1546	

0930)

Figure 16. Example of Pattern 2 temperature structure evolution. Tethersonde data. Yampa Valley, 23 February 1978.

lowest 73 m of the profile. The hyperbolic segment of the profile was surmounted by a near-linear segment having many small potential temperature deformations. A fairly sharp discontinuity at the top of the linear segment marked the beginning of isothermal to neutral stability. The soundings were of insufficient depth to resolve the upper limit of this layer. Successive soundings show the inversion structure evolving according to Pattern 2. The descent of the inversion top began after sounding number 14 and is clearly seen in the data. By 0959 LT a shallow boundary layer, comprised mostly of a superadiabatic sublayer with only a shallow layer of constant potential temperature, had grown upwards from the ground. After reaching a height of approximately 35 m, the boundary layer failed to grow further. Inversion destruction thereafter was accomplished entirely by the descent of the inversion top. During the descent, temperatures within the inversion warmed at about the same rate at all levels. The potential temperature, θ_h , at the top of the inversion warmed 1 to 1.5°K during the day as the inversion destruction progressed.

During the entire period of inversion destruction shown in the figure, potential temperature deformations continued to occur in the nearly linear segment of the profile. There is some evidence for a persistent deformation at the 75-100 m level. By late in the afternoon, the inversion had not been completely destroyed, although the top of the inversion had descended to within 175 m of the ground. Further soundings (22 on) showed the reestablishment of the nocturnal cooling regime and the end of the inversion destruction period.

Winds within the inversion during the Pattern 2 destruction blew predominantly down the valley, but at speeds generally less than 2 m

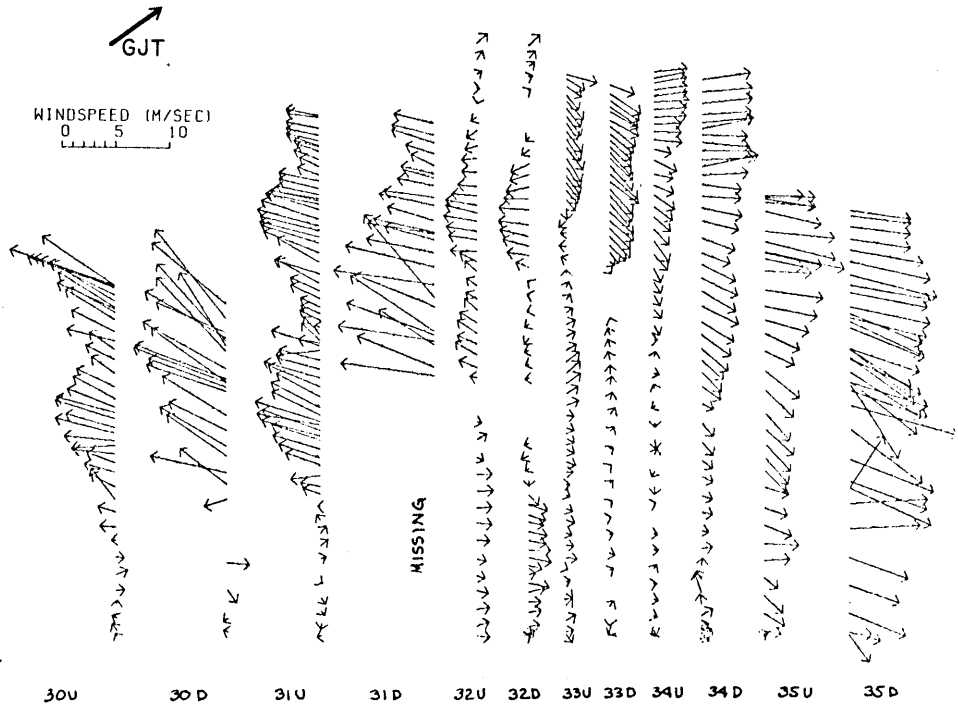
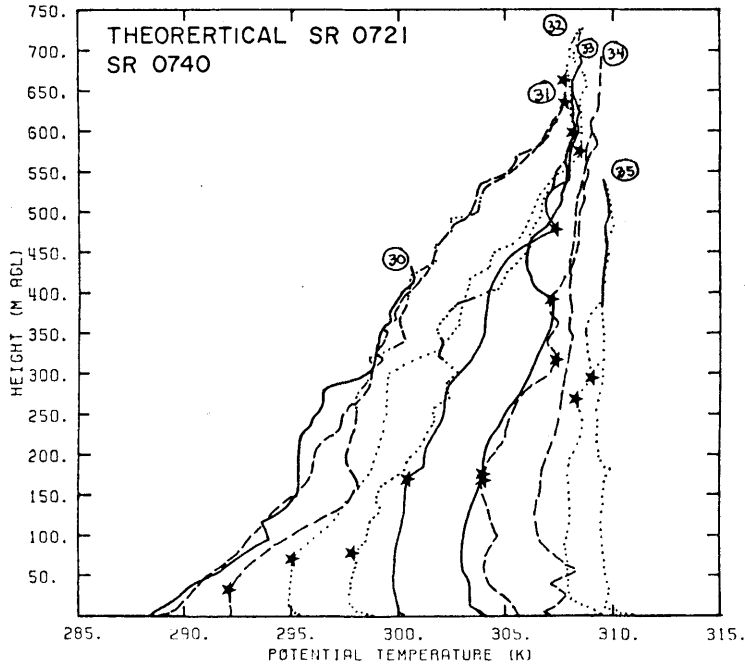
sec^{-1} . Winds in the neutral layer above the inversion blew up the valley at speeds of several meters per second.

3. Example of Pattern 3 Temperature Structure Evolution

A Pattern 3 inversion destruction occurred in the Eagle Valley on 16 October 1977 (Figure 17). Although the first sounding of the morning was terminated at an altitude of only 450 m, it is apparent from the second sounding that the near-sunrise inversion extended to a height of approximately 650 m and had a strength of about 19.5°K . The average potential temperature gradient was 30°K km^{-1} . The initial inversion shape was nearly linear, and the potential temperature evolution followed Pattern 3 very closely. The ascent of the CBL and the descent of the top of the inversion are well marked, as is the strong warming at mid levels of the profiles. During the period of inversion destruction, the elevated remnants of the near-sunrise inversion maintained their potential temperature gradient, and the neutral layer warmed by 1.5°K . The inversion had been completely destroyed by the last down-sounding at approximately 1230 LT.

The along-valley wind systems are particularly well developed in the Eagle Valley. Strong down-valley winds usually begin in the early evening and persist through the night, as evidenced by the strong down-valley winds at mid levels in the inversion in the early morning soundings. Winds within the elevated inversion layer often continue to blow down-valley until the inversion is nearly broken, but usually weaken slowly as the inversion descends. In the CBL below, the winds are typically weak and blow up-valley. Up-valley winds in the neutral layer above the inversion often follow the descent of the inversion top deeper and deeper into the valley until, when the inversion is

RAY MILLERS RANCH EDWARDS COLO
DATE 10/16/77



#	TIME (MDT)	WEATHER	#	TIME (MDT)	WEATHER	#	TIME (MDT)	WEATHER
30U	0659-0717	CLR	32U	0929-0948	CLR	34U	1113-1133	CLR
30D	0717-0730		32D	0948-1013		34D	1133-1155	
31U	0750-0819	CLR	33U	1024-1048	CLR	35U	1206-1221	CLR
31D	0819-0838		33D	1048-1111		35D	1221-1238	

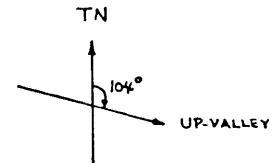


Figure 17. Example of Pattern 3 temperature structure evolution. Tethersonde data. Eagle Valley, 16 October 1977.

broken, they prevail throughout the whole depth of the valley. At this time they often become more turbulent. A more typical example of wind structure evolution during Pattern 3 temperature structure evolution in the Eagle Valley is shown in Figure 93.

B. Vertical Temperature Structure Evolution Data-21 Case Studies

Twenty-one case studies of inversion destruction illustrate the broad range of seasonal, topographic and synoptic conditions for which the previously described inversion evolution patterns were observed. The data were collected at nine sites in four Colorado valleys. The topography of the different sites has been described in Chapter III. A description of the synoptic weather conditions on the days in question is provided in Table 3, including a summary of upper air data at Grand Junction, Colorado. While most case studies were conducted on days with a 500 mb ridge and a surface high pressure area over the western United States, there were a significant number of days on which weather disturbances were present in the experimental areas. Nevertheless most days chosen for analysis were characterized by a lack of significant cloud cover. Wind speeds at 700 mb were consistently light on experimental days, averaging just over 6 m sec^{-1} , although winds were from all quadrants. Wind speeds at 500 mb averaged 10.8 m sec^{-1} , but varied from 1 to 28 m sec^{-1} with winds consistently from the two western quadrants.

Inversion destruction data for the 21 case studies are summarized in Table 4. The original tetheredsonde soundings are included in Appendix D. Several comments on the table are necessary:

(1) t_i , the local time of theoretical sunrise for the latitude and longitude of the site, is entered in column 3 as calculated from equations in Appendix E.

Table 3. Synoptic Data for Selected Case Studies

Date	Time (GMT)	GRAND JUNCTION UPPER AIR DATA						Synoptic Weather Conditions ¹
		700 MB			500 MB			
		T(°C)	θ(°K)	Winds (m sec ⁻¹)	T(°C)	θ(°K)	Winds (m sec ⁻¹)	
12-10-75	1115 2315	2.2 1.4	304.9 304.1	230 ⁰ /10 240/11	-14.9 -16.1	314.9 313.4	260 ⁰ /18 260/20	Weak flat ridge over intermountain plateau. 1017 mb High over Four Corners.
10-13-77	1115 2315	4.4 6.4	307.4 309.6	230/05 030/04	-12.3 -13.5	318.1 316.6	210/07 290/06	Weak trough moving into Colo from W through broad ridge covering W. U. S. Weakening 1028 mb High over Four Corners.
10-14-77	1115 2315	5.0 7.6	308.0 310.9	040/07 035/07	-14.3 -12.5	315.6 317.8	340/06 360/07	Broad trough ND-NM with sharp ridge moving into U.S. from W. Coast. 1032 mb High in N MT. Cold front driving towards site from NE.
10-16-77	1115 2315	6.4 7.4	309.6 310.7	235/06 275/04	-10.9 -12.1	319.8 318.3	220/07 230/11	Short wave moving E to NV through ridge covering W. U.S. Weak ridging surface pressure pattern over W. CO whole period.
10-19-77	1115 2315	6.6 7.8	309.8 311.1	250/06 260/08	-13.1 -15.3	317.1 314.4	205/11 240/06	Ridge over Rockies and weak cut off Low over S. CA. 1020 mb High weakening over W. CO.
02-23-78	1115 2315	-3.3 -1.5	298.8 300.8	255/05 270/06	-18.3 -17.5	310.7 311.7	275/09 300/08	Ridge over W. U.S. 1032 mb High weakening over E. Central UT.
04-20-78	1115 2315	1.4 3.2	304.1 308.3	255/06 225/07	-20.5 -17.9	308.1 311.2	270/10 245/14	Short ridge over Rockies. N-S elongated High over Central U.S. Cold front moving into UT from W.
07-06-78	1115 2315	10.6 12.8	314.2 316.7	260/02 275/05	-12.9 -9.7	317.3 321.2	255/11 240/09	Broad trough W. U.S. Weak pressure pattern over W. CO.
07-07-78	1115 2315	12.0 16.6	315.8 320.9	175/02 200/07	-7.9 -8.5	323.4 322.7	260/15 235/14	Ridge ID-NM with Low on coast of Central CA. High in E WY. Cold front stalled at CO-WY border.
07-08-78	1115 2315	14.0 16.6	318.0 320.9	255/14 240/09	-8.7 -7.9	322.4 323.4	225/23 240/16	Short wave entering W. CO. Weak Low pressure pattern in CO.
07-09-78	1115 2315	14.2 15.6	318.2 319.7	250/08 230/04	-9.3 -7.3	321.7 324.2	235/12 240/15	Weak ridge Alberta-W. CO. Post-frontal High over N and Central Rockies. Front driving S into NM.
08-09-78	1115 2315	13.0 15.4	316.9 319.6	185/07 320/06	-9.9 -7.7	321.0 323.7	320/08 340/06	Ridge over W. U.S. High over most of U.S. with center 1021 mb pressure in NE CO.
08-10-78	1115 2315	12.4 16.8	316.2 321.1	255/07 300/04	-8.7 -7.7	322.4 323.7	310/10 340/10	Ridge over W 1/2 U.S. Weak High pressure pattern in CO.
08-26-78	1115 2315	11.8 14.0	315.6 318.0	245/06 200/03	-11.9 -8.3	318.5 322.9	230/08 240/08	Succession of weak short waves moving over W. U.S. Weak High W. CO. Approaching cold front becoming stationary near NW corner CO.
08-27-78	1115 2315	11.6 13.6	315.3 317.6	275/04 290/08	-10.9 -10.3	319.8 320.5	255/09 265/09	Short wave trough moving into CO from W. Post-frontal High pressure cell in W. U.S. Front N-S in Central Plains.
08-29-78	1115 2315	11.8 13.2	315.6 317.1	300/02 290/08	-11.7 -9.9	318.8 321.0	255/08 295/08	Ridge over W. U.S. Ridge axis from NB to Alberta.
10-11-78	1115 2315	-4.7 -1.3	297.3 301.1	340/07 010/06	-15.1 -11.3	314.6 319.3	320/28 355/27	Post-trough with strong NW'y gradient aloft. Frontolysis of cold front in N. CO.
10-12-78	1115 2315	0.8 5.4	303.4 308.5	025/04 255/04	-10.5 -10.1	320.3 320.7	345/10 290/04	High moving onshore to N. CA and displacing broad trough in Central U.S. Cold front passing S across site. High pressure cell following.
10-19-78	1115 2315	6.6 7.8	309.8 311.1	250/06 260/08	-13.1 -15.3	317.1 314.4	205/11 240/06	Offshore omega block with secondary Low over NV and ridging over site. Large High pressure cell over whole U.S. Center over central CO Rockies.

¹ Synoptic conditions prevailing between 1115 and 2315 GMT on the day indicated. First sentence describes conditions at the 500 mb level. Remainder describes surface charts.

Table 4. Summary of Inversion Destruction Data

(1)	(2)	(3)	(4)	(5)	(6)	(7)	(8)	(9)	(10)	(11)	(12)	(13)	(14)	(15)	(16)
Location	Date	t_i (LT)	t'_i (LT)	t_D (LT)	$t_D - t_i$ (hr min)	h_i (m)	h_v	(7)/(8)	Inversion Strength (°K)	γ_{-1} (°K m ⁻¹)	γ'_{-1} (°K m ⁻¹)	$\Delta t = (b)$ in	Valley Wind System Strength (m sec ⁻¹)	Clouds	Comments
<u>Yampa Valley</u>															
1. Sombrero	02-23-78	0655	0802	--	--	530	450	1.18	30.0	.0566	.0345	1.1	2.1	Clear	Snow Cover
2. Horseshoe	08-09-78	0615	0707	1045	4:30	650	450	1.44	16.0	.0246	.0187	1.5	1.7	Clear	
3. Horseshoe	08-10-78	0616	0708	1100	4:44	535	450	1.19	17.5	.0327	.0256	1.3	1.4	.1+.5Cu	Thunderstorm distant N and S.
<u>S. Fk White Valley</u>															
4. River Cabin	08-26-78	0635	0706	1030	3:55	525	300	1.75	14.1	.0269	.0208	2.5	6.8	.7Cu+CLR+.1Cu	
5. Stillwater	08-27-78	0636	0810	1130	4:54	400	750	.53	10.7	.0268	.0160	1.5	10.0+	Clear	
6. Mobley	08-27-78	0636	0743	1020	3:44	600	350	1.71	20.0	.0333	.0250	0.4	9.8	Clear	
7. Mobley	08-29-78	0638	0744	1110	4:32	530	350	1.51	19.5	.0368	.0280	2.1	9.3	Clear	
8. River Cabin	08-29-78	0638	0719	1135	4:57	525	300	1.75	17.8	.0339	.0154	1.5	7.5	Clear	
<u>Eagle Valley</u>															
9. Ray Miller	10-13-77	0718	0737	1230	5:12	675	700	.96	17.9	.0265	.0288	3.8	7.5	Clear	
10. Ray Miller	10-14-77	0719	0738	1210	4:51	625	700	.89	15.6	.0250	.0222	3.5	5.8	.2+.6+.2Ci	
11. Ray Miller	10-16-77	0721	0740	1230	5:09	650	700	.93	19.5	.0300	.0269	1.5	7.5	Clear	
12. Steve Miller	04-20-78	0527	0545	0945	4:18	625	700	.89	11.7	.0187	.0182	4.2	3.5	CLR+.8-Ci	
13. Steve Miller	07-08-78	0550	0623	1010	4:20	575	700	.82	19.3	.0336	.0280	1.1	2.3	Clear	
14. Steve Miller	07-09-78	0551	0624	1040	4:29	620	700	.89	16.0	.0337	.0238	1.0	6.8	CLR+QAc	
15. Steve Miller	10-11-78	0716	0803	1130	4:14	725	700	1.04	16.3	.0225	.0192	2.3	4.5	QCi+CLR	Sun obscured by clouds near sunrise
16. Steve Miller	10-12-78	0717	0746	1115	3:58	585	700	.84	15.3	.0262	.0200	2.3	4.0	Clear	
17. Steve Miller	10-19-78	0723	0742	1345	6:22	700	700	1.00	15.4	.0220	.0200	5.5	7.5	Clear	Rain yesterday
<u>Gore Valley</u>															
18. Safeway	12-10-75	0720	0900	1200	4:40	525	600	.88	17.0	.0378	.0290	0.0	0.5	Clear	1st sndng 0830. h_i estimated. Snow cover.
19. Municipal Bldg.	10-19-77	0723	0814	1130	4:07	585	700	.84	16.0	.0274	.0216	2.0	4.0	Clear	
20. Municipal Bldg.	07-06-78	0548	0658	1030	4:42	750	700	1.07	17.5	.0233	.0211	0.9	3.6	Clear	
21. Municipal Bldg.	07-07-78	0549	0658	0945	3:56	750	700	1.07	15.2	.0203	.0224	2.1	6.3	Clear	
Mean					4:35	604	590	1.10	17.1	.0295	.0231	2.0	5.4		

(2) t_i' , the local time at which direct sunlight first reached the observational site on the valley floor, is entered in column 4 as recorded from field notes. These times are accurate to within ± 10 minutes.

(3) t_D , an estimate of the local time of final destruction of the inversion, is entered in column 5. These time estimates were based on the series of temperature profiles taken during inversion destruction and indicate the time at which the entire valley depth would attain a constant potential temperature. Most estimates are probably reproducible by the same analyst to ± 30 minutes.

(4) h_i , the initial AGL height of the inversion, is recorded in column 7.

(5) h_v , the valley depth, is given in column 8.

(6) Inversion strength, the potential temperature difference between the base of the sounding and the top of the inversion, is given in column 10.

(7) γ , the average potential temperature gradient recorded on the first sounding of the morning, is given in column 11.

(8) γ' , the average potential temperature gradient within the inversion layer at a time approximately midway through the inversion destruction period, is given in column 12.

(9) $\Delta\theta_h$, the increase in potential temperature of the neutral layer above the valley inversion during the period of inversion destruction, is given in column 13.

(10) The peak strength (m sec^{-1}) of the down-valley wind within the inversion at a time near sunrise is given in column 14. The value given is an average of the wind speeds recorded by the up- and down-soundings at the altitude of the peak down-valley wind. This averaging

was necessary to account for systematic differences between the winds indicated by up- and down-soundings, as discussed in Appendix B. Note that the value given is not necessarily representative of average down-valley wind speeds within the sunrise inversion since some valleys had a shallow layer of strong winds in an otherwise quiescent valley atmosphere.

1. Time Relationships

Previous data have shown that inversion destruction typically begins at a time near theoretical sunrise, t_1 . Actual sunrise, t_1' , at the observation site on the valley floor usually occurs somewhat later, depending on the topography surrounding the site and the earth-sun geometry, which varies with time of day, day of year, latitude, and longitude. Direct sunlight does not reach the floor of some of the valleys studied until up to one hour and 50 minutes after theoretical sunrise. In general, the valley sites that do not receive sunlight on the valley floor until long after theoretical sunrise are deep valleys oriented at right angles to the azimuth angle of the sun at sunrise. In these valleys sunlight moves gradually down one of the sidewalls as the sun rises above the opposite ridgetop, resulting in a strong asymmetry in solar heat flux on the two sidewalls. A number of mathematical models are now available that can predict the temporal and spatial progression of shading in a region of complex topography as well as the solar fluxes on topographic surfaces of different orientation (Williams, et al. 1972; Holben, 1975).

The arrival of direct radiation at the observation site marks the beginning of the growth of the convective boundary layer at the site. The development of a convective boundary layer at the valley floor

depends strongly on the disposition of the solar flux. The energy will not be available for boundary layer development if it is reflected back to the sky, if it goes to evaporate water, or if it is used to heat the ground. For the case studies selected, however, a developing boundary layer was usually readily apparent in temperature soundings within 30-40 minutes after sunlight reached the valley floor.

The amount of time after sunrise required for an inversion to be destroyed varies from $3\frac{1}{2}$ to 5 hours. These are rather narrow limits, considering the wide variation in topography and broad seasonal sampling of data. For 20 cases listed in Table 4, the average time required for destruction was 4 hours and 35 minutes. An exception was the inversion of 23 February 1978 in the snow-covered Yampa Valley, since it was maintained all day, even though it underwent a clear evolutionary cycle. The 19 October 1978 inversion in the Eagle Valley also took an unusually long time to be destroyed. This is probably due to the fact that rain had fallen in the valley on the previous day. The small range in the time required to break the inversions may seem to be a curious result. After all, energy is required to break inversions, and one would perhaps expect inversions to break more rapidly in the summertime than in the winter when insolation is weak. However, application of the solar flux model of Appendix E shows that the integrated (extraterrestrial) solar flux on a horizontal surface at the latitude of the experimental areas for the first four hours after sunrise varies only slightly with season, except for a brief period around the winter solstice (Figures 18 and 19).

2. Characteristics of Fully Developed Inversions

Surface-based radiation inversions in mountain valleys can be described in terms of depth, inversion strength, mean potential

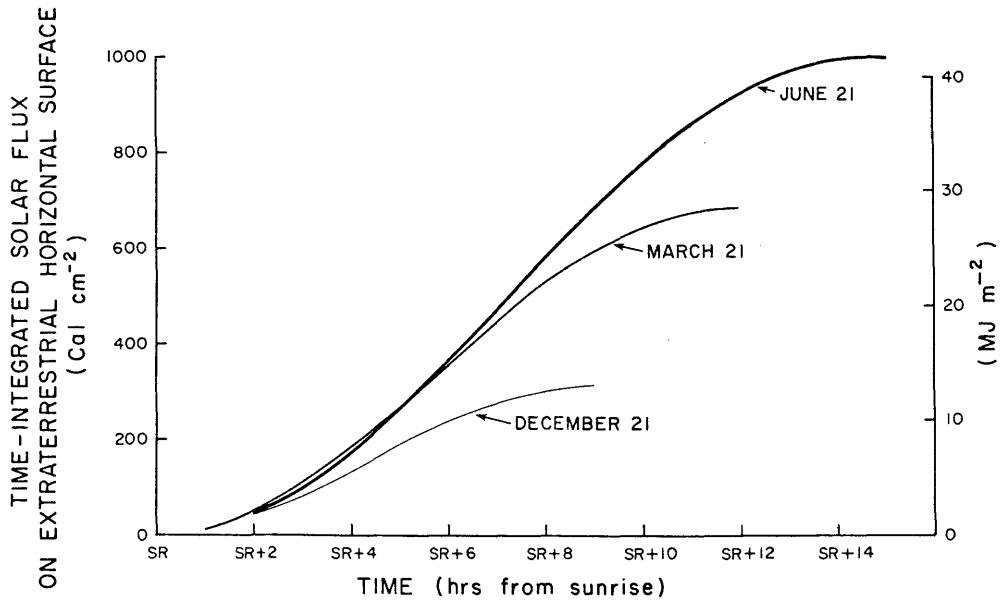


Figure 18. Time-integrated solar flux on an extraterrestrial horizontal surface as a function of time of day for selected days of the year. For latitude and longitude of Steamboat Springs, Colorado.

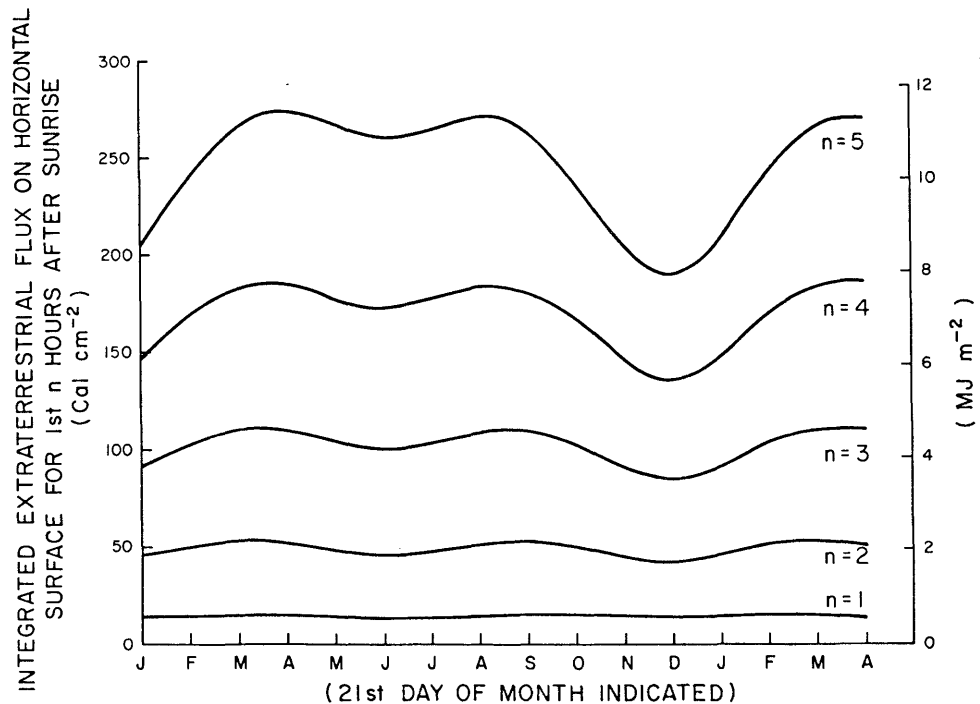


Figure 19. Time-integrated solar flux on an extraterrestrial horizontal surface as a function of month of year for the first n hours following sunrise. For latitude and longitude of Steamboat Springs, Colorado.

temperature gradient, profile shape, and deformations in the temperature structure. They are typically most fully developed near sunrise. The characteristics of the near-sunrise soundings are discussed below for the 21 case studies.

a. Depth of Valley Inversions

The average depth of the valley inversions studied was 604 m (Table 4, column 7). Inversion depths ranged from 400 m at the Stillwater site to 750 m in the Gore Valley. In undisturbed, clear weather, inversions at a particular site attain a depth typical of the site, regardless of season. Thus for the Eagle Valley sites, which are close together, inversions typically grow to about 625 m. Inversions at the two valley sites in the Yampa Valley, which again are not far apart, are 475-650 m deep. Inversions at the Stillwater site on the South Fork of the White River, investigated in only one season, attain heights of only 300 or 400 m. These typical inversion depths at a particular site are determined by the topography of the site.

For the valleys studied, inversions generally built to the level of the ridgetops (Table 4, columns 8 and 9). The average ratio of inversion depth to valley depth was 1.10, although the ratio varied from .53 at the Stillwater site to 1.75 at the River Cabin. While the average inversion top height is slightly above the level of the local ridgetops, the height of the inversion top in all cases is lower than the height of regional terrain features in the vicinity of the sites. For most valley sites it appears that the top of the inversion cannot be much greater than the immediate ridgetops since air in the cold pool of the temperature inversion can then simply diverge from the valley by flowing over the ridges. The fact that most inversions grow to the

level of the ridgetops implies that, during the clear nights studied, cooling was sufficient to fill the entire depth of the valley with cold air. Individual cases where the top of the cold pool is considerably above the local ridgetops at a site are probably due to the existence of a regional inversion that extends over more than one valley. This is a likely explanation for the deep inversions over the River Cabin and Mobley sites on the South Fork of the White River. Inversion depths lower than the local ridgetops may be due to valleys that are too voluminous to be filled during a night or may be due to a terrain constriction upstream of the site (e.g., Stillwater site) or a widening of the valley downstream of the site (e.g., at Paonia, Colorado on the North Fork of the Gunnison River).

b. Strength of Valley Inversions

Inversion strength (Table 4, column 10) averaged 17.1°K for the cases studied and varied from 10.7°K for a shallow summer inversion in the South Fork of the White Valley to 30.0°K for a moderately deep inversion under clear skies in the snow-covered Yampa Valley. The primary factors affecting inversion strength appear to be cloudiness, which decreases inversion strength, and snow cover on the ground, which increases it. Snow cover was present during two campaigns. In February, 1978, the Yampa Valley was covered with a deep snowpack. In December, 1975, the Gore Valley had a cover of snow on the forested north-facing hillside but had only patchy snow cover on the south-facing hillside. Inversion depth has only a limited effect on inversion strength, with deeper inversions being relatively weaker than shallow inversions, other things being equal.

c. Vertical Temperature Gradients in Valley Inversions

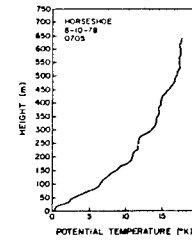
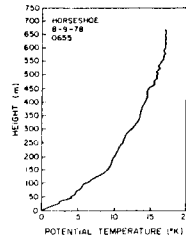
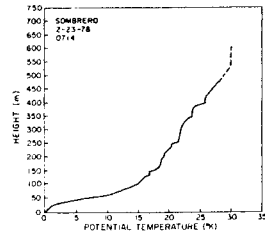
The potential temperature gradient at a particular site (Table 4, column 11), being a ratio of inversion depth and inversion strength, will be controlled by cloudiness and/or snow cover. The average potential temperature gradient for the valleys investigated was $.0295^{\circ}\text{K m}^{-1}$, but values ranged from $.0187$ to $.0566^{\circ}\text{K m}^{-1}$. The average potential temperature gradient, defined as the difference in potential temperature between the top of the inversion and the surface divided by inversion depth, is often not representative of the potential temperature gradient at mid or upper levels of the inversion. This is especially apparent when a shallow, intense inversion is present near the ground. A second calculation of potential temperature gradient for mid and upper levels of the inversion is given in column 12 of Table 4 for a time approximately mid-way through the inversion destruction period. The average of this figure for the 21 case studies is $.0231^{\circ}\text{K m}^{-1}$.

d. Seasonal Differences in Valley Inversions

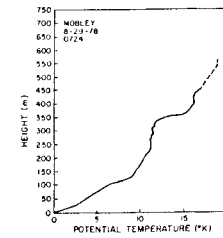
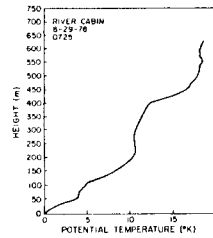
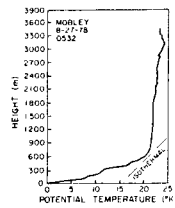
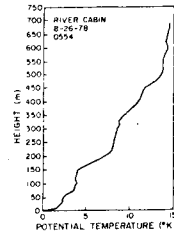
Seasonal differences in the characteristics of valley inversions are not large. As mentioned above, inversion strength is increased by snow cover. There also seems to be a tendency for summer inversions to be slightly deeper, but not stronger. This is most clearly seen in the Yampa and Gore Valley data.

e. General Shape of Temperature Profiles

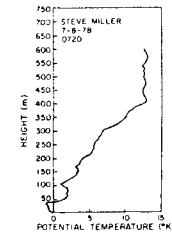
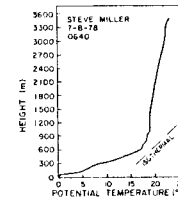
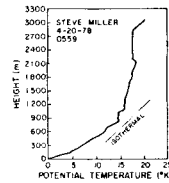
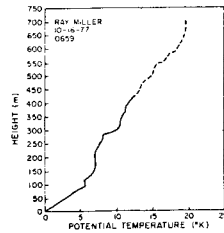
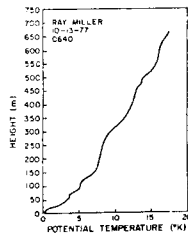
Plots of some of the near-sunrise soundings for the 21 case studies are presented below in Figure 20. A schematic diagram showing the general shape of the soundings is presented in Figure 21. Pre-sunrise soundings typically have a hyperbolic segment near the ground capped by a near-linear segment that terminates at the top of the



YAMPA VALLEY

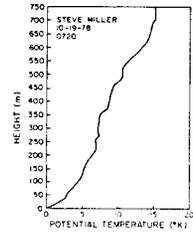
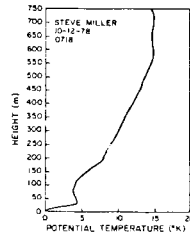
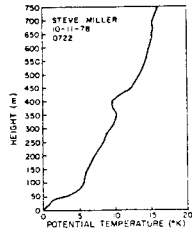
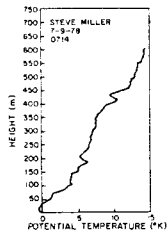


SOUTH FORK WHITE VALLEY

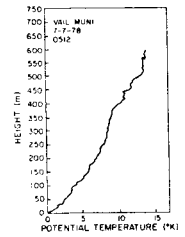
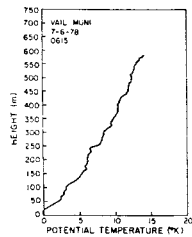
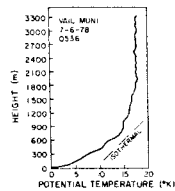
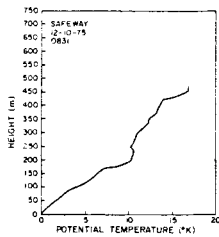


EAGLE VALLEY

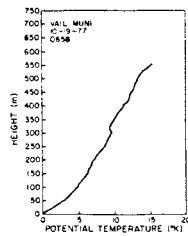
Figure 20. Near-sunrise potential temperature profiles.



EAGLE VALLEY



GORE VALLEY



GORE VALLEY

Figure 20, con'd. Near-sunrise potential temperature profiles.

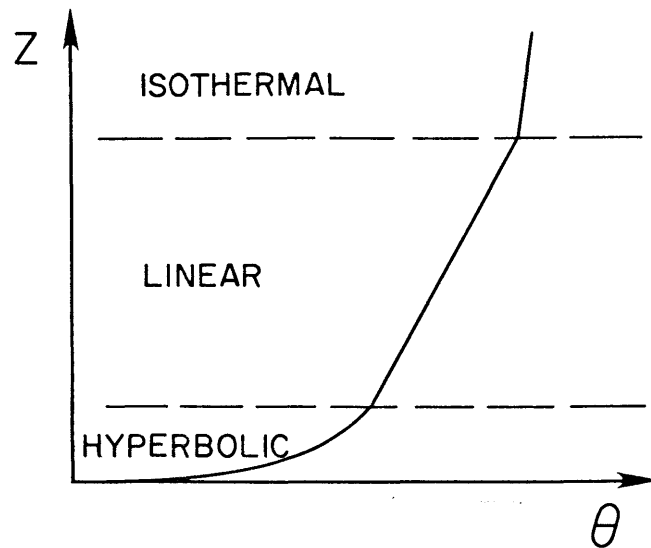


Figure 21. Schematic diagram showing the general shape of the vertical potential temperature profiles at sunrise.

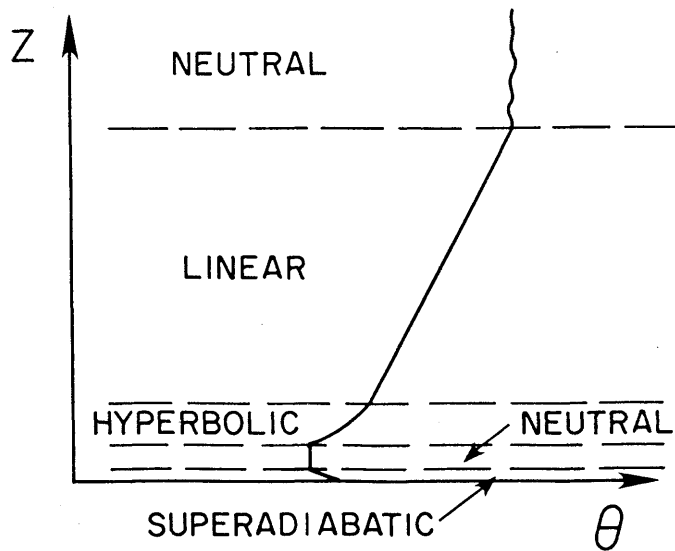


Figure 22. Schematic diagram showing the general shape of the vertical potential temperature profiles soon after sunrise on the valley floor.

inversion where a less stable, near-isothermal profile begins. The layer near the ground often changes significantly after sunrise if sunlight has reached the valley floor (Figure 22). A shallow, super-adiabatic layer typically develops adjacent to the ground capped by a shallow, neutral layer. The remnants of the pre-sunrise hyperbolic layer are found above the neutral layer, surmounted by the linear layer that extends to the top of the inversion. The top of the inversion is usually indicated by a change to a nearly constant potential temperature. Low amplitude potential temperature fluctuations are often superimposed on this section of the profile. The means by which the tops of the profiles change from isothermal to neutral after sunrise is an important question that will be addressed in later sections.

The hyperbolic segment of the profile is usually most pronounced when (a) the ground is snow covered, (b) wind speeds within the inversion are light, or (c) a topographic constriction of the valley cross section occurs downstream. In extreme cases the entire inversion will be hyperbolic, and no near-linear segment will occur in the profile. The near-linear segment of the profile is most apparent when down-valley winds are well-developed within the inversion. Where down-valley winds are strong throughout the whole inversion depth, the hyperbolic segment of the profile may fail to appear. Very strong down-valley winds within an inversion act to linearize the shape of the inversion profile but do not destroy the inversion. Several of the valleys investigated had strong ($7 - 10 \text{ m sec}^{-1}$) down-valley winds and yet maintained inversions that were typical in depth and strength. The strength of valley wind systems varied from valley to valley and seemed to be a function of topography rather than of any factors external to the valley, such as the synoptic situation.

f. Deformations in the Profiles

Many of the inversion profiles (Figure 20) have transient bumps or bulges. Similar deformations have been described by Petkovšek (1978) for soundings taken in closed valleys or valley basins of Yugoslavia. In his study of 70 examples of S-shaped deformations that occurred in temperature profiles in a single valley, he found the average thickness to be 70 m, with a range of 30 to 180 meters. Most of the deformations were observed from 90 to 300 m above the valley floor. The average height was 130 m. A significant diurnal difference in frequency of occurrence was noted with 97% of the deformations occurring in nocturnal soundings. Petkovšek's explanation of the deformations involves the penetration of air masses into the stable air of the valley basin. Influxes of air into isolated layers of the temperature inversion are favored in small valley basins with high plateaus, side valleys, and slopes of different steepness, which serve as effective cooling surfaces during night time. Cooled air sinks down the slopes, warming adiabatically until reaching an equilibrium level where the air leaves the slope and penetrates horizontally into the valley basin air at the level of approximate temperature equilibrium. Because of the intense temperature gradient in the inversion, the air penetrates in a thin layer. Turbulence in this layer produces mixing and causes an S-shaped deformation in the profile following one of the three shapes given in Figure 23, depending on whether mixing is accompanied by warming or cooling of the original profile. Of the 70 deformations studied by Petkovšek, only five were accompanied by warming. Only 44% of the deformations had an adiabatic temperature gradient in the middle

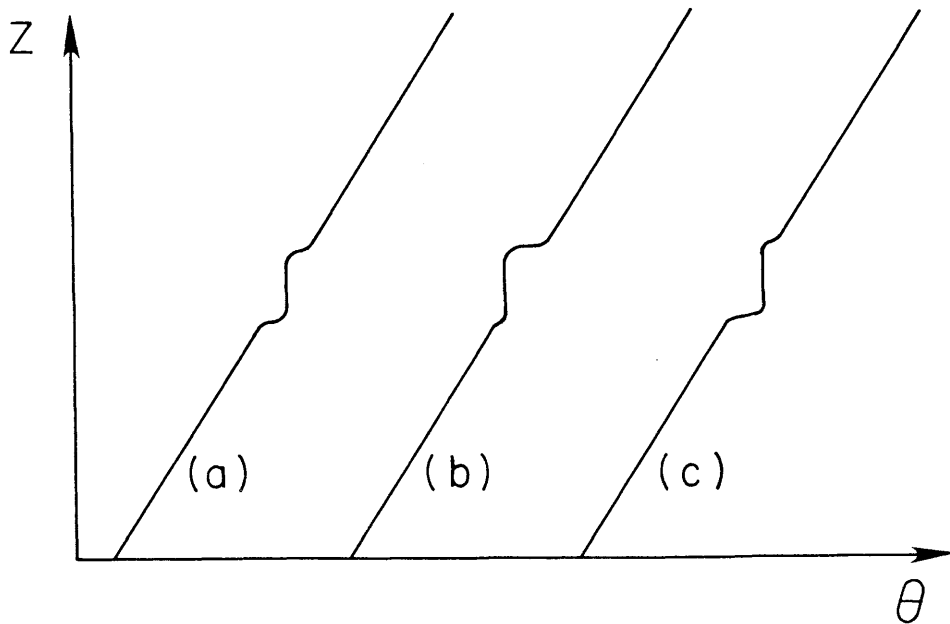


Figure 23. Petkovšek's (1978) three types of potential temperature deformations. (a) Mixing, (b) Mixing with cooling, and (c) Mixing with warming.

of the S-shape. Most had temperature gradients that were more stable, suggesting that mixing was not as intense as assumed in the profiles of Figure 23.

A number of near-sunrise valley soundings in Figure 25 are good examples of potential temperature deformations as described by Petkovšek. Especially good examples are the River Cabin profiles for 26 August 1978 and 29 August 1978; the Eagle Valley profiles for 11 and 12 October 1978; the Mobley Ranch profile for 29 August 1978; and the Gore Valley profile of 10 December 1975. The deformations were usually accompanied by wind shifts or directional wind shears within the overall temperature inversion. Winds in the deformations often had significant cross-valley components, suggesting that they may have originated from the valley sidewall or ridgetops. The deformations at Mobley and River Cabin sites on 29 August 1978 occur at the approximate

altitude of the ridgetops and their persistence in later soundings suggests that they may be closely related to the topography. The Gore Valley was the only valley studied that could be considered a valley basin or closed valley. The presence of profile deformations in other valleys therefore represents an extension of Petkovšek's results, and suggests that similar processes occur in open valleys.

Deformations other than those described by Petkovsek are apparent in many of the soundings. The potential temperature profiles rarely have a smooth shape and often contain small amplitude fluctuations that are shallower and weaker than the ones Petkovšek describes. Many of these are probably small turbulent fluctuations caused by vertical shear of down-valley winds within the inversion. Other temperature deformations are frequently seen in the neutral layer above the valley inversion after sunrise. Turbulent temperature oscillations are frequently seen in this layer. In addition to the nighttime or near-sunrise deformations just discussed, some daytime deformations were observed in the experimental program. The most notable occur in the soundings of 23 February 1978 at Sombrero Ranch in the complicated terrain of the snow-covered Yampa Valley.

g. Comparison of Valley Inversions to Inversions at Grand Junction

Grand Junction, Colorado, the National Weather Service rawinsonde station nearest the experimental sites, is at an altitude of 1475 m on the broad Colorado River west of the study region. Table 5 presents morning rawinsonde data at Grand Junction for the dates of the case studies discussed above (Table 4). Rawinsondes were usually launched at 1115 GMT, before sunrise in all seasons. Data include information on inversions at Grand Junction as well as 700 and 500 mb wind speeds

Table 5. 1115 GMT Grand Junction Rawinsonde Data Corresponding to Valley Data of Table 4

(1) Date	(2) Inversion Depth (m)	(3) Inversion Strength (°K)	(4) (3)/(2) (°K m ⁻¹)	(5) 700 mb Wind (°, m sec ⁻¹)	(6) Along-Valley Component (m sec ⁻¹)	(7) Cross Valley Component (m sec ⁻¹)	(8) 500 mb Wind (°, m sec ⁻¹)	(9) Along-Valley Component (m sec ⁻¹)	(10) Cross-Valley Component (m sec ⁻¹)
<u>Yampa</u>									
1. 02-23-78	306	6.7	.0219	255/05	-0.26	4.99	275/09	2.63	8.61
2. 08-09-78	49	2.6	.0531	185/07	-6.69	2.05	320/08	7.06	3.76
3. 08-10-78	349	5.3	.0152	255/07	-0.37	6.99	310/10	7.88	6.16
<u>S Fk White</u>									
4. 08-26-78	202	6.3	.0312	245/06	5.85	1.35	230/08	7.06	3.76
5. 08-27-78	270	11.2	.0415	275/04	1.88	3.53	255/09	1.25	8.91
6. 08-27-78	270	11.2	.0415	275/04	3.35	2.18	255/09	5.42	7.19
7. 08-29-78	79	6.3	.0797	300/02	1.49	-1.34	255/08	7.99	0.42
8. 08-29-78	79	6.3	.0797	300/02	1.98	0.28	255/08	4.81	6.39
<u>Eagle</u>									
9. 10-13-77	192	3.3	.0172	230/05	2.94	4.05	210/07	1.93	6.73
10. 10-14-77	172	5.3	.0308	040/07	-3.07	-6.29	340/06	3.36	-4.97
11. 10-16-77	140	7.1	.0507	235/06	3.94	4.53	220/07	3.07	6.29
12. 04-20-78	88	5.7	.0648	255/06	5.25	2.91	270/10	9.70	2.42
13. 07-08-78	196	8.5	.0434	255/14	12.24	6.79	225/23	11.85	19.71
14. 07-09-78	266	4.6	.0173	250/08	6.63	4.47	235/12	7.87	9.06
15. 10-11-78	278	5.0	.0180	290/03	2.98	-0.31	335/11	6.92	-8.55
16. 10-12-78	159	11.5	.0723	325/06	4.53	-3.94	320/13	10.52	-7.60
17. 10-19-78	256	8.5	.0332	235/05	3.28	3.77	255/10	8.75	4.85
<u>Gore</u>									
18. 12-10-75	315	10.3	.0327	230/10	9.98	-0.70	260/18	14.92	-10.07
19. 10-19-77	176	6.7	.0381	250/06	5.52	2.34	205/11	4.12	10.20
20. 07-06-78	-	-	-	260/02	1.95	0.45	255/11	10.46	3.40
21. 07-07-78	79	5.9	.0747	175/02	-0.28	1.98	260/15	14.62	3.37
Mean	198	6.7	.0409						
Minimum	49	2.6	.0152						
Maximum	349	11.5	.0797						

and directions. For most of the valley sites, the 700 mb level is just above ridgetops. The 500 mb level is at least 1000 m above the crest of the Rocky Mountains. Columns 6, 7, 9, and 10 give the along-valley and cross-valley components of the Grand Junction winds for the specified valley site. A positive number for the along-valley component indicates an up-valley flow. A positive number for the cross-valley component indicates a flow from right to left when looking up the valley.

Inversions at Grand Junction are usually much shallower than the valley inversions, averaging only 198 m deep, but varying from 49 to 349 m. Inversion strengths at Grand Junction range from 2.6° to 11.5°K , but average 6.7°K , versus 17.1°K for the valley inversions. The potential temperature gradient, averaging $.0409^{\circ}\text{K m}^{-1}$ with a range of $.0152$ to $.0797^{\circ}\text{K m}^{-1}$, is considerably stronger than for the valley inversions. All inversion characteristics at Grand Junction are significantly more variable than the characteristics of valley inversions.

Due to the selection of meteorologically undisturbed experimental periods, valley inversion data were generally collected when 700 and 500 mb wind speeds were low. The effect of upper level winds on the development of valley inversions and Grand Junction inversions can be seen by comparing data in Tables 5 and 4. The Eagle Valley data suggest that strong 700 mb cross-valley winds may result in slightly shallower inversions than normal. But, at least for the range of wind speeds studied, no obvious and consistent relationship between upper air winds and valley temperature inversion development can be determined, even when the upper level winds are resolved into along- and cross-valley components.

3. Inversion Descent and CBL Ascent

The rates of descent of the inversion top and ascent of the CBL for a subset of the 21 case studies are seen in Figures 24-27, where the heights of these features are plotted against time. Figure 24 provides data for the Yampa Valley; Figure 25 for the South Fork of the White River; Figure 26 for the Eagle Valley; and Figure 27 for the Gore Valley. The tops of the inversions descend after sunrise in all of the cases studied, as specified for Pattern 2 and 3 temperature structure evolution. The rate of descent usually increases with time, but in a few of the case studies, the inversion descent rate remains nearly constant during much of the inversion descent rate remains nearly constant during much of the inversion destruction period. This constant rate of descent, previously described by Whiteman and McKee (1977), is particularly marked for the 10 December 1975 inversion destruction in the Gore Valley. Inversion descent in one of the case studies was unusual. In the Yampa Valley on 9 August 1978, the single example approximating Pattern 1 inversion destruction observed in the experiments, the descent of the inversion top was arrested about four hours after sunrise when the inversion top began to ascend. The main feature of the inversion destruction on this day is the growth of the CBL. From Table 4, most inversions are broken in about $4\frac{1}{2}$ hours, and the average inversion is 604 m deep initially. Since the inversion is broken when the descending inversion top meets the ascending CBL at approximately 250 m above the valley floor, the average rate of inversion descent is $604 - 250 \text{ m} / 4.5 \text{ hours} = 79 \text{ m hr}^{-1}$. The observed ascent of the CBL from the valley floor typically begins about one hour after sunrise. The rate of growth of the CBL over the valley floor varies

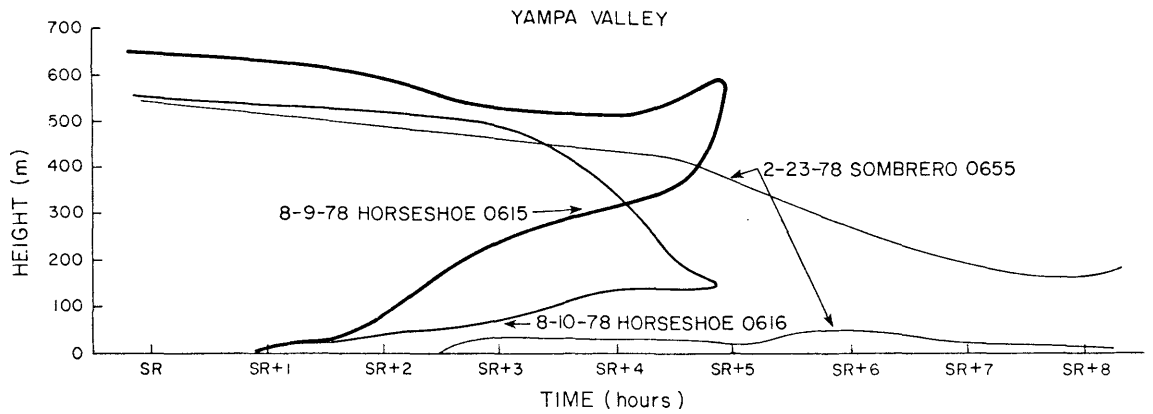


Figure 24. CBL ascent/inversion top descent for inversion destruction in the Yampa Valley. The date, site, and time of sunrise are indicated on the curves.

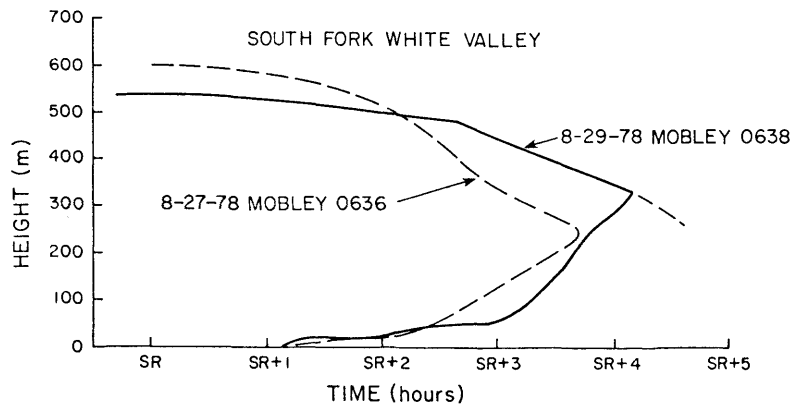


Figure 25. Same as Figure 24 for the South Fork of the White Valley.

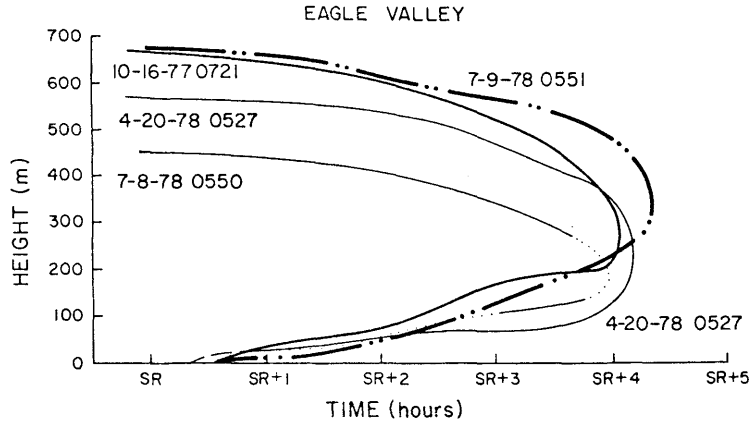


Figure 26. Same as Figure 24 for the Eagle Valley.

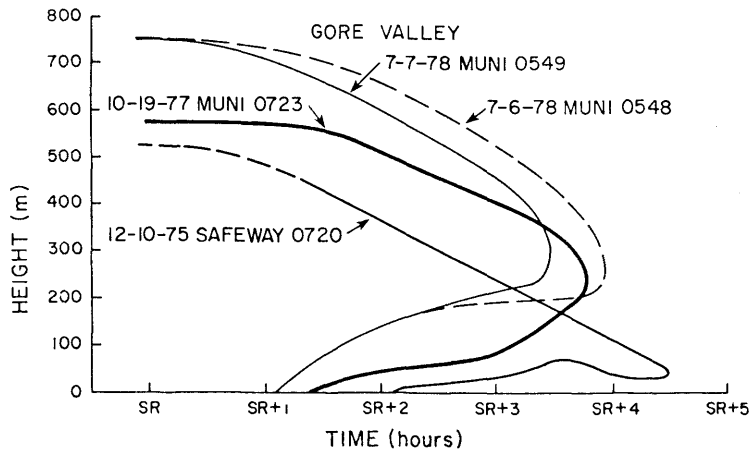


Figure 27. Same as Figure 24 for the Gore Valley.

from site to site and from case to case, but the average rate of ascent is about $250 \text{ m}/3.5 \text{ hrs} = 71 \text{ m hr}^{-1}$. The CBL grows quickly initially, but then the rate of growth usually decreases. This tendency for a decrease in growth rate often occurs when the CBL reaches a depth of about 50 m. The rate of CBL ascent and inversion top descent increase significantly just before the final destruction of the inversion. This may be due to a sudden breakup or overturning of the shallow remnants of the elevated inversion layer. The course of the two curves, constructed from intermittent balloon soundings, is usually rather ill-defined at this critical point, since final destruction may take place rather abruptly. Several different criteria, relying on characteristics of either the wind field or the temperature field, can be used to determine the time of final inversion destruction. The time at which the rising CBL meets the descending inversion top is one example. A vertical temperature profile taken at this time, however, does not show a constant potential temperature profile through the whole valley depth, since it takes some additional time for shear and buoyancy production of turbulence to mix the valley atmosphere completely. The time of inversion destruction recorded in Table 4 is an estimate of the time at which the valley atmosphere attained a constant potential temperature.

4. Temperature Changes in the Valley Atmosphere

Warming of the valley atmosphere occurs in one of three ways, as previously described for the three inversion structure evolution patterns. Destruction of an inversion, no matter which of the warming patterns is followed, requires enough energy to warm the valley from its initial inversion profile to a final state of constant potential

temperature. The actual amount of energy is dependent on the initial energy deficit of the inversion volume relative to the atmosphere above the valley inversion. A simple diagrammatic representation of this concept for a horizontally homogeneous column of unit cross-sectional area is shown in Figure 28. The shaded area represents the energy needed to warm the column from the initial profile at t_i to the final profile at t_D , when the inversion is completely destroyed. The amount of energy required is $Q = \int_0^{h_i} \rho C_p \Delta T dz$ or, in terms of potential temperature, $Q = \int_0^{h_i} \rho C_p \frac{T}{\theta} \Delta\theta dz$, where $\Delta\theta = \gamma(h_i - z)$ and γ is the potential temperature gradient in the inversion layer at time t_i . In order to destroy the inversion, the base of the column must be warmed much more than the top region. Over flat terrain the unequal warming of the top

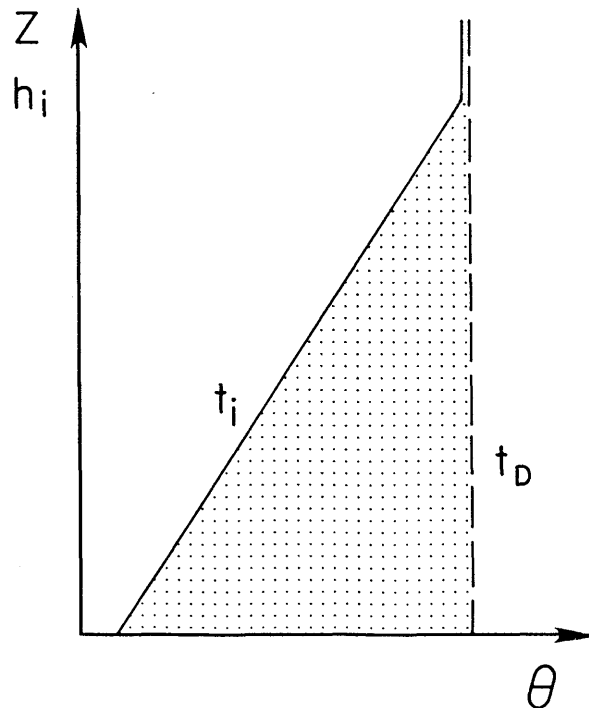


Figure 28. Representation of energy required to break an inversion.

and bottom regions of the column is readily accomplished. The main source of energy is at the ground where the most heat is required, and the warming is directed and controlled by the process of penetrative convection in such a way that a nearly constant potential temperature layer warms with time. On the other hand, in the valley, heated surfaces (sidewalls and valley floor) surround the valley atmosphere, at least in cross section, and the heating can be expected to progress in a different manner. The difference in the way in which the profiles are warmed is easily seen by comparing the first destruction pattern, which will be taken as representative of inversion breakup over flat plains, and the Pattern 3 destruction, characteristic of most mountain valleys. These differences will be discussed by considering the three basic layers in Pattern 2 and 3 soundings of the valley atmosphere as taken from the valley center.

a. Neutral Layer

The layer above the valley inversion changes from isothermal to neutral and begins to warm immediately after sunrise. It thus differs from the atmosphere above a temperature inversion over flat terrain where a phase difference in the onset of warming with height is characteristic. This phase lag is due to the finite time required for diabatic heating processes to transport energy upwards from the underlying surface. In a valley the immediate formation and warming of the neutral layer is probably due to its close proximity to heating surfaces (e.g., ridgetops) and/or the existence of an efficient means to transport heat from the nearby surfaces (e.g., horizontal advection from ridgetops or sidewalls, or transport from slope flows). From Table 4, column 13, observed warming of the neutral layer during the

time of inversion breakup ranges from 0 to 5.5°K. The average rate of warming is 2.0°K in 4 hours and 35 minutes, or about $.4^{\circ}\text{K hr}^{-1}$, a value much lower than that typical of the inversion layer below.

b. Inversion Layer

For the idealized Pattern 2 and 3 temperature structure evolutions, the potential temperature increases at the same rate at all levels in the stable region, consistent with subsidence heating. Warming of the inversion layer begins after sunrise and increases as a function of time. The warming rate of the average inversion layer over the period of inversion breakup is about $2^{\circ}\text{K hr}^{-1}$.

c. Convective Boundary Layer

Since the potential temperature within a CBL does not vary significantly with height but increases with time, all points within the CBL warm at the same rate. In pattern 2 temperature structure evolution, where the CBL does not grow with time, the warming rate of the CBL is the same as the warming rate of the inversion layer above. In Pattern 3 evolution the CBL grows with time, and must, therefore, warm more rapidly than the inversion layer above.

The retarded growth rate of the valley floor CBL relative to that of CBLs over the plains has been previously mentioned, and is especially marked in Pattern 2 valley inversion destruction where the CBL does not grow at all once it attains a certain height. If the reasonable assumption is made that the energy budgets of the valley floor and plains surfaces are similar, it is necessary to explain why the valley floor CBL does not warm faster than the CBL over the plains. After all, a shallow layer is expected to warm more rapidly than a deeper layer, given the same energy input. The explanation for the

discrepancy must be that the sensible heat flux input into the valley CBL is transported to other parts of the valley atmosphere. The two-dimensional structure of the temperature field in the cross-valley plane and the interrelationships between temperature structure and wind system evolution provide further information on the transport and on the warming in the neutral and inversion layers. This will be shown later.

C. Wind Structure Evolution

Case study data presented in previous sections of this chapter have been analyzed primarily for information on temperature structure evolution, rather than for wind structure evolution. Wind structure evolution is, in general, much more variable than temperature structure evolution. Nevertheless, some important relationships between wind and temperature structures are apparent in the data.

Five separate but interrelated wind systems have been identified in the valley data. First, the along-slope wind system blows in a shallow layer above the sidewalls with a component blowing up or down the slope. The second wind system blows in a shallow layer immediately above the valley floor with its major component blowing up or down the valley axis. The third wind system, called the along-valley wind system, prevails in the central volume of the valley with its major components blowing up or down the valley axis. The fourth wind system blows in the neutral layer above the valley inversion and, apparently, over the entire larger-scale western slope of the Rocky Mountains. Winds in this system blow up or down the incline of the western slope. Finally, a fifth wind system, representing the free atmosphere above the mountain range, overlies all the others.

Wind system nomenclature in the literature has been inconsistent. Table 6 presents the nomenclature used in this text. The terms chosen emphasize the essentially bi-directional nature of the local wind systems and their relationship to the underlying topographical features. The first four wind systems are local and generally develop within certain structural features of the temperature profiles as listed in the table. In Figures 29 and 30 the prevailing wind systems during inversion destruction are identified with structural layers in the temperature profiles.

The typical wind system development at mid morning is represented in Figure 31. A convective boundary layer is present over the inclined slopes of the mountain range, the valley sidewalls, and the valley floor. Within the convective boundary layer the air flows up the incline, up the sidewalls, and up the valley floor. The down-valley winds that were present at sunrise within the valley inversion persist in the stable core in the central region of the valley atmosphere. Once the stable core is destroyed, a deep convective boundary layer will be present over all the mountain and valley terrain, and the individual up-floor, up-valley, up-incline and up-slope flows are difficult to differentiate. The gradient level winds overlie the local circulations and will persist above the deep convective boundary layer.

The slow upward growth of the along-floor wind system, the persistence of the down-valley flow in the middle reaches of the valley, and the development and descent into the valley of the up-incline wind system are all features of wind system evolution in Colorado valleys that were not anticipated in conceptual models of wind system evolution (Wagner, 1938; Defant, 1951). These features,

Table 6. Classification of Wind Systems

Wind System Name	Temperature Structure	Previous Wind System Names
Along-Slope	CBL over valley sidewalls	Slope wind, Topographic wind
Along-Floor	CBL over valley floor	Slope wind along the valley floor, Topographic wind
Along-Valley	Stable - Core region of valley	Valley wind, Mountain wind, Day wind, Night wind
Along-Incline	CBL over mesoscale western slope of Rocky Mountains	Topographic wind
Gradient	Stable - Free atmosphere	Gradient wind, Geostrophic wind, Prevailing wind, Synoptic-scale wind

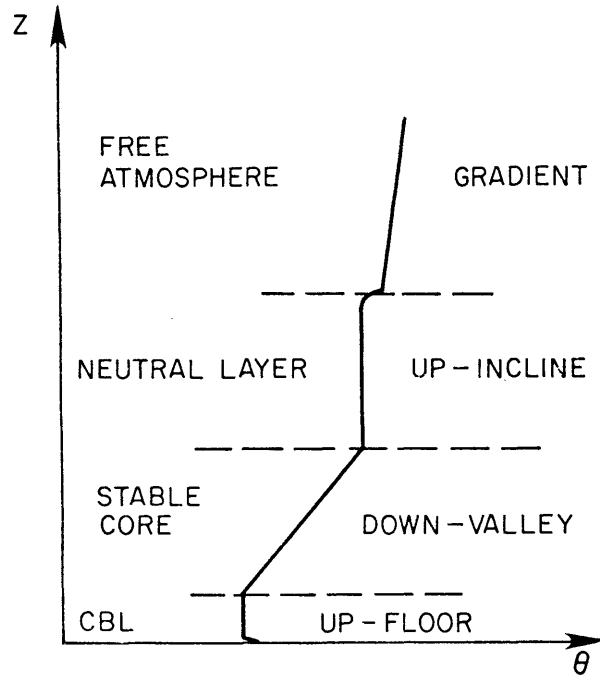


Figure 29. Typical correspondence between temperature and wind structure during valley inversion destruction.

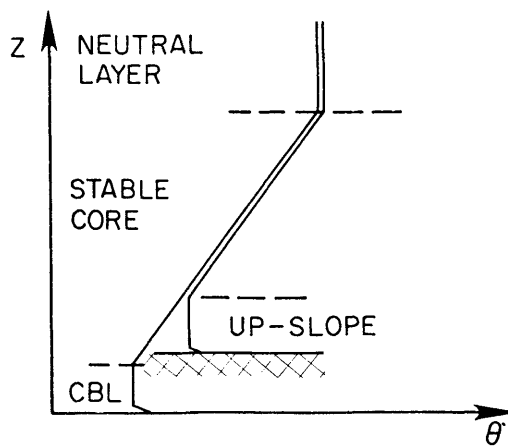


Figure 30. An upslope wind typically blows in the CBL that develops over the sidewalls during inversion destruction. Shown in the figure are two concurrent vertical potential temperature soundings, one from the valley floor and one from a sidewall.

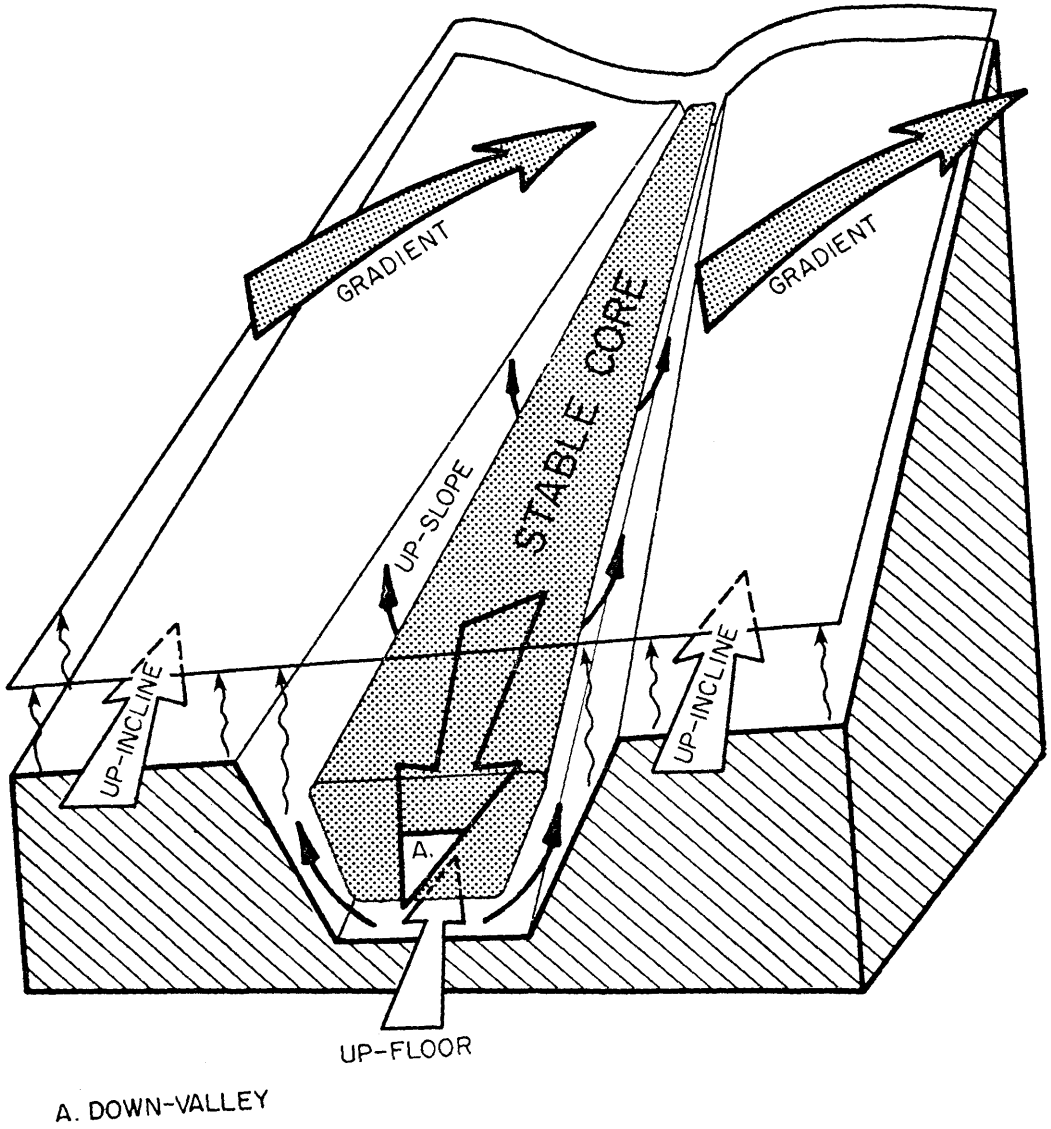


Figure 31. Typical wind system development at mid morning during inversion breakup.

however, are consistent with Wagner's basic theory of local wind systems and provide evidence that allows an extension and generalization of his theory. Wagner attributes the existence of the along-valley and along-slope wind systems to horizontal pressure gradients forced by diurnal changes in temperature over different horizontal length scales. Data from Colorado valleys have confirmed that the four local valley wind systems develop when a thermal boundary layer forms along a topographic slope. A sloping thermal boundary layer will necessarily produce horizontal pressure differences. The wind speeds and directions within each of these boundary layers will depend on the horizontal pressure gradient produced by the sloping boundary layers over the characteristic length scale associated with that boundary layer and will depend on the balance of forces active at that length scale. This concept is illustrated in Figures 32 and 33 where it is assumed that the depths of the thermal boundary layers are constant along the terrain slope, and the topographic and thermal structures are given a simple form. The length scales over which the pressure gradients act at the base of each layer is given by the ratio of layer depth to the slope of the underlying terrain so that, using typical values of layer depths and terrain slopes,

$$L_1 = \text{along-incline length scale} \cong \frac{1000 \text{ m}}{.01} = 100 \text{ km},$$

$$L_2 = \text{along-valley length scale} \cong \frac{500 \text{ m}}{.01} = 50 \text{ km},$$

$$L_3 = \text{along-floor length scale} \cong \frac{50 \text{ m}}{.01} = 5 \text{ km},$$

$$L_4 = \text{along-slope length scale} = \frac{100 \text{ m}}{.2} = .5 \text{ km},$$

From Figures 32 and 33, the denominators of the ratios are estimates of $\tan \eta$ and $\tan \alpha$.

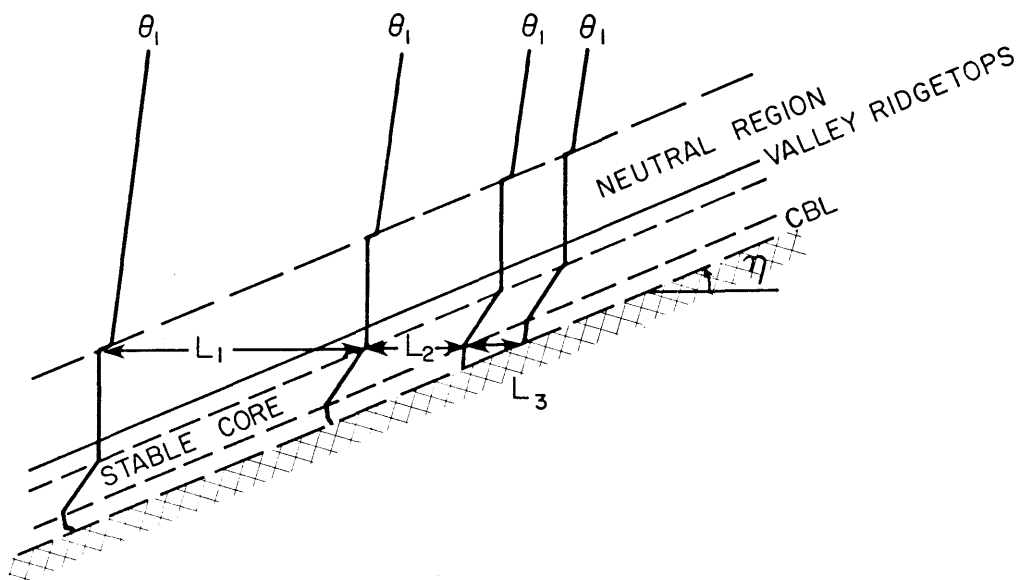


Figure 32. Cross section of the slope of a mountain range at mid morning showing the inclined thermal boundary layers and appropriate length scales. Potential temperature profiles are superimposed. The inclination angle of the slope is given by η .

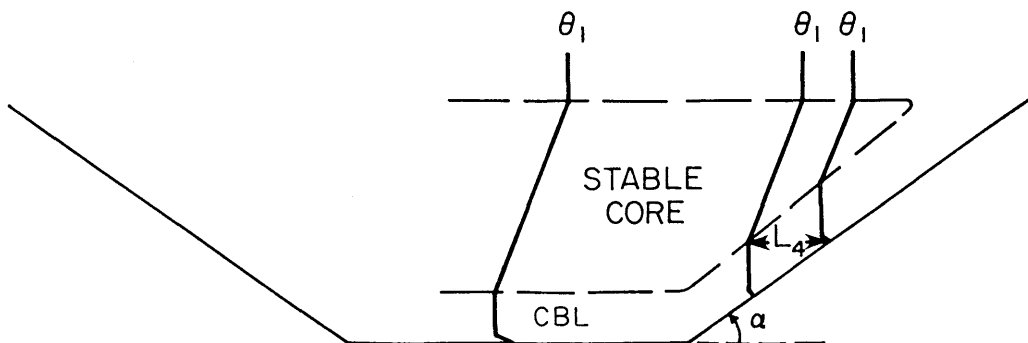


Figure 33. Valley cross section showing the along-slope length scale, L_4 . Potential temperature profiles are superimposed. The inclination angle of the sidewall is given by α .

The wind systems, to be discussed separately below, often exist in close physical proximity to one another and may be interrelated by a number of mechanisms including transfer of momentum, friction effects, or buoyancy. As has been previously mentioned, many of the wind systems exhibit great variability in direction and speed from valley to valley and from time to time.

1. Gradient-Level Wind System

The gradient-level wind system will be defined as the wind system that blows in the free atmosphere above the local-scale wind systems. These winds are forced by pressure gradients on a scale extending beyond the mountainous area and are relatively unaffected by the topography below. Ekhardt (1948) considered them to be representative of the free atmosphere and drew a schematic diagram, reproduced as Figure 34, that illustrates the structure of the free atmosphere above a mountainous region. The depth of the region of free atmosphere in which gradient winds blow varies spatially across a mountain range and varies temporally because of diurnal changes in depth of the atmospheric structure below. The direction and speed of the gradient level winds can be observed directly or can be estimated from wind observations taken on the periphery of the mountain range. Grand Junction winds at the 700 and 500 mb levels at 1115 GMT were used as representative of gradient level winds in the region of the valley experimental sites. It is clear, however, that the 700 and 500 mb winds are often not representative of the gradient level later in the day due to the growth of the convective boundary layer at Grand Junction. In fact, an increase in temperature between the morning and afternoon soundings at Grand Junction (Table 3) shows that diurnal temperature changes generally

reach the 700 mb level and often are apparent at the 500 mb level, especially in summer.

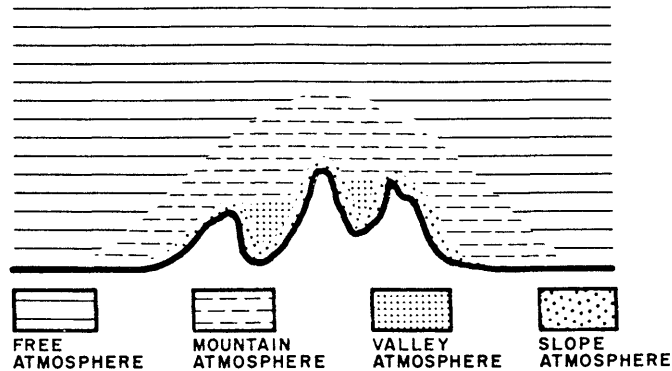


Figure 34. Ekhart's (1948) diagram of the structure of the atmosphere above a mountain range.

2. Along-Incline Wind System

The along-incline wind system is a local diurnal wind system that blows up or down the mesoscale slope of a mountain range in a boundary layer that forms adjacent to the inclined slope. Due to difficulties encountered in collecting upper air data in the experimental program, only limited data are available to illustrate this wind system. To the author's knowledge no experimental data have yet been presented in the literature to document the existence of this wind system in the Rocky Mountains. However, Lettau (1967) described a "thermo-tidal wind" which has some similarities to the along-incline wind system, and Ekhart (1948) described a layer of atmospheric structure that overlies the whole mountain range ("mountain atmosphere"). While Ekhart's scheme bears some similarities to the along-incline layer that will be discussed, he proposes that this layer contains "compensating currents" which transport mass between the mountain range and the adjacent plain.

These currents have not been noted in our admittedly limited number of soundings of the upper air over the Rocky Mountains.

The available data, collected only during daytime, show that a deep convective boundary layer may develop over the Western Slope of the Rockies with winds blowing up the inclined slope towards the crest of the range. Many previous investigators have described "mixed layers" or convective boundary layers that grow after sunrise over land (e.g., Yamada and Berman, 1979; Stull, 1973). A climatology of such layers for western United States rawinsonde stations has been published by Holzworth (1964, 1972). A limited number of field observations taken in the afternoon from valley sites shows the presence of a deep convective boundary layer extending up to two or three kilometers above the valley floor (i.e., $1\frac{1}{2}$ to $2\frac{1}{2}$ km above the ridgetops). The neutral or mixed portion of the layer is usually capped by a potential temperature jump which is surmounted by a temperature profile representative of the free atmosphere. Westerly winds usually prevail within the convective boundary layer, representing air flowing up the Western Slope of the Rockies towards their crest. A wind shift at the top of the layer indicates the transition between convective layer winds and the overlying gradient-level flow. An example of such a convective boundary layer is shown in Figure 35 for the afternoon of 13 October 1978, as observed with airsondes launched from the floor of the Eagle Valley. The first sounding was launched in the late afternoon when a cold layer was already beginning to form on the valley floor. On this day the convective boundary layer attained a height of approximately 4500 m MSL or 2278 m AGL. The potential temperature jump at the top of the boundary layer was 4°K , and winds within the layer were westerly at

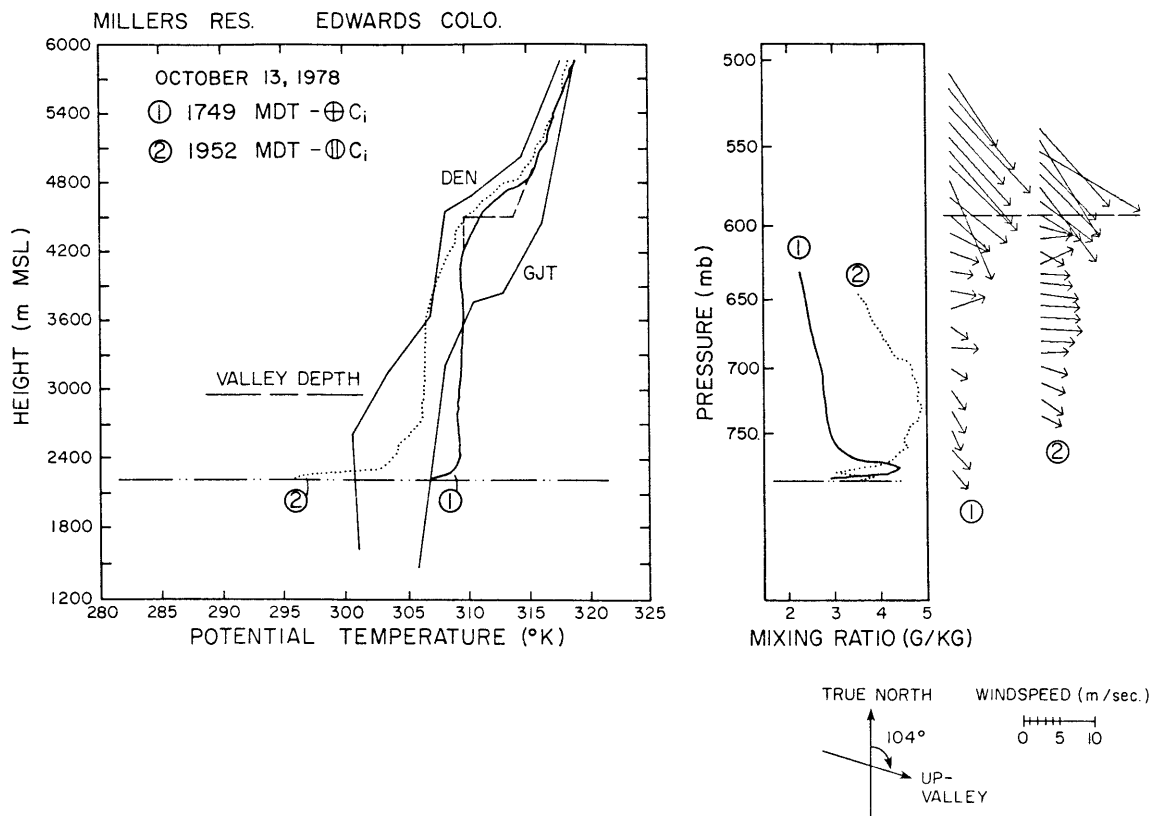


Figure 35. Example of up-incline wind system. Eagle Valley, 13 October 1978. Winds below the dashed line on the right side of the figure blow from west to east up the inclined western slope of the Rocky Mountains. The up-incline flow occurs within a CBL that extends to a height of 4500 m MSL (sounding number 1). The dashed potential temperature line (not data) emphasizes the potential temperature "jump" at the top of the CBL or mixed layer. Denver and Grand Junction afternoon (1715 MDT) rawinsonde soundings are shown for comparison.

7-8 m sec⁻¹. The Grand Junction and Denver 2315 GMT (i.e., 1715 MDT) rawinsonde soundings are included in the figure for comparison. The data show that the soundings converge at the gradient-level just above the mountain boundary layer. There, at 500 mb, the Denver winds are 325° at 31 m sec⁻¹ while Grand Junction winds are 315° at 15 m sec⁻¹. It is interesting to note that a mixed layer similar to the one over the mountains is apparent in the Grand Junction rawinsonde sounding. Within the mountain CBL the up-incline winds are westerly at 6-7 m sec⁻¹, while the 700 mb winds within the Grand Junction CBL are from

25° at 5 m sec^{-1} and at the 700 mb level over Denver are from 290° at 6 m sec^{-1} . Thus, there is a good correspondence of wind and temperature at (and above) the gradient level over Denver, Grand Junction, and the experimental site, but horizontal inhomogeneities in the mountain and plains atmosphere are present below this height due to the mountain topography over which boundary layers develop. Winds should develop in these boundary layers due to diurnal thermal forcing as explained by Wagner's theory of the along-slope and along-valley wind systems.

A wind shift is apparent in Figure 35 at about 3100 m or 700 mb. Above this level, winds in the convective boundary layer blow up the incline of the Western Slope. Below this level the winds shift and parallel the valley axis. This set of observations helps to explain tetheredsonde observations taken on other days during the time of inversion destruction which show up-valley winds in the neutral layer above the stable core rather than up-incline winds. The up-incline winds above may be channeled into the up-valley direction by topographic effects. This concept is shown in Figure 36.

An interesting feature noted in Figure 35 is the rapid cooling between 1749 and 1952 MDT of the entire CBL. It is not known how the rapid cooling could extend through this 2 km deep layer in such a short time. An abrupt increase in the mixing ratio and a decrease in up-incline wind speed also occurred in this layer. It is unfortunate that additional supporting data are not available from other locations or for other dates to determine if this behavior is typical.

At present, it is not known how closely the depth of the CBL follows the structure of the underlying terrain, how its structure varies in the along-incline direction or with time, how the winds

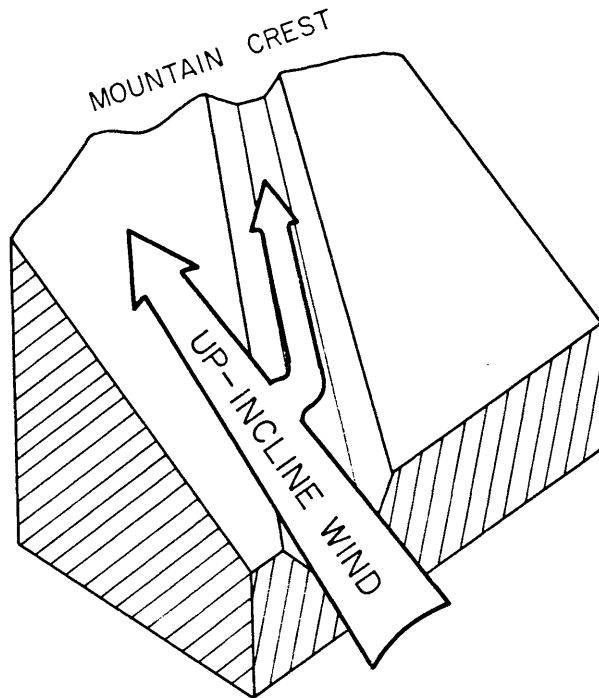


Figure 36. Channeling of up-incline winds into a valley.

within the layer affect its evolution, or how the CBL is coupled with the free atmosphere above or with the local circulations below. The down-incline flow that presumably develops at night has not been studied, nor is it clear what role evolutionary changes of the CBL play in coupling or decoupling local flows from the overlying circulations. In short, while experimental data provide convincing evidence that the CBL exists, a great many questions about the layer are as yet unanswered.

3. Along-Valley Wind System

The along-valley wind system is a local diurnal wind system that blows up or down the valley axis in the central region of the valley volume. It is bounded below by the along-floor wind system and on the sides by the along-slope wind system. The along-valley wind system has been observed and described by many previous investigators, and our

basic knowledge of it has been summarized in the literature review of Chapter II. In the experiments reported here, a great deal of data on this wind system was collected in various valleys during different seasons. Simultaneous recordings of wind and temperature data allow an extension of some of the results of previous investigators.

First, the down-valley flow, invariably present at sunrise, often failed to reverse soon after sunrise as expected from the earlier Alpine studies. Typically, observations showed that the down-valley winds continued to blow in the stable core region of the valley despite a wind reversal in the convective boundary layer that developed below it adjacent to the valley floor, and despite the presence of up-valley winds above it in the neutral layer. In fact, the winds in the stable core frequently maintained their down-valley direction for three or four hours after sunrise. The strength of the down-valley flow, however, usually decreased steadily during this time until, when the stable core became thin, a wind reversal occurred within the layer and the up-valley winds began to increase in strength. After the stable core was destroyed, convective plumes from the valley floor and side-walls could rise through the entire valley depth and into the neutral layer above. At this point the up-floor, up-valley, and up-incline wind systems became difficult to differentiate. When the winds in the neutral layer aloft were weak, the up-valley winds blowing within the valley usually exhibited a maximum speed at mid-levels of the valley. However, when the winds in the neutral layer were strong, it was not uncommon for the peak winds to occur above the middle or upper region of the valley atmosphere. In all cases the up-valley wind system exhibited more turbulence than the relatively laminar down-valley

flows. Following the experimental design, tether sonde observations were usually terminated once the valley inversion was destroyed. Consequently the experiments provide little information on the up-valley winds.

A time-height cross section analysis of the along-valley wind component for the Eagle Valley on 13 October 1977 is presented in Figure 37 as an example of wind structure evolution during the time of inversion destruction in that valley. At the experimental sites in the Eagle Valley, strong down-valley winds usually prevailed in the mid-levels of the valley all night, but with occasional lulls in the wind speeds. On 13 October an apparent lull occurred at around 0700 LT. The persistence of down-valley winds in the mid-levels of the valley during inversion destruction is quite clear in the figure, as is the growth of the up-floor wind regime following sunrise. As discussed in Appendix B, tether sonde observations in high wind conditions result in systematic errors in wind speed data, with wind speeds overestimated in the down-soundings and underestimated in the up-soundings. The actual along-valley wind analysis will therefore be somewhat smoother than the data analysis in the figure.

According to Gleeson's (1951) theory, cross-valley winds arise due to the unequal heating of opposite valley sidewalls, with a cross-valley current flowing towards the most strongly heated sidewall. During October the south-facing slope of the Eagle Valley receives more insolation than the north-facing slope during the period of inversion destruction. An analysis of the cross-valley wind component of the 13 October 1977 data (Figure 38) can therefore be used to test Gleeson's theory. In the figure a positive cross-valley wind component

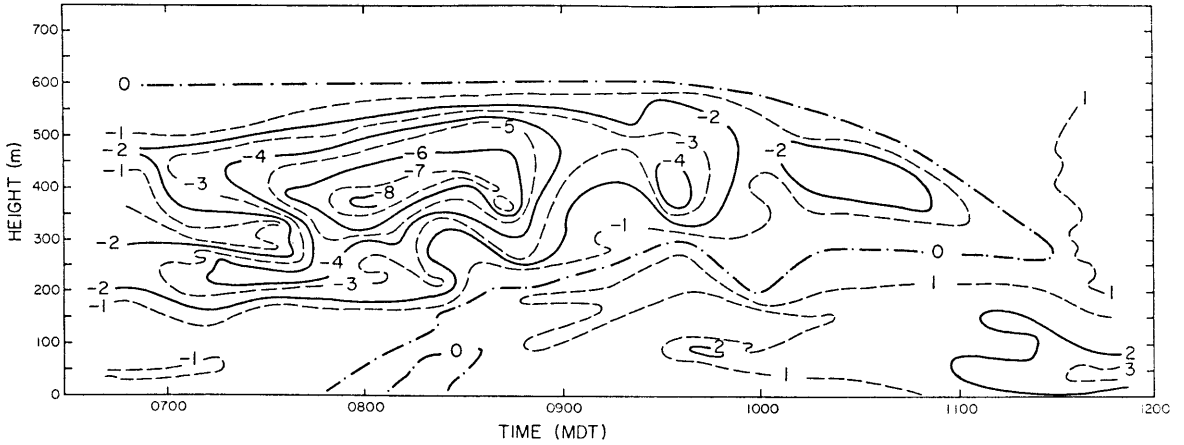


Figure 37. Time-height analysis of along-valley wind components (m sec^{-1}) as determined from tethersonde profiles taken from the floor of the Eagle Valley on 13 October 1977.

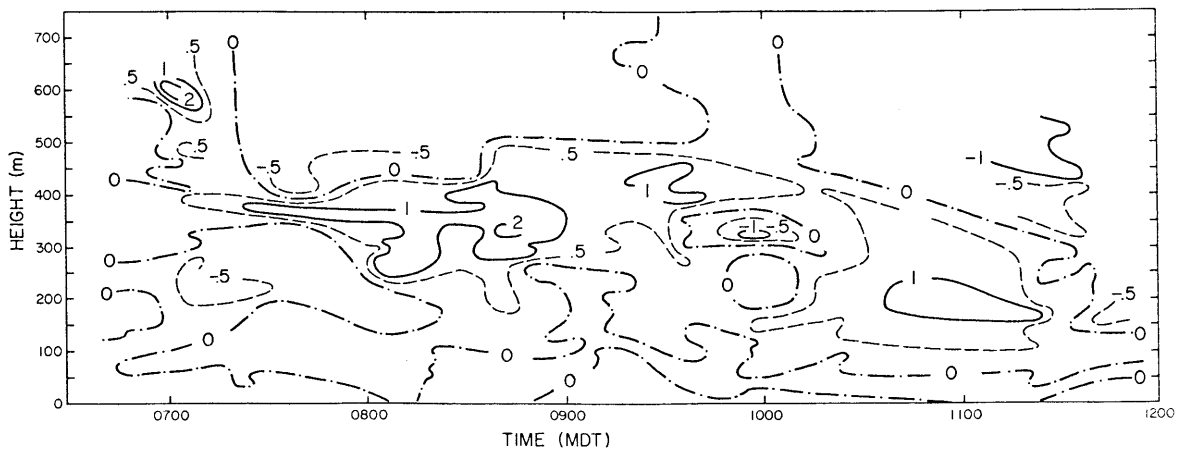


Figure 38. Time-height analysis of cross-valley wind components (m sec^{-1}) as determined from tethersonde profiles taken from the floor of the Eagle Valley on 13 October 1977.

blows towards the strongly heated south-facing valley sidewall. The analysis does not show a coherent cross-valley flow towards the heated sidewall, but shows an incoherent, multi-layered structure of cross-valley flows of alternating direction. These flows may attain significant values of $1-2 \text{ m sec}^{-1}$, but are poorly organized. The failure of Gleeson's theory is perhaps due to the essentially horizontal isotherms across the stable cores of the deep valleys studied.

4. Along-Floor Wind System

The along-floor wind system is a diurnal wind system that blows up or down the valley in a shallow boundary layer over the valley floor. The sloping valley floor, rising upwards towards the mountain crest, represents a topographic surface similar to the sloping valley sidewalls, although the inclination is much smaller. A number of previous investigators have described a shallow layer of winds blowing up the topographic slope of the valley floor during the day and down the slope during the night (Wagner, 1938; Defant, 1951). Wagner called these winds "slope winds along the valley floor" to emphasize that they are of similar origin to winds blowing on other topographic slopes in the mountains. For the Alpine valleys that Wagner investigated, it was often difficult to differentiate these winds from the overlying along-valley wind systems, since they blow in the same direction as the along-valley winds during nearly all hours of the day. In the late afternoon when cooling just begins on the valley floor, the cooled air adjacent to the floor begins to move down-valley at a speed which depends on the slope of the valley floor and the temperature deficit of the cooled air. The down-floor winds are usually easiest to observe at this time since the along-valley winds above have not yet reversed,

and a 180° wind shift occurs at the top of the down-floor layer. Once the reversal of the along-valley winds occurs, it is again difficult to distinguish the down-floor wind system from the overlying down-valley wind system. Similarly, the reversal from down-floor to up-floor usually occurs before the down-valley winds reverse to up-valley. Thus there is a time following sunrise when the up-floor wind system is readily apparent in vertical wind profiles.

As was mentioned in the previous section on along-valley winds, observations in Colorado valleys have shown that the reversal of the down-valley wind system often does not occur until three or four hours after sunrise. During this time period the growing up-floor wind system can be readily observed. In Figure 37, for example, the development of this wind system is seen in a time-height diagram of along-valley wind components. The growth in the depth of the layer reflects the increase in depth of the convective boundary layer in which it occurs. The growth of the CBL depends on the sensible heat flux at the valley floor and does not develop until a positive radiation balance begins at the valley floor after sunrise. The CBL develops simultaneously along the whole length of the valley floor only if sunlight illuminates the valley floor at the same time along its length. The rate of growth of the CBL naturally depends on the surface energy budget of the valley floor. As already mentioned, the growth of the CBL and the associated up-floor wind system may continue after sunrise (Pattern 3) or may be arrested after reaching a certain height (Pattern 2). As the depth of the layer increases, the mass of the layer also increases. This mass must come primarily from the stable core above by means of entrainment, since transport from further down

the valley would imply inhomogeneities in structure in the along-valley direction. The up-floor winds in the growing CBL are typically rather weak, usually $1-2 \text{ m sec}^{-1}$, perhaps due to the strong effect of friction at the ground or to momentum transport from the overlying down-valley flow. Another factor is the rather weak horizontal pressure difference driving the shallow layer and the long length scale over which the pressure difference acts.

From the above description of the development of the along-floor wind system, it is clear that wind measurements from anemometers near the valley floor should not be attributed to the whole depth of the valley atmosphere.

5. Along-Slope Wind System

The along-slope wind system is a diurnal wind system that blows up or down valley sidewalls in a boundary layer that forms above them. Previous descriptions of this wind system have been summarized in Chapter II. In this section the upslope wind regime will be analyzed in detail from slope data taken during the 18 October 1977 experiment in the Eagle Valley. Tethersonde data (to be shown later as Figure 41) were obtained from Slope Site 1, 302 m above the valley floor on the south-facing sidewall. Table 7 presents a summary of the data, giving the sounding numbers, the depth of the convective boundary layer as estimated from potential temperature data, the depth of the upslope flow layer as estimated from wind data, and the peak winds observed in the upslope flow layer.

The CBL grew steadily in depth after sunrise, attaining a depth of 140 m by 1040 LT. The depth of the upslope flow layer corresponds well

Table 7. 18 October 1977 Slope Sounding Data

Sounding Number	Times	Depth of CBL	H' Depth of Upslope Flow	V' max Peak Wind Speeds
38U	0829-0831	34	38	1.1
38D	0841-0844	64	124	0.9
39U	0917-0921	123	74	0.8
39D	0936-0939	78	72	1.2
41U	1020-1027	106	121	3.0
41D	1036-1040	140	137	1.7

to the CBL depth, although showing more variability. The peak wind speeds within the upslope flow layer were variable, but had a tendency to increase as the depth of the layer increased. The shapes of the vertical profiles of upslope wind components are shown in Figure 39, where the height scale has been normalized by the depth of the upslope flow, H' , and the upslope wind velocities have been normalized by the peak wind speed in the layer, V'_{\max} . The profiles, started from a height of about 1 m above ground, show that the wind structure within the layer becomes more complex as the layer deepens, exhibiting multiple layers of wind speed maxima. A great deal of wind speed variability is apparent in the upslope wind layer. Observations of this variability on a shorter time scale were taken in tethered ascent number 40 and are shown in Figure 40. In this figure a time series of upslope wind components is presented as measured from a balloon tethered 10 m above the slope from 0946 to 1013 LT. Wind speeds were sampled every 27 seconds in this experiment and show an average upslope component of 0.7 m sec^{-1} , with values ranging from -0.4 to 2.5 m sec^{-1} .

D. Two-Dimensional Structure of Valley Atmosphere

On four occasions the cross-valley structure of temperature inversions and wind fields was investigated using two tethered balloon data collection systems. In these experiments, conducted in the Eagle Valley, one tethered balloon system was operated from the valley floor, while a second was operated at one of two sites on the slope to the north. The slope sites were approximately 300 m above the valley sites and were separated from them by about $2\frac{1}{2}$ km. The data (Figures 41 through 44) are summarized below in the form of case studies.

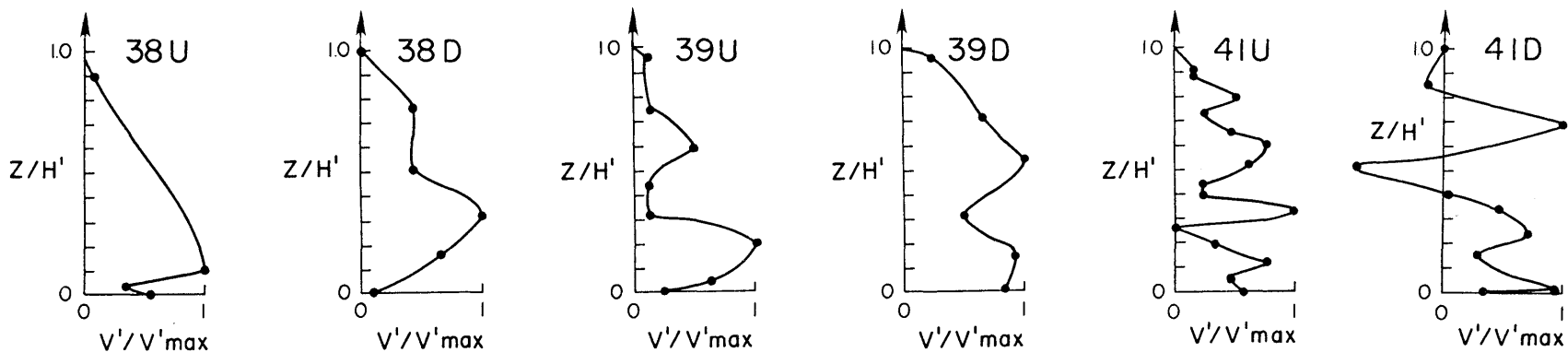


Figure 39. Normalized profiles of upslope wind components in the slope flow layer over Slope Site 1 in the Eagle Valley, 18 October 1977.

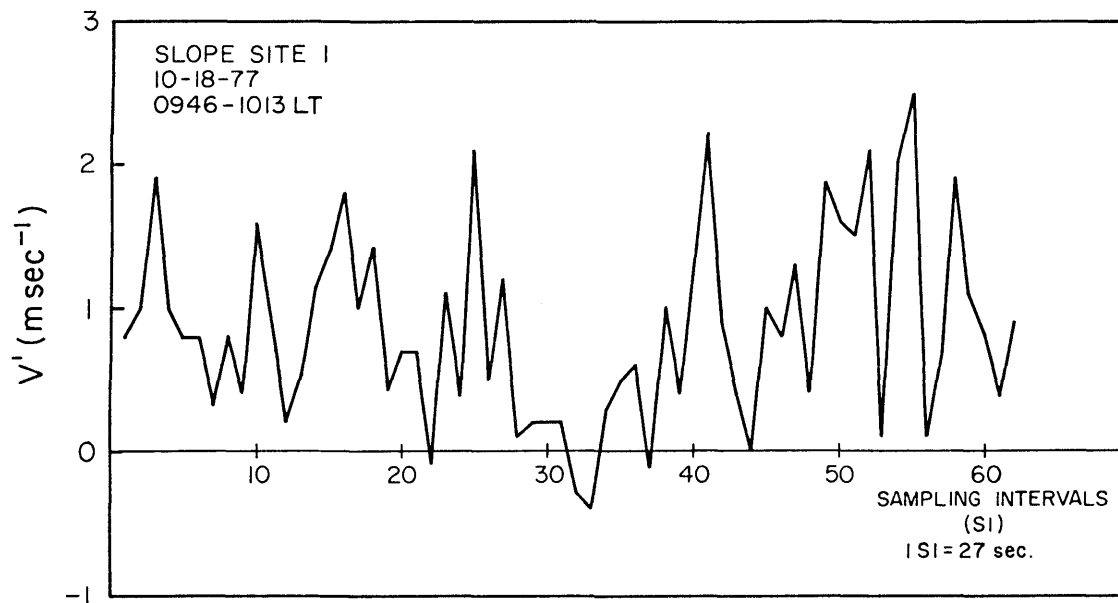


Figure 40. Time series of upslope wind components observed with a tethered sonde 10 meters above Slope Site 1 in the Eagle Valley, 18 October 1977.

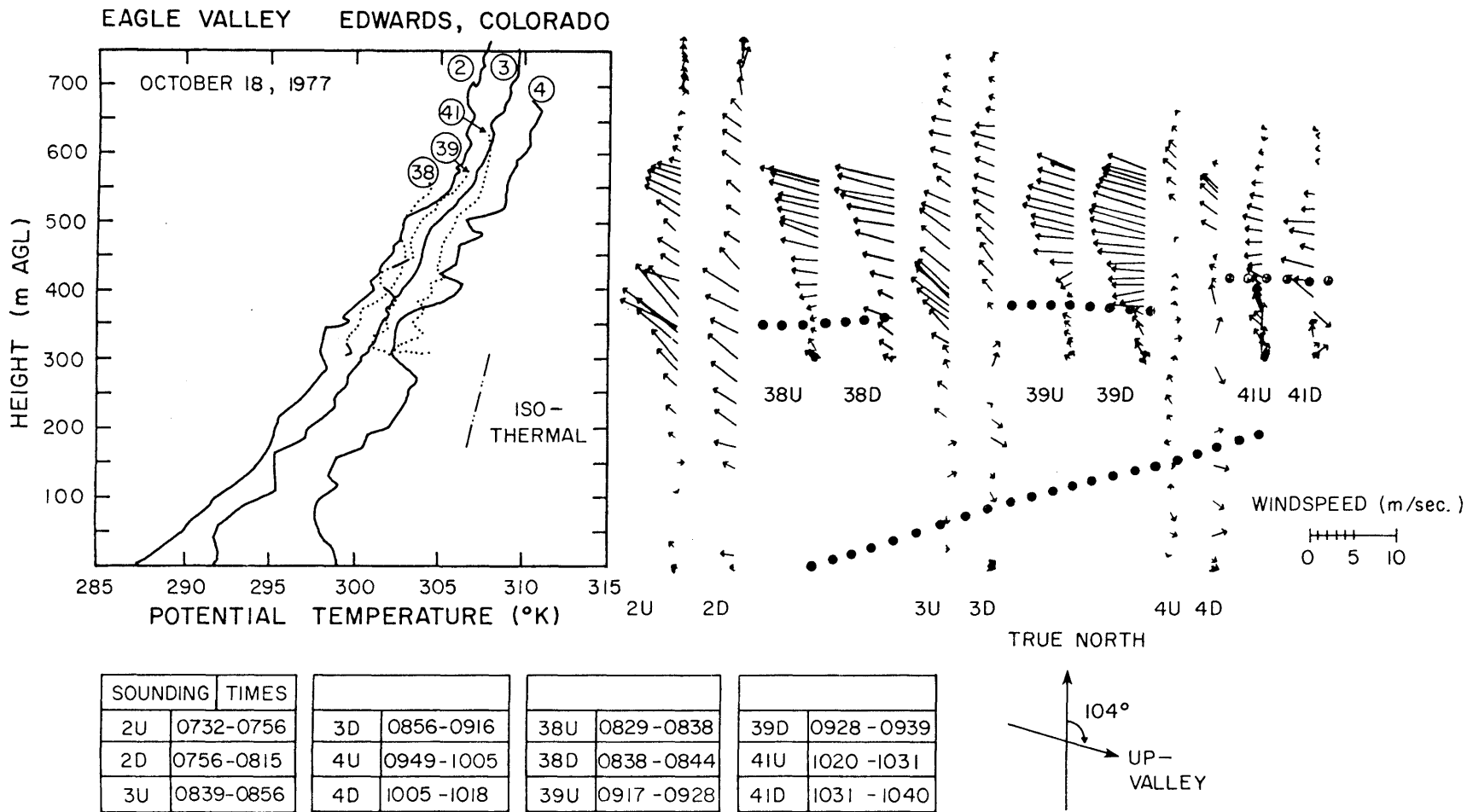
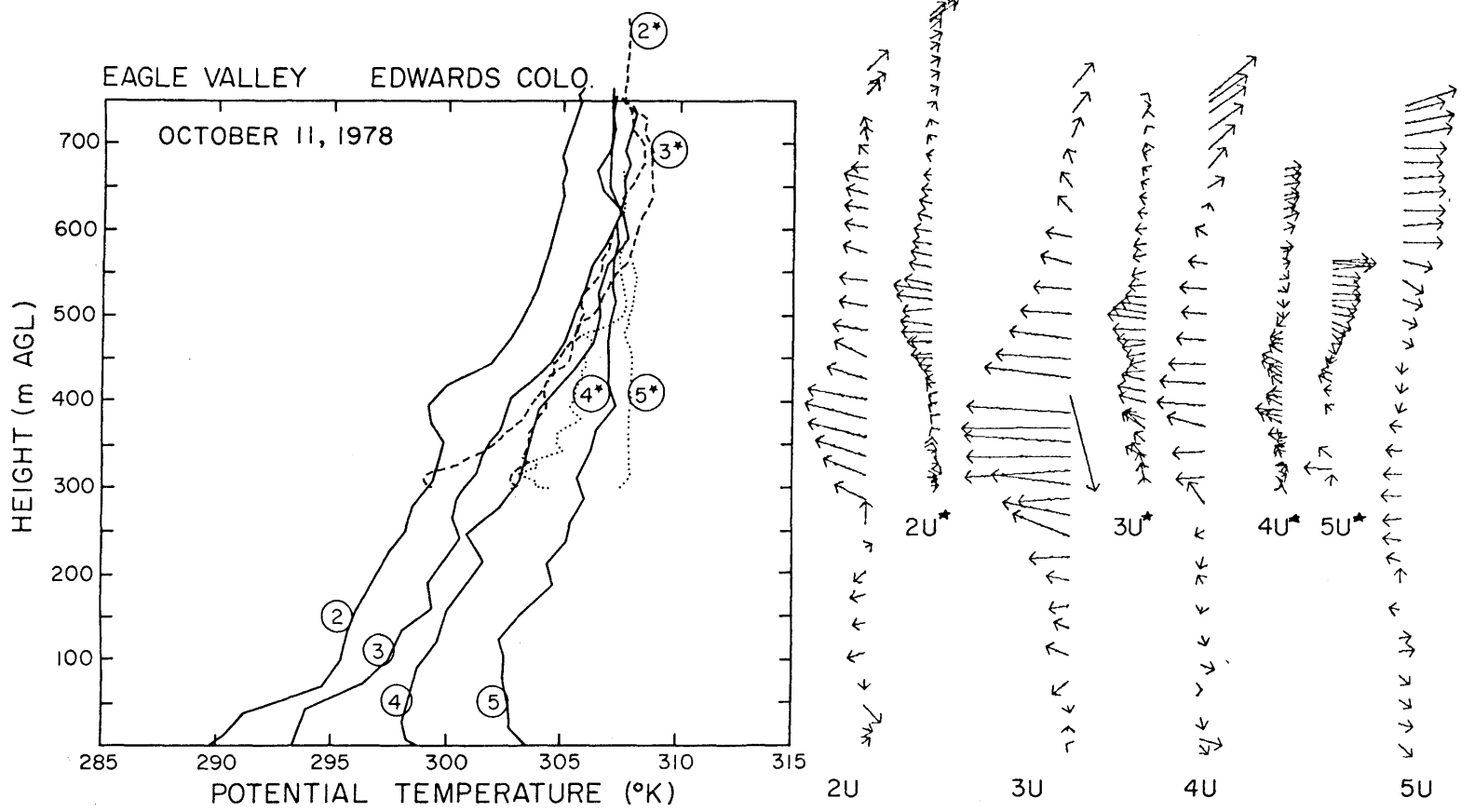


Figure 41. Dual tethersonde data taken from a valley floor site and a valley sidewall site in the Eagle Valley on 18 October 1977. Dotted lines in the sidewall wind soundings show the vertical extent of the upslope wind layer. Dotted lines in the wind soundings taken from a site on the valley floor show the vertical extent of the up-floor wind.



SOUNDING	TIMES				
2*	812 - 827	4*	944 - 957	2	0722 - 0738
3*	902 - 914	5*	1014 - 1022	3	0820 - 0835
				4	0916 - 0930
				5	1015 - 1031

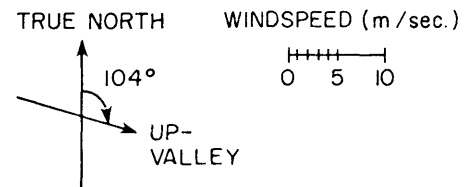


Figure 42. Dual tethersonde data taken from a valley floor site and a valley sidewall site in the Eagle Valley on 11 October 1978.

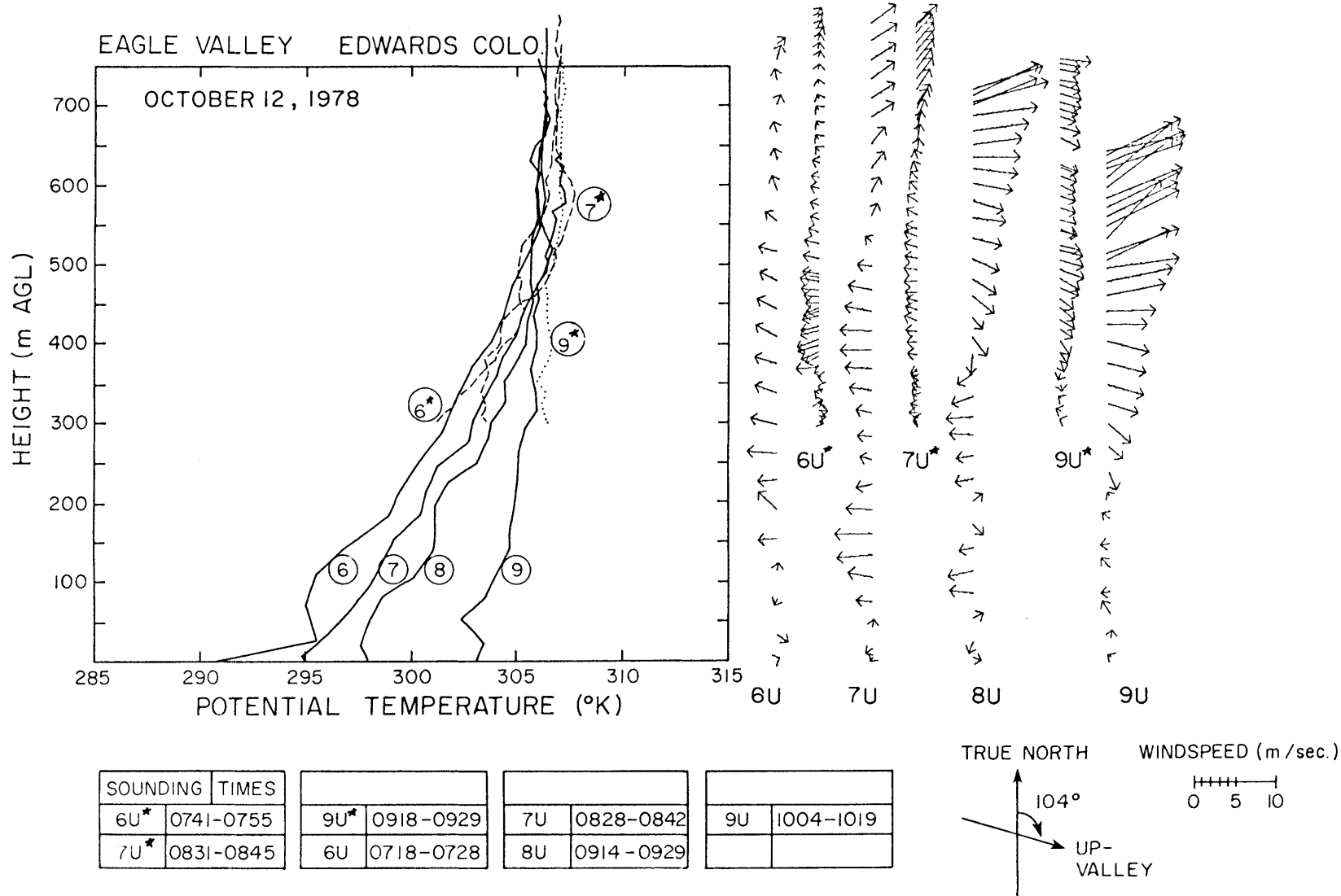
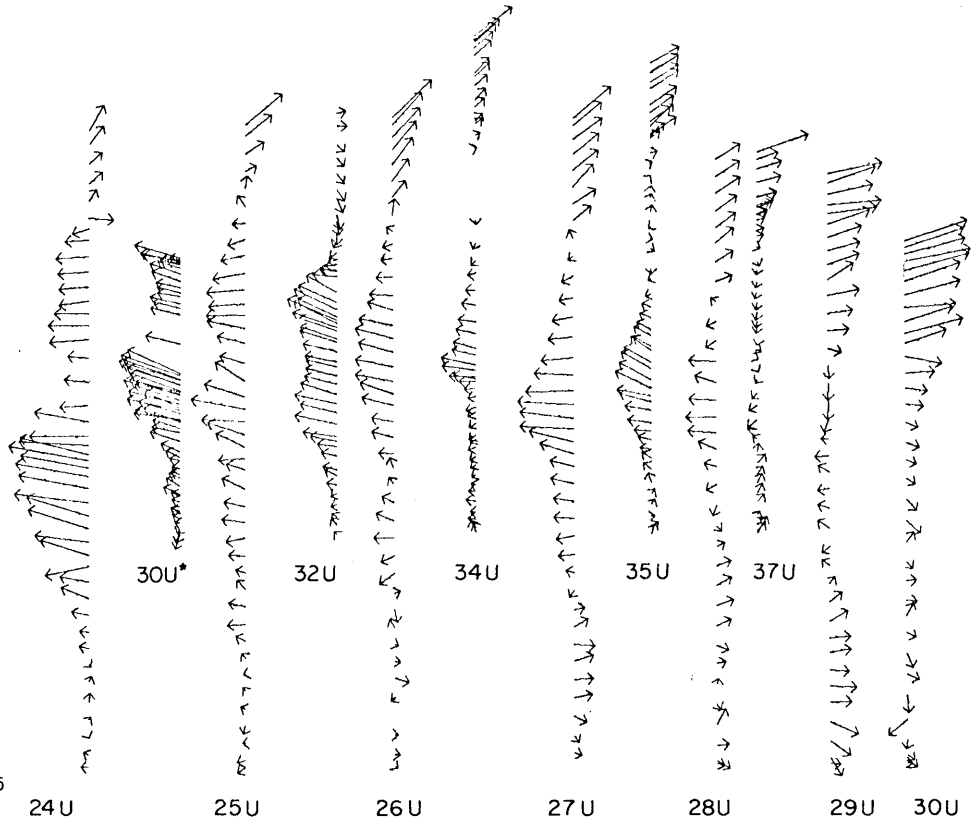
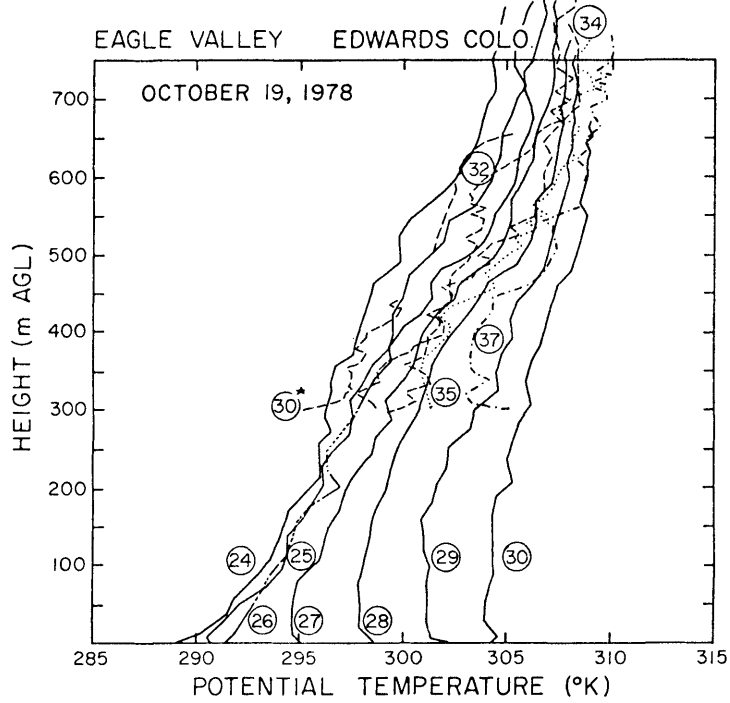


Figure 43. Same as Figure 42 for 12 October 1978.



SOUNDING	TIMES				
24U	0720-0740	28U	1026-1042	32U	0827-0842
25U	0809-0828	29U	1114-1131	34U	0918-0934
26U	0854-0913	30U	1158-1214	35U	0958-1013
27U	0940-0959	30U*	0743-0760	37U	1050-1103

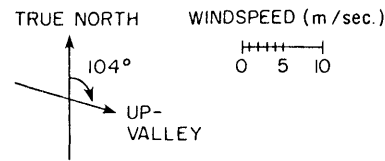


Figure 44. Same as Figure 42 for 19 October 1978.

Corresponding synoptic data are given in Table 3, and the topographic characteristics of the sites are given in Table 1.

1. Case Studies

The 18 October 1977 data (Figure 41), collected at Ray Miller's ranch on the valley floor and at Slope Site 1, 302 m above the ranch, show several important features of cross-valley temperature and wind structure. Within the temperature inversion, temperatures at upper levels of the slope soundings were as much as 2°K colder than over the valley center, and down-valley winds were stronger. Figure 45 shows the growth of CBLs over the slope and the valley floor. The rate of growth of the CBLs was about the same, although growth was initiated at different times due to differing times of sunrise at the two sites. The temperature profile within the slope boundary layer was not strictly adiabatic, but contained temperature deformations or fluctuations. An apparent transport of momentum from the down-valley winds within the stable core caused the up-slope winds in the slope boundary layer to have a relatively strong down-valley component. Unfortunately, soundings were of insufficient depth to determine the height of the top of the inversion over the slope.

The 11 October 1978 data (Figure 42) were collected at the Steve Miller residence on the valley floor and at Slope Site 1. The first slope sounding shows a weak convective boundary layer beginning to grow at the base of a shallow, intense stable layer immediately adjacent to the slope. The slope CBL failed to grow significantly beyond 20 to 30 m in depth until two hours later, possibly because of the presence at sunrise of lenticular clouds over distant mountains to the east. The clouds may also have caused the delay in the development of the CBL

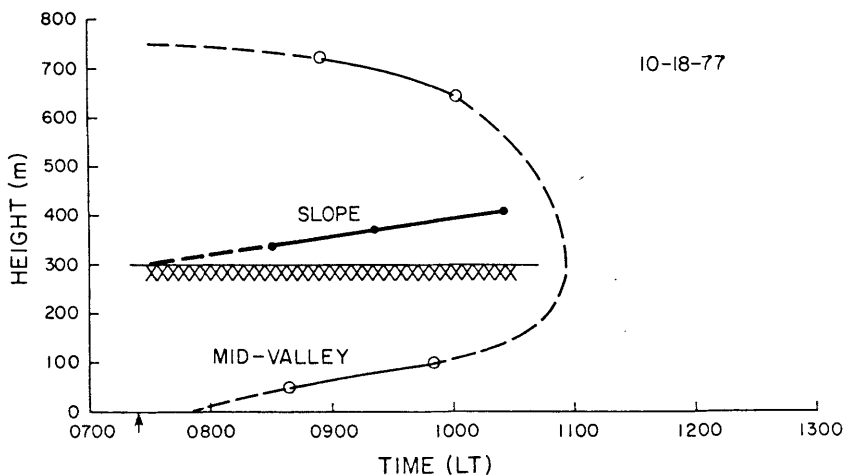


Figure 45. Heights of CBL and inversion top as measured from dual tethersonde soundings taken from sites on the floor and on one sidewall of the Eagle Valley, 18 October 1977. Arrow indicates time of theoretical sunrise.

over the valley floor. Initially, the top of the inversion was higher over the slopes than over the valley center (Figure 46). During the period of slow growth of the slope CBL and weak up-slope winds, the inversion top over mid-valley descended very slowly. Temperatures immediately above the slope were initially colder than over the valley center at the same height, whereas temperatures at upper levels over the slope were somewhat warmer than over the valley center. Later soundings show like temperatures over the slope and over the valley center except in the neutral layer where temperatures over the slope were warmer.

The 12 October 1978 data, presented in Figure 43, were collected at the Steve Miller residence and Slope Site 1. In the initial soundings a shallow layer of cold air was found adjacent to the slope, with temperatures colder than at the same height over the valley

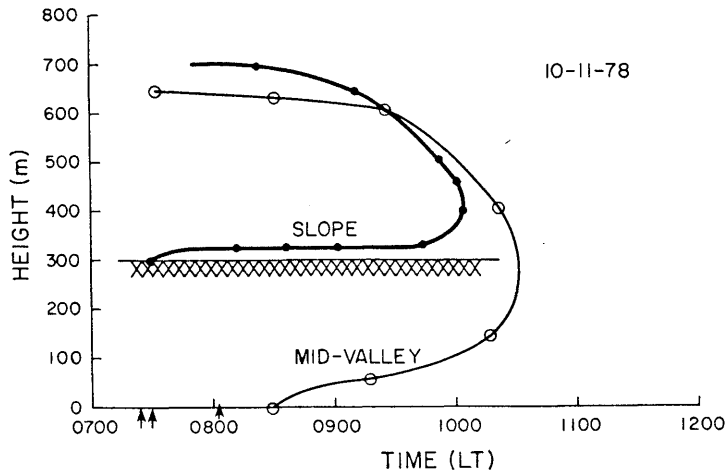


Figure 46. Same as Figure 45 for 11 October 1978. First arrow indicates time of theoretical sunrise, second arrow is time of actual sunrise on the slope, and third arrow is time of actual sunrise at the valley floor site.

center. In these soundings the top of the inversion was at the same height over the valley floor as over the slope site. Later soundings from the slope compare well with mid-valley soundings except for the boundary layer development adjacent to the slope and the consistently warmer neutral layer over the slope. The neutral layer's rate of warming on this day was slow. When the top of the inversion sank below the slope site, a neutral atmosphere existed above the slope, while an inversion was still present over the valley center below the altitude of the slope site. From Figure 47 the initiation of growth of the convective boundary layers over the valley floor and the slope were related to the time of first sunlight at the respective sites. The CBL over the slope developed more rapidly than the CBL over the valley floor. The descent of the inversion top occurred at a faster rate over the valley center than over the slope.

The 19 October 1978 data (Figure 44), taken at the Steve Miller residence and at Slope Site 2 following a 6 or 7 mm rainfall on the previous day, show a long delay in inversion destruction. The first sounding shows colder temperatures adjacent to the slope than at the same height over the valley center. Later soundings show similar temperatures over the slope and over the valley center except for the warmer temperatures over the slope in the neutral layer above the inversion and in the CBL adjacent to the slope. From Figure 48 it is clear that the top of the inversion remained stationary until about 1000 LT. Before this time the CBL over the slope maintained a constant height, and the CBL over the valley floor was poorly developed. After 1000 LT both boundary layers began to grow and the top of the inversion began to sink over the valley center.

2. Cross-sectional Wind and Temperature Structure Evolution

Based on the four case studies discussed above, cross-sectional wind and temperature structures and their evolution can be described as follows. At sunrise, a nearly horizontal top of a temperature inversion stretches across the Eagle Valley. The temperature field is approximately horizontally homogeneous across the valley, although a shallow layer of cold air in which downslope winds prevail is present near the slopes.

When sunlight strikes the slope, a convective boundary layer begins to develop adjacent to the slope. The CBL is characterized by a nearly constant potential temperature. Within the slope CBL the winds reverse from downslope to upslope. Heat is transferred to the air in the slope flow, allowing it to rise up the slope to a new level of buoyancy equilibrium. The depth of the upslope flow usually

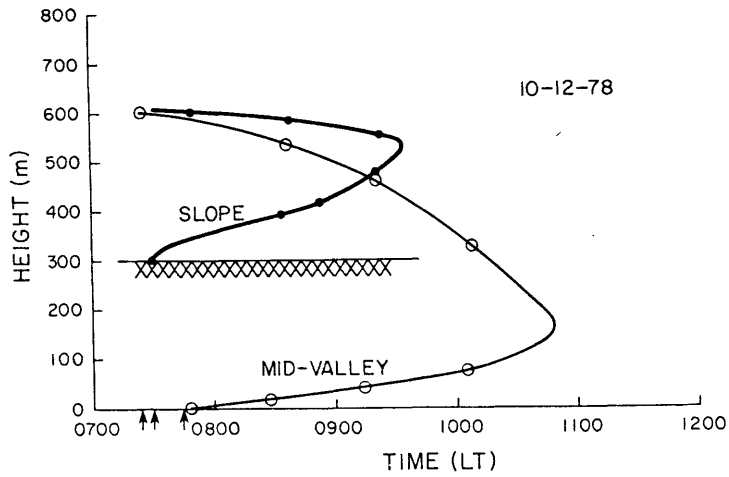


Figure 47. Same as Figure 46 for 12 October 1978.

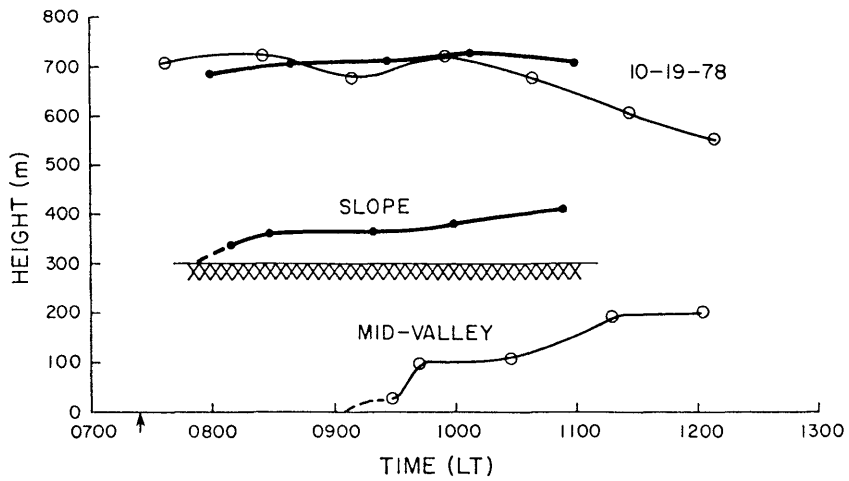


Figure 48. Same as Figure 45 for 19 October 1978.

increases with time, although in some cases the depth remains nearly constant over time. Moll's (1935) research indicates that the depth of the upslope flow increases with distance up the slope. No independent tests of this feature of the slope wind system were conducted in the author's experiments. The upslope flow can be greatly influenced by momentum transport from the down-valley winds blowing in the adjacent stable core. Temperature profile deformations occur frequently within the CBL and may be associated with bent-over convective plumes rising up the boundary layer, with air masses entrained into the boundary layer from the stable core region above, or with convective plumes rising from the heated slopes below.

Once direct sunlight reaches the valley floor and sensible heat flux is produced, a convective boundary layer begins to grow adjacent to the valley floor. Shading of the valley by terrain features thus affects the time of initiation of CBL growth on various valley surfaces. The CBL over the valley floor has fewer temperature profile deformations than are found in the profile of the slope CBL. As inversion destruction progresses, the valley CBL and the slope CBL grow at about the same rate, although either may grow more rapidly than the other.

Solar radiation on the slope initiates not only the growth of the slope CBL, but also the descent of the inversion top. The inversion layer typically has about the same temperature and potential temperature gradient above the slope CBL as over the valley center at the same height. When temperature differences do occur, they may be reflected in the along-valley wind structure in that stronger down-valley winds occur where temperatures are colder. Down-valley wind

directions and speeds, however, do not usually vary greatly across the valley cross section within the inversion except for a noticeable decrease in speed within 50-100 m of the top of the CBL over the slope. See the 19 October 1978 data. While the inversion top is nearly horizontal at sunrise, there is some evidence that its descent progresses more rapidly over the valley center than over the sidewalls. However, the data of 11 October 1978 show just the opposite occurring.

The neutral layer above the inversion is usually warmer above the heated slope than over the valley center. Wind speeds and directions in the neutral layer often differ significantly from the slope site to the valley center, with wind speeds usually lower over the slope, but approach the same values higher in the neutral layer.

Chapter V

MATHEMATICAL DESCRIPTION OF TEMPERATURE INVERSION DESTRUCTION

A. Scale Analysis of General Equations

The Bernoulli equation (Haltiner and Martin, 1957) governs the flow of a compressible fluid and expresses the transformations among mechanical and thermodynamic forms of energy. The equation may be written in terms of temperature, as

$$\frac{dT}{dt} = \frac{1}{c_p} \left[\frac{dQ}{dt} - \frac{d}{dt} \left(\frac{c^2}{2} + gz \right) + \alpha \frac{\partial p}{\partial t} + \vec{V} \cdot \vec{F} \right], \quad (1)$$

where T = air temperature,

t = time,

c_p = specific heat at constant pressure = $1010 \text{ J kg}^{-1} \text{ }^\circ\text{K}^{-1}$,

Q = heat supplied to a unit mass of air,

$c^2 = u^2 + v^2 + w^2$,

g = acceleration due to gravity,

z = height,

α = specific volume,

p = pressure,

\vec{V} = velocity vector, and

\vec{F} = friction force.

The equation states that the rate of temperature change of a parcel of air depends on (a) the rate of diabatic heating, (b) the rate of production of kinetic and potential energies, (c) local pressure changes, and (d) the energy dissipated by the friction forces. The equation may be changed so that potential temperature, rather than actual temperature, is the dependent variable. This is convenient, since potential

temperature is conserved when the parcel undergoes a vertical displacement in the atmosphere, whereas actual temperature (from the equation of state) changes with pressure.

From the definition of potential temperature

$$\theta = T \left(\frac{p_{\text{ref}}}{p} \right)^{R/c_p}, \quad (2)$$

where $R = 287.04 \text{ J kg}^{-1} \text{ }^\circ\text{K}^{-1}$ is the gas constant for dry air, p_{ref} is an arbitrary reference pressure usually taken as 1000 mb or 10^5 Pascals, and T is the temperature of the parcel in Kelvin degrees. The relationship between time changes in actual and potential temperature may be obtained by logarithmically differentiating the defining equation, such that

$$\frac{d\theta}{dt} = \frac{\theta}{T} \frac{dT}{dt} - \frac{R\theta}{c_p} \frac{dp}{dt}. \quad (3)$$

Substituting for $\frac{dT}{dt}$ in the Bernoulli equation results in the equation

$$\frac{d\theta}{dt} = \frac{\theta}{c_p T} \left\{ \frac{dQ}{dt} - \frac{d}{dt} \left[\frac{c^2}{2} \right] + gz \right\} - \alpha (\vec{V} \cdot \vec{\nabla}_p) + \vec{V} \cdot \vec{F}. \quad (4)$$

Substituting the Euler relation with subscript H representing horizontal vector components,

$$\frac{d\theta}{dt} = \frac{\partial\theta}{\partial t} + \vec{V}_H \cdot \vec{\nabla}\theta + w \frac{\partial\theta}{\partial z}, \quad (5)$$

and recognizing that

$$- \frac{d}{dt} (gz) = -wg = \alpha w \frac{\partial p}{\partial z}, \quad (6)$$

and that

$$\gamma = \frac{\partial\theta}{\partial z}, \quad (7)$$

the equation may be written as

$$\frac{\partial\theta}{\partial t} = -\vec{V}_H \cdot \vec{\nabla}\theta - w \gamma + \frac{\theta}{c_p T} \left\{ \frac{d}{dt} \left[Q - \frac{c^2}{2} \right] - \alpha (\vec{V}_H \cdot \vec{\nabla}_p) + \vec{V} \cdot \vec{F} \right\}. \quad (8)$$

Several important processes can affect the potential temperature at a fixed point, $S(x,y,z)$, as expressed on the right hand side of equation (8). The potential temperature may change due to:

(1) Horizontal advection of warmer or colder air toward point S. Advection cannot create warmer temperatures in a field where none existed before, since the effect of advection is simply to move air around.

(2) Vertical advection, if the potential temperature gradient differs from adiabatic (i.e., if $\gamma \neq 0$). The vertical motion may result from orographic lifting, convergence or divergence fields, convection currents, etc.

(3) Diabatic heating. Diabatic processes include radiation and conduction and changes in phase of water substance present in the atmosphere.

(4) A change in the kinetic energy of the air flowing past point S.

(5) Local changes in pressure resulting from horizontal advection. This advection cannot occur when winds are geostrophic since $\vec{V}_g \cdot \vec{\nabla}_p = 0$.

(6) The frictional conversion of kinetic energy into heat.

It should be stressed that an increase in one of the terms on the right hand side of Equation (8) does not necessarily cause a corresponding increase in $\frac{\partial \theta}{\partial t}$, since the equation, in effect, is an energy conservation equation in which no information is available concerning the conversion rates among the different forms of energy. For example, an increase in diabatic heating may cause an increase in kinetic energy production and a corresponding increase in frictional conversion of

kinetic energy to heat, as well as a direct increase in potential temperature.

By differentiating Equation (8) with respect to z , a general equation for the time rate of change of the potential temperature gradient is obtained such that

$$\begin{aligned} \frac{\partial \gamma}{\partial t} = & - \vec{V}_H \cdot \vec{\nabla} \gamma - \frac{\partial \vec{V}_H}{\partial z} \cdot \vec{\nabla} \theta - w \frac{\partial \gamma}{\partial z} - \gamma \frac{\partial w}{\partial z} \\ & + \frac{\theta}{c_p T} \left\{ \frac{\partial}{\partial z} \left(\frac{dQ}{dt} \right) - \frac{\partial}{\partial z} \left[\frac{d}{dt} \left(\frac{c^2}{2} \right) \right] - \frac{\partial}{\partial z} [\alpha (\vec{V}_H \cdot \vec{\nabla} p)] + \frac{\partial}{\partial z} (\vec{V} \cdot \vec{F}) \right\} . \end{aligned} \quad (9)$$

To obtain this result, changes of the ratio $\frac{\theta}{T}$ with height have been ignored. From this equation it is clear that a number of processes can contribute to changes in potential temperature gradient observed at a point in the atmosphere. These processes can cause an increase in stability ($\frac{\partial \gamma}{\partial t} > 0$) or a decrease in stability ($\frac{\partial \gamma}{\partial t} < 0$). Specifically, the stability can be changed by:

(1) Horizontal advection of air having a different stability. This process cannot create new areas of stability or instability but can act to move preexisting areas of stability to a new location.

(2) Shearing advection of potential temperature. In contrast to (1), above, shearing instability can create new areas of instability rather than merely advecting preexisting areas. Stability changes due to shearing advection are favored when winds are ageostrophic (USAF, 1969) since the vertical shear of geostrophic winds is given by

$$\frac{\partial \vec{v}}{\partial z} \approx \vec{k} \times \vec{V}_T ,$$

and the shearing term becomes

$$\frac{\partial \vec{V}}{\partial z} \cdot \vec{\nabla}_H \theta \sim \vec{k} \times \vec{V}_T \cdot \vec{\nabla} \theta \approx 0 .$$

(3) Vertical advection of potential temperature gradient where the vertical motion required may result from orographic lifting, zones of convergence or divergence, etc.

(4) The shrinking or stretching of an air column where the stability differs from adiabatic (i.e., $\gamma \neq 0$). Destabilization occurs when a column is stretched, while stabilization occurs when a column is compressed.

(5) A vertical gradient in the rate of diabatic heating. Such vertical gradients are frequently encountered in the near-ground layers of the atmosphere where radiation and conduction processes undergo a strong diurnal cycle. As a result of this cycle, stabilization is favored at night and destabilization occurs during most days.

(6) Vertical gradients in production of kinetic energy.

(7) Vertical gradients in the rate of work done by pressure forces (Haltiner and Martin, 1957).

(8) Vertical gradients in the rate of frictional dissipation of energy.

Equations (8) and (9) represent general equations for the evolution of potential temperature structure. The general equations can be applied to phenomena on any time and space scales desired. The relative importance of the individual terms, however, will vary from application to application. The use of scale analysis is one means of systematically determining the approximate relative magnitudes of individual terms for applications on a given time and space scale (Haltiner, 1971; Holton, 1972). The scale analysis method of Petkovšek (1973) may be applied to the two general equations to determine the relative importance of the various physical factors affecting potential

temperature change in the valley atmosphere. Using this method on Equation (8), the approximate maximum contribution of each of the terms in the equation to the production of potential temperature changes in the valley atmosphere is determined by assuming that all of the energy in each term is converted into heat and expressed as a potential temperature change. This assumption obviates the necessity of determining the transformation of energy between the different terms in the equation.

For the valleys studied a length scale, X , of 10^4 m and a valley depth scale, D , of 10^2 m are chosen. Valley wind speeds, U , are on the order of 1 m sec^{-1} and an appropriate time scale is of order $T = XU^{-1} = 10^4$ sec, i.e. roughly the time scale of inversion destruction. Potential temperature variations within the valley, θ , on this time scale are of order 10°K , pressure variations, P , are of order 10^2 Pascals or 1 millibar, vertical velocities, W , are of order $DUX^{-1} = 10^{-2} \text{ m sec}^{-1}$. Finally, θT^{-1} is of order 1, ρ is of order 1 kg m^{-3} , c_p is approximately $10^3 \text{ J kg}^{-1}\text{K}^{-1}$, and Q is of order $\rho c_p \theta = 10^4 \text{ J m}^{-3}$. Scale analysis of the various terms of Equations (8) and (9) results in the relative magnitudes of the terms given in Table 8. The scale analysis of the last term in Equation (8) and also Equation (9) is difficult due to the lack of observations of the frictional dissipation of kinetic energy in valley environments. Petkovšek's (1973) analysis of the maximum value of this term for a plains atmosphere was $.02^\circ\text{K hr}^{-1} \sim 5 \times 10^{-6} \text{ K sec}^{-1}$. For a high mountainous region with serrated ridges and peaks he obtained a maximum value of $1^\circ\text{K hr}^{-1} \sim 10^{-4} \text{ K sec}^{-1}$. For the valley atmosphere in the undisturbed synoptic conditions investigated, an intermediate value of $10^{-5} \text{ K sec}^{-1}$ seems appropriate.

Table 8. Scale Analysis of General Equations

Term	A	B	C	D	E	F	G	H	I
Equation (8)	$\partial\theta/\partial t$	$-\vec{V}_H \cdot \vec{\nabla}\theta$	$-w \frac{\partial\theta}{\partial z}$	$\frac{1}{c_p} \frac{dQ}{dt}$	$-\frac{1}{c_p} \frac{d}{dt} \left(\frac{c^2}{2} \right)$	$-\frac{\alpha}{c_p} (\vec{V}_H \cdot \vec{\nabla}p)$	$\frac{1}{c_p} (\vec{V} \cdot \vec{F})$		
Scale	$\frac{\theta}{T}$	$\frac{U\theta}{X}$	$\frac{W\theta}{D}$	$\frac{Q}{c_p T}$	$\frac{U^2}{c_p T}$	$\frac{\alpha UP}{c_p X}$	$\frac{\vec{V} \cdot \vec{F}}{c_p}$		
Magnitude	10^{-3}	10^{-3}	10^{-3}	10^{-3}	10^{-7}	10^{-8}	10^{-5}		
Equation (9)	$\frac{\partial\gamma}{\partial t}$	$-\vec{V}_H \cdot \vec{\nabla}\gamma$	$-\partial\vec{V}_H \cdot \vec{\nabla}\theta$	$-w \frac{\partial\gamma}{\partial z}$	$-\gamma \frac{\partial w}{\partial z}$	$\frac{1}{c_p} \frac{\partial}{\partial z} \left(\frac{dQ}{dt} \right)$	$-\frac{1}{c_p} \frac{\partial}{\partial z} \left[\frac{d}{dt} \left(\frac{c^2}{2} \right) \right]$	$-\frac{1}{c_p} \frac{\partial}{\partial z} \left[\alpha (\vec{V}_H \cdot \vec{\nabla}p) \right]$	$\frac{1}{c_p} \frac{\partial}{\partial z} (\vec{V} \cdot \vec{F})$
Scale	$\frac{\theta}{TD}$	$\frac{U\theta}{XD}$	$\frac{U\theta}{XD}$	$\frac{W\theta}{D^2}$	$\frac{W\theta}{D^2}$	$\frac{Q}{c_p TD}$	$\frac{U^2}{c_p TD}$	$\frac{\alpha UP}{c_p XD}$	$\frac{\vec{V} \cdot \vec{F}}{c_p D}$
Magnitude	10^{-5}	10^{-5}	10^{-5}	10^{-5}	10^{-5}	10^{-5}	10^{-9}	10^{-10}	10^{-7}

As a result of the scale analysis, the general equations can be simplified by dropping the terms that are of secondary importance, with the result that

$$\frac{\partial \theta}{\partial t} = - \vec{V}_H \cdot \vec{\nabla} \theta - w \frac{\partial \theta}{\partial z} + \frac{\theta}{c_p T} \frac{dQ}{dt} , \quad (10)$$

or

$$\frac{dQ}{dt} = \frac{c_p T}{\theta} \frac{d\theta}{dt} , \quad (11)$$

and

$$\frac{\partial \gamma}{\partial t} = - \vec{V}_H \cdot \vec{\nabla} \gamma - \frac{\partial \vec{V}_H}{\partial z} \cdot \vec{\nabla} \theta - w \frac{\partial \gamma}{\partial z} - \gamma \frac{\partial w}{\partial z} + \frac{\theta}{c_p T} \frac{\partial}{\partial z} \left(\frac{dQ}{dt} \right) . \quad (12)$$

The scale analysis of Equation (8) has produced a desirable result. Several physical processes that are capable of changing potential temperature in the valley atmosphere have been shown to produce effects too small to account for the observed changes, given the time and space scales of interest. The scale analysis could, of course, be performed for other scales of time and space. It might, for example, be applied to the layers of the atmosphere identified in the analysis of valley thermal structure, such as the convective boundary layers over the valley floor, sidewalls, and incline, or the stable core region of the valley atmosphere. On the valley scale, for the time scale of inversion destruction, Equation (10) identifies several physical factors, including horizontal and vertical advection and diabatic heating, that may be important in producing temperature changes of the observed magnitude. The effects of these terms are illustrated in Figure 49.

The scale analysis tells us which terms may be important, but does not tell us which terms are important in a particular instance. For

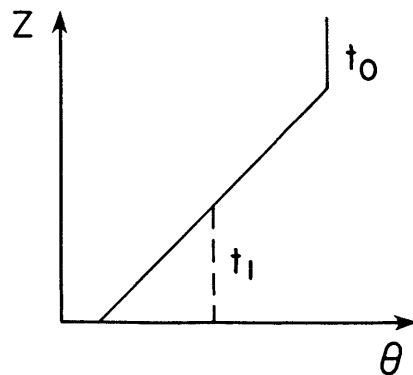
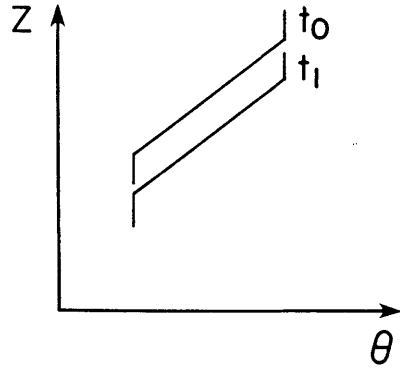
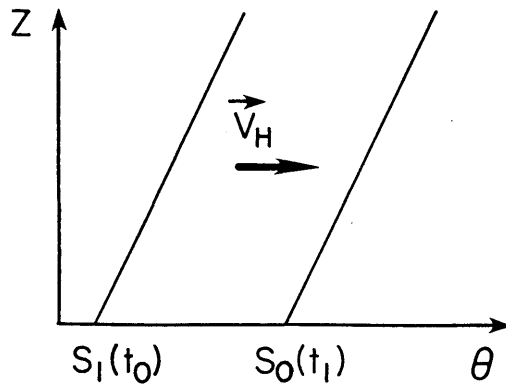


Figure 49. Effect of various physical processes on temperature structure. Top to bottom, advection, subsidence, and heat flux convergence.

this, actual data must be considered. Observations in western Colorado valleys have shown that the valley temperature structure evolves in the same way from day to day and from valley to valley despite differences in the strengths of along-valley winds and even differences in the timing of along-valley wind reversal during the inversion destruction period. Thus, from actual data, it appears that the effect of the along-valley winds in the stable core in producing temperature changes is small. This must be due to weak potential temperature gradients in the along-valley direction, as observed by Edinger (1963) for valleys in Argentina. Additionally, the temperature structure evolves following the same timing and patterns regardless of the strength and direction of winds in the neutral layer, suggesting that turbulent erosion is not significant factor causing descent of the inversion top in the synoptic conditions studied. Cross-valley circulations within the central, stable core region of the Eagle Valley atmosphere are quite variable and unorganized during the inversion destruction period and from day to day. Observations show that temperature lines are approximately horizontal across the stable core. Thus, the cross-valley circulations may have little effect on temperature for the valleys studied. The convective boundary layer over the slopes, however, contains significant cross-valley and vertical wind components that blow against a potential temperature gradient.

From an application of the data and consideration of the mathematical equations, an hypothesis can be developed to explain the observations of potential temperature evolution during inversion destruction.

B. Hypothesis--An Explanation of Valley Inversion Destruction

Typical inversion destruction in mountain valleys differs from inversion breakup over the plains. Over the plains an inversion is broken as a convective boundary layer grows upward from the ground. The increase in depth of the CBL and the increasing potential temperature within it come from turbulent sensible heat flux convergence and entrainment of mass into the layer through the action of penetrative convective plumes (Ball, 1960a; Stull, 1973). The energy available for sensible heat flux depends on solar heat flux and the partitioning of energy in the surface energy budget. The normal growth of the CBL can be retarded by divergence of mass from the CBL or, equivalently, subsidence at the top of the CBL (Lilly, 1968; Tennekes, 1973).

In western Colorado valleys in clear, undisturbed weather the cause of inversion destruction is the same as over flat terrain, namely the input of solar energy modified by the surface energy budgets to produce sensible heat flux. However, due to the effects of valley topography, this energy is utilized in a fundamentally different way to produce temperature changes in the valley atmosphere. Over the plains the energy is used to deepen and warm a convective boundary layer. In a valley, as is shown schematically in Figure 50, the energy may be used to deepen and warm CBLs, but it may also drive the slope flows that carry mass up the sidewalls. Sensible heat flux from valley surfaces causes a convective boundary layer to develop over the valley floor and sidewalls. As over the plains, mass and heat are entrained into these boundary layers from the stable core above. Convergence of heat into the boundary layers warms the air mass within them, causing an upslope flow to develop within the boundary layers over the sidewalls. The divergence of mass from the valley inversion in the upslope

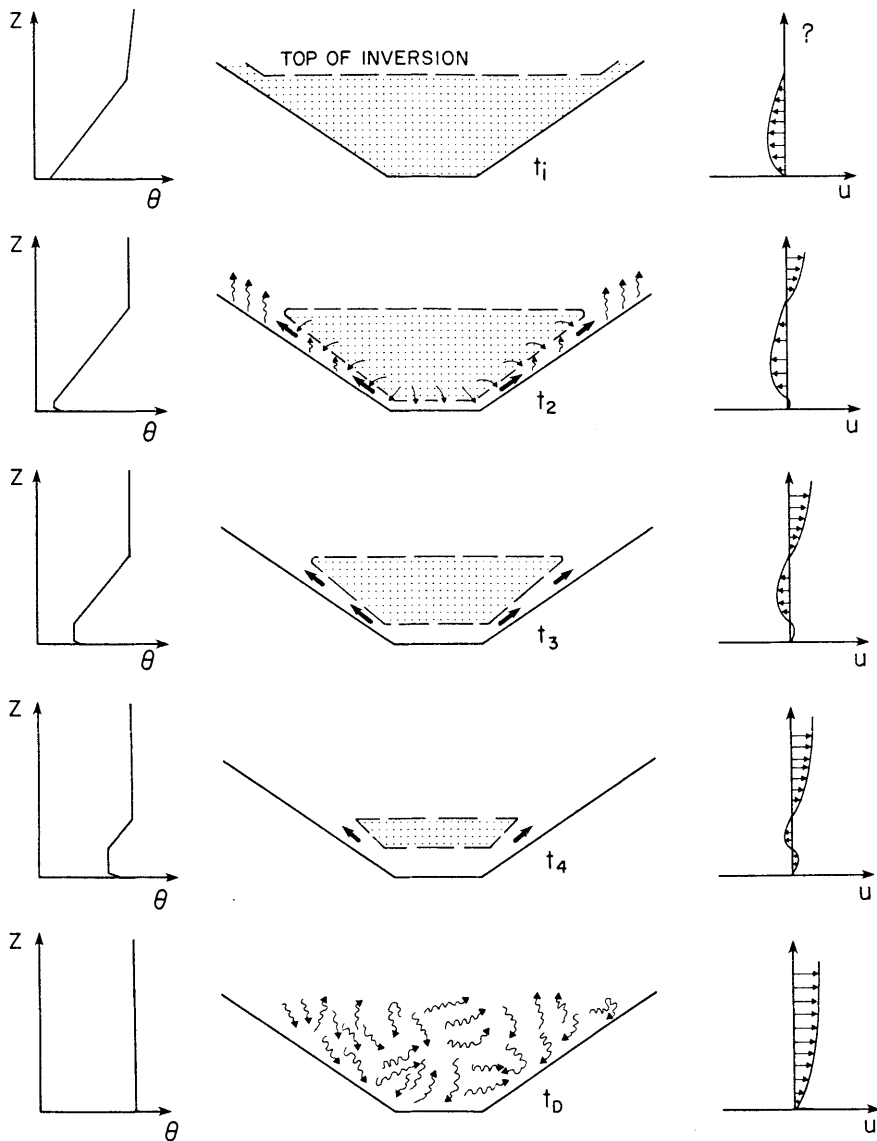


Figure 50. Illustration of the hypothesis of inversion destruction. On the right side of the diagram cross sections of a valley are shown at times t_1 , t_2 , t_3 , t_4 , and t_D . On the left are corresponding potential temperature profiles as taken from the valley center. At sunrise, t_1 , an inversion is present in the valley. At t_2 , a time after sunlight has illuminated the valley floor and slopes, a growing CBL is present over the valley surfaces. Mass and heat are entrained into the CBLs from the stable core above and carried up the sidewalls in the upslope flows. This results in a sinking of the stable core and growth of the CBLs (t_3 and t_4) until the inversion is broken (t_D) and a turbulent well-mixed, neutral atmosphere prevails through the valley depth.

flows requires energy, since parcels can be carried up the slope only if they are warmed to the potential temperature of the top of the inversion. From the principle of mass continuity and the assumption of no mass convergence or divergence in the along-valley direction, as mass is removed from the base of the stable core and carried away in the upslope flows, the stable core must sink. The evolution of the temperature structure within the valley is thus characterized by the development of convective boundary layers above the valley surface, and sinking or downward advection of the potential temperature structure in the stable core.

This hypothesis can explain many of the observed structural features of the valley atmosphere. The dependence on insolation explains why inversion destruction begins at sunrise. Following the hypothesis, the morning temperature inversion represents an energy deficit that is overcome by continued input of energy into the valley atmosphere. When the valley is snowcovered or wet, the available energy is reduced by high albedos or high latent heat. The hypothesis explains the role of the convective boundary layers that have been observed to develop over the valley floor and sidewalls and attributes their retarded growth to divergence of mass from them, or, equivalently, to the strong subsidence field superimposed on them. The hypothesis also explains why the whole depth of the stable core warms at the same rate while the temperature gradient remains constant. The sinking of the stable core can be explained on the basis of the mass continuity equation, where a slow sinking of the broad stable core compensates for stronger rising motions in the shallow boundary layers at its sides. Due to the sinking motion in the stable core, the available energy is utilized to warm the entire valley atmosphere rather than to warm only

a boundary layer near the surfaces. Once the valley inversion is destroyed, any further sensible heat flux from the valley surfaces supports the growth of a larger convective boundary layer over the entire mountainous region.

Referring back to Equations (8) and (9), the hypothesis calls for different physical processes to change the temperatures in the different layers of the valley atmosphere. The CBL over the valley floor is an advective boundary layer with winds blowing up the valley floor. Sensible heat flux convergence drives this boundary layer, and mass sinks into the top of it. Potential temperatures within the layer are constant with height but change as a function of time. The vertical potential temperature gradient does not change with time. Similarly, the CBLs over the sidewalls are advective boundary layers driven by heat flux convergence with mass sinking into their tops. They differ from the valley floor CBL primarily in the direction of their wind systems. Temperature changes in the stable core are due solely to vertical advection. The neutral layer appears to be a convective boundary layer that develops on a larger scale over the whole Western Slope of the Rocky Mountains. Its growth may be affected by larger scale subsidence fields when they are present.

C. Mathematical Model of Inversion Destruction

1. General Equations

Two approaches can be used to develop a mathematical model able to simulate temperature changes in the valley atmosphere. In the first approach detailed mathematical equations can be developed for the individual components of the overall system, including the various boundary layers and stable core. However, the valley atmosphere consists of many interrelated layers, and the coupling of the equations

for the different layers to simulate potential temperature changes in the valley atmosphere as a whole would be difficult due to geometrical considerations and lack of detailed information on physical characteristics of the various layers. Consequently, a second approach is taken in which a bulk thermodynamic model is developed for the valley inversion. As more is learned about the individual components of the system, the model can be refined to introduce greater detail into the simulation of the individual components.

The thermodynamic model of valley temperature structure evolution developed here is based on the hypothesis of the previous section. Figure 51 shows a unit thick cross-section of a mountain valley having sidewalls of inclination α_1 and α_2 and valley floor width ℓ . At sunrise, t_i , the valley is assumed to have an inversion of depth h_i and constant potential temperature gradient γ . The variable width of the valley at the top of the inversion is designated by L , and the origin of a y - z coordinate system is placed at the center of the valley floor at point 0. After sunrise a typical Pattern 3 potential temperature evolution ensues, in which a convective boundary layer develops over the valley floor and sidewalls. Removal of mass from the valley in these CBLs allows the stable core to sink so that a sounding taken at

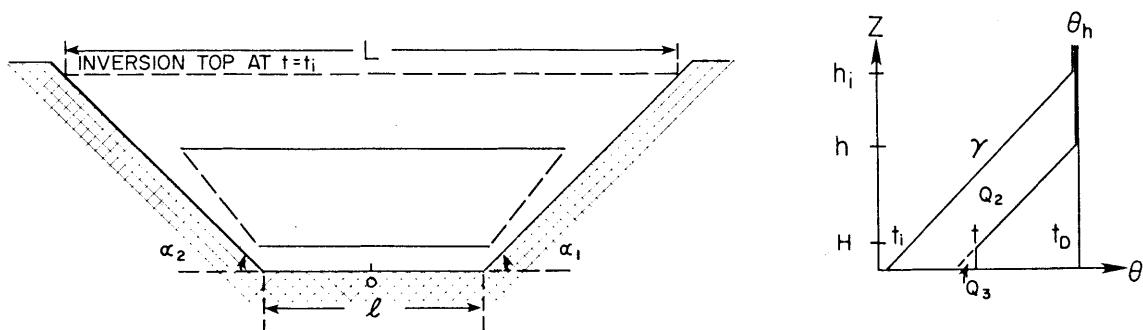


Figure 51. Valley geometry and potential temperature profiles used to formulate a mathematical model of inversion destruction.

an arbitrary later time, t , will show a lower inversion top height $h(t)$ and a shallow CBL near the ground. A later sounding, taken at a time t_D when the inversion has just been destroyed, will show a neutral atmosphere having a potential temperature of $\theta = \theta_h$.

From the First Law of Thermodynamics, the increment of energy required to increase the potential temperature of a mass of air m by the potential temperature increment $\Delta\theta$ is

$$\Delta Q = mc_p \frac{T}{\theta} \Delta\theta = \rho V c_p \frac{T}{\theta} \Delta\theta, \quad (13)$$

where $\frac{T}{\theta} \equiv \left[\frac{P}{1000} \right]^{R/c_p} \approx 1$, ρ is density (assumed constant) and V is volume. Using equation (13), the energy required to change the valley potential temperature profile at time t_i to the profile at time t can be obtained by an integration over the valley volume below the height of the inversion top. The total energy requirement is composed of two parts: the energy increment Q_2 that removes mass from the valley and allows the top of the inversion to sink, and the energy increment Q_3 that causes a CBL to grow. These energies are represented by the areas designated in Figure 51 and are given by the equations

$$Q_2 = \rho c_p \frac{T}{\theta} \left[\int_0^{h_i} \int_{y_L}^{y_R} \int_0^1 \Delta\theta_i dx dy dz - \int_0^h \int_{y_L}^{y_R} \int_0^1 \Delta\theta_1 dx dy dz \right] \quad (14)$$

$$= \rho c_p \frac{T}{\theta} \gamma \left[\frac{\ell}{2} (h_i^2 - h^2) + \frac{C}{6} (h_i^3 - h^3) \right], \quad (15)$$

where

$$\Delta\theta_i = \gamma(h_i - z), \quad (16)$$

$$y_L = - \left(\frac{\ell}{2} + \frac{z}{\tan \alpha_2} \right), \quad (17)$$

$$y_R = \frac{\ell}{2} + \frac{z}{\tan \alpha_1}, \quad (18)$$

$$C = \frac{1}{\tan \alpha_1} + \frac{1}{\tan \alpha_2} , \quad (19)$$

$$\Delta\theta_1 = \gamma(h-z), \quad (20)$$

and

$$Q_3 = \rho c_p \frac{T}{\theta} \int_0^H \int_{y_L}^{y_R} \int_0^1 \Delta\theta_2 \, dx dy dz \quad (21)$$

$$= \rho c_p \frac{T}{\theta} \gamma \left[\frac{\ell}{2} H^2 + \frac{C}{6} H^3 \right] , \quad (22)$$

where

$$\Delta\theta_2 = \gamma(H-z) . \quad (23)$$

In order to simplify the integration, it is assumed that the valley temperature structure is horizontally homogeneous across the valley, that mass is removed from the valley in such a way that the potential temperature gradient in the inversion layer does not change with time, and that ρ and c_p are constant. By differentiating the individual energies Q_2 and Q_3 with respect to time, the rates of change of the height of the top of the inversion and the height of the CBL are obtained, such

$$\frac{dQ_2}{dt} = \rho c_p \frac{T}{\theta} \gamma \left[-h \frac{dh}{dt} \left(\ell + \frac{hC}{2} \right) \right] , \quad (24)$$

and

$$\frac{dQ_3}{dt} = \rho c_p \frac{T}{\theta} \gamma \left[H \frac{dH}{dt} \left(\ell + \frac{HC}{2} \right) \right] . \quad (25)$$

The total rate of energy input into the valley to accomplish these changes is the fraction A_0 of solar irradiance F coming across the area of the top of the inversion, L , that is converted to sensible heat. The solar irradiance may be approximated by a sine function having a certain amplitude A_1 and period τ , so that the total rate of energy input becomes

$$\frac{dQ_1}{dt} = A_o LF = A_o (\ell+hC) A_1 \sin \frac{\pi}{\tau} (t-t_i) . \quad (26)$$

An energy balance for the valley inversion is obtained by equating (26) to the sum of (24) and (25). Alternatively, a fraction of the energy input is available to drive the growth of the CBL while the rest of the incoming energy is used to remove mass from the valley. The fraction of energy input used to drive the CBL growth is assumed to be of the form

$$k \left[\frac{\ell+HC}{\ell+hC} \right] ,$$

where k is a number between 0 and 1. This form is chosen in order to simplify later equations. Equating this fraction of the energy input to Equation (24) and the remainder to Equation (25) and solving for dH/dt and dh/dt results in the final model equations

$$\frac{dH}{dt} = \frac{\theta}{T} \frac{k}{\rho c_p} \left[\frac{\ell + HC}{\ell + \frac{HC}{2}} \right] \frac{A_o A_1}{\gamma H} \sin \frac{\pi}{\tau} (t-t_i) , \quad (27)$$

and

$$\frac{dh}{dt} = - \frac{\theta}{T} \frac{1}{\rho c_p} \left[\frac{\ell + hC - k(\ell + HC)}{\ell + \frac{hC}{2}} \right] \frac{A_o A_1}{\gamma h} \sin \frac{\pi}{\tau} (t-t_i) . \quad (28)$$

These equations specify the dependence of the rate of ascent of the CBL and the rate of descent of the inversion top on inversion characteristics, incoming energy, and valley topography. An integration of the coupled equations allows the simulation of the time dependent behavior of the heights of the CBL and inversion top. If the potential temperature at the top of the inversion, θ_h , is known and is independent of time, and γ is constant, knowledge of the variation of h and H with time is sufficient to specify how vertical profiles of potential

temperature change with time. When $k = 0$, the equations provide an approximate simulation of Pattern 2 inversion destruction in which destruction occurs solely due to the removal of mass from a valley in the slope flows, resulting in a descent of the inversion top. When $k = 1$, the equations provide a simulation of Pattern 1 inversion destruction, in which destruction occurs mainly due to the growth of a CBL over the valley floor. When $k = 1$ and the valley floor becomes very wide, the simulation approaches that of inversion destruction over the plains. When k is between 0 and 1, the equations provide a simulation of Pattern 3 inversion destruction in which the inversion is destroyed by the combined effect of a growing CBL and a descending inversion top. A fuller description of the characteristics of the model equations for Pattern 1, 2, and 3 temperature structure evolution follows.

2. Pattern 2 Inversion Destruction

The physical hypothesis of Pattern 2 inversion destruction requires a shallow CBL to form over the sidewalls so that additional energy can be used to cause mass to flow up them. Nevertheless, Pattern 2 destruction may be approximated by assuming that all the energy available to destroy the inversion goes solely to move mass up the sidewalls, causing the top of the inversion to descend. This can be accomplished by setting k equal to zero in Equations (27) and (28) resulting in the two equations

$$\frac{dH}{dt} = 0 \quad (29)$$

$$\frac{dh}{dt} = - \frac{\theta}{T} \left[\frac{\ell + hC}{\ell + \frac{hC}{2}} \right] \frac{A_o A_1}{\rho c_p y h} \sin \frac{\pi}{\tau} (t - t_i) \quad (30)$$

Following these equations, the CBL does not grow as a function of time, and the inversion is destroyed as the top of the inversion sinks. The rate of descent of the top of the inversion increases as the inversion descends. The descent rate is faster when more energy is available and when the potential temperature gradient of the inversion is weaker. The factor in brackets in Equation (30) is a topographic factor that varies from 1 to 2 depending on the shape of the valley cross-section. This accounts for the reduced volume of air within the mountain valley relative to that over the plains for the same energy flux on a horizontal surface. Since the valley has less volume to be heated by the same incoming energy, it warms more rapidly. By separating variables h and t and integrating from the initial conditions $h = h_i$ and $H = 0$ at $t = t_i$ to $h = h$ and $H = H$ at $t = t$, analytical expressions are obtained which describe how H and h vary with time,

$$H = 0 \quad (31)$$

and

$$\frac{h^2 - h_i^2}{4} + \frac{\ell}{2C} (h - h_i) + \frac{\ell^2}{2C^2} \ln \frac{\ell + h_i C}{\ell + h C} = \frac{\theta}{T} \frac{A_o A_1}{\rho c_p \gamma} \frac{\tau}{\pi} \left[\cos \frac{\pi}{\tau} (t - t_i) - 1 \right] \quad (32)$$

Figure 52 illustrates the shapes of the curves of h versus t for a reference simulation and for two cases where one parameter in the reference simulation is changed. The reference simulation uses representative values of valley parameters observed in western Colorado including $\ell = 1000$ m, $\alpha_1 = \alpha_2 = 15^\circ$, $h_i = 500$ m, $\gamma = .025^\circ\text{K m}^{-1}$, $\tau = 12$ hours = 43200 sec, $\frac{T}{\theta} = 1$, $\rho = 1$ kg m⁻³, and $A_o A_1 / \rho c_p = .25^\circ\text{K m sec}^{-1}$. The reference inversion takes nearly 4½ hours to be destroyed when $A_o A_1 / \rho c_p = .25^\circ\text{K m sec}^{-1}$. Figure 52 was obtained by a numerical integration of equation (30) using a forward finite difference scheme and a time step of 10 minutes.

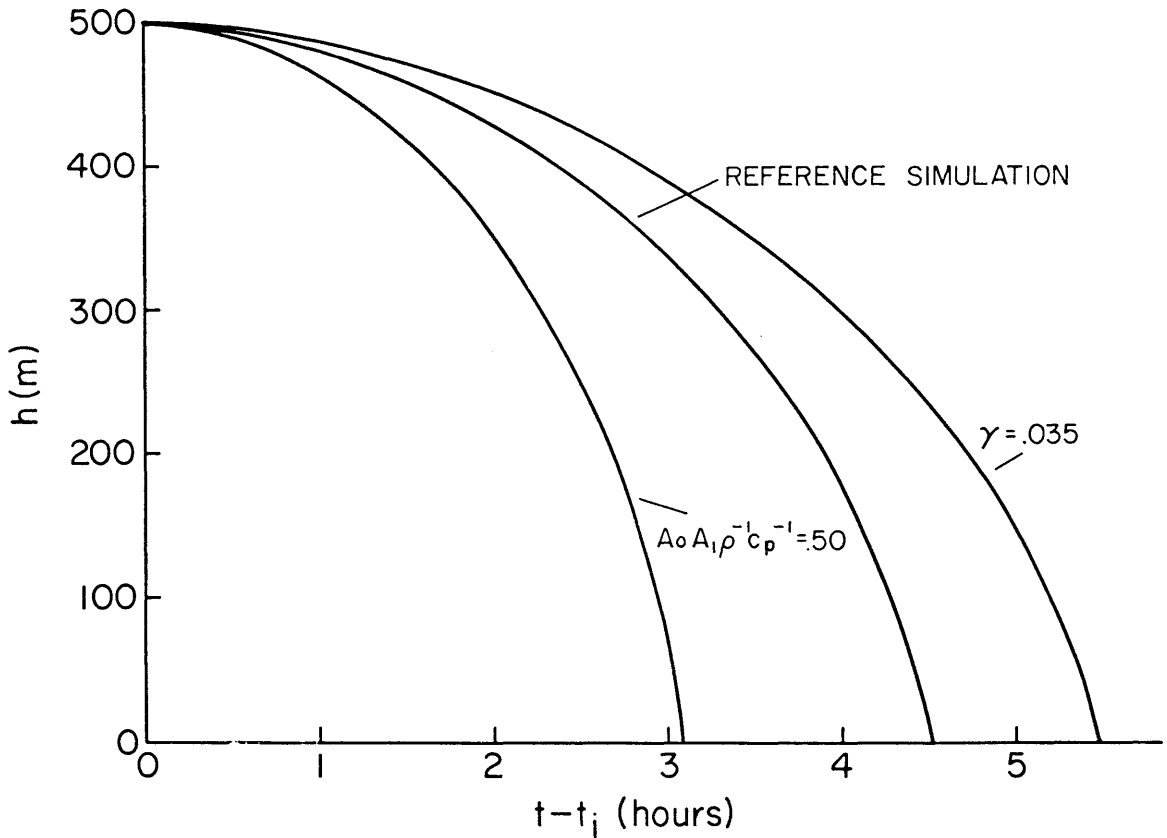


Figure 52. Descent of inversion top as a function of time for the reference inversion simulation and for two simulations for which the single parameters indicated were changed. Pattern 2 destruction.

An analytical expression for the time required to destroy an inversion can be obtained by integrating Equation (30) from the initial conditions to the final conditions of $h = 0$ at $t = t_D$. This expression,

$$t_D - t_i = \frac{\tau}{\pi} \cos^{-1} \left\{ 1 - \frac{T}{\theta} \frac{\rho_c p \gamma}{A_0 A_1} \frac{\pi}{\tau} \left[\frac{h_i^2}{4} + \frac{\ell h_i}{2C} + \frac{\ell^2}{2C^2} \ln \frac{\ell}{\ell + h_i C} \right] \right\}, \quad (33)$$

enumerates the factors affecting inversion breakup time. The sensitivity of inversion breakup time (measured from sunrise) to the various

parameters is illustrated in Figure 53 using the reference simulation above. The reference inversion takes 4.4 hours to break (vertical line in Figure 53). The effect on the time required to destroy the reference inversion by varying the individual parameters is obtained by following the labeled curves. Thus, varying the initial height of the inversion from 400 to 600 m, other parameters being equal, changes the time required to destroy the inversion from 3.5 to 5.4 hours. For the reference inversion, the most sensitive parameters affecting the time required to break an inversion are the available energy and the initial potential temperature gradient and inversion height. In the normally dry Colorado valleys the most important factors affecting the available energy are albedo (snow versus no snow) and latent heat flux. The effect of valley shape on the breakup time is relatively small for normal ranges of α and ℓ encountered in valleys of western Colorado. Nevertheless, it is apparent that the valley width and sidewall angles may affect the mode of inversion destruction since they control, to a certain extent, the divergence of mass in the CBLs and thus determine whether inversion destruction more nearly follows Pattern 1 or Pattern 2. Overall, predictions of the time required to destroy inversions, given typical values of the parameters observed in field experiments, are consistent with the observed range of 3.5 to 5 hours.

3. Pattern 1 Inversion Destruction

A useful approximation to Pattern 1 inversion destruction can be obtained from the model equations by setting $k = 1$. The general equations then reduce to the two equations

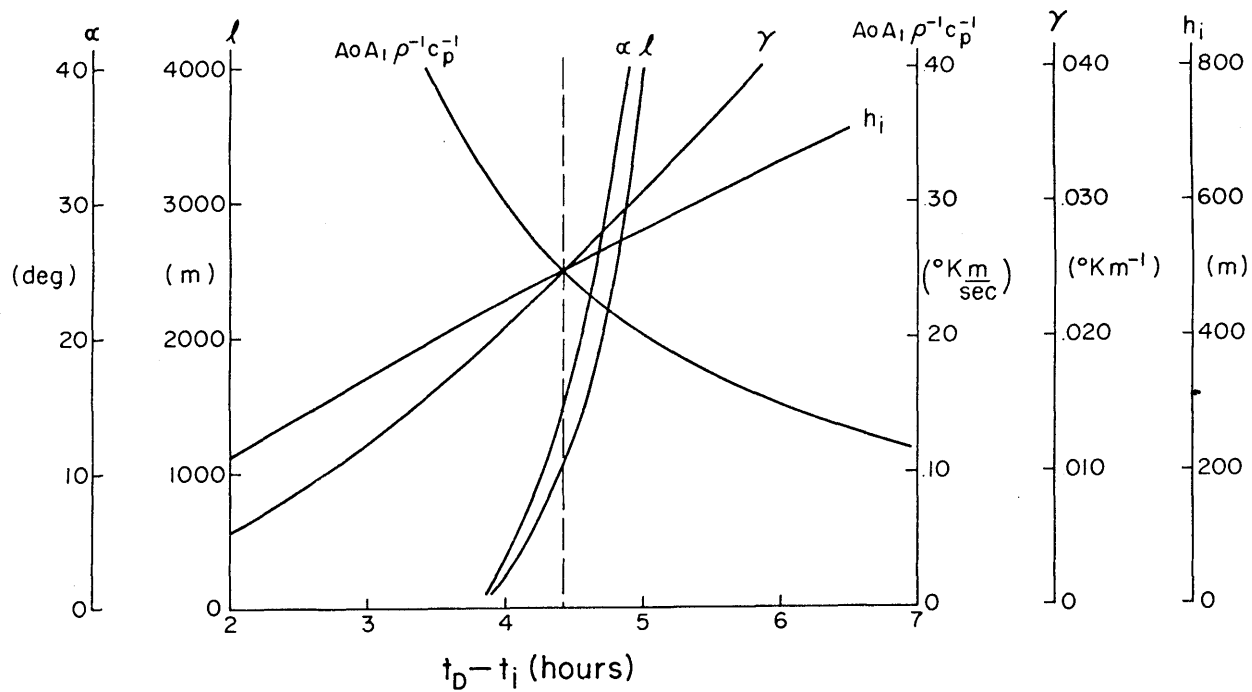


Figure 53. Sensitivity of inversion destruction time to various model parameters for Pattern 2 destruction.

$$\frac{dH}{dt} = \frac{\theta}{T} \frac{\ell + \frac{HC}{2}}{\ell + \frac{HC}{2}} \frac{A_o A_1}{\rho_c \gamma H} \sin \frac{\pi}{\tau} (t-t_i) , \quad (34)$$

and

$$\frac{dh}{dt} = - \frac{\theta}{T} \frac{(h-H)C}{\ell + \frac{hC}{2}} \frac{A_o A_1}{\rho_c \gamma h} \sin \frac{\pi}{\tau} (t-t_i) . \quad (35)$$

Application of these equations to a valley that is very wide or approaches a plain ($\ell \rightarrow \infty$) results in the equations

$$\frac{dH}{dt} = \frac{\theta}{T} \frac{A_o A_1}{\rho_c \gamma H} \sin \frac{\pi}{\tau} (t-t_i) , \quad (36)$$

and

$$\frac{dh}{dt} = 0 . \quad (37)$$

Thus, over flat terrain where no topographically-induced mass divergence occurs from the CBL, the inversion is destroyed solely by the growth of a CBL. Performing integrations on equation (36) as described in the previous section results in an analytical expression for H,

$$H(t) = \left\{ 2 \frac{\theta}{T} \frac{\tau}{\pi} \frac{A_o A_1}{\rho_c \gamma} [1 - \cos \frac{\pi}{\tau} (t-t_i)] \right\}^{\frac{1}{2}} , \quad (38)$$

and an expression for the breakup time,

$$t_D - t_i = \frac{\tau}{\pi} \cos^{-1} \left[1 - \frac{T}{\theta} \frac{\rho_c \gamma}{A_o A_1} \frac{\pi}{\tau} \frac{h_i^2}{2} \right] . \quad (39)$$

Equation (38) is nearly identical to an equation for CBL growth over homogeneous terrain as derived by Leahey and Friend (1971). Following Equation (38), Figure 54 presents plots of H versus time for the reference simulation and for two cases where one parameter in the reference simulation has been changed. The reference inversion is destroyed in

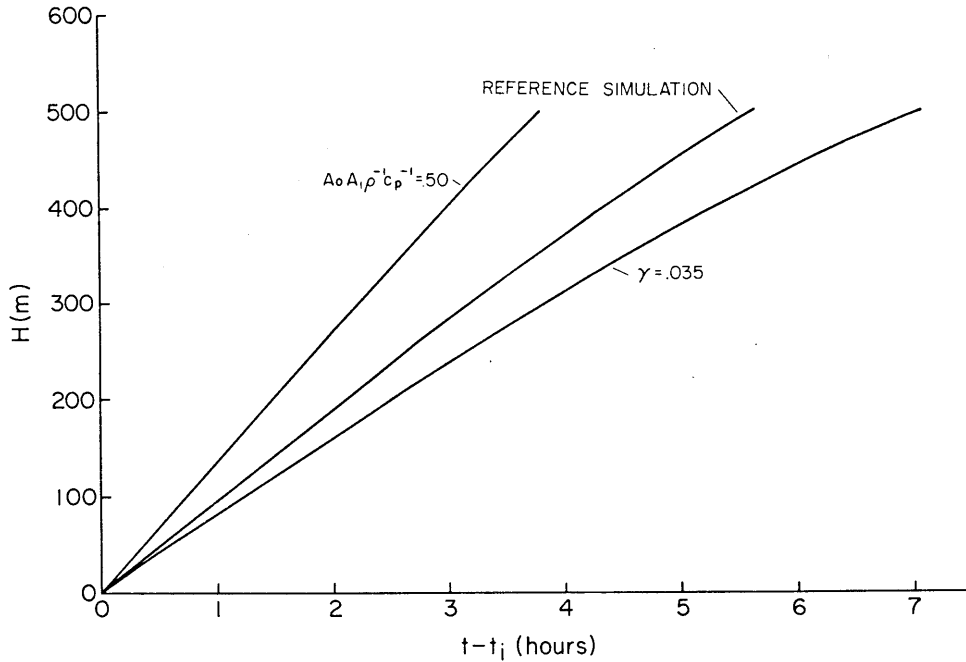


Figure 54. Growth of CBL over flat terrain as a function of time for the modified reference inversion ($\alpha = 0$, $l \rightarrow \infty$) and for two simulations in which single parameters were changed to the values indicated. Pattern 1 destruction.

5.65 hours by a near-linear increase in the depth of the CBL. If the incoming energy is doubled, the inversion takes 3.8 hours to break, and if the potential temperature gradient is increased to $.035^\circ\text{K m}^{-1}$, the inversion is broken in about 7.1 hours. Figure 55 indicates the sensitivity of the time required to break an inversion on the different parameters of Equation (39). The effect on the breakup time of changing individual parameters in the reference simulation is obtained by following the individual curves.

Returning to Equations (34) and (35), Equation (34) is formulated so that the entire fraction A_0 of the energy coming across the area $(l + HC)$ of the top of the CBL is used to cause the CBL to grow. The energy used to cause the top of the inversion to descend is the fraction A_0 of the difference between the energy coming across the top of

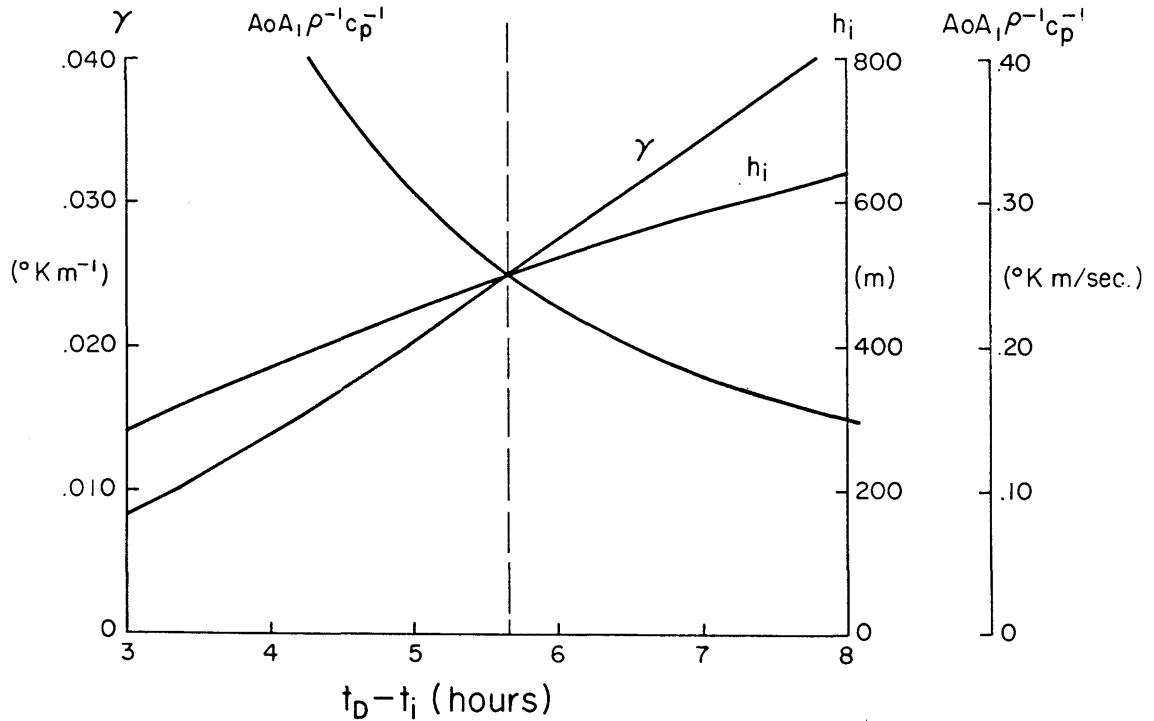


Figure 55. Sensitivity of inversion destruction time to various model parameters for Pattern 1 inversion destruction over flat terrain.

the inversion and the energy coming across the top of the CBL. The time-dependent behavior of the height of the CBL can be obtained by an integration of Equation (34) from the initial condition of $H = 0$ at $t = t_i$ to the final condition of $H = H$ at $t = t$, such that

$$\frac{H^2}{4} + \frac{\partial H}{2C} + \frac{\partial^2}{2C^2} \ln \frac{\partial}{\partial + HC} = \frac{\theta}{T} \frac{A_o A_1}{\rho c_p \gamma} \frac{\tau}{\pi} [1 - \cos \frac{\pi}{\tau} (t - t_i)] \quad (40)$$

The integration of Equations (34) and (35) can be accomplished numerically to determine how h and H change with time in a Pattern 1 inversion destruction in a mountain valley. This is done for the reference simulation and for two simulations in which a single parameter of the reference simulation is changed. The resulting plots are shown in Figure 56. The characteristics of the plots include a

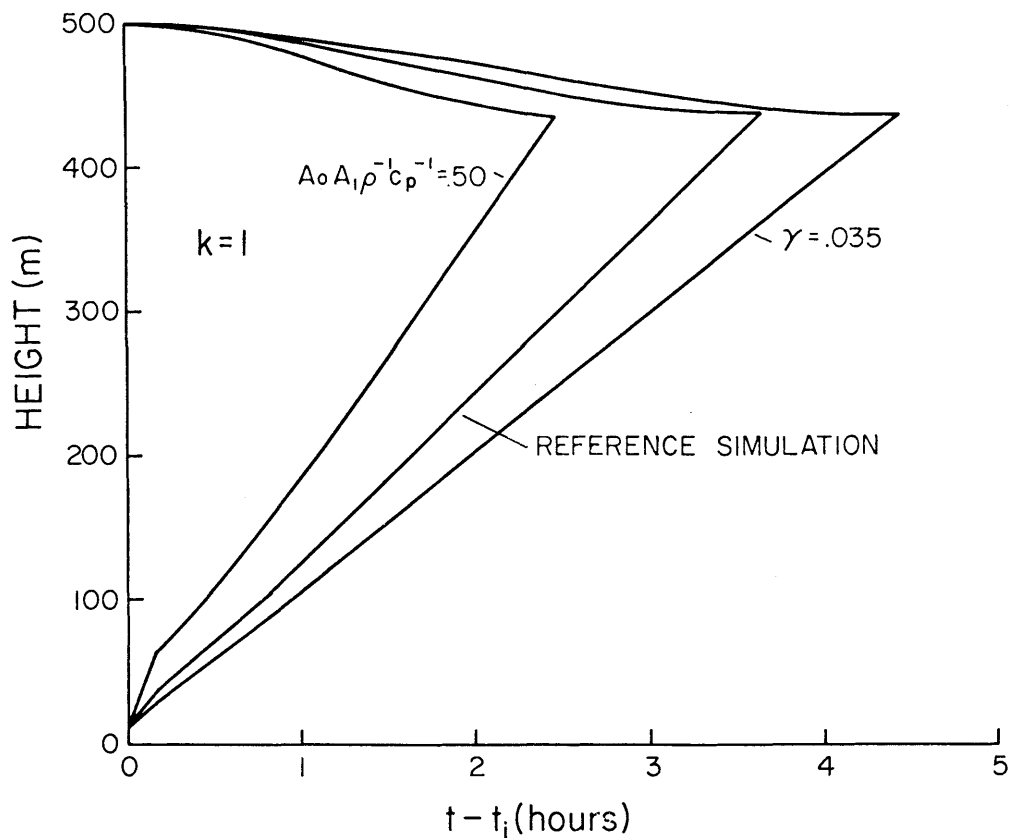


Figure 56. Ascent of CBL and descent of inversion top as a function of time for Pattern 1 inversion destruction in a valley for the reference simulation and for two simulations in which single parameters were changed to the values indicated.

near-linear growth of the CBL with time, a slow descent of the inversion top, and a more rapid breakup than for Pattern 2 destruction. Pattern 1 destruction takes 3.7 hours versus the 4.4 hours required for Pattern 2 breakup. The same total amount of energy is required to destroy the reference inversion, whether it is destroyed following Pattern 1 or Pattern 2. However, since the energy available to destroy the inversion comes across the area of the top of the inversion, and this area is larger when the inversion top sinks more slowly, the total amount of energy required to destroy the inversion is attained earlier in the day, resulting in an earlier inversion breakup.

4. Pattern 3 Inversion Destruction

A simulation of Pattern 3 inversion destruction uses the general model Equations (27) and (28), in which a partitioning of energy is required to allow both CBL growth and inversion top descent. In order to use the general model equations, the fraction of sensible heat flux $K = k \left(\frac{\ell + HC}{\ell + hC} \right)$ that drives the growth of the CBL must be determined. It is apparent that the fraction K is a function of time, since the initial energy input must be used primarily to develop the CBLs before appreciable mass can be carried up them. Factor K also depends on the topographic characteristics of the valley, since K must approach 1 as the valley width approaches infinity. It seems probable that K may also be a function of sensible heat flux. Since the functional dependences of K are not yet known, it is assumed that k is a constant and, by comparing model simulations to actual data, the constant value of k that results in the best fit to data is determined. This approach allows an investigation of the effect of k on the simulation. Further research is necessary to determine the actual functional form of K , so that a better understanding of the energy partitioning phenomenon can be obtained, resulting in more accurate simulations.

The equations used to simulate Pattern 3 destruction are thus

$$\frac{dH}{dt} = \frac{\theta}{T} \frac{k}{\rho c_p} \left[\frac{\ell + HC}{\ell + \frac{HC}{2}} \right] \frac{A_o A_1}{\gamma H} \sin \frac{\pi}{\tau} (t - t_i), \quad (41)$$

and

$$\frac{dh}{dt} = - \frac{\theta}{T} \frac{1}{\rho c_p} \left[\frac{\ell + hC - k(\ell + HC)}{\ell + \frac{hC}{2}} \right] \frac{A_o A_1}{\gamma h} \sin \frac{\pi}{\tau} (t - t_i), \quad (42)$$

where

$$0 \leq (k = \text{constant}) \leq 1. \quad (43)$$

These equations can be integrated numerically to determine how H and h vary with time, given a constant value of k . This is done by using a finite difference form of Equation (41) to calculate H at a given time using the equations

$$\Delta H_j = \frac{\theta}{T} \frac{k}{\rho c_p} \left[\frac{\ell + H_j C}{H_j C} \right] \frac{A_o A_1}{\gamma H_j} [\sin \frac{\pi}{T} (t-t_i)] \Delta t , \quad (44)$$

and

$$H_{j+1} = H_j + \Delta H_j , \quad (45)$$

and

$$j = 0, 1, 2, 3, \dots n , \quad (46)$$

$$H_o \equiv H_i \neq 0 , \quad (47)$$

and

$$t = (j+1) \Delta t . \quad (48)$$

A finite difference form of Equation (42) is then used to calculate height h , such that

$$\Delta h_j = - \frac{\theta}{T} \frac{1}{\rho c_p} \left[\frac{\ell + h_j C - k(\ell + H_j C)}{\ell + \frac{h_j C}{2}} \right] \frac{A_o A_1}{\gamma h_j} [\sin \frac{\pi}{T} (t-t_i)] \Delta t, \quad (49)$$

and

$$h_{j+1} = h_j + \Delta h_j . \quad (50)$$

Figure 57 shows several numerical integrations using the above method, time steps of 10 minutes, the reference simulation, and several values of k . Replotted on the same figure are some of the limiting cases of the general equations for destruction of the reference inversion discussed earlier. The time required to break the reference inversion decreases from 4.4 to 3.7 hours as the value of k is increased from 0 to 1. For all values of k the growth of the CBL is nearly linear.

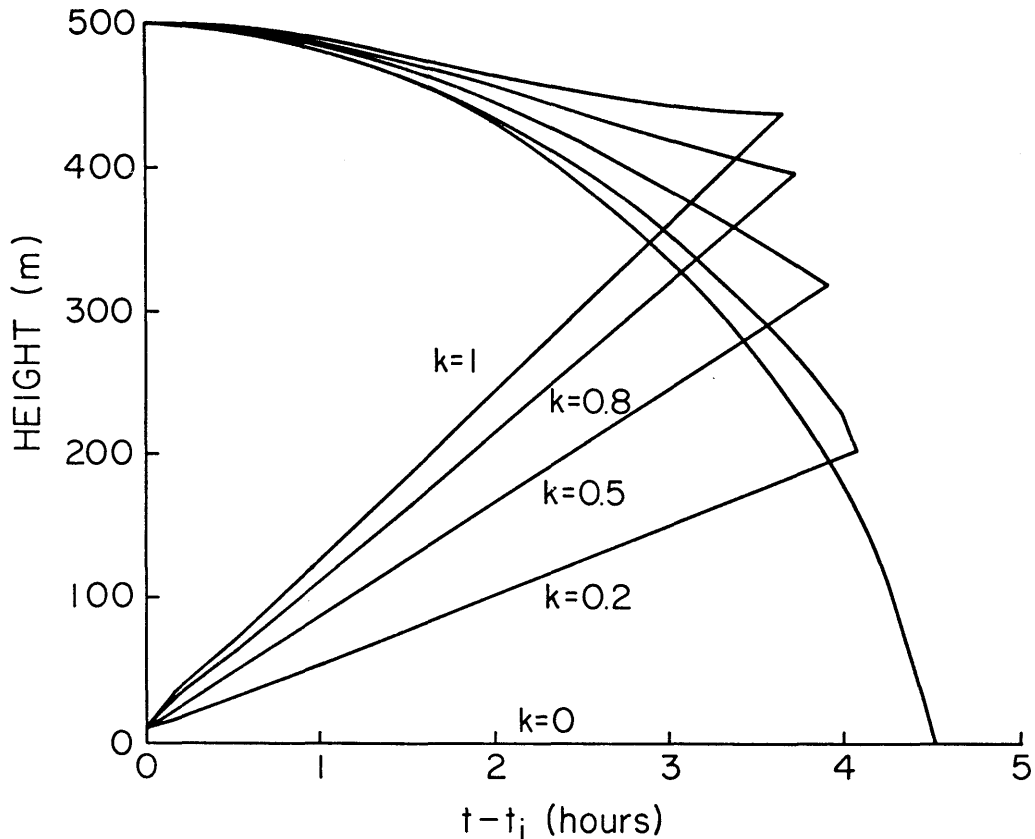


Figure 57. Ascent of CBL and descent of inversion top as a function of time for Pattern 3 destruction of the reference inversion for different values of k .

Figure 58 shows the effect of varying individual parameters in the reference simulation with k fixed. The inversion is destroyed when the ascending CBL and the descending inversion top meet at a height of $H_D = h_D = 205$ m. The fact that the fraction k uniquely determines the height at which the ascending CBL meets the descending inversion top at the time of inversion destruction, suggests a means of fitting the model results to actual data that will be used in a later section.

5. Model Modification to Account for Warming of the Neutral Layer

Field observations show that the potential temperature at the top of the inversion, θ_h , usually increases slowly with time. The warming

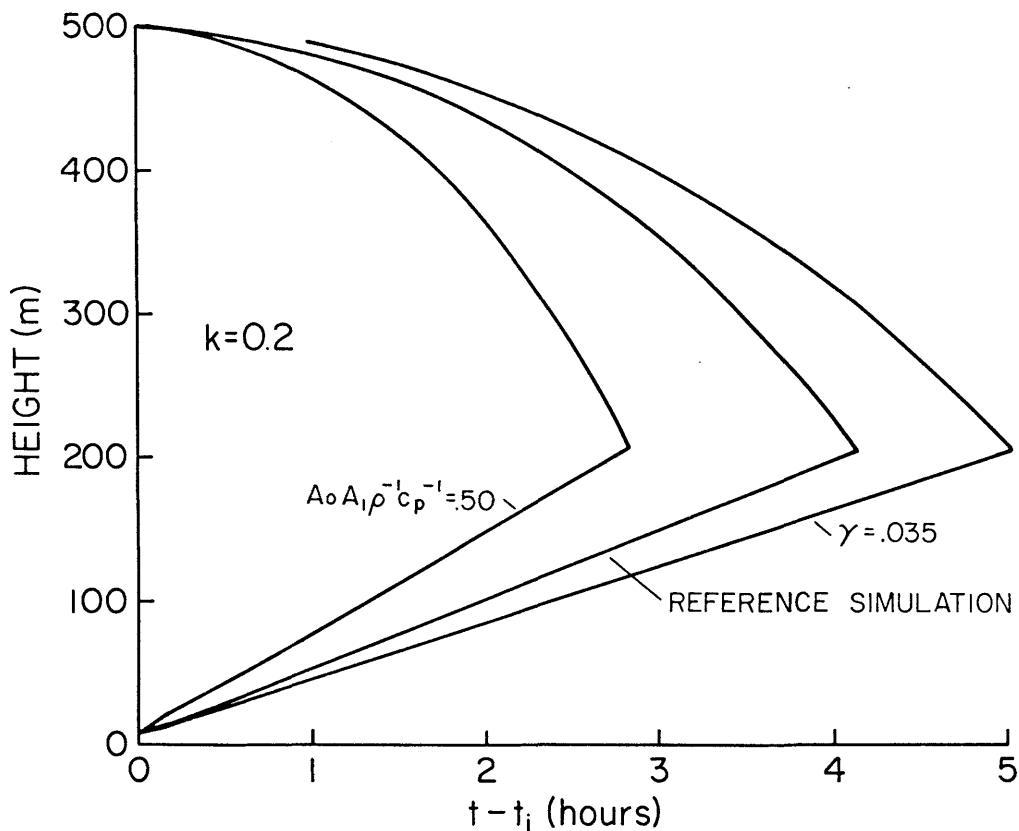


Figure 58. Ascent of CBL and descent of inversion top for Pattern 3 destruction ($k = 0.2$) of the reference inversion, and for two simulations in which single parameters were changed to the values indicated.

rate varies from valley to valley and from day to day with the average warming rate being about $0.4 \text{ K}^\circ \text{ hr}^{-1}$. From the physical hypothesis, this warming requires that more energy be spent to move mass up the sidewalls, since the parcels must be warmed to a higher temperature $\theta_h = d\theta_h/dt \delta t$ to be removed from the valley. The energy requirement can be calculated by considering that the mass of air removed from the valley to allow the top of the inversion to sink from h_i to h is given by

$$\text{mass removed} = \rho V = \rho(h_i - h) \left(\ell + \frac{h_i + h}{2} C \right), \quad (51)$$

and that the energy required to move this mass across a potential temperature jump at the top of the inversion, $\theta_h(t) - \theta_h(t_i)$, can be approximated by

$$Q_4 = \rho V c_p \frac{T}{\theta} \frac{\theta_h(t) - \theta_h(t_i)}{2} . \quad (52)$$

If the warming in the neutral layer occurs linearly in time, the potential temperature jump is given by $\beta(t-t_i)$, where $\beta = \partial\theta_h/\partial t$ is the rate of warming. Then

$$Q_4 = \rho c_p \frac{T}{\theta} \frac{\beta}{2} (h_i - h)(t-t_i) \left(\ell + \frac{h_i+h}{2} C \right) , \quad (53)$$

and

$$\frac{dQ_4}{dt} = \rho c_p \frac{T}{\theta} \frac{\beta}{2} \left[(h_i - h) \left(\ell + \frac{h_i+h}{2} C \right) - (t-t_i) \frac{dh}{dt} (\ell + hC) \right] . \quad (54)$$

The model equations are modified to account for this extra energy requirement by specifying that the fraction $k \left(\frac{\ell+HC}{\ell+hC} \right)$ of the inversion energy input dQ_1/dt drives the CBL growth, or

$$k \left(\frac{\ell+HC}{\ell+hC} \right) \frac{dQ_1}{dt} = \frac{dQ_2}{dt} , \quad (55)$$

while the remainder of the energy input drives the descent of the inversion and carries parcels across the potential temperature jump, such that

$$\left[1 - k \left(\frac{\ell+HC}{\ell+hC} \right) \right] \frac{dQ_1}{dt} = \frac{dQ_3}{dt} + \frac{dQ_4}{dt} . \quad (56)$$

Substituting Equations (24), (25), (26) and (54), the modified model equations are

$$\frac{dH}{dt} = \frac{\theta}{T} \frac{k}{\rho c_p} \left[\frac{\ell + HC}{\ell + \frac{hC}{2}} \right] \frac{A_o A_1}{\gamma H} \sin \frac{\pi}{\tau} (t-t_i) , \quad (57)$$

and

$$\frac{dh}{dt} = - \frac{\theta}{T} \frac{1}{\rho c_p} \left\{ \frac{[\ell+hC-k(\ell+HC)] A_o A_1 \sin \frac{\pi}{\tau} (t-t_i) - \rho c_p \frac{T}{\theta} \frac{\beta}{2} (h_i - h) \left(\ell + \frac{h_i+h}{2} C \right)}{h\gamma \left(\ell + \frac{hC}{2} \right) + \frac{\beta}{2} (t-t_i) (\ell + hC)} \right\} \quad (58)$$

These equations can be used to simulate inversion breakup when significant warming occurs in the neutral layer during inversion breakup. Equation (58) reduces to Equation (42) when β is zero. It is important to note that Equation (57) has the same form as before but, since more energy is required to move mass up the sidewalls, the partitioning of energy may be affected. If this actually occurs in nature, then the functional dependency of k is more complicated than previously discussed, since it will depend not only on time, energy input, and valley width, but also on the rate of warming of the neutral layer above the inversion. As before, Equations (57) and (58) may be integrated numerically to simulate valley inversion data. If the potential temperature at the top of the inversion is known at sunrise along with its dependence on time, it is possible to simulate changes in the vertical structure of potential temperature, since γ is constant in the stable core region from height h to H , and the potential temperature below H is independent of height. Thus Equations (57) and (58) are sufficient to simulate valley potential temperature structure evolution if $\theta_h(t)$ is known. If θ_h does not vary with time, Equations (41) and (42) can be used for the simulation.

D. Comparison of Model Results with Data

A finite-difference form of Equations (57) and (58) may be used to simulate Patterns 1, 2, and 3 temperature structure evolution. The form of the equations used is as follows:

$$H_{j+1} = H_j + \Delta H_j, \quad (59)$$

where

$$\Delta H_j = \frac{\theta}{T} \frac{k}{\rho c_p} \frac{\ell + H_j C}{H_j C} \frac{A_o A_1}{\gamma H_j} [\sin \frac{\pi}{\tau} (t - t_i)] \Delta t \quad (60)$$

and

$$h_{j+1} = h_j + \Delta h_j, \quad (61)$$

where

$$\Delta h_j = - \frac{\theta}{T} \frac{1}{\rho c_p} \frac{[\ell + h_j C - k(\ell + H_j C) A_0 A_1 \sin \frac{\pi}{\tau} (t - t_i) - \rho c_p \frac{T}{p \theta} \frac{\beta}{2} (h_i - h_j) (\ell + \frac{h_i + h_j}{2} C)]}{h_j \gamma (\ell + \frac{j}{2} C) - \frac{\beta}{2} (t - t_i) (\ell + h_j C)} \Delta t \quad (62)$$

and

$$H_0 \equiv H_i \neq 0, \quad h_0 \equiv h_i; \quad (63)$$

$$t = (j+1) \Delta t. \quad (64)$$

The simulation is ended when $H_{j+1} = H_n \geq h_{j+1} = h_n$. The input parameters needed to solve the equations are listed below in Table 9 along with a summary of how they may be obtained. The output of the model is $h(t)$ and $H(t)$. From these outputs and the assumptions that γ is constant for altitudes between H and h , that potential temperature is independent of height in the CBL and neutral layer, and that $\theta_h(t_i)$ and $\partial \theta_h / \partial t$ are known, $\theta(t, z)$ for the CBL, stable core and neutral layer can be determined.

In the following sections the model equations will be applied to simulate actual data collected in the valleys of western Colorado. Unfortunately, since two of the input parameters to the thermodynamic model (k and A_0) were not observed in the field programs, the equations cannot be applied directly. Instead, arbitrary values for k and A_0 are chosen until the best simulation of the data is obtained with the model. It is then determined whether the values of k and A_0 are reasonable for the situation at hand. Both k and A_0 are bounded, since they are fractions between 0 and 1. The value of k specifies the constant fraction of sensible heat flux that is used to cause the CBL to deepen.

Table 9. Model Input Parameters

MODEL INPUT		SOURCE
Constants	i) θ/T ii) ρc_p	from average P and T of valley atmosphere
Valley Topography	iii) l iv) C	from topographical maps
Initial Inversion Characteristics	v) γ vi) $h_i = h_o$	from sunrise sounding
Solar Irradiance	vii) A_1 viii) τ ix) t_i	from extraterrestrial solar irradiance model, Appendix E, or field notes for t_i
External Conditions (Neutral Layer Warming)	x) β	from sequential soundings taken during observation of inversion buildup
Energy Partition	xi) k	comparisons of theory and data
Surface Energy Balance	xii) A_o	measurements, if available
Numerical	xiii) $H_i = 0$ xiv) Δt	arbitrary

By considering the individual components of the energy budgets of valley surfaces, it is possible to determine more realistic bounds for the fraction A_0 . First, however, A_0 and $A_1 \sin \frac{\pi}{\tau} (t-t_i)$ are redefined slightly in order to simplify the model. A_0 has been previously specified as the fraction of the solar energy coming across the top of the inversion ($A_1 \sin \frac{\pi}{\tau} (t-t_i)$) that is converted to sensible heat. Using these definitions, A_0 is a bulk parameter characterizing the energy budgets of the valley surfaces where the energy transformations actually take place. Since the solar irradiance model of Appendix E calculates extraterrestrial radiation, it is convenient to allow $A_1 \sin \frac{\pi}{\tau} (t-t_i)$ to represent extraterrestrial radiation and to redefine A_0 as the fraction of extraterrestrial radiation that is converted to sensible heat. This redefinition incorporates the transmissivity of the earth's atmosphere into the parameter A_0 along with the surface energy budget information.

To determine a realistic upper limit for A_0 , the joint effect of the energy budgets of the three valley surfaces (valley floor and two sidewalls) is approximated by the energy budget of an equivalent horizontal surface (Figure 59). Following Oke's (1978) terminology, four radiative components make up the net all-wave radiative flux on the surface, Q^* . These include the incoming long-wave and short-wave radiative fluxes, $L\downarrow$ and $K\downarrow$, and the long- and short-wave radiative fluxes emitted by the surfaces, $L\uparrow$ and $K\uparrow$. Considering the long- and short-wave components individually, the net long-wave radiative flux, L^* , is given by $L\downarrow - L\uparrow$ and the net short-wave radiative flux, K^* , is given by $K\downarrow - K\uparrow$. The net all-wave radiative flux on a surface may be used to heat the air above the surface, to heat the ground, or to

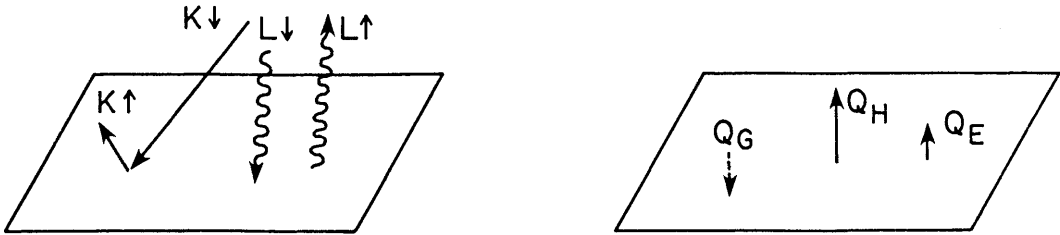


Figure 59. Representation of the surface energy budget.

evaporate water. The appropriate heat fluxes are the sensible heat flux, Q_H ; the ground heat flux, Q_G ; and the latent heat flux, Q_E . Thus, equations for the surface energy budget are

$$K^* = K\downarrow - K\uparrow , \quad (65)$$

$$L^* = L\downarrow - L\uparrow , \quad (66)$$

$$Q^* = K^* + L^* = Q_G + Q_H + Q_E , \quad (67)$$

and

$$Q_H = Q^* - Q_G - Q_E = K\downarrow - K\uparrow + L\downarrow - L\uparrow - Q_G - Q_E . \quad (68)$$

A_o is the ratio of sensible heat flux, Q_H , to extraterrestrial solar irradiance on a horizontal surface (designated Q_{Sh} in Appendix E), or

$$A_o = \frac{Q_H}{Q_{Sh}} = \frac{K\downarrow - K\uparrow + L\downarrow - L\uparrow - Q_G - Q_E}{Q_{Sh}} . \quad (69)$$

An approximate upper limit to A_o can be obtained by evaluating the individual terms in this equation. Since A_o is assumed to be invariant with time on a given day, it is convenient to consider the limiting values of the individual terms at solar noon. To determine the upper limit of A_o , $K\downarrow$ and $L\downarrow$ must be maximized and $K\uparrow$, $L\uparrow$,

Q_G , and Q_E must be minimized. The amplitude of Q_{Sh} at solar noon is A_1 . Taking the individual terms in turn:

$$(1) \quad K\downarrow = k_T A_1$$

At solar noon, the incoming short-wave radiative flux is given by the product of the extraterrestrial solar flux, A_1 , and the transmissivity of the atmosphere, k_T . A reasonable maximum value of $K\downarrow$ for the period of inversion breakup, considering the high altitude location of the experimental sites and the likelihood of reflections from side-walls and high mountains east of most sites, is $k_T = .95 Q_{Sh}$ or, at solar noon, $K\downarrow = .95 A_1$.

$$(2) \quad K\uparrow = A_L K\downarrow$$

The outgoing short-wave flux may be given as the product of the incoming shortwave flux and the surface albedo, A_L . The south-facing slopes of most valleys studied had surface cover of bare, often rocky, soil with occasional shrubs or sagebrush. Most of the north-facing slopes were covered with mixed open stands of aspens and evergreen trees. Following Oke's (1978) table of the radiative properties of natural materials, a mixed forest would have an albedo of approximately 0.15, while the south-facing slopes would have an albedo of perhaps 0.30. A minimum albedo for the whole valley could then be estimated at 0.20.

$$(3) \quad L^* = L\downarrow - L\uparrow$$

Using a radiative transfer computational routine described by Cox et al., (1976), McKee and Whiteman (1977) calculated net long-wave radiation from mean Grand Junction, Colorado, rawinsonde soundings, by assuming that the ground radiating temperature was the same as the screen temperature. For an average January sounding the net radiation

loss was 106 W m^{-2} , while for an average July sounding it was 96 W m^{-2} . Following the theoretical radiance calculations for simplified valley topography and considering the effects of radiating sidewalls and temperature inversions, a reasonable minimum value of L^* for the valleys of interest is -90 W m^{-2} .

$$(4) \quad Q_G = a_f Q^*$$

Little information is available from the literature concerning the ground heat flux in situations similar to those encountered in the valleys of western Colorado. However, it is clear from references by Oke (1978) and from Terjung et al., (1969) that the ground heat flux, while time-dependent, is generally a small fraction of Q^* . A reasonable minimum value of Q_G would be $0.15 Q^*$.

$$(5) \quad Q_E = 0$$

An absolute minimum value of Q_E for the dry valleys of western Colorado would be 0. The actual value of Q_E would approach this limit only after long periods with no rain.

An estimate of the maximum value of A_o is obtained with Equation (69) from the values of $K\downarrow$, $K\uparrow$, L , Q_G , and Q_E given above, with the result that

$$A_o = .65 - \frac{76 \text{ W m}^{-2}}{A_1 \text{ W m}^{-2}} . \quad (70)$$

Using this formulation, A_o is a fraction which varies seasonally with the amplitude of the extraterrestrial solar flux. The seasonal dependence of extraterrestrial solar flux at noon, A_1 , is shown in Figure 60. Given this range of A_1 , the probable maximum value of A_o ranges from .53 in winter to .59 in summer.

Simulations of actual data have been accomplished using model Equations (59) through (64) with a time step of 10 minutes. The

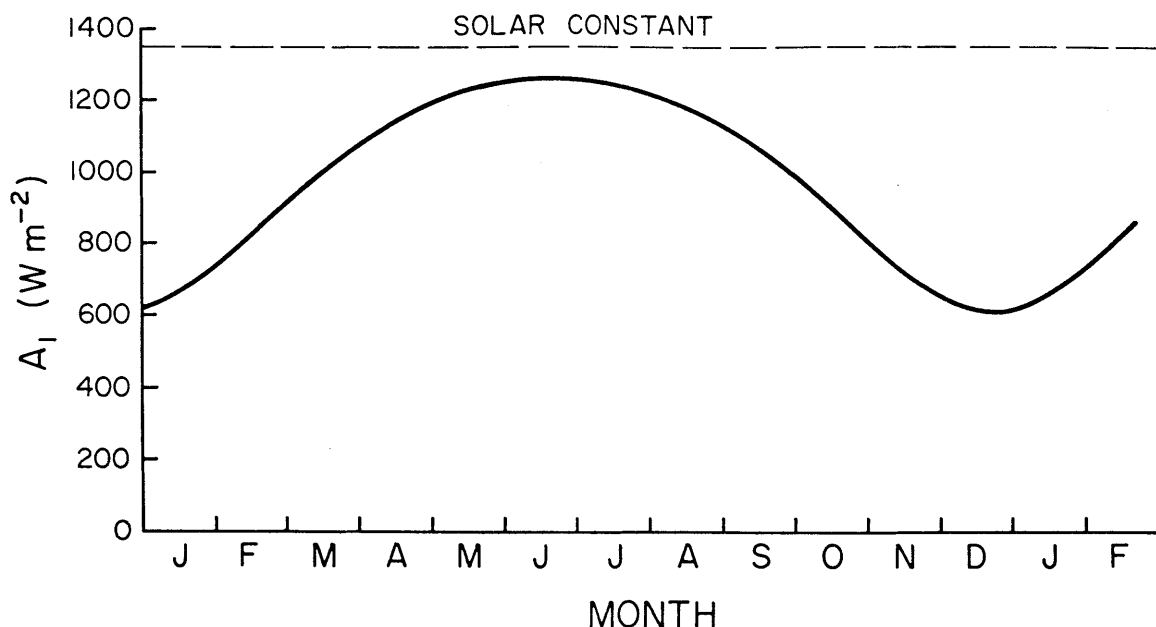


Figure 60. Seasonal dependence of extraterrestrial solar irradiance at solar noon for latitude of Steamboat Springs, Colorado. The value of the solar constant ($1353 W m^{-2}$) is given for reference.

results are presented below for a winter Pattern 2 inversion destruction in the wide Yampa Valley and for a fall Pattern 3 inversion destruction in the Eagle Valley.

1. Pattern 2 Simulation--Yampa Valley, 23 February 1978

The model input parameters required to simulate the Pattern 2 inversion destruction observed in the snow covered Yampa Valley on 23 February 1978, were obtained as follows. First, $\theta T^{-1} = 1.07$ and $\rho c_p = 1040 J m^{-3} K^{-1}$ were calculated using the approximate mean pressure (780 mb) of the early morning inversion and an average temperature of the valley atmosphere ($-10^{\circ}C$) from Equation (2) and the equation of state, respectively. Second, the valley topographic parameters ($\ell = 2580 m$, $\alpha_1 = 9^{\circ}$, $\alpha_2 = 16^{\circ}$, $C = 9.80$) were obtained from topographic maps as recorded in Table 1. Third, the initial inversion parameters

($h_i = 530 \text{ m}$, $\gamma = .0345^\circ\text{K m}^{-1}$) were estimated from a straight line fit to the top of the 0714 MST sounding on this date as recorded in Table 4. The hyperbolic lower region of the sounding could not be adequately fit with a straight line, so it is ignored in the analysis. Fourth, a sinusoidal fit to the extraterrestrial solar flux curve obtained from the solar irradiance model of Appendix E provides solar irradiance parameters ($A_1 = 878 \text{ W m}^{-2}$, $t_i = 0655 \text{ MST}$, $\tau = 10.9 \text{ hours}$). The output of the model for the horizontal surface of interest is presented in Figure 61. For reference, the solar fluxes on extraterrestrial surfaces with the same aspect and inclination angles as the valley sidewalls are indicated on the figure. The input required to run the solar irradiance model of Appendix E includes the Julian date corresponding to February 23rd ($D = 54$), and the latitude and longitude of the Yampa Valley site (Table 1). The remaining parameters necessary to run the inversion destruction model are fractions k and A_0 , and the neutral layer warming rate β . To simulate a Pattern 2 destruction, k must be zero. The neutral layer warmed only 1.1°K during the inversion destruction, for a warming rate, β , of $2.8 \times 10^{-5}^\circ\text{K sec}^{-1}$. The best fit of the model output, $h(t)$, to the inversion top data of Figure 62 was obtained with $A_0 = 0.19$ by a trial-and-error procedure. Using this value, the simulation of the height of the top of the inversion agrees to within 25 m of the data over a 7 hour period. In mid-afternoon, however, the simulation continues to call for the descent of the inversion top, when the actual data indicate that the descent stopped. This is probably due to afternoon shading of the valley by a mountain peak southwest of the site. The model, using a simple sine function to simulate solar flux, does not account for this shading. In Figure 63

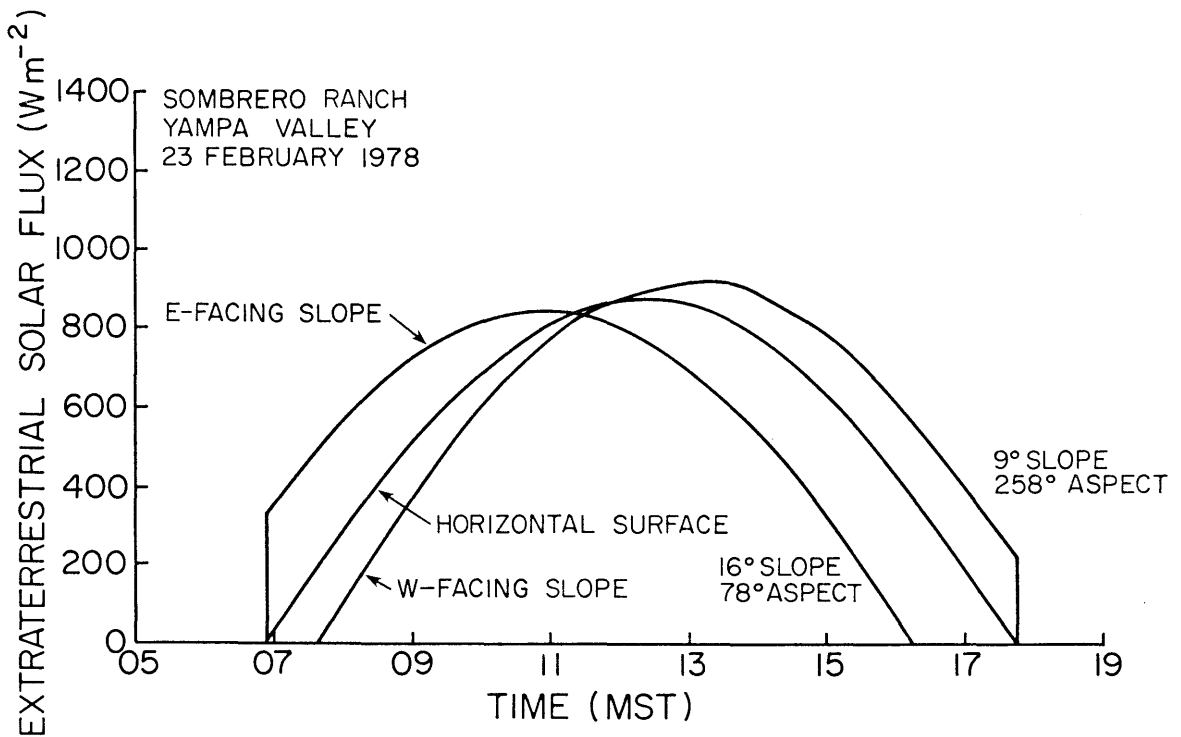


Figure 61. Extraterrestrial solar flux calculated for valley floor and sidewall surfaces of the Yampa Valley, 23 February 1978.

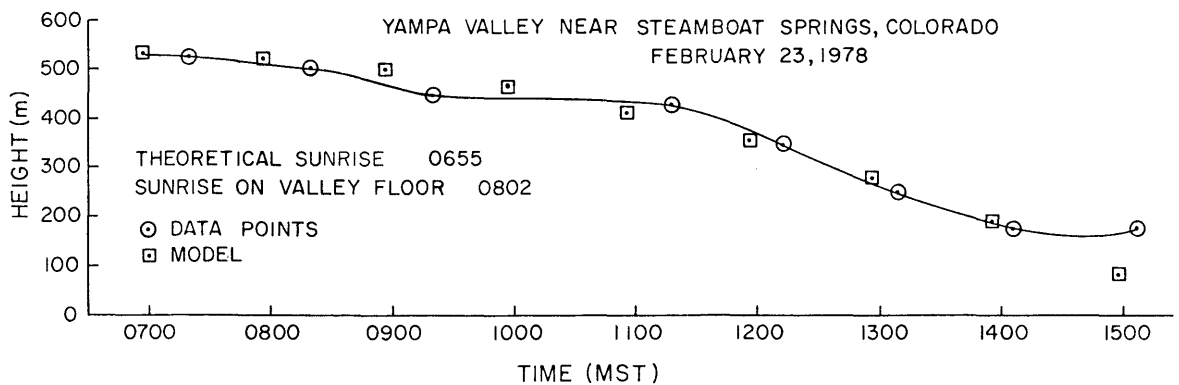


Figure 62. Comparison of model simulation of $h(t)$ with actual data for the Yampa Valley, 23 February 1978.

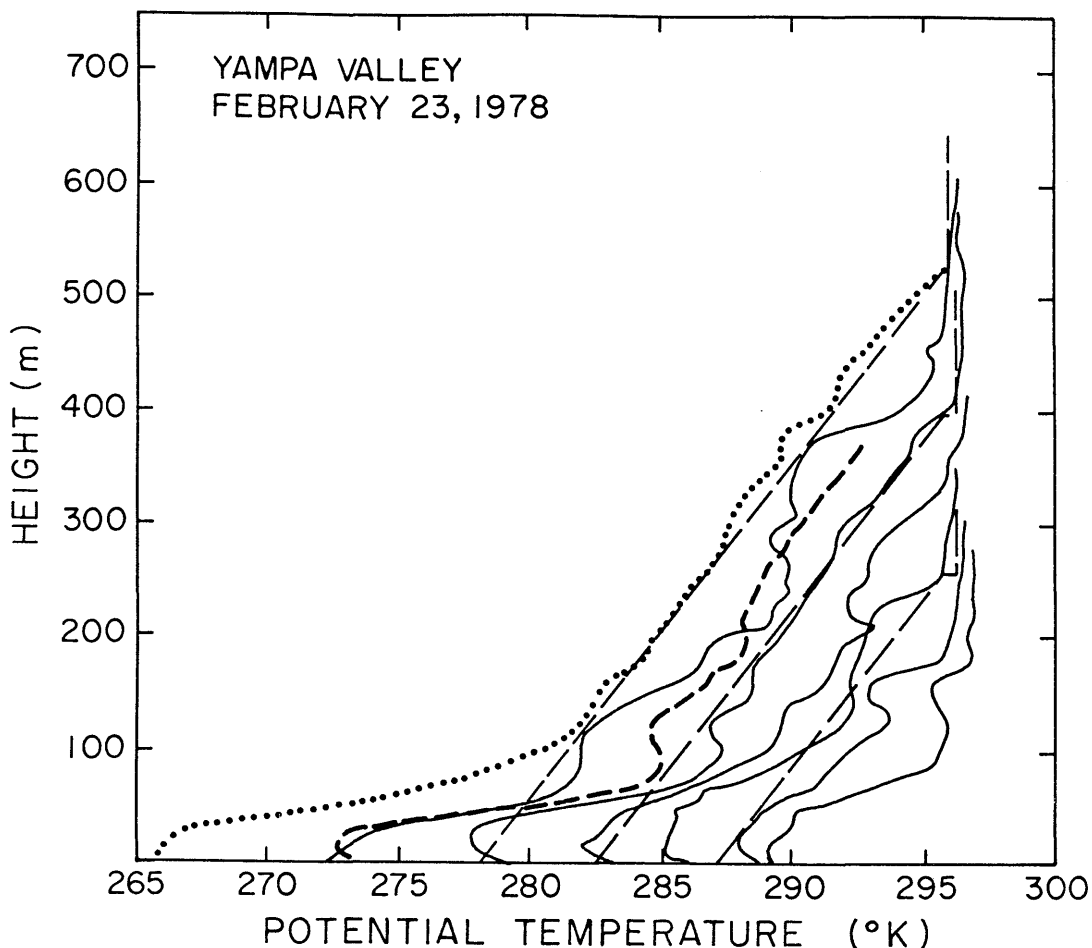


Figure 63. Comparison of model simulation of potential temperature structure with data for the Yampa Valley on 23 February 1978.

the corresponding potential temperature profile simulations are compared to actual sounding data. The sounding data consist of eight consecutive potential temperature soundings taken at approximately one hour intervals throughout the day. The soundings (only the up-soundings are given) were initiated at times 0714, 0905, 0959, 1100, 1202, 1259, 1359, and 1508 MST. The characteristics of the initial inversion were obtained from the 0714 MST sounding and are indicated by the straight line fit to the sounding in the figure. The slow neutral layer warming is also apparent in the figure. The excellent

fit of the model simulations to the data in the stable core above the 50 m deep surface layer is apparent in the 1100 and 1259 MST soundings. The value of A_0 required to obtain these results seems reasonable for the snow covered valley with evergreen forests covering much of the valley sidewall above the observation site. It is particularly interesting that the model assumption of constant potential temperature gradient was satisfied well during the long period of inversion destruction in the complicated topography of the Yampa Valley. The case study is an excellent example of the effect of enhanced albedo due to snow cover in retarding the normal breakup of an inversion. Despite the fact that the temperature inversion was not destroyed on this clear day, the diurnal range of temperature at the ground was quite large.

2. Pattern 3 Simulation--Eagle Valley, 16 October 1977

Pattern 3 inversion breakup in the Eagle Valley is remarkably consistent in all seasons when snow cover is not present in the valley. To test the mathematical model, the Pattern 3 breakup on the clear day of 16 October 1977 is chosen for simulation. The input parameters to the model are obtained as for the Pattern 2 simulation above. Thus, values of the constants θT^{-1} (1.08) and ρc_p ($990 \text{ J m}^{-3} \text{ K}^{-1}$) are determined from the mean pressure (768 mb) and temperature (0°C) of the valley inversion. The valley topographic parameters, $\ell = 1450 \text{ m}$, $\alpha_1 = 21^\circ$, $\alpha_2 = 10^\circ$, and $C = 8.28$, are determined from topographic maps as recorded in Table 1. The initial values of the inversion parameters, $h_i = 650 \text{ m}$ and $\gamma = .0269^\circ\text{K m}^{-1}$, were taken from the 0750-0819 MDT sounding (Table 4), since the pre-sunrise sounding was of insufficient height to determine h_i . The solar irradiance model of Appendix E was

used to determine the parameters $A_1 = 906 \text{ W m}^{-2}$, $t_i = 0721 \text{ MDT}$, and $\tau = 11 \text{ hours}$ (Figure 64). The value of β ($8.3 \times 10^{-5} \text{ }^\circ\text{K sec}^{-1}$) was taken from Table 4 as recorded from valley temperature sounding data.

The fitting of the model output to the data of Figure 65 was accomplished first by choosing the value of k so that the ascending CBL and descending inversion top met at the proper observed height at the time of inversion destruction. The value of A_0 was then varied until the model outputs, $h(t)$ and $H(t)$, fit the data well. The fit in Figure 65 was obtained with $k = 0.14$ and $A_0 = 0.45$. The value of A_0 is realistic considering the dry nature of the valley surface on this date. The equations were integrated from the initial conditions of $h = 650 \text{ m}$ and $H = 10 \text{ m}$ at $t = 0805 \text{ MDT}$ using a time step of 10 minutes. From Figure 65 it is clear that a good fit to the data is obtained with the chosen values of the two parameters A_0 and k . The simulation of CBL height and inversion top height agrees with the data within 50 m over most of the period of inversion destruction. The CBL height was overpredicted early in the inversion period, due to the bulk nature of the model. Following sunrise, the CBLs are developed first over the illuminated sidewall or sidewalls, and CBL growth over the valley floor usually occurs somewhat later, when it is sunlit. The bulk model, however, does not differentiate between CBL growth over the three different valley surfaces. All energy going into CBL growth is attributed, in the model, to growth of the valley floor CBL. Thus, the initial overprediction of CBL growth over the valley floor is a characteristic feature of the model equations. The behavior of the simulation at mid-levels of the valley atmosphere near the time of inversion destruction should also be mentioned. The data typically

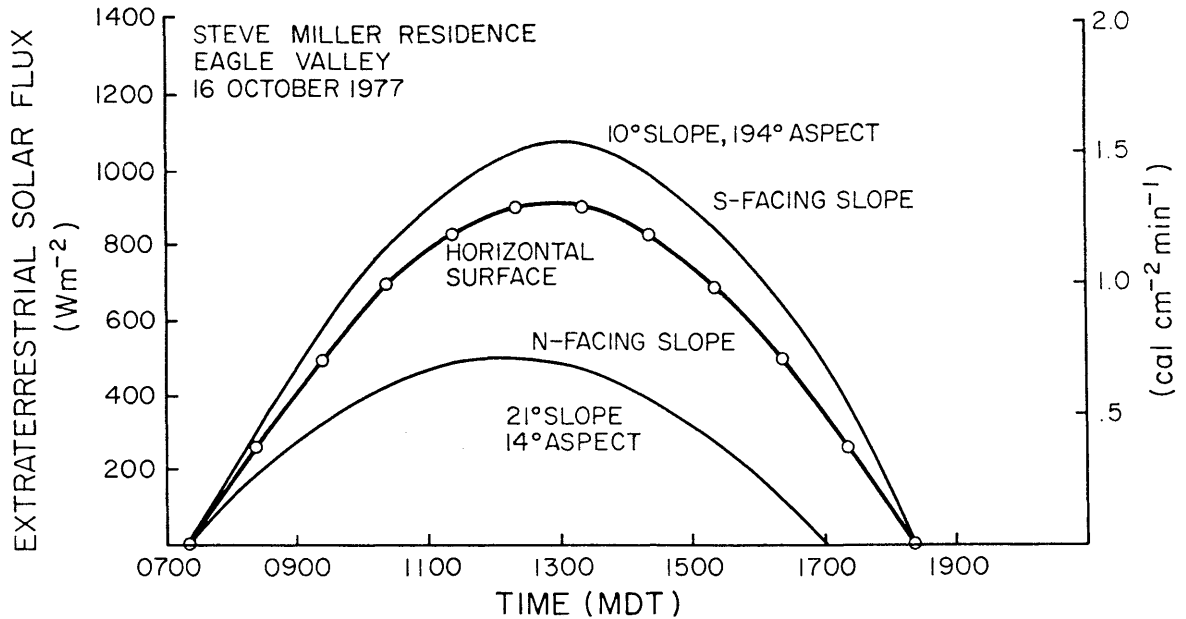


Figure 64. Extraterrestrial solar flux calculated for valley floor and sidewall surfaces of Eagle Valley, 16 October 1977.

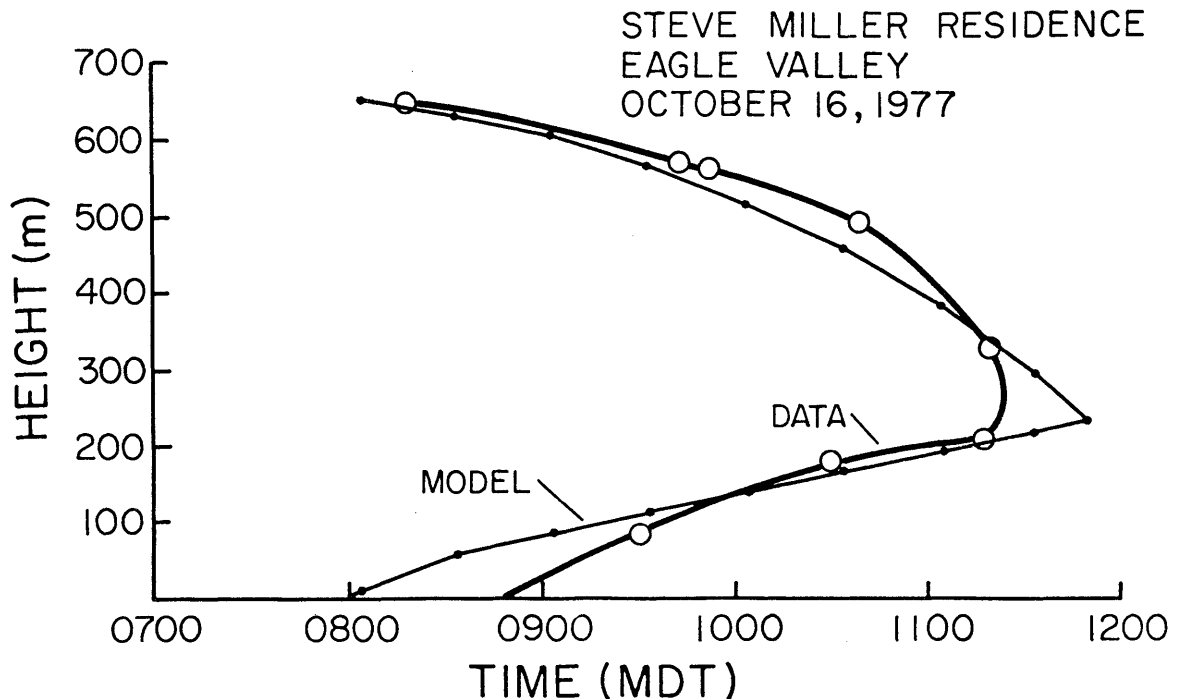


Figure 65. Comparison of model simulation of $H(t)$ and $h(t)$ with actual data for the Eagle Valley, 16 October 1977.

show a more sudden inversion breakup is to be expected in nature since the final remnants of the stable core will break up in convective overturning, once the stable core becomes thin enough and the convective plumes rising from the valley floor become vigorous enough. Due to the chaotic nature of the breakup, actual soundings taken during this time will often show deformations in the vertical potential temperature profiles. Estimates of heights h and H from soundings are difficult to make during this time. A continued flux of energy into this region is necessary before the deformations in the profiles are destroyed and well-organized convection through the entire depth of the valley results in smooth neutral profiles. When this occurs, the breakup can be considered as finished.

The potential temperature profiles corresponding to the data and simulation of Figure 65 are presented in Figure 66. The potential temperature data are from tethersonde up-soundings taken at 0750-0819, 0929-0948, 1024-1048, 1113-1133, and 1206-1221 MDT. The corresponding potential temperature simulations are plotted for the approximate mid-times of the tethersonde up-soundings at 0940, 1035, 1125, and 1215. Again, the model provides a good simulation of the actual data, reproducing the warming and growth of the CBL, the warming of the stable core, and the descent of the inversion top.

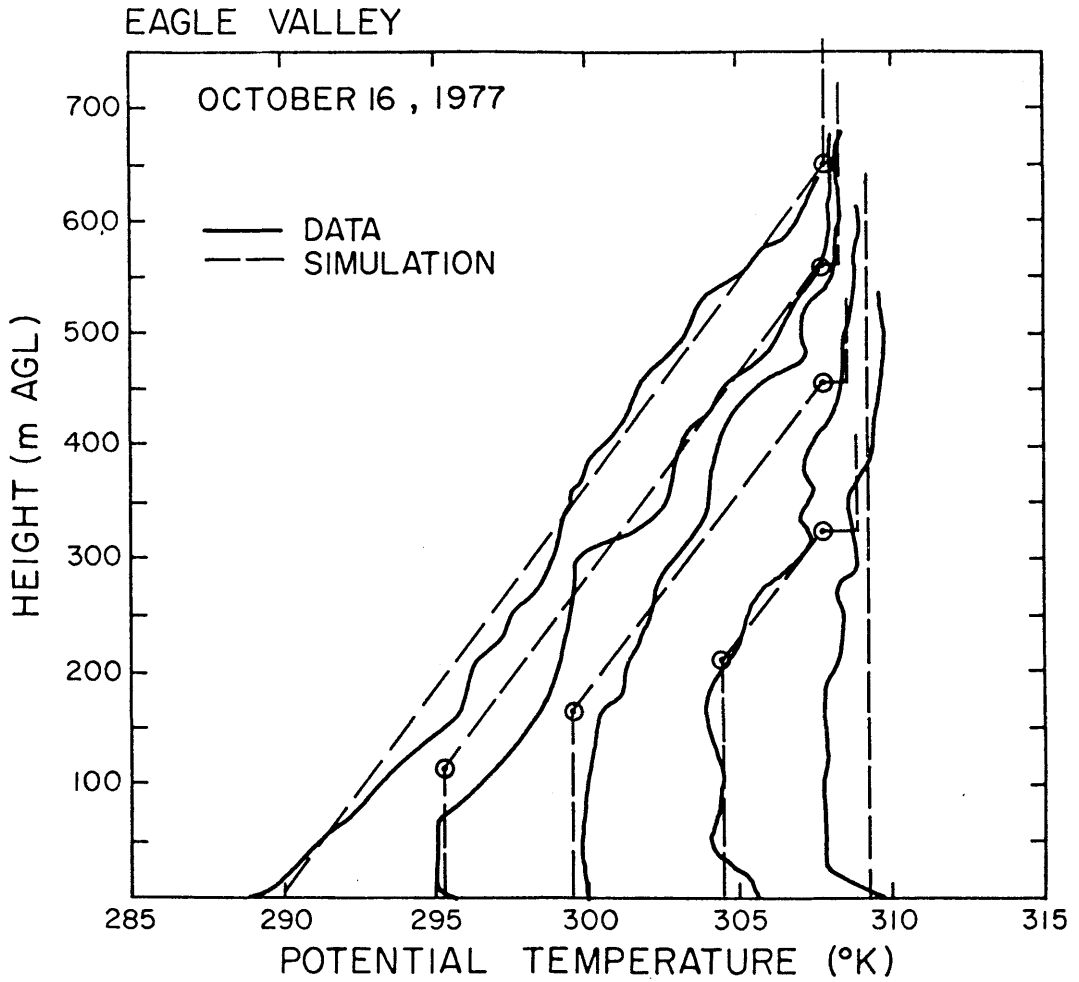


Figure 66. Comparison of model simulation of potential temperature structure with data from the Eagle Valley on 16 October 1977.

Chapter VI

SUMMARY AND CONCLUSIONS

An extensive observational program was conducted in seven valleys of western Colorado to determine how the temperature structure of the valley atmosphere evolves following sunrise during the time when the nocturnal surface-based radiation inversions are destroyed. Experiments were conducted mainly in clear, undisturbed weather in valleys of widely varied topography. A tethered balloon sounding system was used to collect temperature, humidity, pressure, wind speed, and wind direction data.

At sunrise, nocturnal inversions in most of the valleys were built up to about the level of the surrounding ridgetops. The average depth, based on 21 case studies, was 604 m. Vertical potential temperature gradients within the inversions averaged $.0295^{\circ}\text{K m}^{-1}$, but ranged from $.0187$ to $.0566^{\circ}\text{K m}^{-1}$. The strength and direction of prevailing winds aloft, as determined from the Grand Junction, Colorado, morning rawinsonde sounding, had no demonstrable effect on the characteristics of valley inversions and the valley inversions showed much less variability from day to day and season to season than inversions over Grand Junction. This suggests that, at least for a narrow range of synoptic conditions, valley topography produces more consistent inversions, perhaps by protecting them from the winds aloft.

When the along-valley winds were weak, the valley vertical potential temperature profiles frequently were hyperbolic, especially near the ground. This shape was also observed when the valley floor was snow covered. In most valleys where along-valley winds were of at least moderate strength, the inversion profiles were nearly linear with height. Deformations were observed in some of the profiles.

Temperature inversions in all of the valleys investigated were destroyed after sunrise following one of three patterns of temperature structure evolution. The first pattern, observed in the widest valley studied, approximates inversion destruction over flat terrain, in which the nocturnal inversion is destroyed after sunrise by the upward growth from the ground of a warming convective boundary layer. The second pattern, observed in snow covered valleys, differs significantly from the first. Here the growth of the CBL, which begins after sunrise, is arrested once the CBL has attained a depth of 25 to 50 m. The inversion is then destroyed as the top of the nocturnal inversion descends into the valley. Successive profiles of the valley atmosphere show a warming consistent with a simple subsidence of the previous profiles. The third pattern of temperature structure evolution, being a more general case of the first and second patterns, was observed in all the valleys when snow cover was not present and describes the majority of case studies observed in field experiments. Following this pattern, inversions are destroyed by two processes: the continuous upward growth from the valley floor of a warming CBL and the continuous descent of the top of the nocturnal temperature inversion. Warming of the elevated inversion layer above the CBL is consistent with a simple subsidence of the previous profiles. In the Colorado valleys studied, the time required to break an inversion and establish a neutral atmosphere within the valley was typically $3\frac{1}{2}$ to 5 hours after sunrise. Temperature structure evolution during clear, undisturbed weather was surprisingly uniform from day to day and season to season. Thus, in future work, one may be fairly confident of observing typical inversion breakup during short field studies in undisturbed weather.

The common element of all three patterns of temperature structure evolution is the development of a CBL over the valley floor after it is illuminated by direct sunlight. Observations taken from the sidewall of one valley also show the development of a CBL after direct sunlight illuminates the sidewall. Due to the shading effects of surrounding topography, the different valley surfaces can be illuminated at significantly different times, thus affecting the initiation of CBL growth. The temperature structure of the sidewall CBL is similar to that of the CBL over the valley floor, but winds blow up the sidewall CBL at speeds of up to 3 m sec^{-1} . Concurrent observations taken from the center of the valley floor and one sidewall of the Eagle Valley show that the top of the inversion is nearly horizontal across a valley section despite unequal insolation on the opposite sidewalls.

Five different temperature structure layers have been observed during the inversion destruction period. Above the valley floor CBL and the sidewall CBL just mentioned is the stable core of the potential temperature inversion. A neutral stability layer above the stable core appears to be part of a larger scale convective boundary layer that forms over the Western Slope of the Rocky Mountains. Above this layer is the free atmosphere, characterized by a more stable temperature structure.

Each of the five temperature structure layers, while identified primarily by their potential temperature structure, can also be identified by the winds that prevail within them. During inversion destruction, the CBLs over the valley floor and sidewalls contain winds which blow up the floor of the valley and up the slopes. The CBL, or neutral layer, above the valley inversion has winds which blow up the

inclined Western Slope of the Rocky Mountains during the day. Winds in the stable core typically continue to blow down-valley after sunrise at least until the stable core is nearly destroyed. Winds in the stable free atmosphere may blow from any direction with speeds determined by synoptic-scale pressure gradients. A great variability was observed from day to day and from valley to valley in the wind structure within the free atmosphere, the neutral layer, the stable core, and the valley floor CBL. Despite this variability in the strength and timing of reversal of the winds, the temperature structure evolved uniformly from day to day.

On the basis of the wind and temperature observations summarized above, an hypothesis has been developed to explain the temperature structure evolution. Since energy is required to change the temperature structure, and the changes begin at sunrise, it is reasonable to hypothesize that solar radiation is the driving force. A fraction of the solar radiation, received on the valley floor and sidewalls, is converted to the sensible heat flux that provides energy to the valley atmosphere. Sensible heat flux from a surface, as over flat terrain, causes a convective boundary layer to develop over the surface. Penetrative convective plumes entrain mass and heat from the stable core above into the CBL. Mass entrained into the valley floor and sidewall CBLs, however, is carried from the valley in the upslope flows that develop in the convective boundary layers over the sidewalls. This removal of mass from the base and sides of the stable core causes the elevated inversion to sink deeper into the valley and to warm adiabatically due to subsidence, and decreases the rate of growth of the CBLs. Following this hypothesis, the rate of warming depends directly on the

rate of energy input into the valley atmosphere. This energy may be used to deepen the CBLs or to move mass up the sidewalls, allowing the stable core to sink.

From the preceding physical hypothesis, a mathematical model of valley temperature structure evolution has been developed. By differentiating the First Law of Thermodynamics, the rate of energy input into the valley atmosphere is equated to the rate of descent of the inversion top and the rate of ascent of the CBL under the following assumptions:

(1) the potential temperature gradient in the stable core is constant;

(2) the temperature structure is horizontally homogeneous in the cross-valley direction;

(3) the valley topography can be adequately represented by a horizontal valley floor of arbitrary width and two linear sidewalls of arbitrary slope;

(4) the initial inversion at sunrise can be adequately represented by a constant potential temperature gradient layer of arbitrary depth; and

(5) convective boundary layers can be adequately represented as constant potential temperature layers of arbitrary height.

The rate of energy input into the valley atmosphere is approximated as a constant fraction of the solar energy flux (assumed to be a sinusoidal function of time from sunrise to sunset) coming across the horizontal upper surface of the inversion. To complete the model, the partitioning of the energy input into CBL growth and mass transport must be estimated. As a first approximation, it is assumed that a

constant fraction of the energy input is used to cause the CBLs to grow. The remaining energy is used for mass transport in the upslope flows. Energy going into the growth of the CBL causes the CBL depth to increase with time. Energy causing air parcels to flow up the sidewall CBLs results in the descent of the top of the inversion. When most of the available energy drives the growth of the CBLs, a temperature structure evolves in which the inversion is destroyed predominantly by the upward growth of a CBL from the ground. When most of the available energy drives mass up the sidewalls, a temperature structure evolves in which the inversion is destroyed by the descent of the inversion top.

The inputs to the model are:

- (1) the initial inversion characteristics (depth and average potential temperature gradient);
- (2) valley topography (floor width and inclination angles of the two sidewalls);
- (3) the neutral layer potential temperature;
- (4) the rate of energy input;
- (5) the fraction of energy available to increase the depth of the CBL; and
- (6) the neutral layer warming rate.

The model output is the behavior with time of the height of the inversion top and the depth of the CBL. From this output, potential temperature profiles of the valley atmosphere can be constructed for any time in the simulation.

Sensitivity analyses were conducted for the limiting cases of the model. The results indicate that the time required to destroy an inversion depends primarily on the initial height of the inversion, on

its potential temperature gradient, and on the amount of energy available to destroy it. Using a reference simulation in which model parameters were given values typical of valley inversions, inversion destruction took approximately $3\frac{1}{2}$ to $4\frac{1}{2}$ hours after sunrise. These times correspond well with actual observations. Less time is required to destroy a valley inversion than an inversion of like dimensions over the plains, because the available energy is used to warm a smaller volume of air. For the dry valleys of western Colorado, the amount of energy available depends to a large extent on the presence or absence of snow cover or surface moisture in the valley. Valley inversions were destroyed sooner by the growth of a CBL than by the descent of the inversion top. Valley width and inclination angles of the sidewalls had only limited effect on the time required to destroy an inversion. Increased valley width and steeper sidewalls both increased slightly the time required.

The thermodynamic model was used to simulate two specific sets of inversion breakup data for Pattern 2 and 3 temperature structure evolution in the topographically diverse Eagle and Yampa Valleys. Simulations were obtained by fitting two constants in the model (relating to the surface energy budget and energy partitioning) to the data. The model output fit the Pattern 2 inversion breakup in the snow covered Yampa Valley very well using an energy input equal to 19% of the extraterrestrial solar flux on a horizontal surface, and assuming that all of this energy was used to drive the slope flows. A good fit to the Eagle Valley data was obtained using an energy input equal to 45% of the extraterrestrial solar flux and assuming that 14% of this energy was used to cause the valley floor CBL to grow. The remaining energy

was used to remove mass from the valley in the slope flows. The model provides new insights into the evolution of valley temperature structure and quantifies the influence of the various parameters affecting temperature inversion breakup. The model explains the importance of the initial sunrise inversion characteristics; the observed timing of the beginning of inversion destruction; the mean time required to destroy typical inversion in the deep valleys of western Colorado; the weak seasonal dependence of the time period required to destroy the inversions; the effects of snow cover and ground moisture and of valley topography; the patterns of warming observed in the various layers of the temperature structure; the typical observed inversion top descent rates of 40-150 m hr⁻¹; and the retarded growth of the valley CBLs relative to the flat plains case. The thermodynamic model, while implicitly incorporating up-slope mass transport, is able to simulate temperature structure evolution in a wide range of valley topography without taking account of along-valley wind systems.

Perhaps the most significant result of the observational/theoretical approach taken in the research is the confirmation that temperature structures evolve in a similar way in different valleys. It is the author's hope that further basic research will be conducted to determine other similarities in the meteorology of different valleys, so that a broader understanding of valley meteorology can be applied to the solution of Colorado's and the nation's current and future environment problems.

Chapter VII

SUGGESTIONS FOR FUTURE RESEARCH

The research on temperature inversion evolution in deep mountain valleys reported here is a preliminary look at the phenomenon of valley inversion destruction. More questions have been raised by this investigation than have been answered. Further work is needed to test the hypothesis of inversion destruction; to verify, extend, and define the limits of the thermodynamic model of valley inversion destruction; and to investigate further largely unexplored research paths identified in this study.

The proposed inversion destruction hypothesis could be tested by directly measuring the sinking motions postulated in the stable core and the divergence of mass from the valley in the slope flows. Determining mass divergence in the slope flows will be a difficult observational problem, since the upslope flow varies with distance up the sidewall and is known to be unsteady and dependent on the microscale characteristics of the underlying surface. The effects on inversion descent of along-valley mass divergence (i.e., terrain-induced accelerations of the along-valley wind field) and of turbulent erosion of the top of a valley inversion by shear from strong winds aloft should be investigated further.

The present bulk thermodynamic model of inversion destruction, based on experimental data collected by the author, should be further tested against independent data collected in valleys of varied topography. The independent data should include sensible heat flux measurements or, at least, good estimates of sensible heat flux on the various valley surfaces. If the hypothesis of inversion destruction is verified, the model can be used in reverse to deduce information on

the bulk energy budget of the valley surfaces. A means of determining the partitioning of available energy for boundary layer growth and for slope flow transport must be developed. If this is to be accomplished empirically, it will be necessary to observe inversion destruction in valleys of greatly varied widths, since valley width affects the manner in which the inversions are destroyed. Significant improvements in the thermodynamic model can be expected if it becomes possible to predict the rate of warming in the neutral layer above the valley inversion. Finally, the synoptic limits of the bulk thermodynamic model and the modifications required to account for cloud cover or strong upper level wind conditions must be determined.

Further research on the component parts of the valley atmosphere during the period of inversion destruction is needed to clarify their interrelationships and to allow the development of a more detailed mathematical model of inversion destruction. In particular, the development of the sidewall and valley floor CBLs, the stable core, and the neutral region above the stable core must be studied further. The relationships between the temperature and wind structures within and between the individual layers of the valley atmosphere must be understood more fully. An understanding of the relationship between the along-valley winds within the stable core and the evolution of valley temperature structure may be of great practical value in air pollution work. The neutral layer above the stable core also warrants further study. Not only can this layer be expected to affect long-range transport of pollutants, but it also serves as a buffer zone between the gradient winds aloft and the local winds within a valley, thus affecting the coupling and decoupling of valley circulations from the prevailing upper level flow.

Chapter VIII

REFERENCES

- ASHRAE. 1975. Procedure for Determining Heating and Cooling Loads for Computerizing Energy Calculations - Algorithms for Building Heat Transfer Subroutines. New York, American Society of Heating, Refrigerating, and Air Conditioning Engineers, Inc., 173+ p.
- Austin, J. M. 1957. Low-Level Inversions. Final Report, Quarterm. Res. Eng. Command DA 19-129-QM-377, Department of Meteorology, MIT, Cambridge, Mass., 153 p.
- Ayer, H. S. 1961. On the Dissipation of Drainage Wind Systems in Valleys in Morning Hours. J. Meteor., 18(4), pp. 560-563.
- Ball, F. K. 1960a. Control of Inversion Height by Surface Heating. Quart. J. Roy. Meteor. Soc., 86, pp. 483-494.
- Ball, F. K. 1960b. Winds on the Ice Slopes of Antarctica. International Symposium on Antarctic Meteorology, Melbourne (1959), Pergamon Press, pp. 10-13.
- Banta, R., and W. R. Cotton. 1979. Horizontal and Vertical Structure of Diurnal Boundary Layer Flow Patterns Over Mountainous Terrain. Preprint Volume, Fourth Symposium on Turbulence, Diffusion, and Air Pollution, January 15-18, 1979, Reno, Nevada. Published by American Meteorological Society, Boston, MA, pp. 217-224.
- Baynton, H. W. 1975. The FOF Wind Tunnel. Atmos. Tech. 6, pp. 100-104.
- Belmont, A. D. 1958. Lower Tropospheric Inversions at Ice Island T-3. Polar Atmosphere Symposium, Part I, Meteorology Section, Pergamon Press, pp. 215-284.
- Bergen, J. D. 1969. Cold Air Drainage on a Forested Mountain Slope. J. Appl. Meteor. 8(6), pp. 884-895.
- Bernstein, A. B. 1967. A Note on the Use of Cup Anemometers in Wind Profile Experiments. J. Appl. Meteor., 6(2), pp. 280-286.
- Buettner, J. K. and N. Thyer. 1966. Valley Winds in the Mount Rainier Area. Arch. Meteor. Geophys. Bioklimat., Ser. B, 14(2), pp. 125-147.
- Call, D. B. 1978. Personal Communication.
- Call, D. B. and H. W. Baynton. 1975. The FOF Computer-Controlled Environmental Chamber. Atmos. Tech., 6, pp. 105-110.
- Carson, D. J. and F. B. Smith. 1974. Thermodynamic Model for the Development of a Convectively Unstable Boundary Layer. Advances in Geophysics, 18A, pp. 111-124.

- Cox, S. K., M. C. Polifka, K. Griffith, A. Rockwood, and D. Starr. 1976. Radiative Transfer Computational Routines for Atmospheric Science Applications. Department of Atmospheric Science, Colorado State University, Fort Collins, August 1, 1976, 76 p.
- Cross, C. M. 1950. Slope and Valley Winds in the Columbia River Valley. Bull. Amer. Meteor. Soc., 31(3), pp. 79-84.
- Davidson, B. and P. K. Rao. 1958. Preliminary Report on Valley Wind Studies in Vermont, 1957. Final Report, Contract AF 19(604)-1971, AFCRC-TR-58-29, College of Engineering, New York University, 54 p.
- Davidson, B. and P. K. Rao. 1958. Experimental Studies of the Valley-Plain Wind. Int. J. Air Water Pollut., 7(9/10), pp. 907-923.
- Deardorff, J. W., G. E. Willis, and D. K. Lilly. 1969. Laboratory Investigation of Nonsteady Penetrative Convection. J. Fluid Mech., 35, pp. 7-31.
- Defant, F. 1949. Zur Theorie der Hangwinde, Nebst Bemerkungen Zur Theorie der Berg- und Talwinde. Arch. Meteor. Geophys. Bioklimat., Ser. A, 1(3-4), pp. 421-450.
- Defant, F. 1951. Local Winds. Compendium of Meteorology, T. M. Malone, Ed., Boston, American Meteorological Society, pp. 655-672.
- Dickerson, M. H. and P. H. Gudiksen. 1980. The Department of Energy's Atmospheric Studies in Complex Terrain (ASCOT) Program. Proceedings, AMS/APCA Second Joint Conference on Applications of Air Pollution Meteorology, March 24-27, 1980, New Orleans, LA. To be published by the American Meteorological Society, Boston, MA.
- Edinger, J. G. 1963. The Nocturnal Cold Layer in the Tunuyan Valley. Fasciculo 4, Departamento de Meteorologia, Universidad de Buenos Aires, 57 p.
- Ekhart, E. 1934. Neuere Untersuchungen zur Aerologie der Talwinde: Die periodischen Tageswinde in einem Quertale der Alpen, Beitr. Physik fr. Atmos., 21, pp. 245-268.
- Ekhart, E. 1948. De la structure thermique de l'atmosphere dans la montagne. Météorologie, 4(9), pp. 3-26.
- Ekhart, E. 1949. Uber Inversionen in den Alpen. Meteor. Rund., 2 (5/6), pp. 153-159.
- Fleagle, R. G. 1950. A Theory of Air Drainage. J. Meteor., 7(3), pp. 227-232.
- Fox, D. G., G. Wooldridge, T. McKee, and D. Whiteman. 1976. An Experimental Study of Mountain Meteorology. Preprint Volume, Third Symposium on Atmospheric Turbulence, Diffusion and Air Quality, October 19-22, 1976, Raleigh, NC. Published by the American Meteorological Society, Boston, MA.

- Freytag, C. and B. Hennemuth, Eds. 1979. Hangwindexperiment Innsbruck Oktober 1978 - Datensammlung. Wissenschaftliche Mitteilung Nr. 36, Meteorologisches Institut, Universität München, 261 p. (Available from Meteorologisches Institut, Theresienstraße 37, 8000 München 2, West Germany).
- Geiger, R. 1965. The Climate Near the Ground, rev. ed. Cambridge, Harvard University Press, 611 p. (Translated by Scripta Technica, Inc. from the 4th German edition, 1961).
- George, R. L. 1979. Evolution of Mesoscale Convective Systems Over Mountainous Terrain. Atmos. Sci. Pap. No. 318, Colorado State University, 160 p. (Available from Department of Atmospheric Science, Colorado State University, Fort Collins, Colorado 80523).
- Gill, G. C. 1967. On the Dynamic Response of Meteorological Sensors and Recorders. Proceedings of the First Canadian Conference on Micrometeorology, Part I, Meteorological Service of Canada, Toronto, Canada, 27 p.
- Gleeson, T. A. 1951. On the Theory of Cross-Valley Winds Arising from Differential Heating of the Slopes. J. Meteor., 8(6), pp. 398-405.
- Gleeson, T. A. 1953. Effects of Various Factors on Valley Winds. J. Meteor., 10(4), pp. 262-269.
- Hall, F. F., Jr. 1972. Temperature and Wind Structure Studies by Acoustic Echo-Sounding. Remote Sensing of the Troposphere, V. E. Derr, Ed., U.S. Government Printing Office, pp. 18.1-18.26.
- Haltiner, G. J. 1971. Numerical Weather Prediction. New York, John Wiley and Sons, Inc., 317 p.
- Haltiner, G. J. and F. L. Martin. 1957. Dynamical and Physical Meteorology. New York, McGraw-Hill Book Company, Inc., 470 p.
- Hawkes, H. B. 1947. Mountain and Valley Winds with Special Reference to the Diurnal Mountain Winds of the Great Salt Lake Region. Ph.D. dissertation, Ohio State University, 312 p.
- Hewson, E. W. and G. C. Gill. 1944. Meteorological Investigations in Columbia River Valley near Trail, B. C.. Bur. Mines Bull., U.S. Department of Interior, 453, 23-228.
- Hewson, E. W. and R. W. Longley. 1944. Meteorology, Theoretical and Applied. New York, John Wiley and Sons, Inc., 468 p.
- Hindman, E. E., II. 1973. Air Currents in a Mountain Valley Deduced from the Breakup of a Stratus Deck. Mon. Wea. Rev., 101(3), pp. 195-200.
- Holben, B. N. 1975. The Development and Sensitivity Analysis of a Model for Estimating Insolation Climate in Mountainous Topography. Unpublished M.S. Thesis, Department of Earth Resources, Colorado State University, Fort Collins, 159 p.

- Holton, J. R. 1972. An Introduction to Dynamic Meteorology. New York, Academic Press, 319 p.
- Holzworth, G. C. 1964. Mean Maximum Mixing Depths in the Contiguous United States. Mon. Wea. Rev., 92(5), pp. 235-242.
- Holzworth, G. C. 1972. Mixing Heights, Wind Speeds, and Potential for Urban Air Pollution Throughout the Contiguous United States. Office of Air Programs Publication No. AP-101, U.S. Environmental Protection Agency, 118 p.
- Holzworth, G. C. and R. W. Fisher. 1979. Climatological Summaries of the Lower Few Kilometers of Rawinsonde Observations. EPA-600/4-79-026, U.S. Environmental Protection Agency, 141 p. (Available from NTIS, Springfield, VA 22161).
- Kreith, F. and J. F. Kreider. 1978. Principles of Solar Engineering. Washington, D.C., Hemisphere Publishing Corporation, 778 p.
- Leahey, D. M. and J. P. Friend. 1971. A Model for Predicting the Depth of the Mixing Layer Over an Urban Heat Island with Applications to New York City. J. Appl. Meteor., 10, pp. 1162-1173.
- Lenschow, D. H., B. B. Stankov and L. Mahrt. 1979. The Rapid Morning Boundary Layer Transition. J. Atmos. Sci., 36(11), pp. 2108-2124.
- Lettau, H. H. 1967. Small to Large-Scale Features of Boundary Layer Structure Over Mountain Slopes. Proceedings of the Symposium on Mountain Meteorology, Atmos. Sci. Pap. No. 122, Colorado State University, 74 p. (Available from Department of Atmospheric Science, Colorado State University, Fort Collins, Colorado 80523).
- Lilly, D. K. 1968. Models of Cloud-Topped Mixed Layers Under a Strong Inversion. Quart. J. Roy. Meteor. Soc., 94, pp. 292-309.
- MacCready, P. B., Jr. 1966. Mean Wind Speed Measurements in Turbulence. J. Appl. Meteor., 5, pp. 219-225.
- Machalek, A. 1974. Inversionsuntersuchungen in einem Gebirgstal. Wetter und Leben, 26(3), pp. 157-168.
- Manins, P. C. and B. L. Sawford. 1979a. A Model of Katabatic Winds. J. Atmos. Sci., 36, pp. 619-630.
- Manins, P. C. and B. L. Sawford. 1979b. Katabatic Winds: A Field Case Study. Quart. J. Roy. Meteor. Soc., 105, pp. 1011-1025.
- McCullough, E. C. 1968. Total Daily Radiant Energy Available Extraterrestrially as a Harmonic Series in the Day of the Year. Arch. Meteor. Geophys. Bioklimat., Ser. B, 16, pp. 129-143.
- McKee, T. B. and C. D. Whiteman. 1977. Components of Infrared Net Radiation in a Mountain Valley. Atmos. Sci. Pap. No. 279, Colorado State University, 102 p. (Available from Department of Atmospheric Science, Colorado State University, Fort Collins, Colorado 80523).

- Moll, E. 1935. Aerologische Untersuchung periodischer Gebirgswinde in V-förmigen Alpentälern. Beitr. Physik fr. Atmos., 22(3), pp. 177-197.
- Morris, A. L., D. B. Call, and R. B. McBeth. 1975. A Small Tethered Balloon Sounding System. Bull. Amer. Meteor. Soc., 56(9), pp. 964-969.
- Oke, T. R. 1978. Boundary Layer Climates. New York, John Wiley and Sons, 372 p.
- Petkovsek, Z. 1973. Vergleichen der lokalen Temperaturänderungen im Gebirgsgebiete, Flachland und freie Atmosphäre. Meteorologie, 10-11, pp. 135-150.
- Petkovsek, Z. 1978. Deformationen der Temperaturprofile in kleinen Talbecken. Arb. ZentAnst. Meteor. Geophys. (Vienna), 31, pp. 85/1-85/7.
- Petkovšek, Z. and A. Hočevár. 1971. Night Drainage Winds. Arch. Meteor. Geophys. Bioklimat., Ser. A, 20, pp. 353-360.
- Pollak, L. W. 1924. Berg und Talwind von Trient. Meteor. Z., 41, pp. 18-24.
- Prandtl, L. 1942. Führer durch die Strömungslehre. Braunschweig, Vieweg und Sohn, 382 p.
- Quiroz, R. S. 1956. An Annotated Bibliography on Temperature Inversions in the Troposphere. Meteor. Abstr. Bibliogr., 7(6), pp. 742-789.
- Rao, P. K. 1960. Observations and Theory of Local Wind Systems. Quarterly Report No. 5, Contract DA-36-039 SC 78127, College of Engineering, New York University, 19 p.
- Rayment, R. and C. J. Readings. 1974. A Case Study of the Structure and Energetics of an Inversion. Quart. J. Roy. Meteor. Soc., 100, pp. 221-233.
- Reid, J. D. 1976. Dispersion in a Mountain Environment. Atmos. Sci. Pap. No. 253, Colorado State University, 150 p. (Available from Department of Atmospheric Science, Colorado State University, Fort Collins, Colorado 80523).
- Schnelle, F., Ed. 1963. Frostschutz im Pflanzenbau. München, BLV-Verlagsgesellschaft mbH, Vol. 1, 480+ p.
- Scorer, R. S. 1958. Natural Aerodynamics. Pergamon Press, 313 p.
- Scorer, R. S. 1973. Pollution in the Air-Problems, Policies and Priorities. London, Routledge and Kegan Paul Ltd., 148 p.
- Sellers, W. D. 1965. Physical Climatology. Chicago, The University of Chicago Press, 272 p.

- Sterten, A. K. 1963. A Further Investigation of the Mountain and Valley Wind System in South-Eastern Norway. Intern Rapport K-254, Forsvarets Forskningsinstitut, Norwegian Defence Research Establishment, Kjeller, Norway, 51 p.
- Sterten, A. K. and J. Knudsen. 1961. Local and Synoptic Meteorological Investigations of the Mountain and Valley Wind System. Intern Rapport K-242, Forsvarets Forskningsinstitut, Norwegian Defence Research Establishment, Kjeller-Lillestrøm, Norway, 139 p.
- Streten, N. A., N. Ishikawa and G. Wendler. 1974. Some Observations of the Local Wind Regime on an Alaskan Arctic Glacier. Arch. Meteor. Geophys. Bioklimat., Ser. B, 22, pp. 337-350.
- Stull, R. B. 1973. Inversion Rise Model Based on Penetrative Convection. J. Atmos. Sci., 30(6), pp. 1092-1099.
- Tennekes, H. 1973. A Model of the Dynamics of the Inversion Above a Convective Boundary Layer. J. Atmos. Sci., 30(4), pp. 558-567.
- Tennekes, H. and A. P. van Ulden. 1974. Short Term Forecasts of Temperature and Mixing Height on Sunny Days. Preprints, Symposium on Atmospheric Diffusion and Air Pollution. September 9-13, 1974, Santa Barbara, California. Published by the American Meteorological Society, Boston, MA, 434 p.
- Terjung, W. H., R. N. Kickert, G. L. Potter, and S. W. Swarts. 1969. Terrestrial, Atmospheric and Solar Radiation Fluxes on a High Desert Mountain in Mid-July: White Mountain Peak, California. Solar Energy, 12, pp. 363-375.
- Thyer, N. H. 1966. A Theoretical Explanation of Mountain and Valley Winds by a Numerical Method. Arch. Meteor. Geophys. Bioklimat., Ser. A, 15(3-4), pp. 318-348.
- Thyer, N. H. and K. J. K. Buettner. 1962. Part A: On Valley and Mountain Winds III (Thyer and Buettner), Part B: Valley Wind Theory (Thyer). Final Report, Geophysics Research Directorate, Contract AF 19(604)-7201, AFCRL-62-1082, Department of Atmospheric Sciences, University of Washington, 203 p.
- United States Air Force. 1969. Use of the Skew T, Log P Diagram in Analysis and Forecasting. (Available from Air Weather Service, Scott Air Force, Illinois 62225, AWS Manual 105-124).
- Urfer-Henneberger, C. 1964. Wind- und Temperaturverhältnisse an ungestörten Schönwettertagen im Dischmatal bei Davos. Mitt. Schweiz. Anst. Forstl. Versuchsw., 40(6), pp. 389-441.
- Urfer-Henneberger, C. 1970. Neuere Beobachtungen über die Entwicklung des Schöwetterwindsystems in einem V-förmigen Alpentale (Dischmatal bei Davos). Arch. Meteor. Geophys. Bioklimat., Ser. B, 18, pp. 21-42.
- Wagner, A. 1932. Hangwind - Ausgleichsströmung - Berg- und Talwind. Meteor. Z., 49(6), pp. 209-217.

- Wagner, A. 1938. Theorie und Beobachtung der periodischen Gebirgswinde. Gerlands Beitr. Geophys. (Leipzig), 52, pp. 408-449.
- Waugh, A. E. 1973. Sundials: Their Theory and Construction. New York, Dover Publications, Inc., 228 p.
- Whiteman, C. D. and T. B. McKee. 1977. Observations of Vertical Atmospheric Structure in a Deep Mountain Valley. Arch. Meteor. Geophys. Bioklimat., Ser. A, 26, pp. 39-50.
- Whiteman, C. D. and T. B. McKee. 1978. Air Pollution Implications of Inversion Descent in Mountain Valleys. Atmos. Environ., 12, pp. 2151-2158.
- Whiteman, C. D. and T. B. McKee. 1979. Temperature Inversion Destruction in Mountain Valleys-Implications for Air Pollution Dispersion. To appear in Proceedings, NATO/CCMS Air Pollution Pilot Study, 10th International Technical Meeting on Air Pollution Modeling and Its Application. Rome, Italy, October 23-26, 1979.
- Whiteman, C. D. and T. B. McKee. 1980. A Time-Dependent Model of Temperature Inversion Structure in Mountain Valleys. Proceedings, AMS/APCA Second Joint Conference on Applications of Air Pollution Meteorology. March 24-27, 1980, New Orleans, LA. To be published by the American Meteorological Society, Boston, MA.
- Williams, L. D., R. G. Barry and J. T. Andrews. 1972. Application of Computed Global Radiation for Areas of High Relief. J. Appl. Meteor., 11(3), pp. 526-533.
- Yamada, T. and S. Berman. 1979. A Critical Evaluation of a Simple Mixed-Layer Model with Penetrative Convection. J. Appl. Meteor., 18(6), pp. 781-786.
- Yoshino, M. M. 1975. Climate in a Small Area. Tokyo, University of Tokyo Press, 549 p.

APPENDIX A

Topographic Maps of Valley Experimental Areas

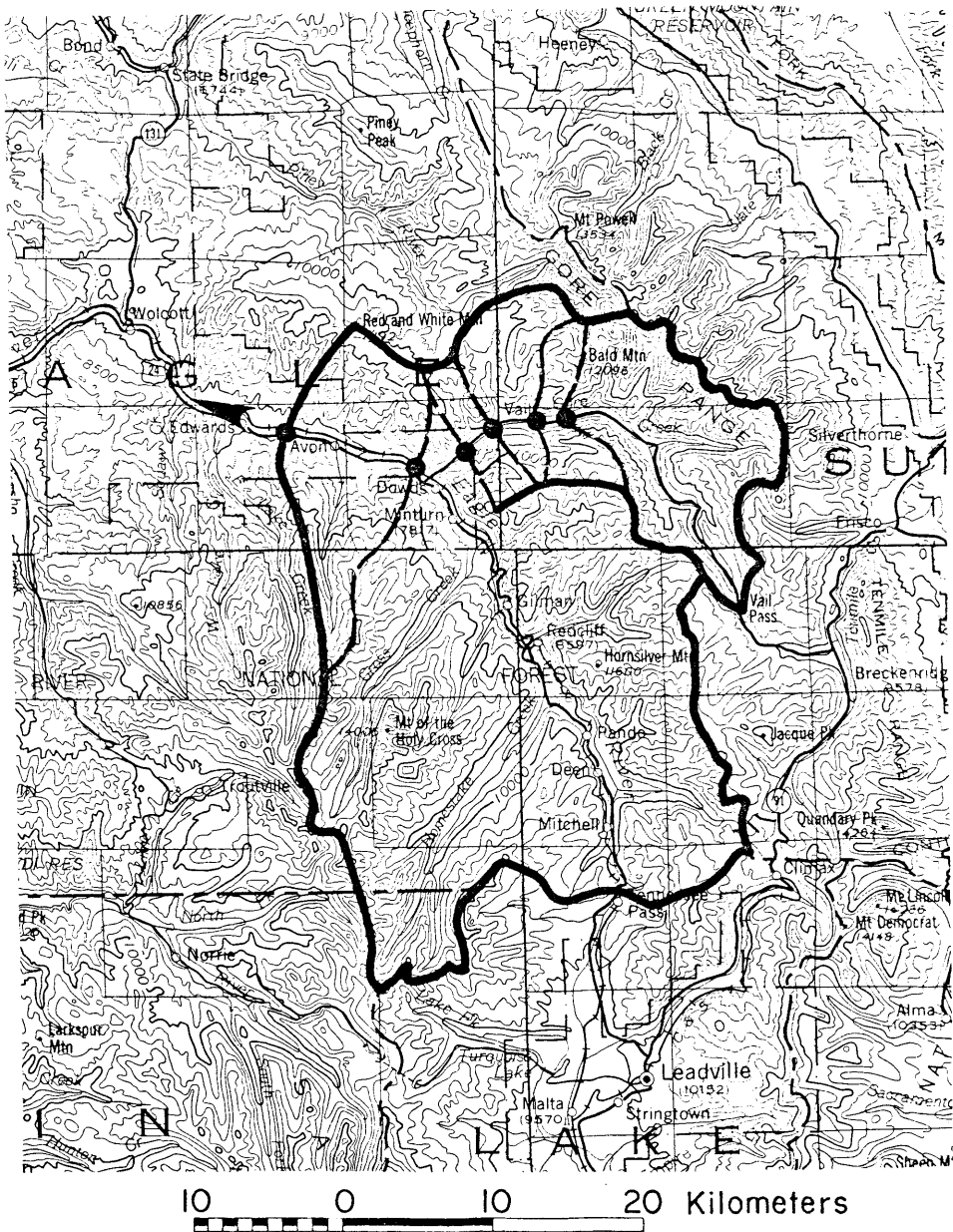


Figure 67. Topographic map of Eagle and Gore Valleys. North is at the top of the figure. Contour interval is 500 feet. The first dot on the left indicates the location of the Steve Miller Residence and the Ray Miller Ranch (sites 8 and 9, Table 1). The remaining dots indicate (left to right) sites 13, 14, 15, 16 and 17.

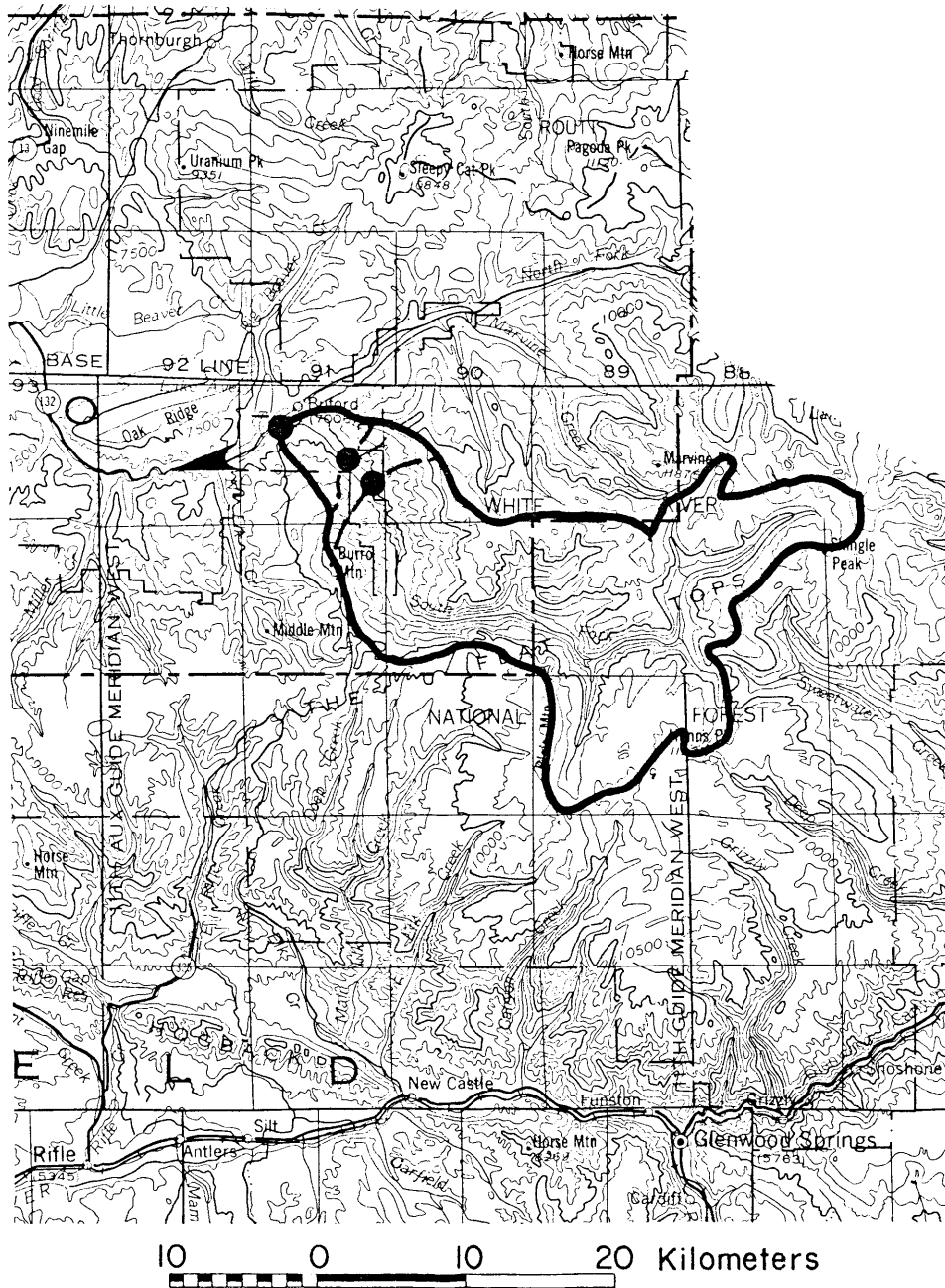


Figure 68. Topographic map of South Fork of White Valley. North is at the top of the figure. Contour interval is 500 feet. The three dots (left to right) indicate sites 4, 5 and 6, Table 1.

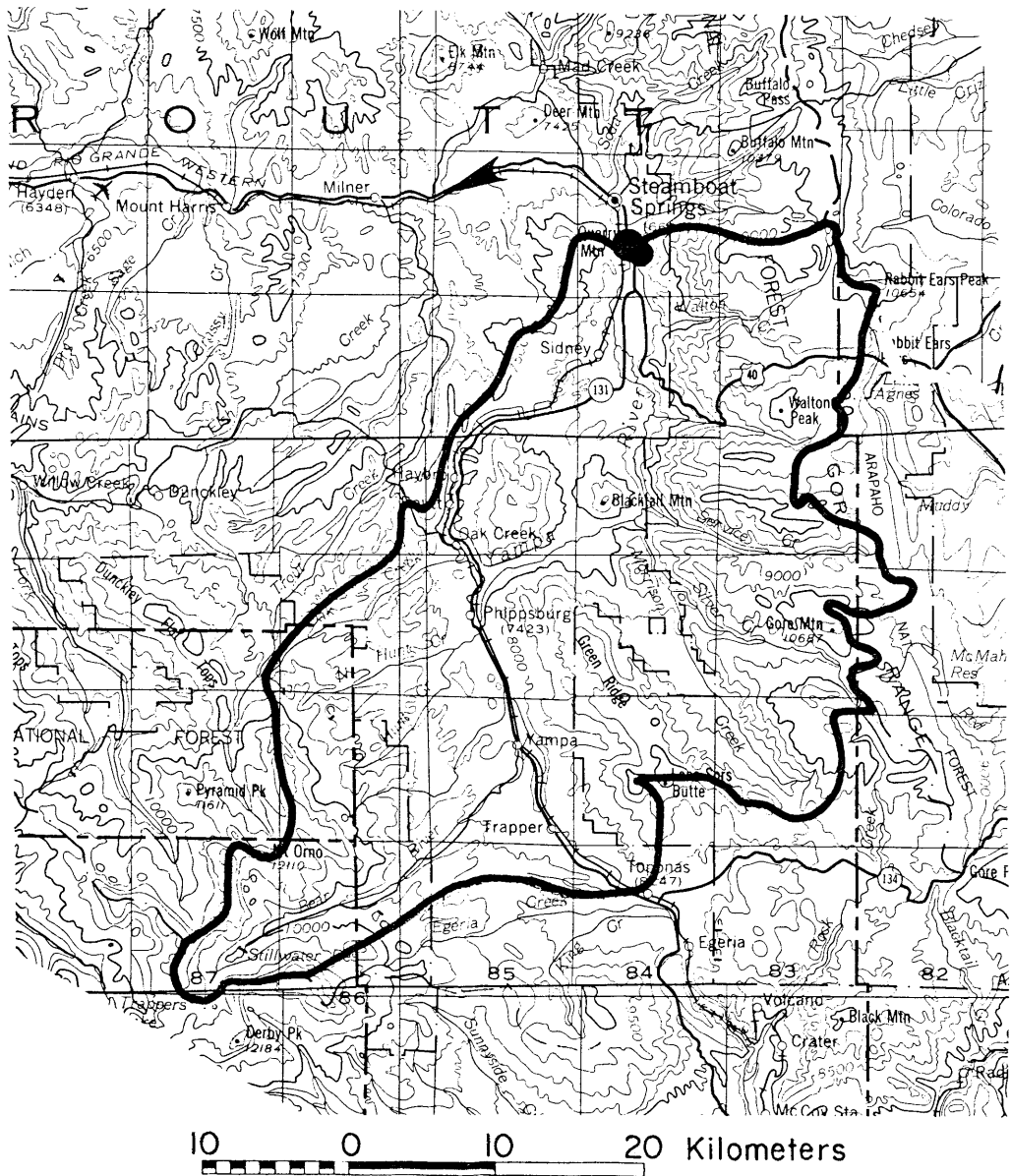


Figure 69. Topographic map of Yampa Valley. North is at the top of the figure. Contour interval is 500 feet. The two dots (left to right) indicate sites 2 and 3, Table 1.

APPENDIX B

Tests of Tethersonde Data Collection System

APPENDIX B

Tests of Tethersonde Data Collection System

Tests of the operating characteristics of the Tethersonde® data collection system¹ were performed using NCAR facilities in Boulder, Colorado. Wind speed sensor tests were conducted in the NCAR Wind Tunnel Test Facility (Baynton, 1975), and temperature and pressure sensor tests were performed using the NCAR Computer-Controlled Environmental Chamber (Call and Baynton, 1975). Photographs of these test facilities are presented as Figures 70, 71, and 72. The purpose of the tests were to determine independently the operating characteristics of the tethersonde system over a range of normal atmospheric conditions so that the data collected with the system could be properly evaluated. To accomplish this, the final data as processed by the entire system (sensor plus system plus processing) should be compared with the ambient atmospheric values of meteorological variables. A controlled environment in which the value of the meteorological variable is known and can be carefully varied is therefore necessary.

A. Wind Speed

In actual use the wind speed sensor is exposed to ambient winds while hanging from a tethered balloon. It is exposed to both steady and fluctuating winds. In turbulent conditions the sensor may swing back and forth below the balloon and, under some conditions, be moving with a balloon that is drifting with the prevailing wind.

Four tests of wind speed system performance were conducted in the NCAR Wind Tunnel Facility. In the first test the airborne package was

¹Airborne package Model TS-1A-1-23,
Ground station Model TS-1A-1, S/N 23, Atmospheric Instrumentation
Research Co., Boulder, CO 80303.



Figure 70. NCAR Wind Tunnel. Photo courtesy of NCAR.

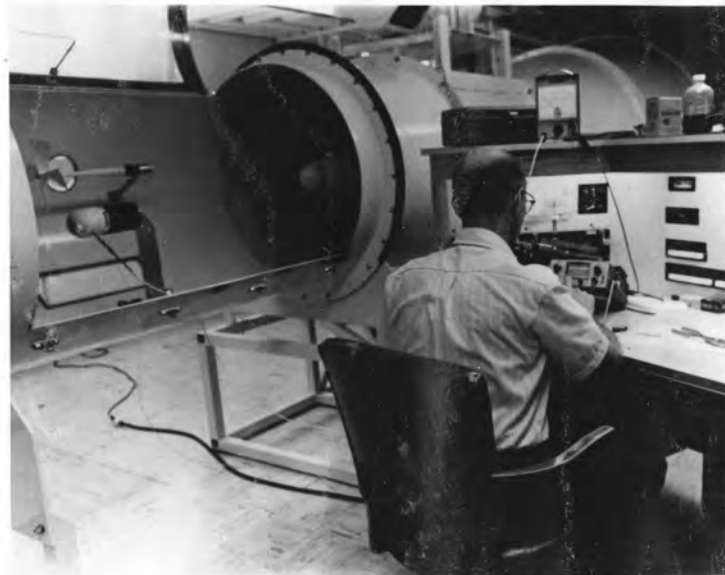


Figure 71. Closeup of test section of NCAR Wind Tunnel. Control panels are on the operator's console at right. Photo courtesy of NCAR.

Figure 72. NCAR Computer-Controlled Environmental Chamber. The one-cubic-meter chamber is on the left and the computer controller is on the right. Photo courtesy of NCAR.

mounted vertically in the wind tunnel so that it presented the smallest cross-sectional area to the airflow (its normal operating configuration), and the ambient flow in the tunnel was stepped up from zero to 12 m sec^{-1} at 2 m sec^{-1} intervals. The airflow in the tunnel was allowed to stabilize at the desired air speed before tethersonde readings were taken. Similar air speed steps were taken as the speed was reduced to zero. The results of these tests are shown in Figure 73. Digital data from the tethersonde are accurate to $.3 \text{ m sec}^{-1}$ over the speed range of $0\text{-}12 \text{ m sec}^{-1}$, reading somewhat too low at the lower wind speeds and somewhat too high at the higher wind speeds. Note that the tethersonde reads somewhat higher during the downsteps than during the upsteps, suggesting that the tethersonde and wind tunnel had not been allowed to come to a full equilibrium when the readings were made.



Figure 72. NCAR Computer-Controlled Environmental Chamber. The one-cubic-meter chamber is on the left and the computer controller is on the right. Photo courtesy of NCAR.

mounted vertically in the wind tunnel so that it presented the smallest cross-sectional area to the airflow (its normal operating configuration), and the ambient flow in the tunnel was stepped up from zero to 12 m sec^{-1} at 2 m sec^{-1} intervals. The airflow in the tunnel was allowed to stabilize at the desired air speed before tethersonde readings were taken. Similar air speed steps were taken as the speed was reduced to zero. The results of these tests are shown in Figure 73. Digital data from the tethersonde are accurate to $.3 \text{ m sec}^{-1}$ over the speed range of $0\text{-}12 \text{ m sec}^{-1}$, reading somewhat too low at the lower wind speeds and somewhat too high at the higher wind speeds. Note that the tethersonde reads somewhat higher during the downsteps than during the upsteps, suggesting that the tethersonde and wind tunnel had not been allowed to come to a full equilibrium when the readings were made.

The second test was designed to measure the threshold or starting speed of the cup assembly. In this test the airflow in the wind tunnel was increased very slowly from zero, and the speed at which the cups just started to turn was recorded. Several determinations gave values ranging from 0.4 to 0.7 m sec⁻¹. The lower starting speed occurred when one of the cups was directly facing the flow. A reverse procedure determined the stopping speed to be 0.3 m sec⁻¹.

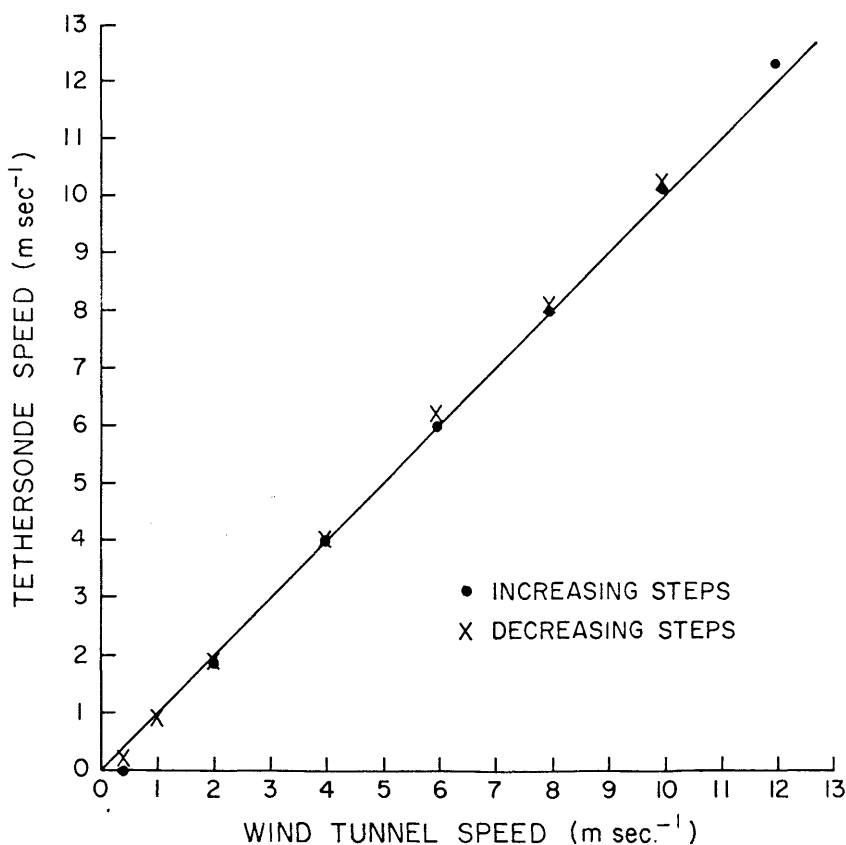


Figure 73. Comparison of tether sonde wind speed data to wind tunnel data.

A third test was conducted to measure the response of the tether sonde wind system to stepwise increases and decreases in wind speed. A fast-response strip chart recorder was used with the ground station for these determinations. In this test the anemometer cups

were held stationary by inserting a long rod into the wind tunnel while the speed in the tunnel was increased to 10 m sec^{-1} . The cups were then released and were observed to speed up quickly to the ambient tunnel wind speed. Two determinations resulted in time constant calculations of 0.31 and 0.53 seconds, corresponding to distance constants of 3.1 and 5.3 meters, respectively. A well-known characteristic of cup anemometers is their differing rate of response to accelerating and decelerating wind speeds (MacCready, 1966; Bernstein, 1967). The cups are known to respond more quickly to accelerating winds than to decelerating winds with the result that the average wind speed measured by a cup anemometer in a gusty or turbulent wind regime will be somewhat too high.

The final test was designed to measure the effect of the angle of attack of the anemometer on the accuracy of wind speed data. In this test the central axis about which the cups rotate was tilted forward into the airflow at three different angles - 10, 20, and 30 degrees. For each of these angles the airflow in the tunnel was stepped up to 9 m sec^{-1} . At each step the readings of the tethersonde system were compared to the measured airflow in the tunnel. Unfortunately, due to the physical environment of the tunnel it was difficult to measure the angles of attack accurately. Nevertheless, tethersonde measurements of air speed were consistently lower than true air speed in the tunnel, roughly by a factor of the cosine of the angle of attack, as expected from theory. As an example, in a 10 m sec^{-1} horizontal wind the airborne tethersonde package, if tilted 30° from the vertical, will measure a wind speed of approximately 8.7 m sec^{-1} (i.e., $10 \cos 30^\circ$).

Tethersonde wind speed data are also affected by the movement of the balloon. This effect, not tested in the wind tunnel, is noticeable

in the tethersonde data when ambient wind speeds are greater than about 5 m sec^{-1} . The aerodynamic drag of the balloon in strong winds often causes the balloon to drift downwind on an up-sounding. When the balloon is retrieved, the winch must pull the balloon up-wind as well as downwards. The translational speed of the balloon thus acts to produce wind speed data that are too low during ascent and too high during descent. Impressions of the balloon trajectory under strong winds are presented in schematic form in Figure 74. The important feature of this trajectory is the fact that the balloon, on descent, tends to maintain its elevation until it gets nearly above the site. The difference in the balloon trajectories of the up- and down-soundings argues against simply averaging the two soundings to get a mean wind profile. The lack of data on the variable wind speed and actual balloon trajectories precludes determination of a numerical correction to the data. Consequently the data are left in an uncorrected form. Fortunately, most wind data collected in the observational program were for wind speeds below 5 m sec^{-1} where the effect is minimized. For wind speeds above 5 m sec^{-1} the effect can be easily detected by comparing wind speed measurements of the up- and down-soundings.

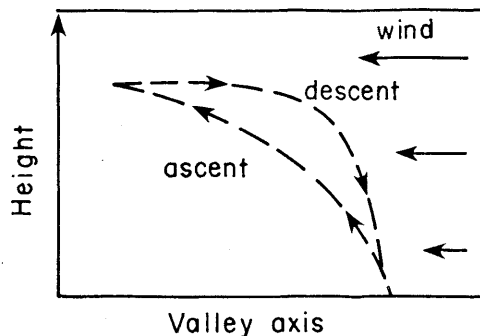


Figure 74. Tethersonde balloon trajectory in strong winds.

B. Wind Direction

Tethersonde measurement of wind direction relies on the balloon being an effective wind vane. The airborne package is suspended below the balloon on a wide rope ladder which is torsionally rigid. The package may swing forwards or backwards in gusty winds but will not twist very far from the orientation of the balloon. Wind direction is measured by means of a magnetic compass which is mounted on the floor of the airborne package. When wind direction is to be sensed, an electromagnetic field locks the compass needle, which is pointing north, to a potentiometer winding which is fixed in the base of the compass and turns with the balloon. The resistance of the potentiometer winding then is a direct indication of wind direction. The compass needle, floating in a viscous oil, will have a characteristic response time to a change in balloon orientation. The balloon itself will have certain characteristics normally attributed to a more conventional wind vane such as a damping coefficient and a response time (Gill, 1967). While these characteristics were not measured directly, some impressions of the balloon's behavior as a wind vane were gained in the field during the course of the research.

First, the balloon seemed to be quite responsive to the very light steady winds frequently encountered within valley temperature inversions. Even when the wind speed was insufficient to turn the anemometer cups the balloon seemed to respond well to prevailing wind direction. It must, however, be kept in mind that the response of the balloon to small directional eddies is limited by the dimensions of the balloon. The effect of the long balloon is to cut down the response of the system to eddies smaller than about half the length of the balloon

(Figure 75). Secondly, in normal profiling operations the balloon seemed to respond rather slowly to large step-wise changes in wind direction. For example, when ascending through a zone in which winds changed 180° , the tethered balloon often maintained its original orientation and drifted over the profiling site until a tight tether line was encountered and the balloon turned and oriented itself to the new wind direction (Figure 76). Finally, when the balloon was flown in turbulent convective conditions, the package would swing significantly and some twisting of the airborne package occurred, perhaps as much as 20° away from the balloon orientation. Few episodes of turbulence were encountered in the field experiments, however, since the balloon was flown predominantly in stable atmospheric conditions.

No quantitative tests of the tethersonde wind direction system were conducted while the sonde was attached to the balloon in its normal profiling mode of operation. However, a quantitative test of wind direction accuracy was performed on the ground using the airborne package. In this test the sonde was oriented in various directions using a magnetic compass. The tethersonde indications of direction were then compared to the magnetic orientation of the sonde. The results, shown in Figure 77, show that the tethersonde indications of direction are accurate to within 4° over the entire 360° range. The largest errors appear near magnetic north. Presumably this is due to a gap in the potentiometer winding at this position. The actual wind direction accuracy for the sonde in its normal operating position will be a complicated function depending on the response time and damping coefficient of the balloon, the response time of the tethersonde compass, the angle of attack of the sonde, and the swinging and twisting of the tethersonde relative to the balloon.

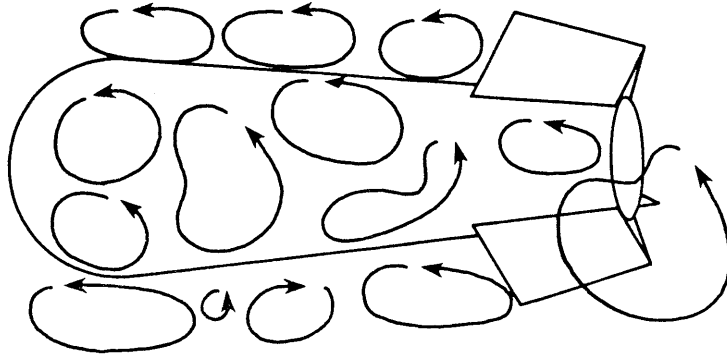


Figure 75. The tethered balloon does not respond to eddies less than about $\frac{1}{2}$ the size of the balloon.

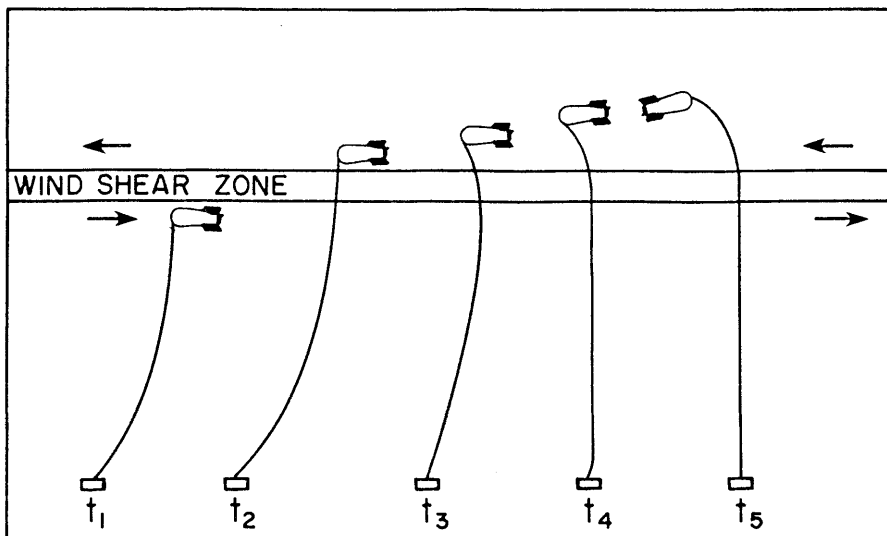


Figure 76. The balloon may respond slowly to a 180 degree wind direction change when profiling. The balloon may drift overhead, and change direction only when a tight tether line is encountered.

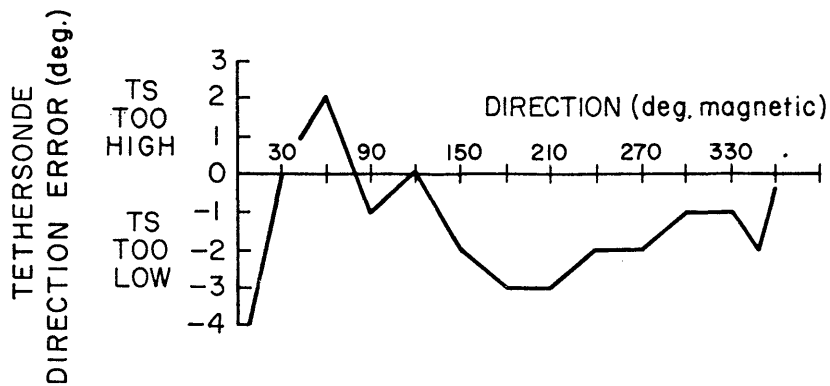


Figure 77. Test of tethersonde wind direction data.

C. Dry and Wet Bulb Temperature

Bead thermistors are the temperature sensors used in the tethersonde airborne package. The sensors are exposed in a horizontally-oriented radiation shield that consists of two concentric plastic tubes painted with a white coating that reflects solar radiation. The inner tube is largely thermally isolated from the outer tube since the inner tube is held in place inside the larger diameter tube by means of six small stand-off insulators. Ambient air is drawn through the two tubes by means of a small electric fan attached to the back of the larger diameter tube. The fan's speed is sufficient to draw air past the thermistors at the rate of $2\text{-}3 \text{ m sec}^{-1}$ (Call, pers. comm., 1978). The two bead thermistors are located on the central axis of the inner tube. The first thermistor exposed to the airstream, hereafter called the dry bulb thermistor, is a bare, white, bead thermistor. Several centimeters behind the dry bulb thermistor is an identical thermistor that is covered with a close-fitting wick which is connected

to a reservoir of distilled water by means of a cotton cord. This thermistor is the wet bulb thermistor. Wet and dry bulb temperatures are used to calculate ambient humidity variables by means of standard psychrometric formulas.

Two tests were performed on the dry bulb temperature sensor. In the first test the tethersonde airborne package was placed in the NCAR Environmental Chamber, and temperature steps were accomplished at constant pressure, allowing sufficient time at each step for an equilibrium to be established between the chamber and the tethersonde. Temperatures indicated by the two systems were then compared. Results are shown in Figure 78. The comparisons show that the two instrument systems agree within 0.8°C over a 30°C range of temperature.

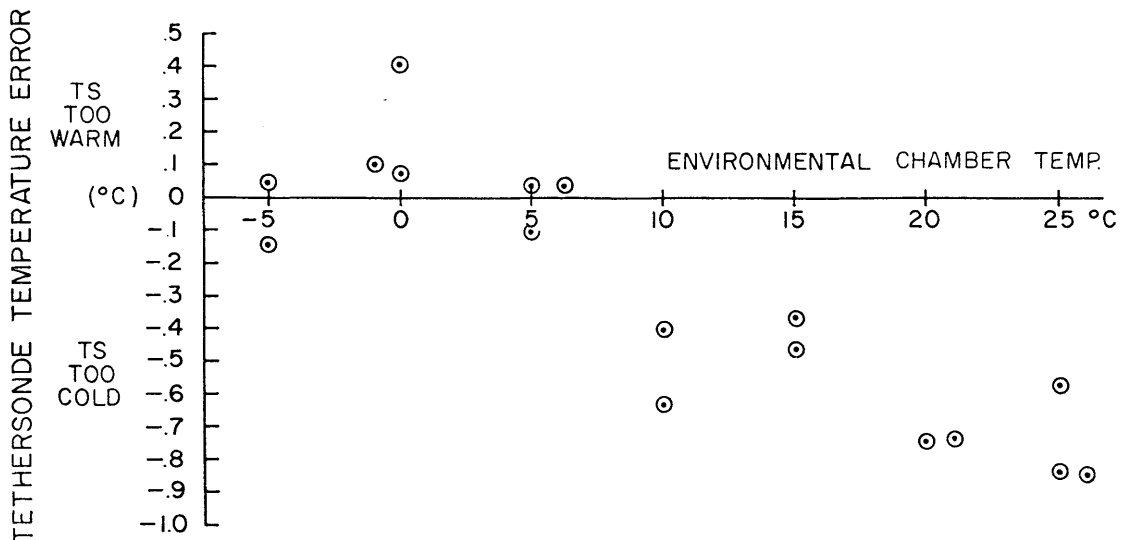


Figure 78. Tests of tethersonde temperature data in the NCAR Environmental Chamber.

A determination of the time constant for the tethersonde temperature system could not be performed in the environmental chamber since an instantaneous step-wise change in temperature could not be accomplished. Additionally, the door of the chamber could not be opened quickly enough to remove the package to simulate a step-wise temperature change. Consequently an alternate test was devised whereby the airborne package was brought to an equilibrium temperature in a heated building on a winter day. Once the package had attained an equilibrium it was quickly carried out of the building into the winter air and left to attain a new equilibrium temperature in a shady location several meters upwind of the building. The tethersonde response was measured on a quick-response strip chart recorder connected to a continuous tethersonde data channel containing thermistor data. An example of a strip chart record of the test is shown in schematic form in Figure 79. Following Gill (1967), the time constant was calculated as the time required after a sudden stepwise change in environmental temperature for the thermistor to indicate $100(1-1/e)\% = 63.2\%$ of the total change, where e is 2.718. Using this definition, Table 10 provides information on the number of time constants required in order for the instrument to respond to different percentages of the full stepwise temperature change. As an example, 3 time constants must elapse before the thermistor responds to 95% of a stepwise temperature change.

Table 10. Recovery Versus Elapsed Time for a First Order Sensor.

recovery	50%	63.2%	90%	95%	99%	99.5%	99.9%
elapsed time	0.7T	1.0T	2.3T	3.0T	4.6T	5.3T	6.9T

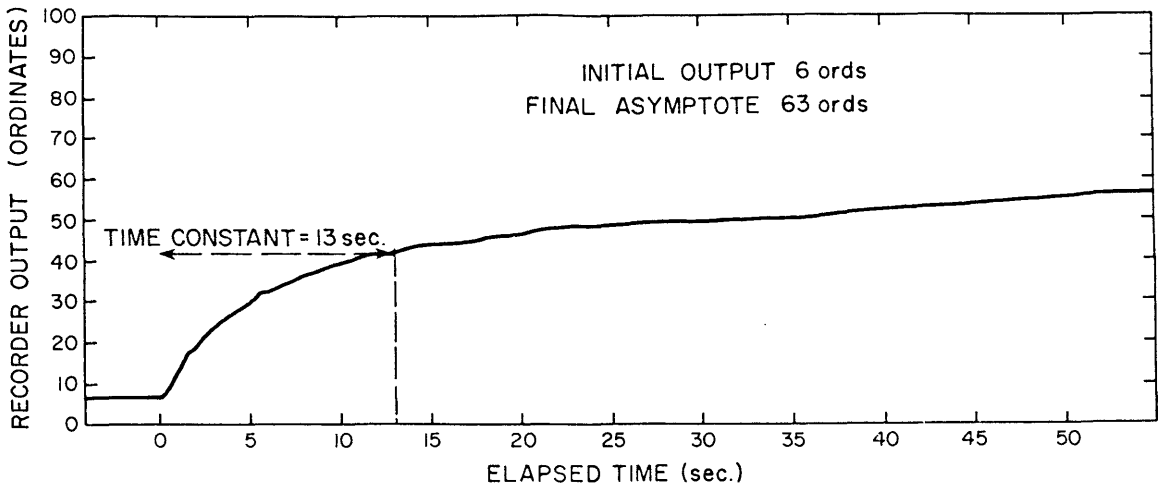


Figure 79. Test of response time of tethered sonde temperature system.

Four time constant determinations were made, allowing investigation of the effect of the radiation shield and the airborne battery voltage. Results are given in Table 11 below.

Table 11. Tethered sonde Temperature Time Constant Determinations.

Radiation Shield (on/off)	Battery Power (% of full power)	T (sec)
on	93.9	13
on	92.5	13
on	76.4	18
off	92.5	10.5

The thermistor manufacturer's specifications are for a time constant of 10 seconds in free, still air. Aspiration of the thermistor should produce a shorter time constant. From the results of the time constant experiments in the table we must conclude that the temperature data collection system has a longer time constant than the sensor alone.

Perhaps this is due to the effects of the thermal mass of the radiation shield or of the entire airborne package. This contention is supported by the fourth time constant determination, when the plastic radiation shield (but not the fan or thermistor assembly) was removed, resulting in a time constant of 10.5 seconds. In contrast, the effect of weak airborne batteries is to increase the time constant, presumably because of a decrease in aspiration efficiency of the battery-powered fan. In actual practice, however, batteries were normally replaced when they fell to 80-85% of their full power. After the time constant tests discussed above were performed, the voltage to the fan was increased to improve the aspiration rate and operational procedures were changed to gain better temperature data in the field. Data collection procedures were modified so that balloon profiles were conducted more slowly, especially in the near-ground layer where temperature inversions were especially strong.

Other factors affecting temperature data should be mentioned. First, during up-soundings the airborne package may follow in the wake of the balloon, and the question arises as to the possibility of "contamination" of the temperature data due to the thermal wake of the balloon. No such contamination of data was apparent in any of the ascents. Second, the accuracy of the temperature data depends on whether the airborne package is allowed to come to an equilibrium with the air temperature near the surface before ascent. This was done routinely. On the other hand, once it had attained the top of the sounding, the package was not routinely stopped long enough to attain a new equilibrium before descent. At the end of the down-sounding the package was allowed to continue transmission until a temperature

equilibrium was attained. Due to the above factors and the desire to gain the most accurate soundings possible in the near-ground layer the up-soundings were preferred for analysis. Use of up-soundings only (or down-soundings only) in an analysis results in a better time-portrayal of the data since data at all levels of the soundings are separated by approximately the same time increment.

No tests of tethersonde wet bulb temperature were performed except for the routine comparison tests with an Assmann psychrometer conducted under field conditions before each sounding. These comparisons were not conducted in a controlled environment and thus differences between the wet bulb temperatures can be attributed to many factors such as solar radiation, wind, the differing response times of the two temperature systems, and the differing times and locations of sampling with the two systems. Where the comparisons were carefully done, allowing for the slow response of the Assmann psychrometer and being careful to ensure that both systems were sampling the same air, the systems generally agreed with $\pm 0.5^{\circ}\text{C}$.

A special problem arose when wet bulb temperatures were desired in near-freezing conditions since thawing or freezing of the ice or water on the wick could not occur instantaneously as the ambient temperature changed across the freezing point. Wet bulb temperature data should therefore be interpreted with care on soundings where the 0°C isotherm is crossed. These phase change problems were recognized in the field and, when possible, soundings were delayed at the ground until the proper phase of the wet (or ice) bulb was attained.

D. Pressure

Tests of tethersonde pressure data were conducted in the NCAR Environmental Chamber by means of pressure steps taken at constant

temperature. Before the tests were begun, the tethersonde was set to the pressure indicated by the environmental chamber sensor. The results of the pressure steps, shown in Figure 80, indicate that the pressure data from the two systems agreed within ± 1.5 mb over the 60 mb range.

Drifting of the tethersonde pressure sensor while the sonde was on the ground was sometimes observed, although the drifting was generally less than 1 mb. The drifting could be easily observed in the digital data where the pressure resolution was 0.1 mb. The strip chart output of the NCAR tethersonde systems, on the other hand, had a

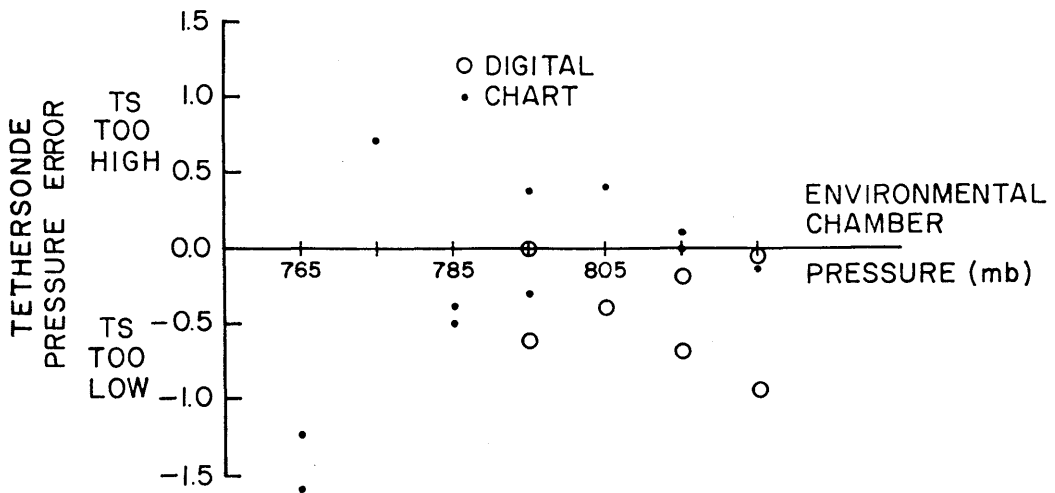


Figure 80. Tests of tethersonde pressure data in the NCAR Environmental Chamber.

resolution of 1 mb and the pressure drift with these systems was occasionally greater than 1 or 2 mb. Part of this apparent drift was no doubt due to the drift of the zero and full-scale signals on the strip chart recorder. One explanation for the pressure drifts is a hysteresis error in the aneroid. This possibility was tested in the environmental chamber by causing the pressure in the chamber to undergo computer-controlled, long period pressure oscillations similar to oscillations that would occur in a series of successive tethersonde soundings. The tests were not entirely satisfactory since the environmental chamber's pressure sensor seemed to have a much longer response time than the tethersonde's. Pressure increases in the environmental chamber were accomplished by the opening and closing of valves--a process which generated pressure spikes within the chamber. The tethersonde pressure sensor responded quickly to these pressure fluctuations, producing noisy data. The environmental chamber had a similar response to the pressure noise but responded with a longer time constant. Data points from the two pressure measuring systems were not collected concurrently, thereby increasing the difficulty of analysis. The results nevertheless seemed to indicate that hysteresis errors on the order of one or two millibars could be occurring in a normal sounding. These errors could explain the observed pressure drift. Future investigators may wish to test this possibility further.

E. Summary

Table 12 below presents the operating characteristics of the tethersonde data collection system as determined from a series of field, environmental chamber, and wind tunnel tests. A summary of conditions that will cause a deterioration of system performance from the values listed in the table are given below.

Table 12. Operating Characteristics of Tethersonde System TS-1A-1

 Dry Bulb Temperature

sensor	thermistor network
range	-50 to 50°C
resolution	0.1°C
precision	±0.8°C
time constant	13 sec

Differential Barometric Pressure

sensor	aneroid strain gauge
range	0-100 mb
resolution	0.1 mb
precision	±1.5 mb

Horizontal Wind Speed

sensor	3-cup anemometer
range	0.4-20 m sec ⁻¹
resolution	0.1 m sec ⁻¹
precision	±0.3 m sec ⁻¹
starting speed	0.4-0.7 m sec ⁻¹
stopping speed	0.3 m sec ⁻¹
time constant (0-10 m sec ⁻¹)	0.3-0.5 sec
distance constant	3-5 m

Wind Direction

sensor	magnetic compass
range	0-360°
resolution	1°
precision	±4°

Dry and wet bulb temperatures: The time constant may be longer under conditions of low battery voltage. The wet bulb temperature precision and time constant were not tested. Wet bulb temperature precision may be adversely affected when phase changes occur on the wet bulb.

Pressure: Hysteresis errors may adversely affect precision.

Windspeed: The precision of wind speed data during strong or turbulent wind conditions is adversely affected by the swinging of the airborne package below the balloon (i.e., angle of attack and translational speed of package relative to balloon), the different rate or response of the anemometer to accelerating and decelerating windspeeds, and the translational speed of the balloon relative to the ground.

Wind direction: In turbulent conditions the precision of wind direction data may be adversely affected by twisting of the airborne package. The balloon will not respond well to horizontal eddies smaller in size than half the length of the balloon. Response to large changes in wind direction may be slow.

APPENDIX C

Test of Airsonde Data Collection System

APPENDIX C

Test of Airsonde Data Collection System

Two sets of tests were performed on the Airsonde® data collection system.¹ In the first set, airsondes were flown along with rawinsondes and intercomparisons were made between the data collected with the two data collection systems. In the second set of tests, conducted in the NCAR Environmental Chamber, the accuracy of airsonde temperature and pressure data was checked. As much as possible the tests were conducted to evaluate the overall performance of the airsonde data collection system, rather than testing individual sensors or components of the system. The goals of the tests were:

- (1) to determine the operating specifications of the overall data collection system;
- (2) to determine what corrections, if any, should be made to field data already collected with the airsonde system; and
- (3) to provide information to the airsonde manufacturer regarding desirable future modifications to the data collection system.

A. Rawinsonde-Airsonde Intercomparisons

Arrangements were made with NCAR and the National Oceanic and Atmospheric Administration (NOAA) to participate in rawinsonde launches conducted in a joint field experiment at the Boulder Atmospheric Observatory (BAO) tower near Erie, Colorado (20 km ENE of Boulder) during the month of September, 1978. During the field experiments rawinsondes were launched two or three times per day and, by attaching an airsonde to the rawinsonde drive train (Figure 81), it was possible

¹Ground station Model TS-2A, S/N 23
Atmospheric Research Co., Boulder, CO 80303.

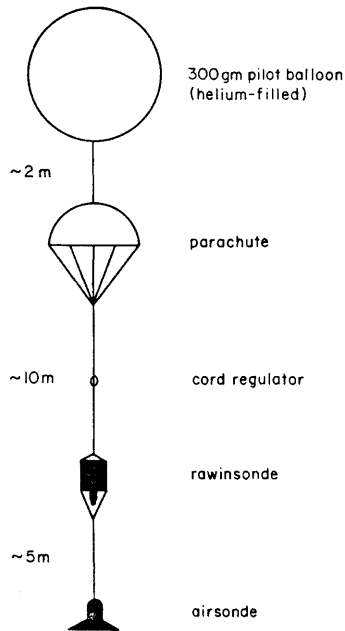


Figure 81. Drive train for Rawinsonde/Airsonde intercomparison flights.

to make dual soundings of the atmosphere. For these dual soundings VIZ Accu-Lok rawinsondes were used. These new sondes require an abbreviated baseline test, contain an improved thermistor temperature sensor, and use a smaller water-activated battery than their predecessors. The battery was sealed in a plastic bag in the rawinsonde before launch to decrease the effect of the moist battery on humidity readings with either of the sondes. Standard pre-launch procedures were followed with the airsonde system, as detailed in Chapter III, and with the rawinsondes.

1. First Intercomparison

In the first test, conducted on September 22, two independent airsonde ground stations were used to receive airsonde signals. The second ground station was operated by the airsonde manufacturer and allowed intercomparison of data from two ground stations receiving

signals from the same sonde. The ground stations were identical except that the manufacturer's ground station had been modified with a new phase-lock loop noise rejection circuit. Figure 82 shows the comparison of the three data sources. Several features are apparent in the data:

(1) Soundings from the two airsonde ground stations were nearly coincident. Thus only a few points of the AIR Co. sounding are plotted--these mostly where differences occurred between the two ground stations.

(2) Differences between the two airsonde soundings were due to occasional noisy signals received by the CSU ground station. The noisy signals were readily apparent when they occurred in the pressure data since they generally produced anomalously large pressure fluctuations. Noisy pressure data are not plotted on the figure. However, noisy signals sometimes caused temperature data to fluctuate by 0-2°C. It was difficult to reject these data points since atmospheric temperature fluctuations of this amplitude can occur. The noisy data points (e.g., at 790 and 640 mb) can be easily identified, however, by comparing data from the two airsonde ground stations. This test pointed out the advisability of modifying the CSU ground station with the new noise rejection circuitry. It should be mentioned that the CSU sounding in Figure 82 (and in following airsonde plots) contains only half the data sent back by the airsonde. The HP-97 printer output, from which the data is plotted, lists only every other data frame from the airsonde, since the rate of data transmission is too fast for the printer to keep up. Twice as many data points would be available if the airsonde data were recorded using the optional cassette tape system. The

availability of twice as much data would facilitate rejection of noisy temperature data.

(3) Field plots of rawinsonde data, indicated on Figure 82 by x's, follow the airsonde soundings fairly closely but, particularly at upper levels of the sounding, seem to diverge somewhat. The discrepancy is approximately 1 or $1\frac{1}{2}^{\circ}\text{C}$, corresponding to a pressure discrepancy of about 10 mb.

2. Second Intercomparison

The second intercomparison failed when the airsonde signal became noisy just after launch. It is thought that the sonde was off-frequency.

3. Third Intercomparison

The third sounding (Figure 83), taken on 26 September 1978, showed many of the characteristics of the first sounding. Occasional noisy data frames occurred with this sounding, although most could be clearly identified as bad data. The points at 600-610 mb, however, are suspect and it is hard to tell which points are correct. Data above the 540 mb level were noisy. Above this level only a few of the data points are plotted. Of more concern than the occasional bad data points is the divergence of the airsonde and rainsonde soundings at upper levels. This divergence is in a different direction than for the first intercomparison and amounts to $5\text{-}6^{\circ}\text{C}$ or 25 mb at the 350 mb level.

4. Fourth Intercomparison

Line power fluctuations at the ground station or frequency drift in the airsonde caused a failure of the fourth intercomparison. After this intercomparison the CSU ground station was modified with a new noise rejection circuit.

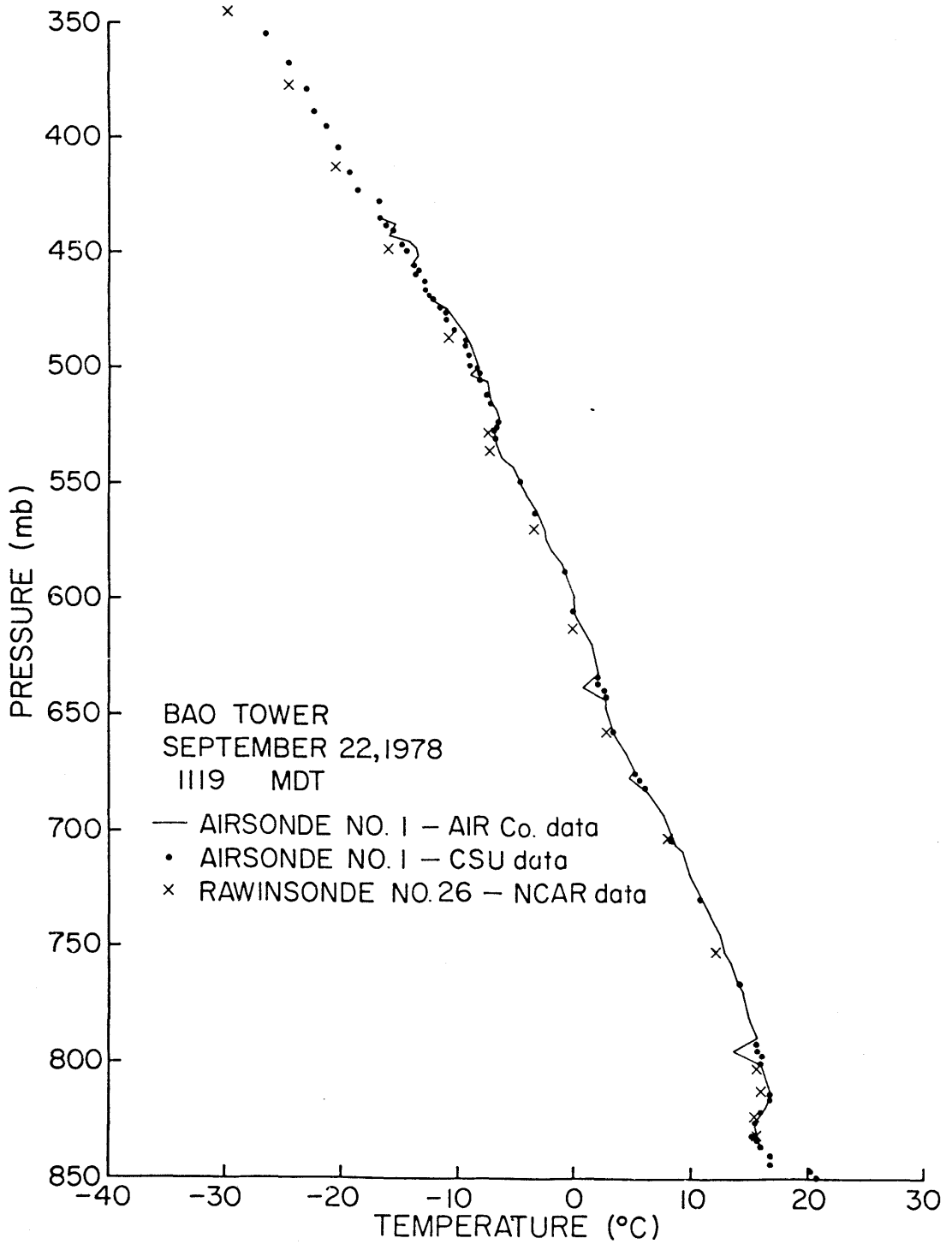


Figure 82. Airsonde/Rawinsonde intercomparison, 22 September 1978.

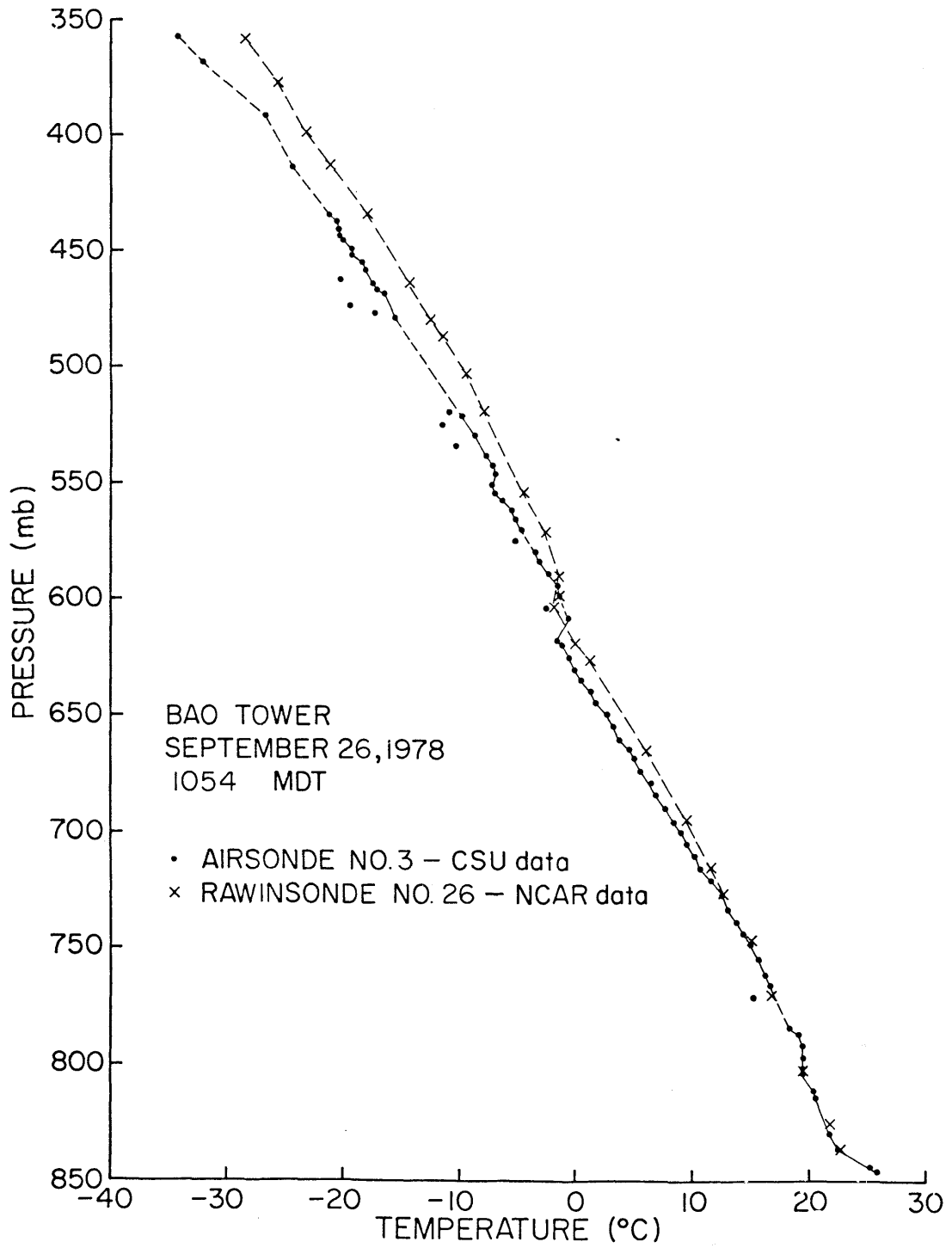


Figure 83. Airsonde/Rawinsonde intercomparison, 26 September 1978.

5. Fifth Intercomparison

The purpose of the fifth intercomparison was to determine whether the divergence of airsonde and rawinsonde data was due to errors in airsonde temperature or pressure data. For this purpose rawinsonde data was called out by the rawinsonde operator as the balloon ascended, and real-time comparison was made with airsonde data. The results showed a very good agreement between airsonde and rawinsonde temperature values. These values generally agreed within several tenths of a degree Celsius. Data are shown in Table 13 below. The pressure values, as seen in the table and in Figure 84 below, diverge at upper levels. The divergence amounted to 5 or 10 mb at the upper levels of the sounding, somewhat less than for intercomparisons 1 and 3. At the conclusion of the fifth intercomparison a decision was made to conduct further experiments in a controlled environment where a large number of airsondes could be tested for pressure errors.

B. Environmental Chamber-Airsonde Tests

Arrangements were made with NCAR to use their Environmental Chamber for further airsonde tests. Using this chamber it is possible to vary temperature and pressure independently in a computer-controlled environment. The facility is not, strictly speaking, a calibration facility, since NCAR does not have the personnel or funding to maintain the chamber at a calibration standard. At the time of the airsonde tests the chamber was not fully operational and could not be operated under computer control. The chamber was therefore operated under manual control. The main disadvantage of manual control was that it was difficult to maintain the chamber at a truly constant setting.

Table 13

Comparison of Concurrent Airsonde and Rawinsonde Data

Rawinsonde		Airsonde	
Pressure (mb)	Temperature (°C)	Pressure (mb)	Temperature (°C)
681.6	6.5	681	6.5
634.8	1.4	636	1.3
591.0	-3.0	589	-3.0
548.2	-8.1	546	-8.0
508.0	-11.5	507	-11.5
470.6	-15.8	466	-16.1
434.4	-20.2	431	-20.1
400.6	-25.1	395	-25.0
368.6	-27.9	363	-27.4
338.2	-32.8	330	-32.8
309.8	-37.6	301	-37.9
283.0	-42.8	--	-42.8

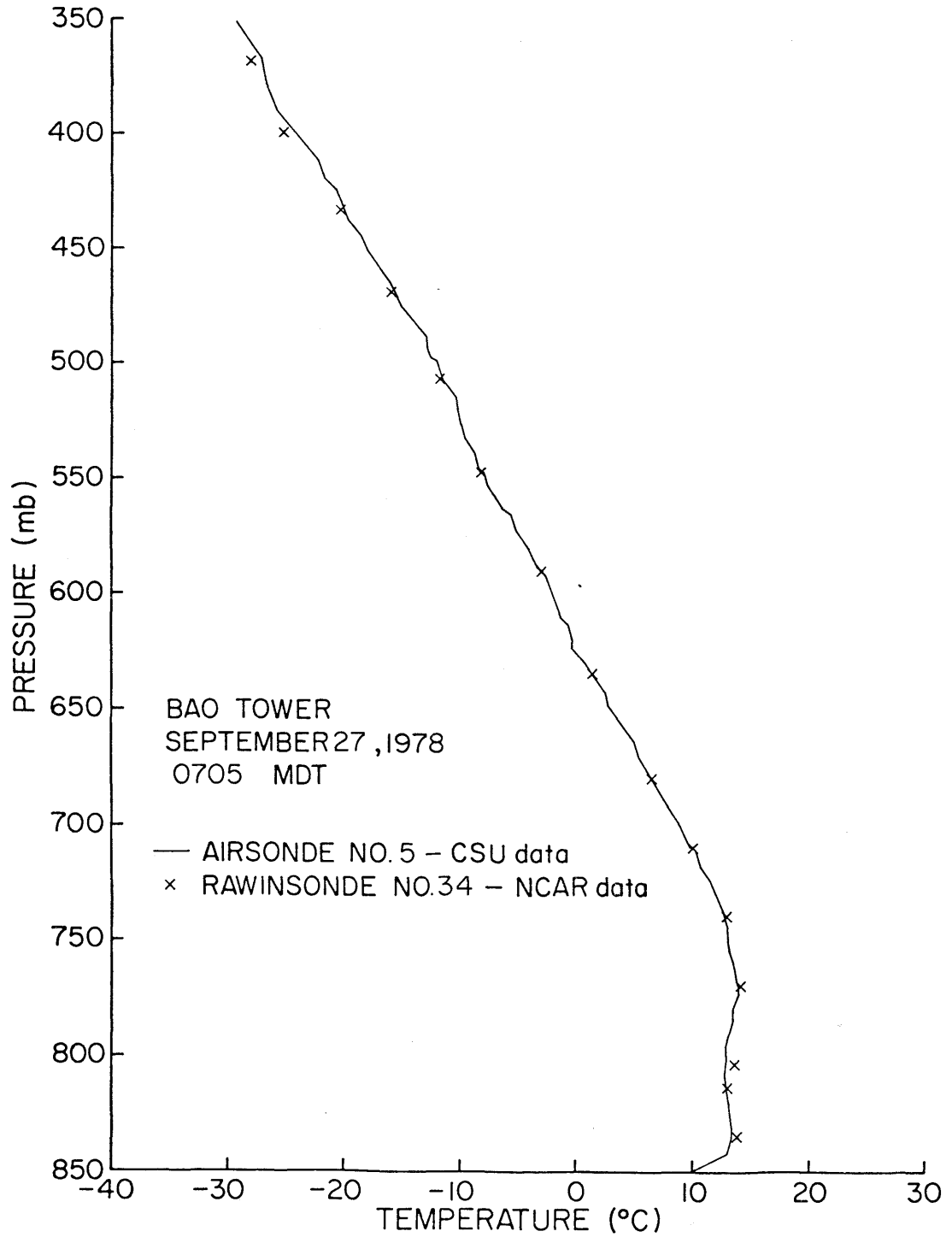


Figure 84. Airsonde/Rawinsonde intercomparison, 27 September 1978.

1. Pressure Steps at Constant Temperature

In this test five airsondes were strung on an insulated wire and suspended across the center of the environmental chamber. The individual airsondes could be alternately turned on and off from outside the chamber. The ground station was operated from a laboratory bench nearby and data were printed using an HP-97 Printer/ Calculator. Each of the airsondes was activated in turn, and the airsonde manufacturer's four pre-calibration constants were keyed into the ground station (Chapter III). The final constant was adjusted so that pressure readings coincided with actual ambient pressure. The constants were checked twice to ensure against keying errors and were recorded and used in all subsequent tests. The chamber was then put into operation and pressure steps were accomplished at "constant" (22.8-30.4°C) temperature. Once a pressure step had been accomplished and the chamber had reached a stable value, the sondes were alternately turned on and readings were taken. The results (Figure 85) showed that the five sondes agreed with environmental chamber sensors within ± 3 or 4 mb over the pressure range from 850 mb to 300 mb. Note that the temperature was not strictly constant during these tests, so that the "pressure error" may be partially due to temperature fluctuations. The pressure errors determined in this experiment seemed to be unrelated to adjustments of the fourth constant, as described above. The conclusion therefore was that the airsondes had been successfully pre-calibrated by the manufacturer for pressure changes at constant temperature.

2. Temperature Steps at Constant Pressure

After the results of the foregoing tests, attention was focused on the possibility of airsonde pressure errors being due to temperature

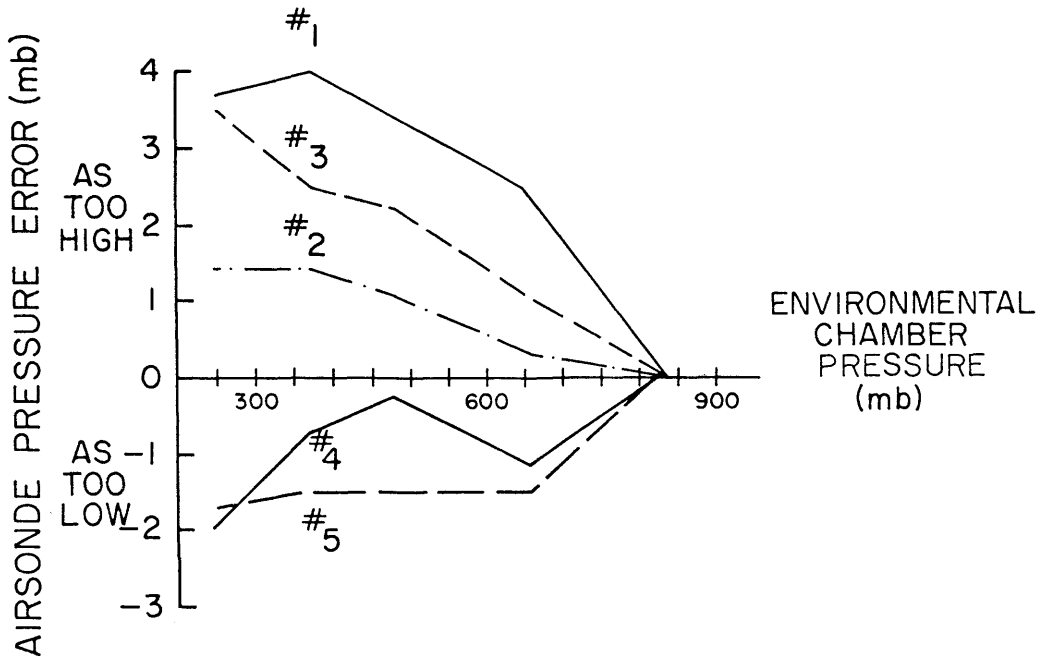


Figure 85. Pressure comparison data for five airsondes in NCAR Environmental Chamber tests.

changes as the sondes ascended. The most likely cause seemed to be improper temperature compensation of the airsonde aneroids. A brief digression is needed to provide background on this feature of the airsonde system.

The airsonde pressure sensor is an aneroid pressure element. Such elements respond to temperature changes as well as pressure changes. The pressure value indicated by such a sensor must consequently be corrected or "compensated" to remove this temperature dependence. In the airsonde this is done by monitoring the temperature of the aneroid cell using a special temperature sensor. Knowing that a change in aneroid temperature of 1°C corresponds to an apparent decrease (or increase) in pressure of x mb, the sensed pressure value can be corrected to get the actual pressure value. The correction of the pressure value is accomplished in the software of the ground station

after the linear aneroid temperature response factor (i.e., x mb/1°C) is entered into the software. This factor is the first of four constants that must be entered into the ground station in the airsonde preflight procedures. All sondes used in field experiments and tested in the environmental chamber were compensated using the same temperature response factor. This was done at the suggestion of the aneroid manufacturer in view of the lack of suitable test facilities for checking each aneroid individually at the airsonde manufacturer's.

To conduct a test of temperature compensation of airsonde aneroids, an experiment was designed whereby the environmental chamber would be maintained at constant pressure but would undergo temperature steps over a wide range of temperatures. In order to insure that aneroids would quickly attain temperature equilibrium with the chamber it was necessary to conduct tests on airsondes that had been removed from their insulating foam shells. The airsondes were then exposed in a rack on the floor of the environmental chamber. The sondes then underwent tests as temperature steps were accomplished. Results of the tests, provided in Figure 86, show that there is considerable difference in the temperature response of individual aneroids. Use of the same temperature response factor for all airsondes results in some of the aneroids being overcompensated while others are undercompensated. Using the suggested temperature response factor results in pressure errors of up to 30 mb when the temperature range is 40°C. It is not clear, however, whether the aneroids would undergo temperature changes of this magnitude in a normal flight to 300 mb when covered by their insulating foam shells.

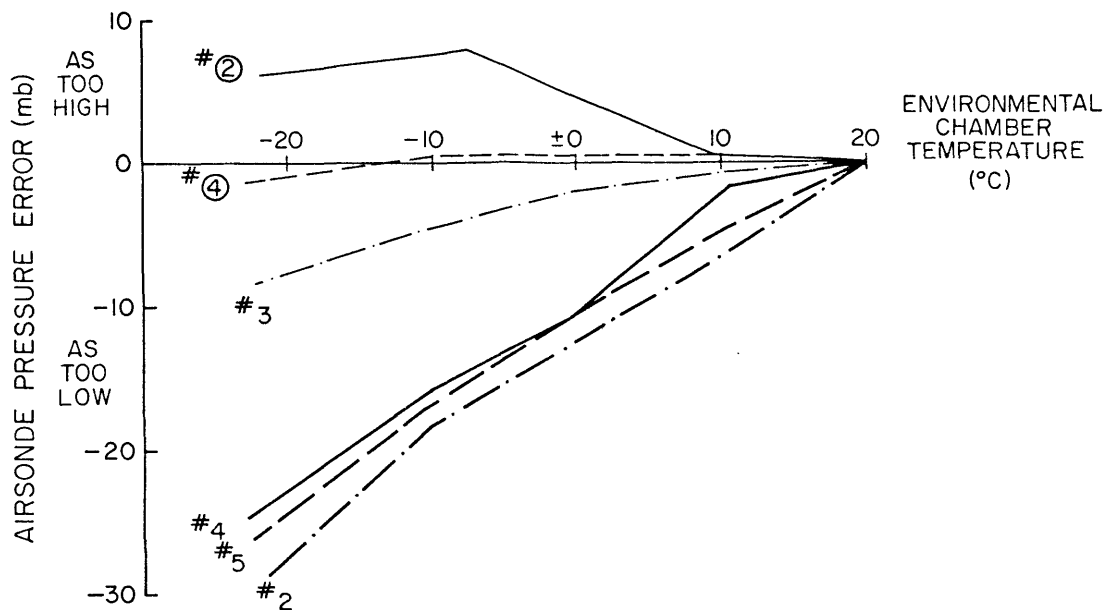


Figure 86. Temperature comparison data for six airsondes in NCAR Environmental Chamber tests.

C. Conclusions

Airsonde temperature data compare favorably to rawinsonde data. The high frequency of transmission of airsonde data allows better height resolution of atmospheric features. Pressure data from the early airsonde models tested were found to be in error due to the use of improper temperature compensation factors. The errors ranged from 0 to 30 mb by the time the sondes ascended to the 300 mb level. The insulating effect of the foam airsonde bodies minimized these errors in the near-ground layer, extending upwards to perhaps 150 mb above ground level.

Both temperature and pressure data were affected by electronic noise when signal strength became weak. Noisy pressure data was fairly easy to detect. Noisy temperature data was somewhat hard to

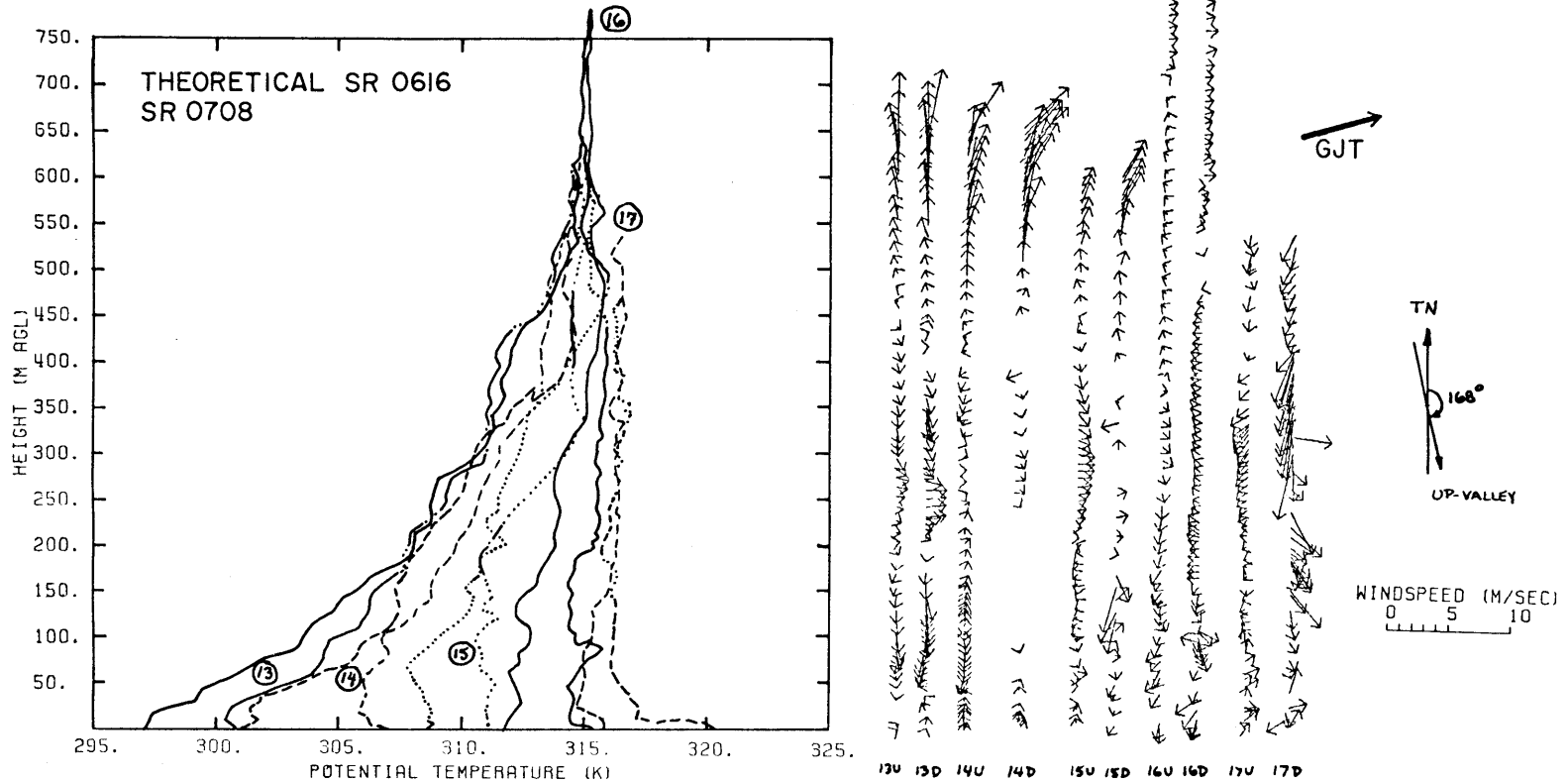
distinguish from good data. Acceptance of the noisy temperature data results in temperature errors of up to 1 or 2°C.

Occasional problems were experienced with an apparent frequency drift of the airsondes. This occurred infrequently during field experiments but happened twice during the airsonde testing program. Field data were collected from about 60 sondes before the testing program was begun. Correction of this field data was accomplished using the results of the testing program and is described in Chapter III.

Many of the problems experienced with the airsonde data collection system are the types of problems often encountered in the development of new instrument systems. One of the goals of the airsonde testing program was to aid in the development of this promising observational tool by thoroughly testing early versions of the system and providing the test results to the manufacturer so that improvements could be made. The system has been greatly improved since the early tests and is continually undergoing tests and modifications.

APPENDIX D
Tethersonde Data

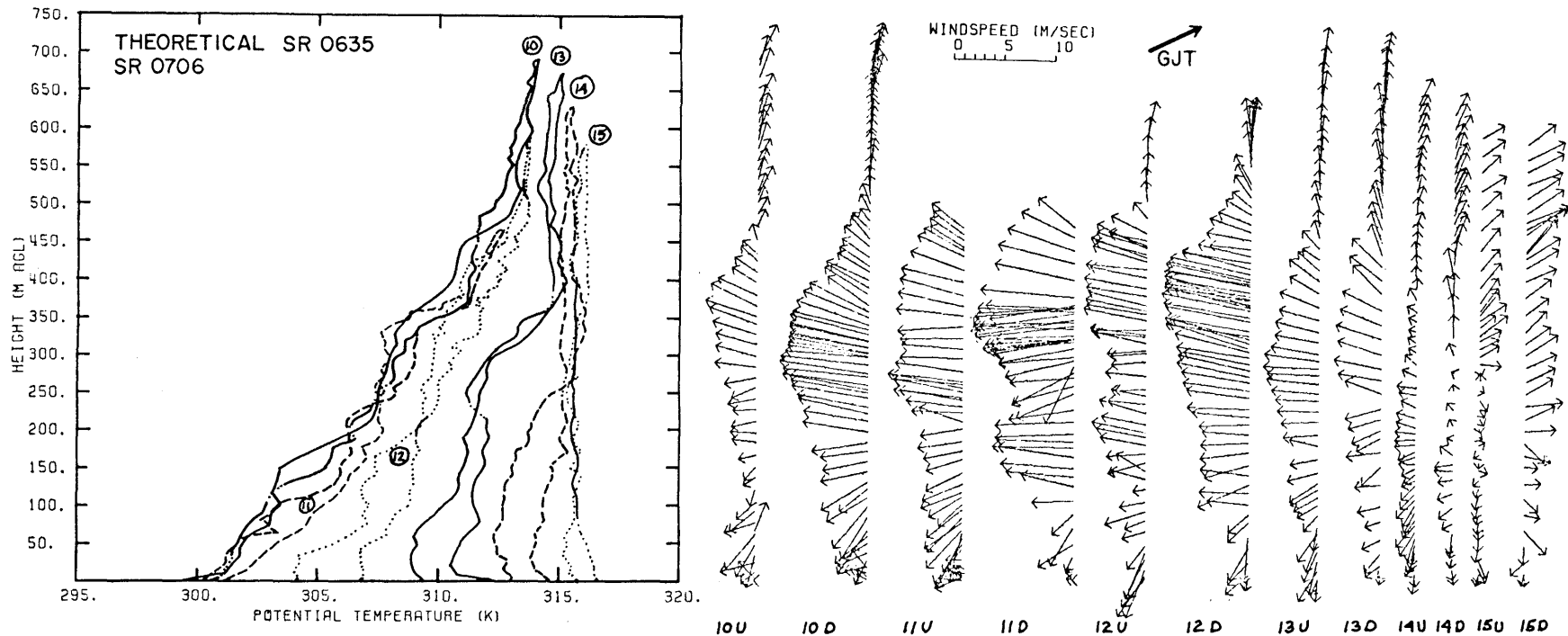
HORSESHOEING SCHOOL STEAMBOAT
DATE 08/10/78



#	TIME (MDT)	WEATHER	#	TIME (MDT)	WEATHER	#	TIME (MDT)	WEATHER
13U	0705-0723	1/10 Cu	15U	0912-0930	2/10 Cu, R DSNT N & S	17U	1102-1118	3/10 Cu & Ac
13D	0723-0745		15D	0930-0942	3/10 Cu & Ac	17D	1118-1136	
14U	0815-0838	2/10 Cu MSTLY N &	16U	1007-1026	4/10 Cu			
14D	0838-0857	JUST S of SITE	16D	1026-1052				

Figure 87. Tethersonde data. Yampa Valley, 10 August 1978.

RIVER CABIN S FK WHITE R.
DATE 08/26/78



#	TIME (MDT)	WEATHER	#	TIME (MDT)	WEATHER	#	TIME (MDT)	WEATHER
10U	0554-0609	7/10 Cu	12U	0804-0821	CLR	14U	0950-1007	CLR
10D	0609-0634	3/10 Cu	12D	0821-0842		14D	1007-1019	
11U	0659-0714	2/10 Cu (MOSTLY DSNT)	13U	0906-0921	CLR	15U	1029-1043	1/10 Cu (MOSTLY
11D	0714-0730	EAST)	13D	0921-0934		15D	1043-1054	EAST OVER MTHS)

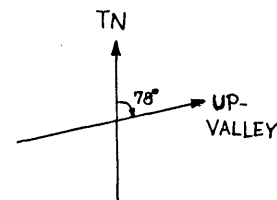
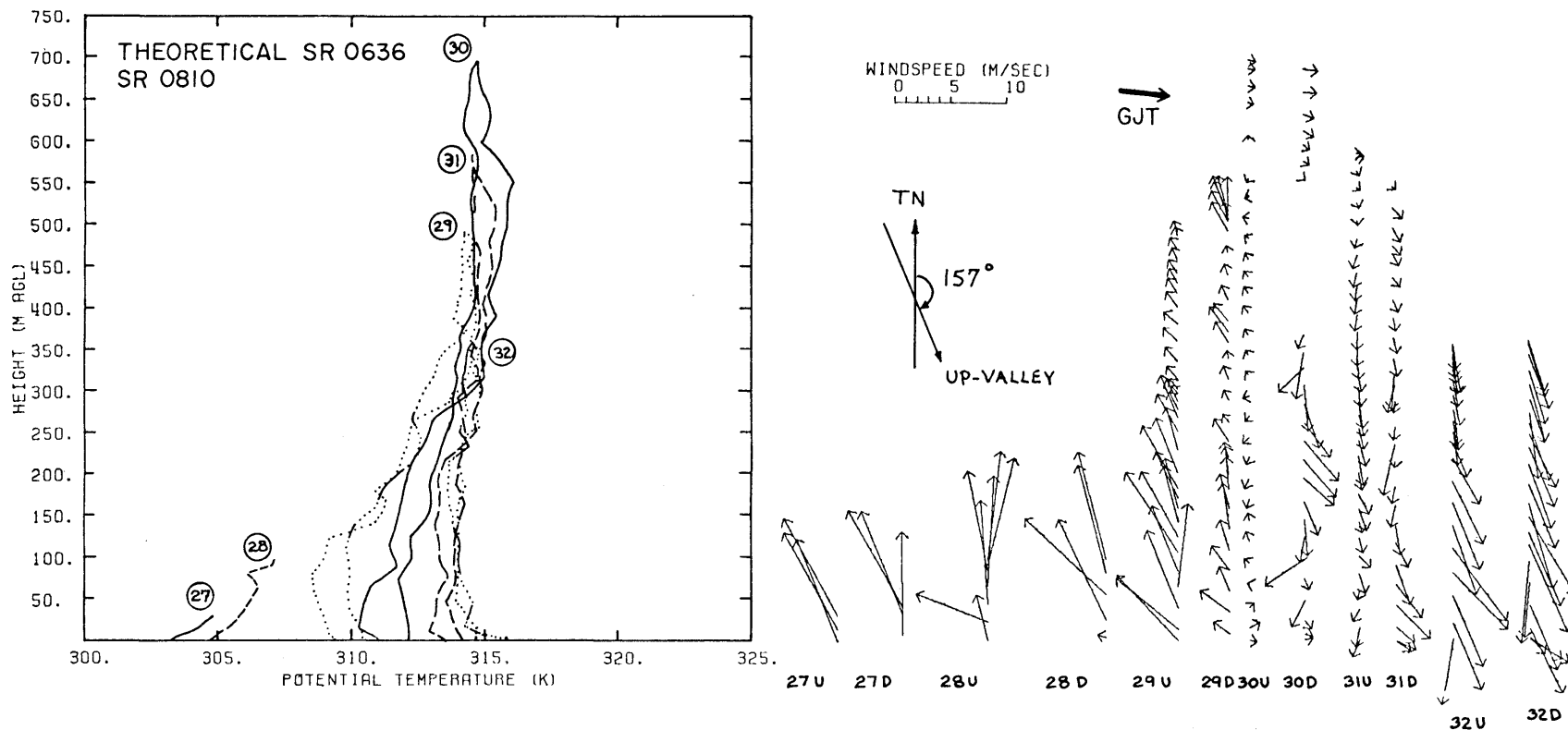


Figure 88. Tethersonde data. South Fork White Valley, 26 August 1978.

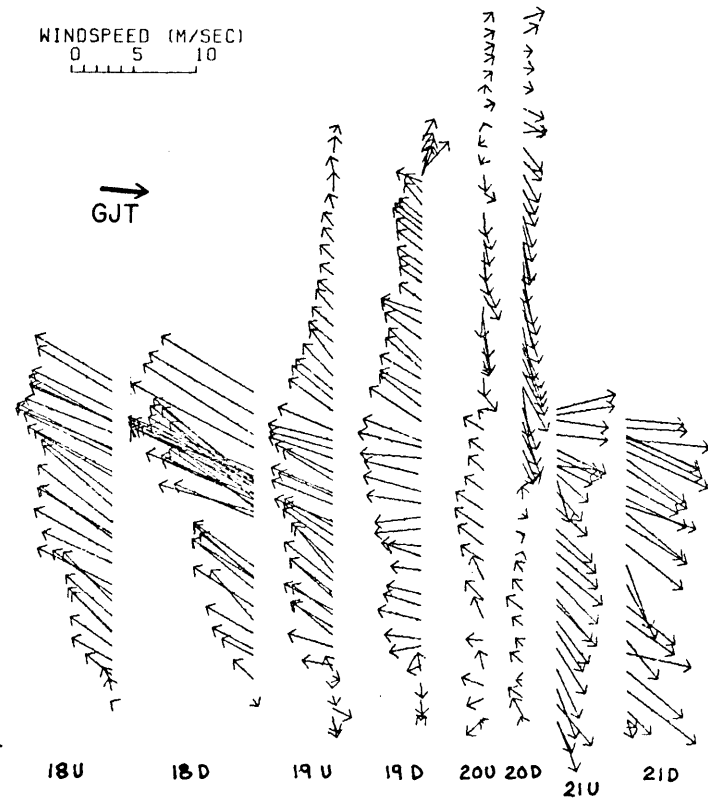
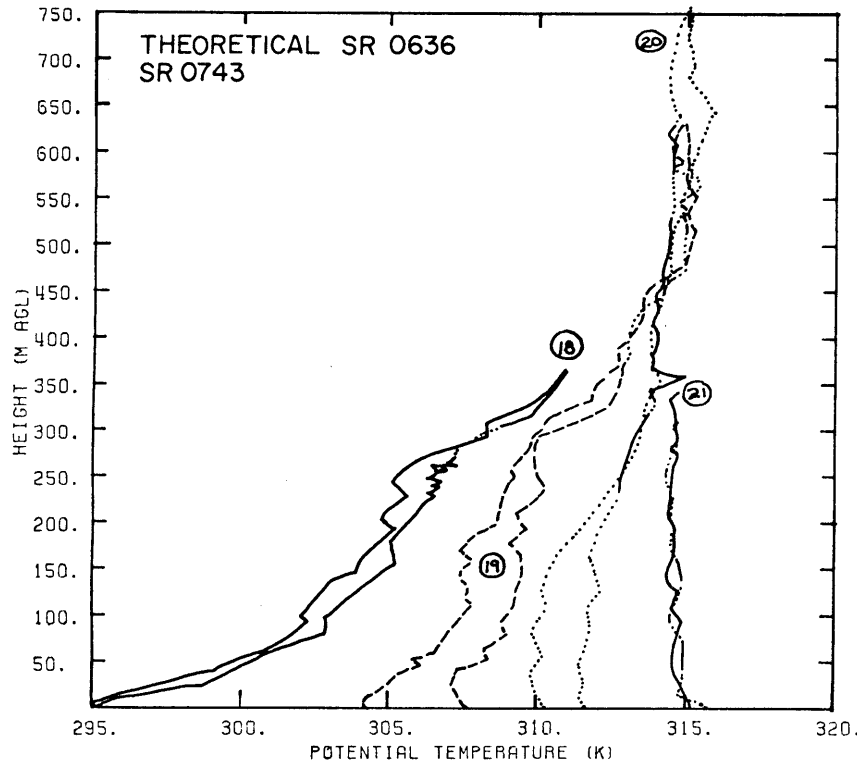
STILLWATER S FK WHITE RIVER
DATE 08/27/78



#	TIME (MDT)	WEATHER	#	TIME (MDT)	WEATHER	#	TIME (MDT)	WEATHER
27U	0715-0716	CLR	29U	0900-0914	CLR	31U	1004-1019	CLR
27D	0716-0717		29D	0914-0927		31D	1019-1032	
28U	0810-0813	CLR	30U	0930-0944	CLR	32U	1038-1047	CLR
28D	0813-0815		30D	0944-0959		32D	1047-1058	

Figure 89. Tethersonde data. South Fork White Valley, Stillwater Site, 27 August 1978.

MOBLEY Y-Z RANCH S FK WHITE R
 DATE 08/27/78



#	TIME (MDT)	WEATHER	#	TIME (MDT)	WEATHER
18U	0707-0717	CLR	20U	0921-0934	CLR
18D	0717-0732		20D	0934-0949	
19U	0836-0851	CLR	21U	1051-1059	CLR
19D	0851-0906		21D	1059-1107	

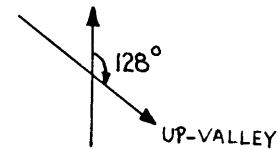
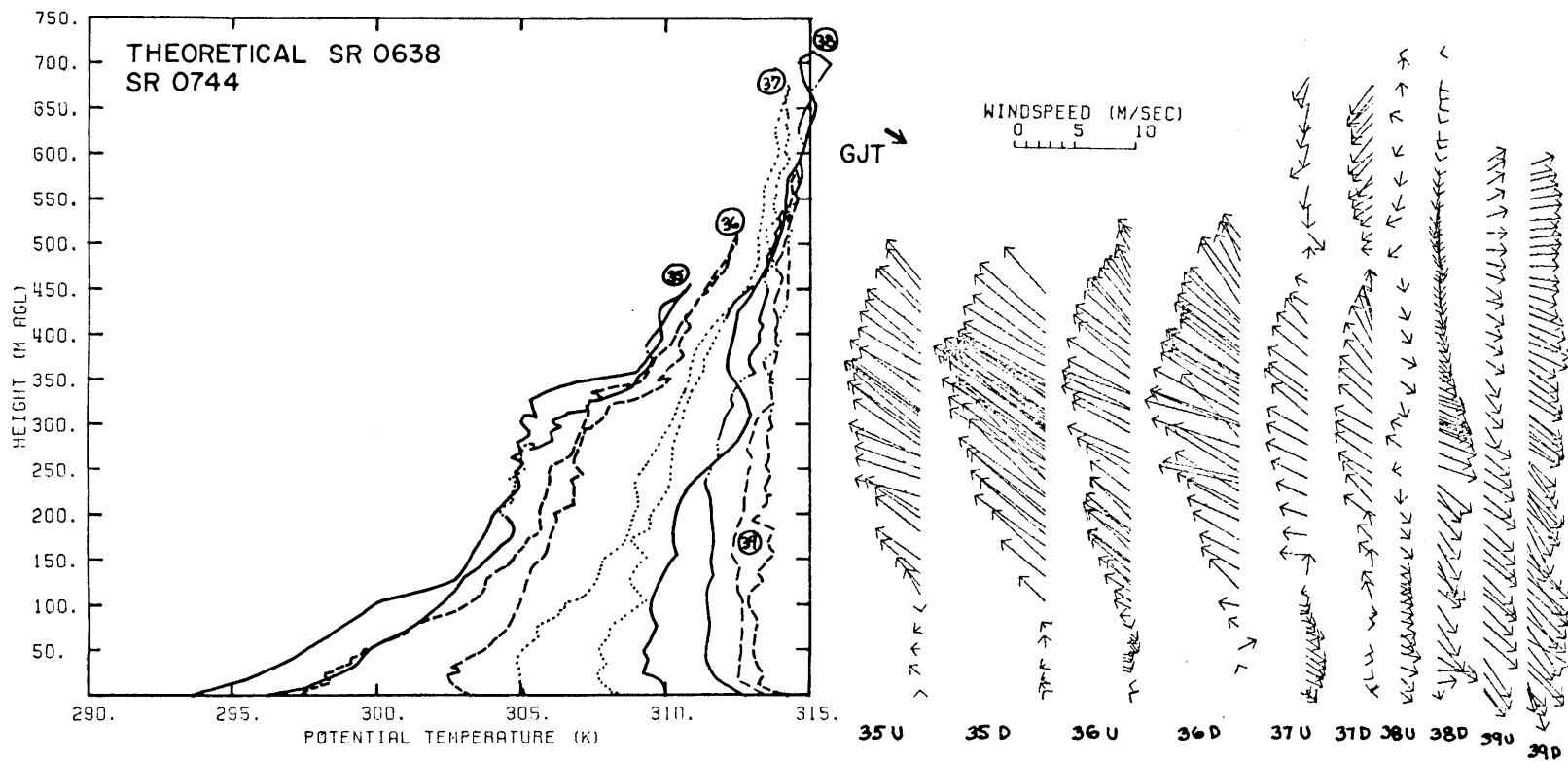


Figure 90. Tethersonde data. South Fork White Valley, Mobley Site, 27 August 1978.

MOBLEY Y-Z RANCH S FK WHITE R
 DATE 08/29/78



#	TIME (MDT)	WEATHER	#	TIME (MDT)	WEATHER	#	TIME (MDT)	WEATHER
35U	0724-0735	CLR	37U	0901-0916	CLR	39U	1040-1052	CLR
35D	0735-0750		37D	0916-0932		39D	1052-1111	
36U	0803-0820	CLR	38U	0953-1005	CLR			
36D	0820-0835		38D	1005-1028				

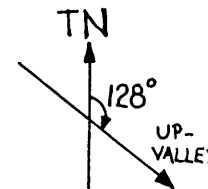
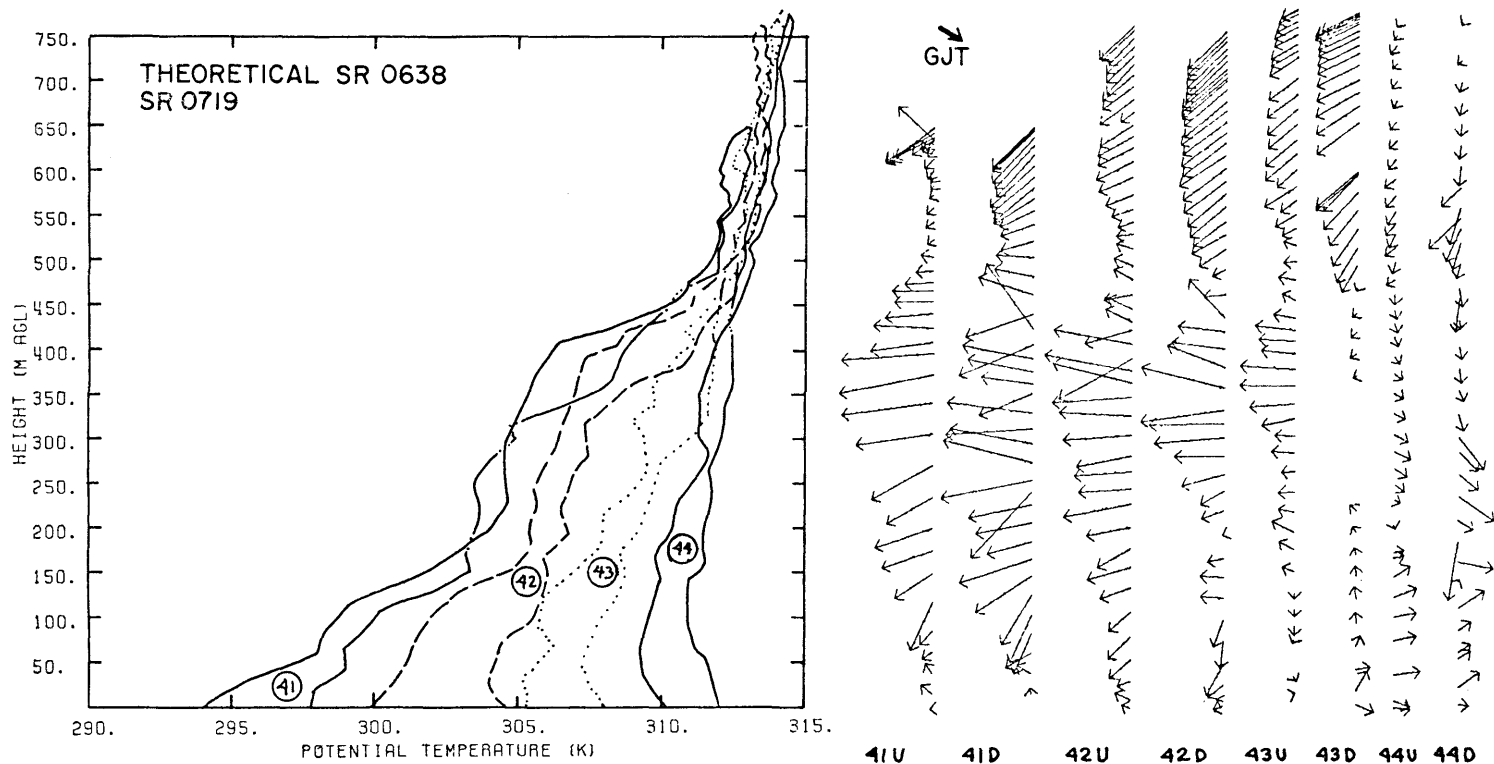


Figure 91. Tethersonde data. South Fork White Valley, Mobley Site, 29 August 1978.

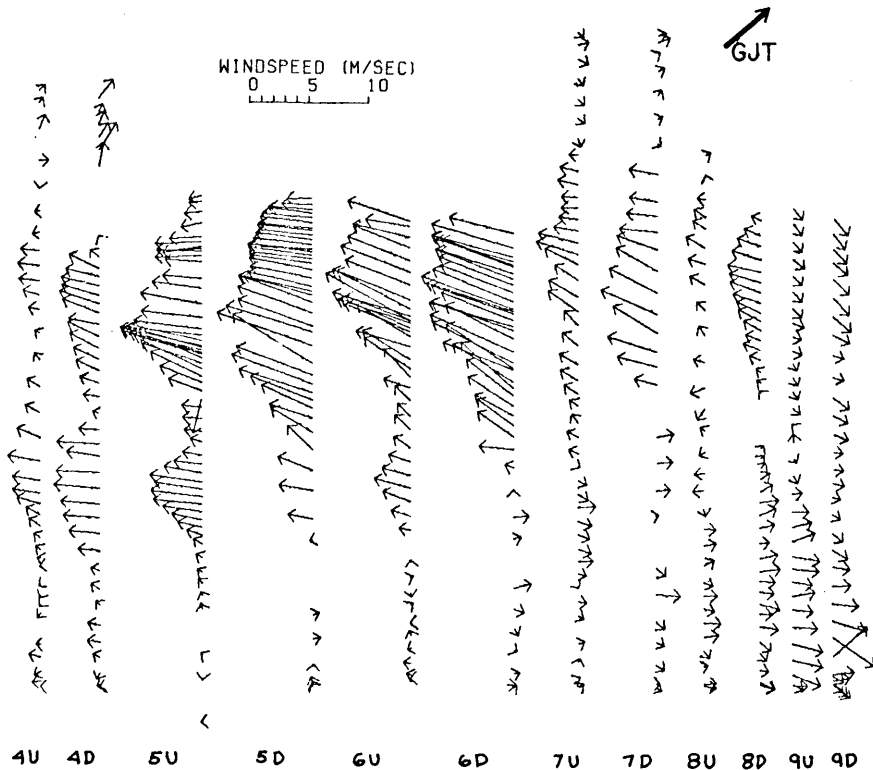
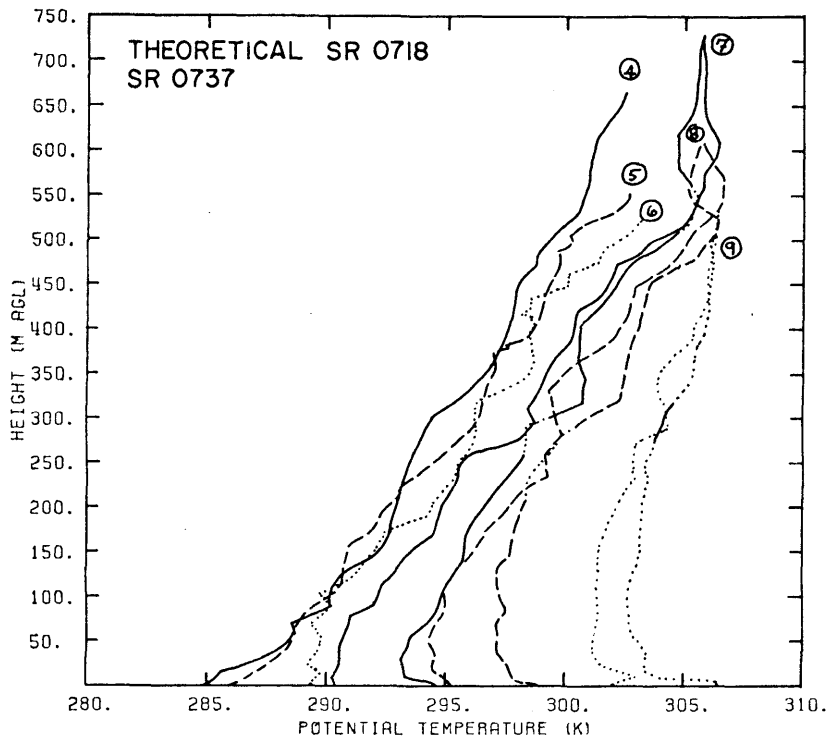
RIVER CABIN S FK WHITE R.
DATE 08/29/78



#	TIME (MDT)	WEATHER	#	TIME (MDT)	WEATHER
41U	0725-0744	CLR	43U	0915-0937	CLR
41D	0744-0804		43D	0937-0957	
42U	0815-0837	CLR	44U	1015-1034	CLR (FEW C: E)
42D	0837-0859		44D	1034-1051	

Figure 92. Tethersonde data. South Fork White Valley, River Cabin Site, 29 August 1978.

RAY MILLERS RANCH EDWARDS COLO
DATE 10/13/77



#	TIME (MDT)	WEATHER	#	TIME (MDT)	WEATHER	#	TIME (MDT)	WEATHER
4U	0640-0658	CLR	6U	0815-0834	CLR	8U	0953-1007	CLR
4D	0658-0717		6D	0834-0853		8D	1007-1028	
5U	0723-0749	CLR	7U	0906-0926	CLR	9U	1118-1133	CLR
5D	0749-0810		7D	0926-0941		9D	1133-1147	

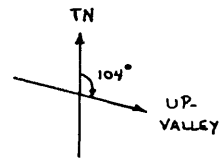
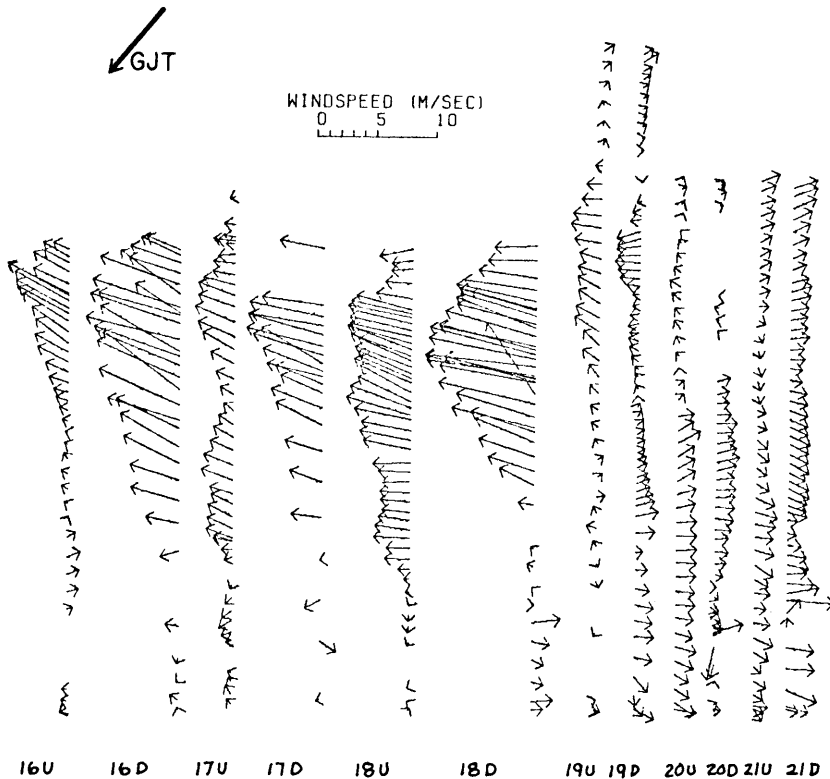
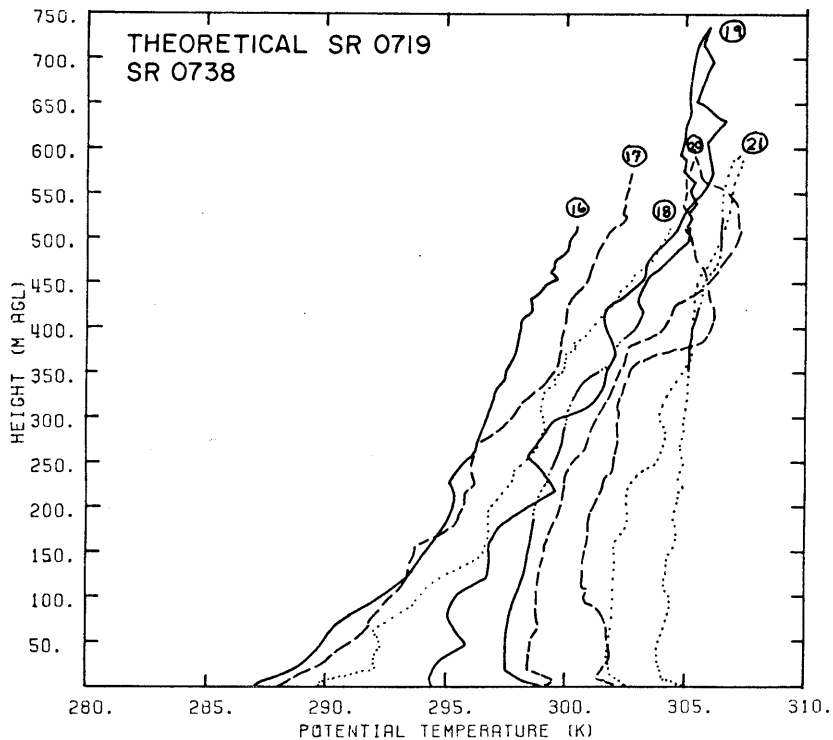


Figure 93. Tethersonde data. Eagle Valley, 13 October 1977.

RAY MILLERS RANCH EDWARDS COLO
 DATE 10/14/77



#	TIME (MDT)	WEATHER	#	TIME (MDT)	WEATHER	#	TIME (MDT)	WEATHER
16U	0644-0702	2/10 Ci	18U	0818-0840	2/10 Ci	20U	1011-1029	3/10 Ci
16D	0702-0717		18D	0840-0900		20D	1029-1054	
17U	0725-0746	2/10 Ci	19U	0915-0933	6/10 Ci	21U	1101-1119	2/10 Ci
17D	0746-0802		19D	0933-1002		21D	1119-1141	

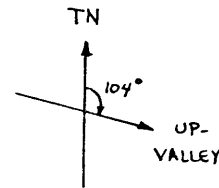
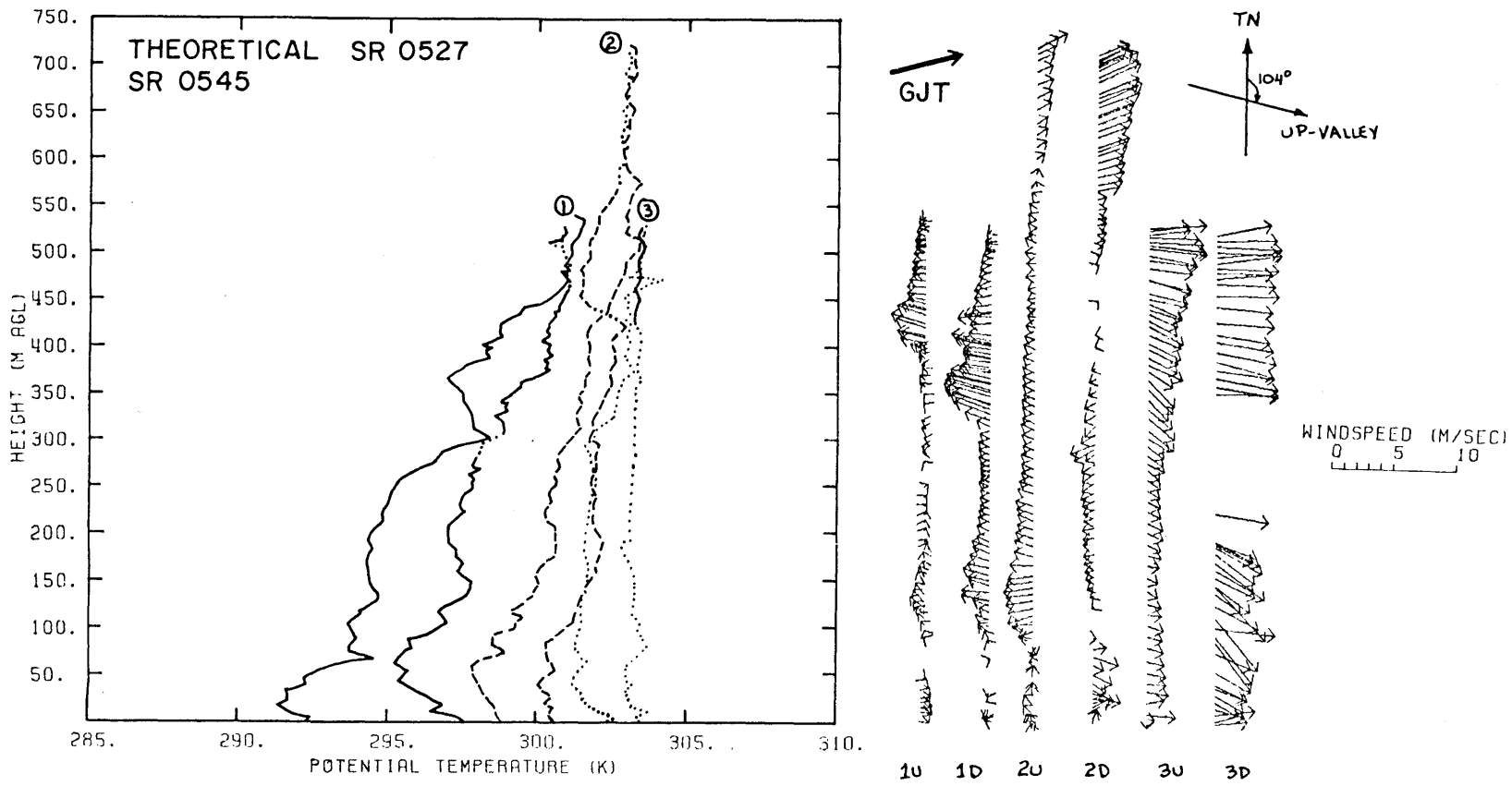


Figure 94. Tethersonde data. Eagle Valley, 14 October 1977.

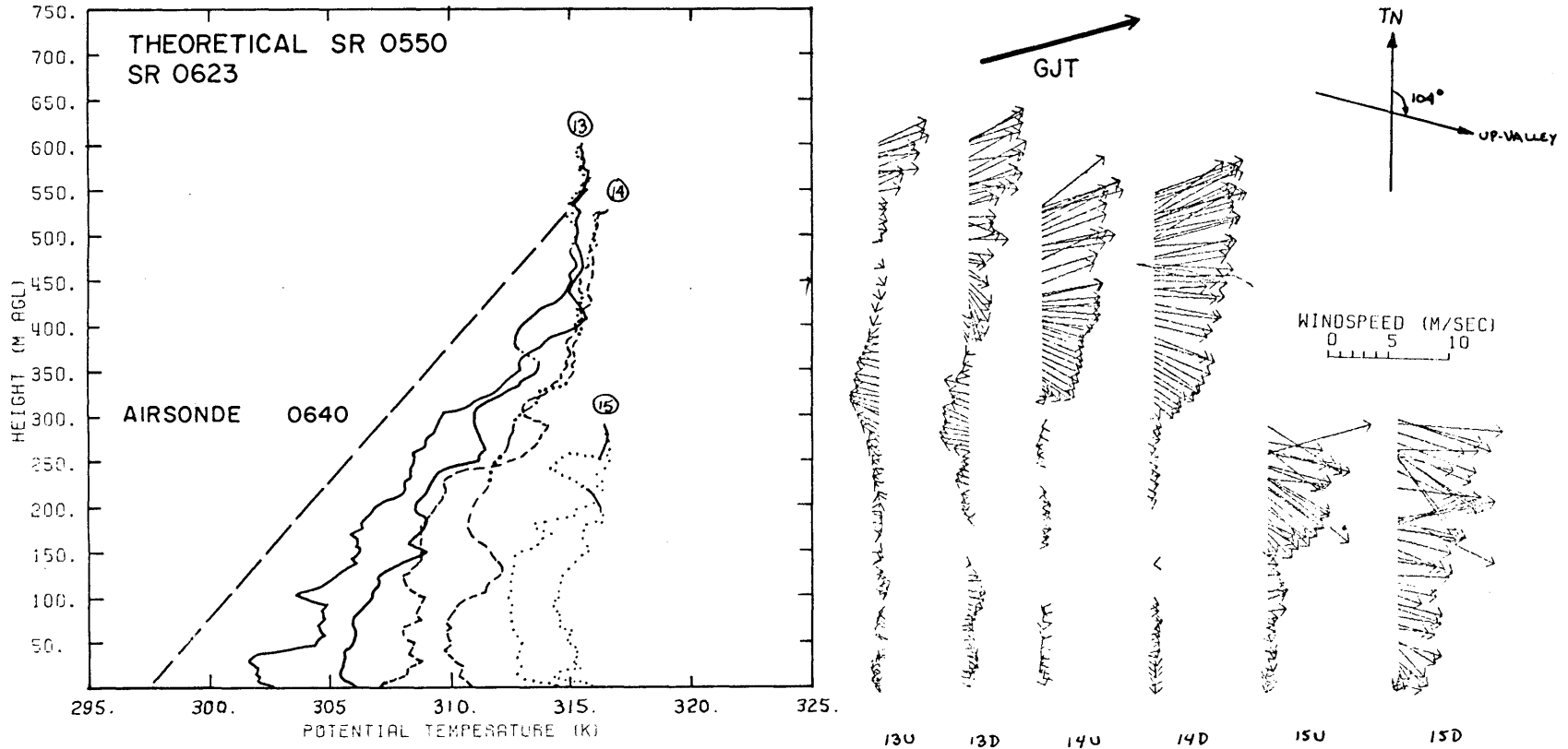
STEVE MILLER RES EDWARDS COLO
 DATE 04/20/78



#	TIME (MST)	WEATHER	#	TIME (MST)	WEATHER	#	TIME (MST)	WEATHER
1U	0653-0719	CLR	2U	0811-0835	8/10 THIN CI	3U	0909-0928	8/10 THIN CI (LGT Cu
1D	0719-0747	-OC; MSTLY W	2D	0835-0902		3D	0928-0952	OVR RDGS)

Figure 95. Tethersonde data. Eagle Valley, 20 April 1978.

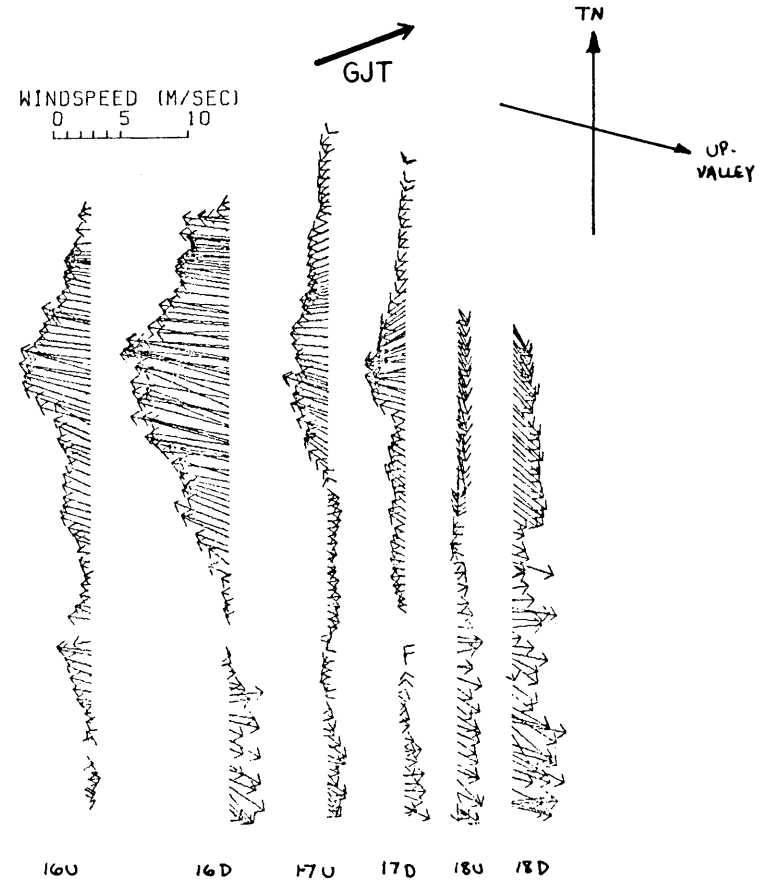
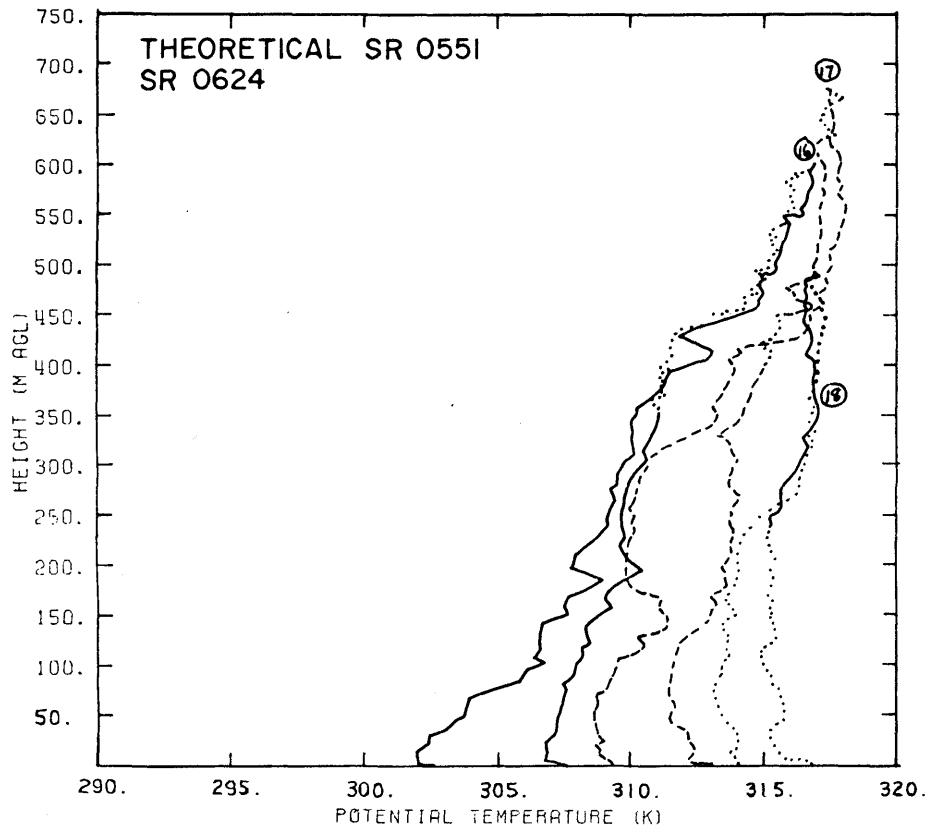
STEVE MILLER RES EDWARDS' COLO
 DATE 07/08/78



#	TIME (MDT)	WEATHER	#	TIME (MDT)	WEATHER	#	TIME (MDT)	WEATHER
13U	0720-0746	CLR	14U	0828-0852	CLR	15U	0938-0951	CLR
13D	0746-0813		14D	0852-0916		15D	0951-1005	

Figure 96. Tethersonde data. Eagle Valley, 8 July 1978.

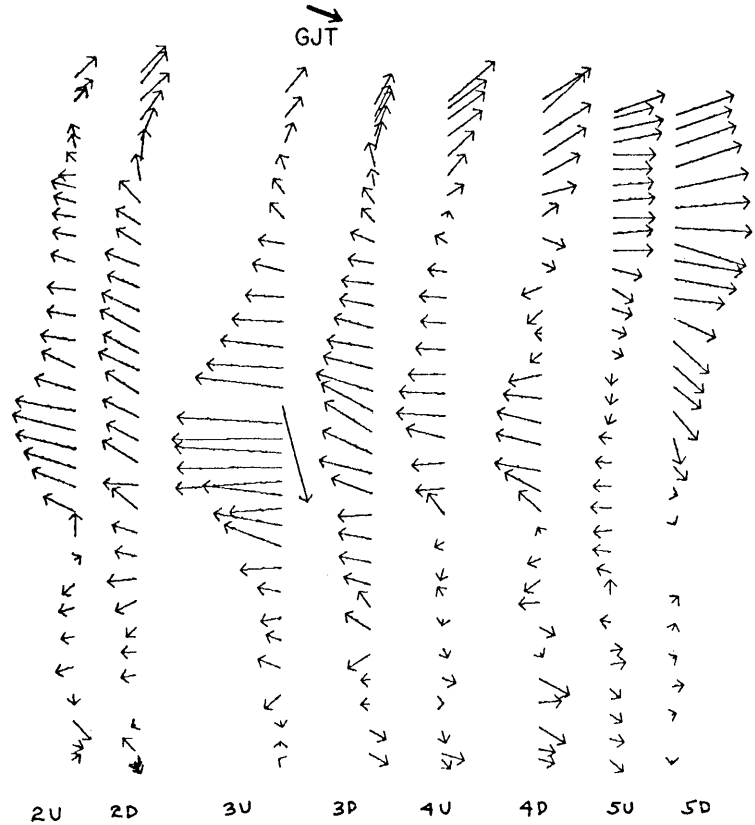
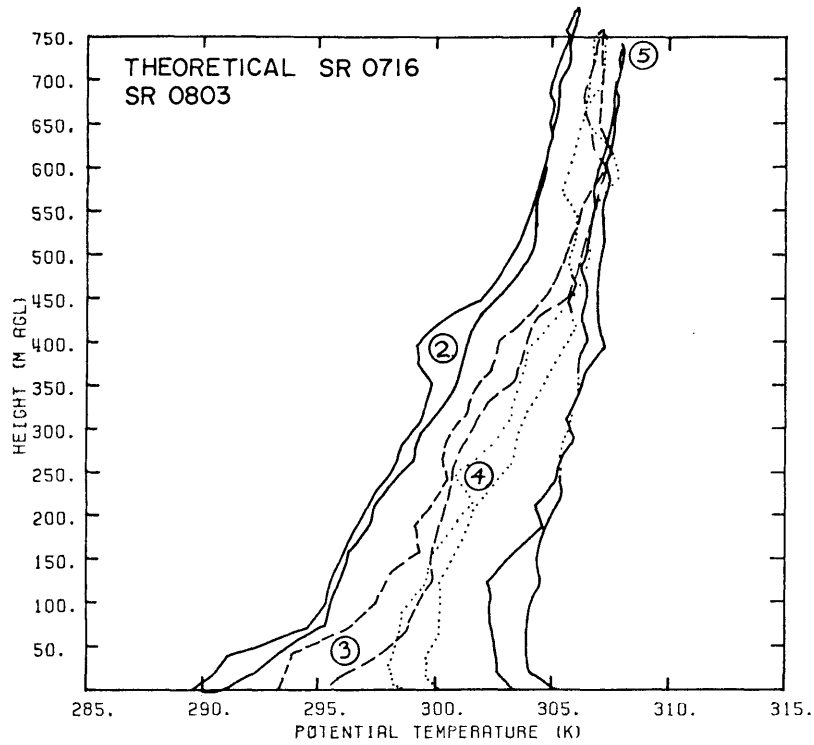
STEVE MILLER RES EDWARDS COLO
 DATE 07/09/78



#	TIME (MDT)	WEATHER	#	TIME (MDT)	WEATHER	#	TIME (MDT)	WEATHER
16U	0714-0742	CLR (FEW Ac FAR	17U	0828-0859	CLR	18U	0942-1002	⊙ Ac
16D	0742-0816	E OVR MTNS)	17D	0859-0929	⊙ Ac	18D	1002-1023	5/10 Ac + 1/10 Cl

Figure 97. Tethersonde data. Eagle Valley, 9 July 1978.

STEVE MILLER RES EDWARDS COLO
 DATE 10/11/78



#	TIME (MDT)	WEATHER	#	TIME (MDT)	WEATHER
2U	0722-0738	DC; ALQDS	4U	0916-0930	FEW C; EAST
2D	0738-0755		4D	0930-0945	
3U	0820-0835	C; ALONG DIVIDE	5U	1015-1031	FEW C; EAST
3D	0835-0850		5D	1031-1045	

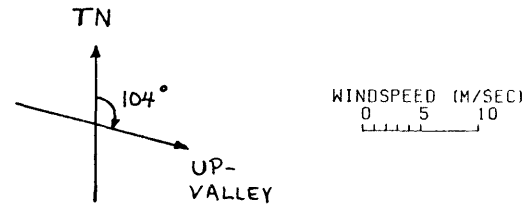
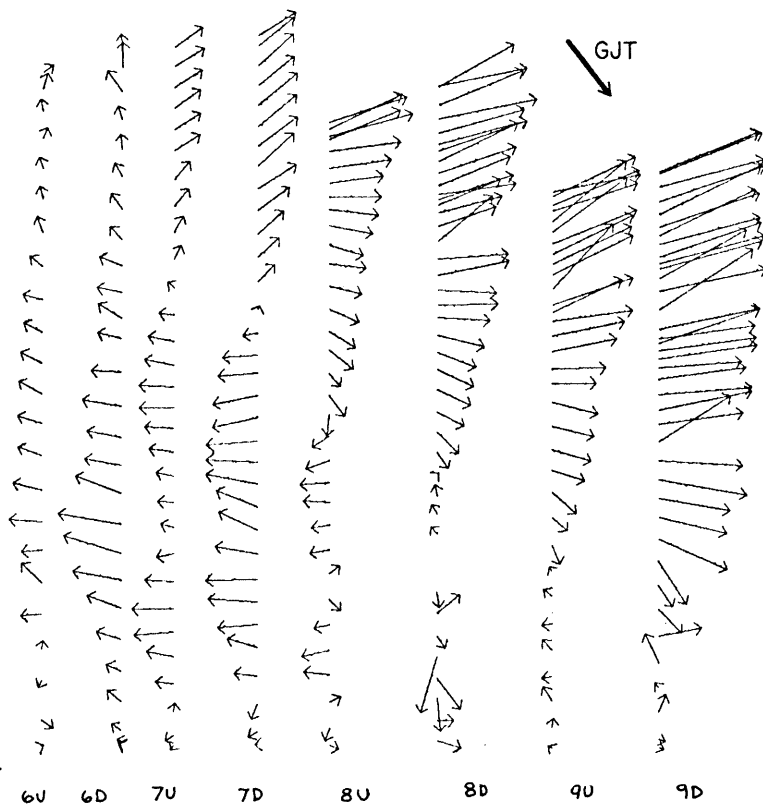
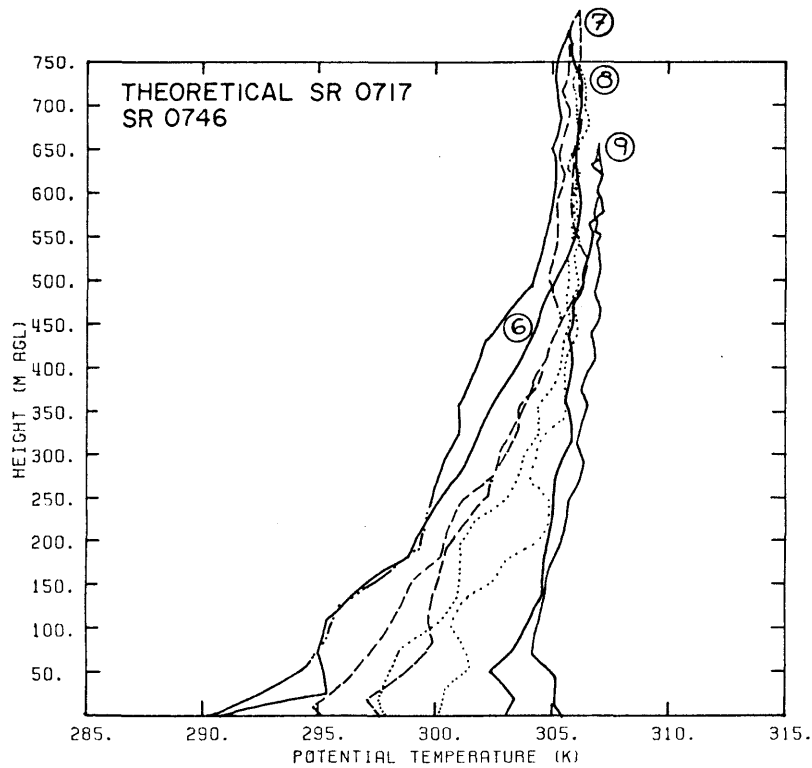


Figure 98. Tethersonde data. Eagle Valley, 11 October 1978.

STEVE MILLER RES EDWARDS COLO
 DATE 10/12/78



#	TIME (MDT)	WEATHER	#	TIME (MDT)	WEATHER
6U	0718-0728	C: EAST	8U	0914-0929	C: EAST
6D	0728-0742		8D	0929-0949	
7U	0828-0842	C: EAST OVER MTNS	9U	1004-1019	C: EAST & WEST
7D	0842-0857		9D	1019-1037	

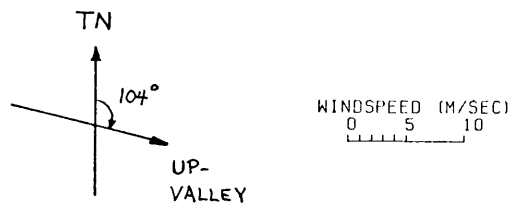
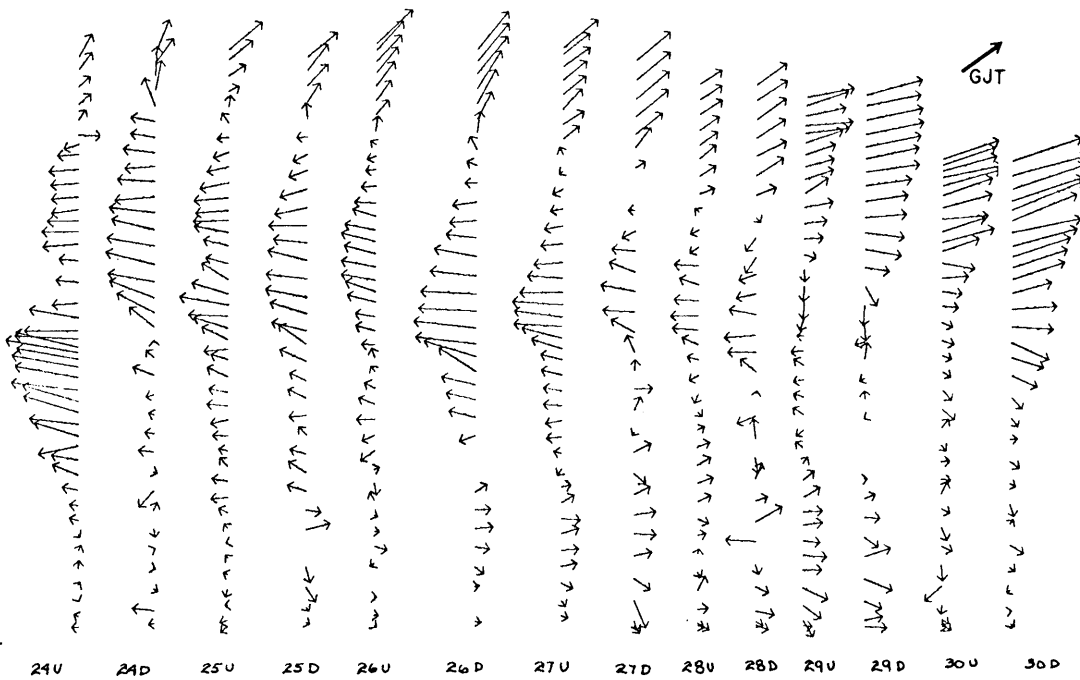
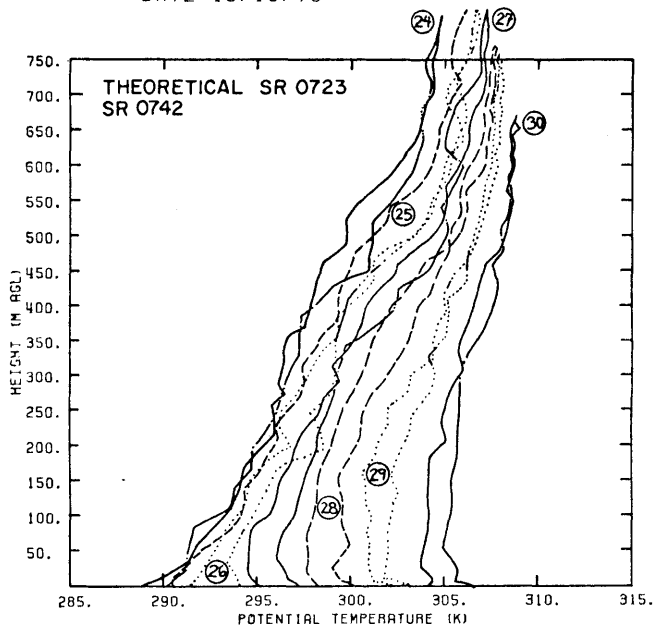
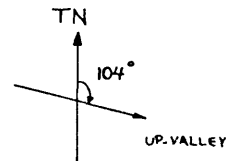


Figure 99. Tethersonde data. Eagle Valley, 12 October 1978.

STEVE MILLER RES EDWARDS COLO
DATE 10/19/78



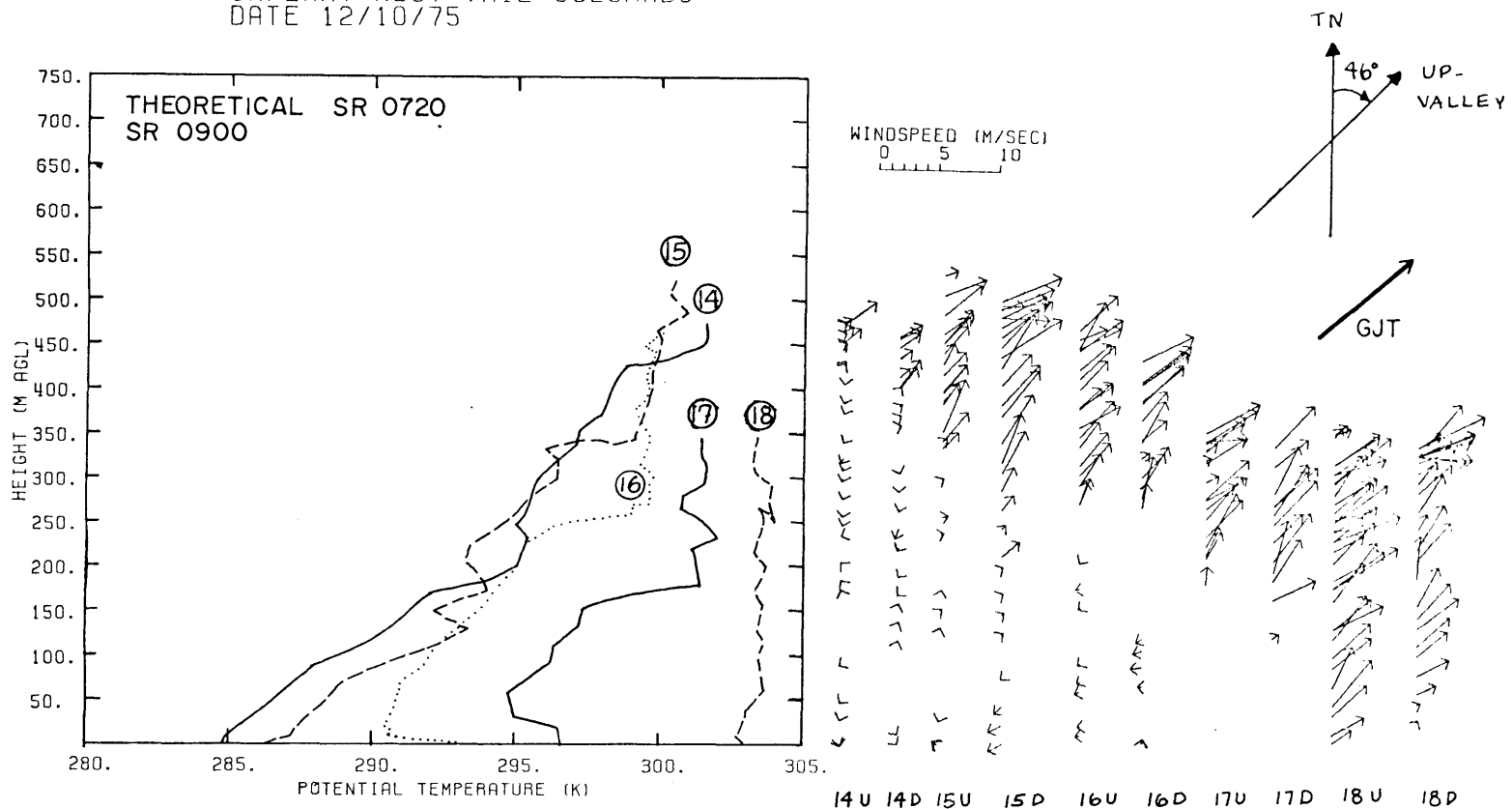
#	TIME (MDT)	WEATHER	#	TIME (MDT)	WEATHER	#	TIME (MDT)	WEATHER
24U	0720-0740	CLR	27U	0940-0959	CLR	30U	1150-1214	CLR (SMALL Cu)
24D	0740-0757		27D	0959-1013		30D	1214-1228	OUR RIDGETOPS
25U	0809-0828	CLR	28U	1026-1042	CLR			EAST + SOUTHEAST)
25D	0828-0844		28D	1042-1055				
26U	0854-0913	CLR	29U	1114-1131	CLR			
26D	0913-0930		29D	1131-1147				



WINDSPEED (M/SEC)
0 5 10

Figure 100. Tethersonde data. Eagle Valley, 19 October 1978.

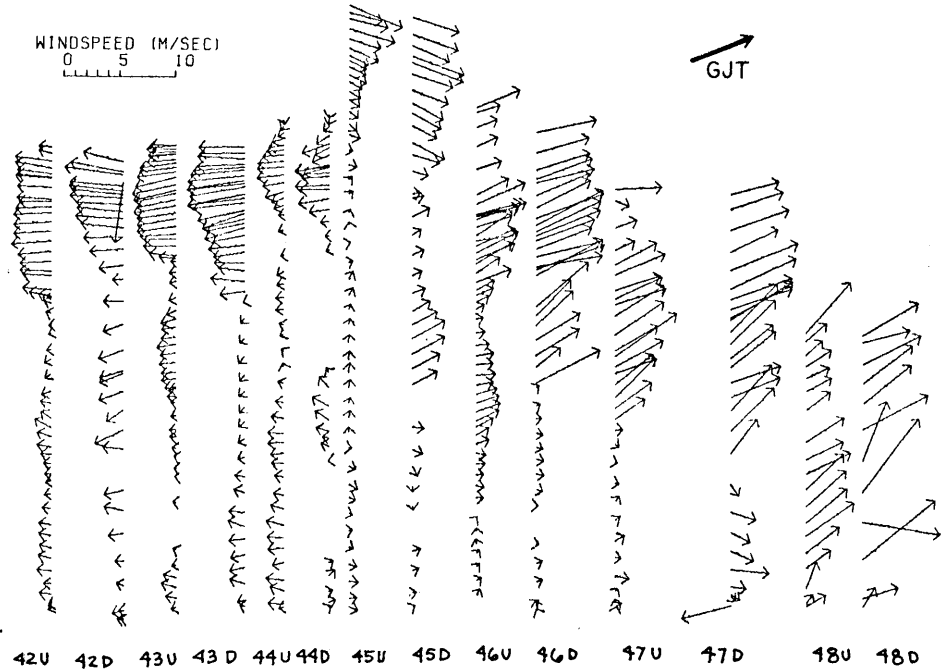
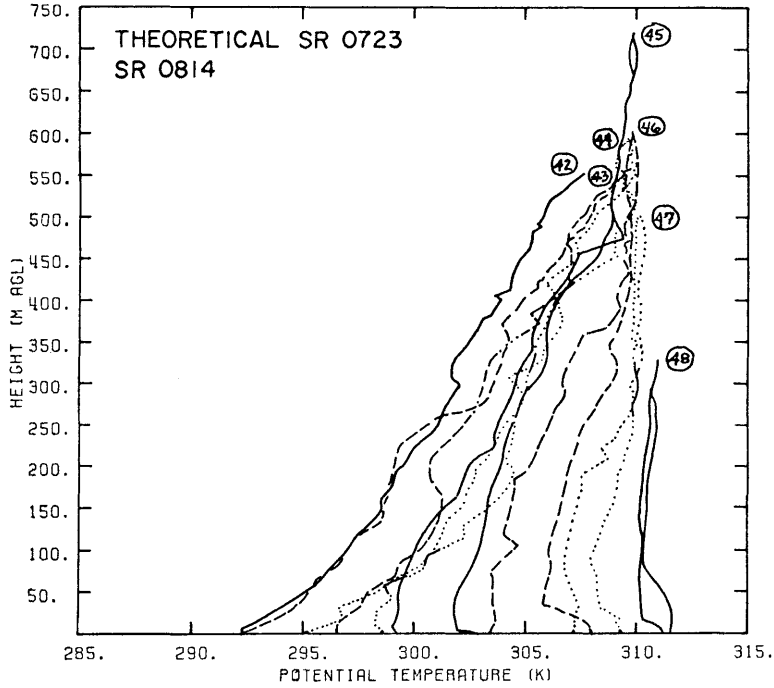
SAFeway WEST VAIL COLORADO
DATE 12/10/75



#	TIME (MST)	WEATHER	#	TIME (MST)	WEATHER	#	TIME (MST)	WEATHER
14U	0831-0850	CLEAR	16U	1002-1021	CLEAR	18U	1545-1604	
14D	0850-0907		16D	1021-1037		18D	1604-1621	
15U	0911-0932	CLEAR	17U	1100-1114				
15D	0932-0948		17D	1114-1127				

Figure 101. Tethersonde data. Gore Valley, 10 December 1975.

VAIL MUNI BLDG
DATE 10/19/77



#	TIME (MDT)	WEATHER	#	TIME (MDT)	WEATHER	#	TIME (MDT)	WEATHER
42U	0658-0721	CLR	45U	0928-0948	CLR	48U	1134-1143	CLR
42D	0721-0736		45D	0948-1006		48D	1143-1148	
43U	0747-0813	CLR	46U	1016-1039	CLR			
43D	0813-0833		46D	1039-1057				
44U	0838-0858	CLR	47U	1100-1114	CLR			
44D	0858-0919		47D	1114-1126				

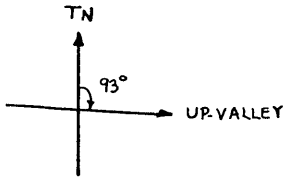
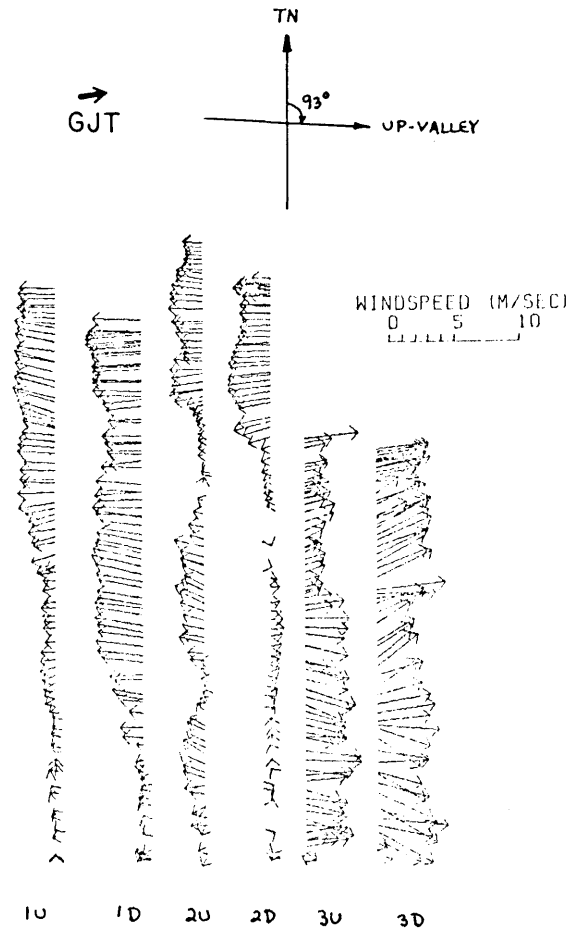
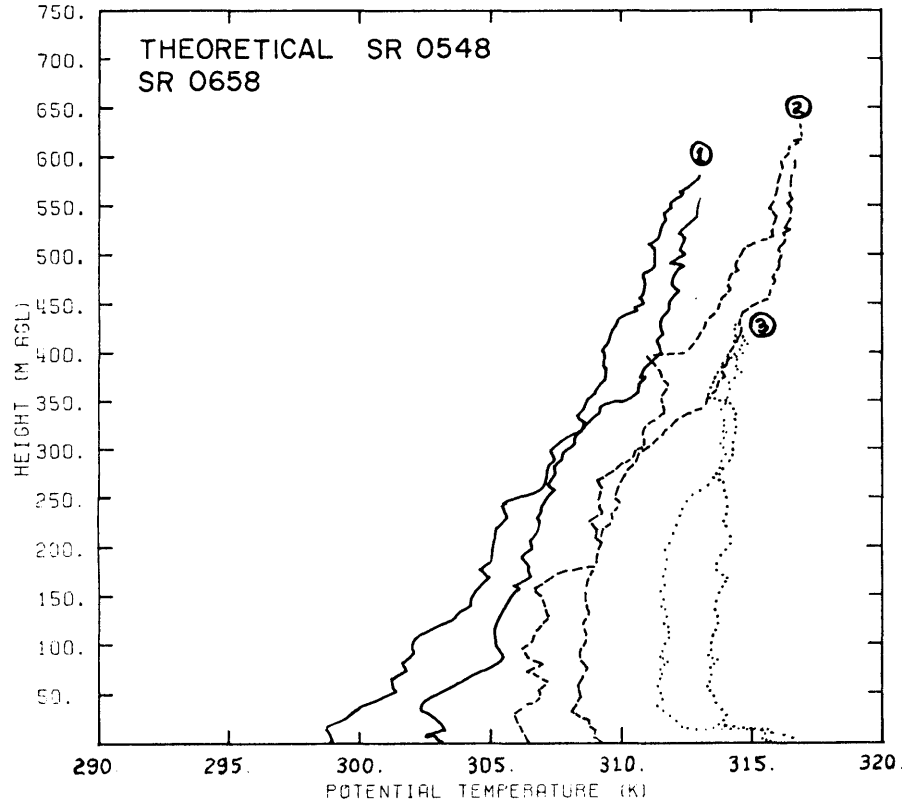


Figure 102. Tethersonde data. Gore Valley, 19 October 1977.

VAIL MUNICIPAL BUILDING COLO
 DATE 07/06/78



#	TIME (MDT)	WEATHER	#	TIME (MDT)	WEATHER	#	TIME (MDT)	WEATHER
1-U	0615-0639	CLR	2-U	0749-0816	CLR	3-U	0931-0952	CLR
1-D	0639-0705		2-D	0816-0842		3-D	0952-1011	

Figure 103. Tethersonde data. Gore Valley, 6 July 1978.

APPENDIX E

Extraterrestrial Solar Radiation

APPENDIX E

Extraterrestrial Solar Radiation

Solar radiation on a plane surface above the earth's atmosphere can be calculated using basic principles of spherical trigonometry. The basic formulas for solar fluxes on horizontal and inclined plane surfaces are:

$$Q_{Sh} = S_o \left(\frac{\bar{d}}{d}\right)^2 \cos Z \quad (71)$$

$$Q_{Si} = S_o \left(\frac{\bar{d}}{d}\right)^2 \cos \beta \quad (72)$$

where S_o is the so-called solar constant (1353 Wm^{-2}) defined as the solar flux on a plane surface perpendicular to the sun's rays at the mean earth-sun distance, \bar{d} . The factor $\left(\frac{\bar{d}}{d}\right)^2$ modifies the solar constant to account for the fact that the earth-sun distance, d , varies during the year as the earth travels in an elliptical orbit about the sun. The cosine terms account for the projection of solar flux onto the plane surfaces of interest. These terms are clearly a function of earth-sun geometry, depending on the time of day, day of year and latitude of the surface. Z and β are the angles between the normals to the surfaces and the direction to the sun. From spherical trigonometry (Sellers, 1965; Kreith and Kreider, 1978) these are given as:

$$\cos Z = \sin \phi \sin \delta + \cos \phi \cos \delta \cos h \quad (73)$$

$$\cos \beta = \cos Z \cos i + \sin Z \sin i \cos (a-a') \quad (74)$$

where

ϕ = latitude

δ = sun's declination

h = sun's hour angle, i.e., an angular measure of time reckoned from solar noon. One hour = 15° . $-30^\circ = 2$ hours before solar noon. $30^\circ = 2$ hours after solar noon.

i = inclination angle of plane surface (from horizontal)

a = azimuth angle of sun

a' = azimuth angle of normal to slope. a and a' are measured from south, - if counterclockwise, + if clockwise.

Combining Equations 72 and 74 and rewriting Equation 73, we get the two basic equations for solar flux on an inclined surface.

$$Q_{si} = S_o \left(\frac{\bar{d}}{d}\right)^2 \{\cos Z \cos i + \sin Z \sin i \cos (a-a')\} \quad (75)$$

$$\cos Z = \sin \phi \sin \delta + \cos \phi \cos \delta \cos h \quad (73)$$

In these equations both the declination, δ , and the factor $\left(\frac{\bar{d}}{d}\right)^2$ are a function of the day of year (D , from 1 to 365). McCullough (1968) gives some approximate analytical formulas that allow the calculation of these terms, utilizing the longitudinal of the earth (λ) in its orbit around the sun as reckoned from the earth-sun radius vector at vernal equinox ($D = D_o$). The formulas are:

$$\delta = \sin^{-1}(\sin \epsilon \sin \lambda) \quad (76)$$

$$\lambda = \omega(D-D_o) + 2e(\sin \omega D - \sin \omega D_o) \quad (77)$$

$$\left(\frac{\bar{d}}{d}\right)^2 = (1 - e \cos \omega D)^{-2} \quad (78)$$

where

$\epsilon = 23^\circ 26'$ = maximum solar declination

$\omega = 2\pi/365$

$D_o = 80$ = day of vernal equinox

$e = 0.0167$ = eccentricity of earth's orbit

The azimuth angle to the sun, a , is given by Sellers (1965) as

$$a = \sin^{-1} \left(\frac{\cos \delta \sin h}{\sin Z} \right) . \quad (79)$$

Using Equations 75, 73, 76, 77, 78, and 79, the extraterrestrial solar flux on an arbitrarily oriented plane surface can be calculated as a function of hour angle, h . Input to the equations must include information on the inclined surface including latitude, inclination, and azimuth, as well as the day of year for which calculations are required.

The equations are used to calculate the solar flux at any time from the hour angle of sunrise, h_{SR} , to the hour angle of sunset, h_{SS} . For a horizontal surface, the times of sunrise and sunset are generally specified in terms of half-day length, H , calculated from Equation 73 for $\cos Z = 0$, or

$$H = \cos^{-1} (-\tan \phi \tan \delta) . \quad (80)$$

Then

$$h_{SR} = -H \quad \text{and} \quad h_{SS} = H \quad (81)$$

For an inclined surface of finite extent, sunrise and sunset are given by Equation 81 if $a - a' < \pi/2$, i.e., if the slope is facing the sun at sunrise or sunset. If $a - a' \geq \pi/2$ at either sunrise or sunset, sunrise (sunset) will be later (earlier) than for a horizontal surface. In this case, Equation 74 can be solved for h_{SR} or h_{SS} with $\cos \beta = 0$.

Care must be taken when the above equations are utilized to calculate solar fluxes in the summer half-year ($\delta > 0$ in the Northern Hemisphere), since the arc sine function used in Equation 79 will return azimuth angles in the wrong quadrant when the sun rises or sets north of east or west. During these days the azimuth angles are

incorrect during the time when the sun is north of an east-west line through the site. The errors in Equation 79 can be detected and corrected by a computer algorithm.

Calculations using the above set of equations are made in terms of hour angle and are thus referenced to solar noon at a given site. To convert the times to actual clock times it is necessary to determine the actual clock time of solar noon and to adjust all the times accordingly. This is accomplished by the use of three corrections applied to the time of solar noon (12h 00m 00s) in the local solar time coordinate system (Waugh, 1973).

$$\begin{aligned} \text{Clock time of solar noon} &= 12\text{h } 00\text{m } 00\text{s} + \text{Equation of time correction} + \text{Longitude correction} + \text{Daylight time correction} \\ &= 12\text{h } 00\text{m } 00\text{s} + C_{ET} + C_L + C_{DT} \end{aligned}$$

First, the equation of time correction is applied by adding the appropriate number of minutes and seconds from Table 14. Second, a longitude correction accounting for the difference in geographical longitude between the site and the reference meridian of its time zone is applied. The correction is +4 minutes for each degree of longitude west of the meridian. The reference meridian for the Mountain Time Zone is 105° W longitude. Thus, for a site at 106° W longitude the correction is $C_L = 4(106^\circ - 105^\circ) = +4$ minutes. Finally, if daylight time is in effect a further correction, $C_{DT} = +1\text{h}$, must be added. In the United States, daylight time is in effect from the last Sunday in April to the last Sunday in October.

The day of the year, D, on which these Sundays fall varies from year to year, but is calculable using a simple computer algorithm (ASHRAE, 1975).

Table 14

Equation of Time Correction

D*	C _{ET} **	D	C _{ET}						
1	3m 12s	91	4m 08s	181	3m 21s	271	-9m 06s	361	0m 47s
16	9 32	106	-0 01	196	5 46	286	-13 33		
31	13 24	121	-2 51	211	6 21	301	-16 06		
46	14 16	136	-3 44	226	4 44	316	-15 53		
61	12 23	151	-2 33	241	1 07	331	-12 34		
76	8 39	166	0 10	256	-3 50	346	-6 34		

* D = day of year

** C_{ET} = equation of time correction (minutes and seconds)

307257